NASA CR-135078
R76AEG461

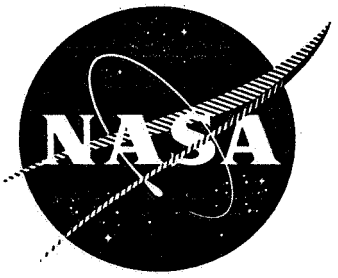

FIBER COMPOSITE FAN BLADE IMPACT IMPROVEMENT PROGRAM

Final Report

by

T.L. Oller

GENERAL ELECTRIC COMPANY

prepared for

NATIONAL AERONAUTICS AND SPACE ADMINISTRATION

c 8

NASA-Lewis Research Center

NASA3-17836

1. Report No.	2. Government Accession No.	3. Recipient's Catalog No.
CR 135078		

4. Title and Subtitle	5. Report Date
FIBER COMPOSITE FAN BLADE IMPACT IMPROVEMENT PROGRAM FINAL REPORT	December 1976
	6. Performing Organization Code
7. Author(s)	8. Performing Organization Report No.
T.L. Oller	R76AEG461
	10. Work Unit No.
9. Performing Organization Name and Address	11. Contract or Grant No.
General Electric Company 1 Jimson Road Cincinnati, Ohio 45215	NAS3-17836
	13. Type of Report and Period Covered
12. Sponsoring Agency Name and Address	Contractor Report
National Aeronautics and Space Administration Washington, D.C. 20546	14. Sponsoring Agency Code

15. Supplementary Notes

Technical Adviser, James Faddoul
NASA-Lewis Research Center, Cleveland, Ohio 44135

16. Abstract

This report describes the results of a 20-month program, beginning in June 1974, designed to investigate parameters which effect the foreign object damage resulting from ingestion of birds into fan blades of a QCSEE-type engine. Work performed on this program included the design, fabrication, and impact testing of QCSEE fan blades to demonstrate improvement in FOD resistance relative to existing blades and also the design and demonstration of a pin root attachment concept.

In the first phase of the program, it was found that, in general, for the small objects used, the strains in the blade are proportional to the mass of the impacting object and the square of the relative velocity component normal to the blade chord at the impact location. These parameters can be further combined into an average or nominal force normal to the blade at the impact location. A finite element computer program gave results that compare well with the test data. In the second phase of the program four improved blades exhibited substantial improvement in FOD resistance relative to former designs.

17. Key Words (Suggested by Author(s))	18. Distribution Statement
Composite Blades Fan Blades Aircraft Propulsion and Power Impact Analysis	

19. Security Classif. (of this report)	20. Security Classif. (of this page)	21. No. of Pages	22. Price*
Unclassified	Unclassified	170.	

* For sale by the National Technical Information Service, Springfield, Virginia 22151

NASA-C-168 (Rev. 6-71)

TABLE OF CONTENTS

LIST OF ILLUSTRATIONS

LIST OF ILLUSTRATIONS (Continued)

LIST OF ILLUSTRATIONS (Continued)

LIST OF ILLUSTRATIONS (Continued)

LIST OF ILLUSTRATIONS (Concluded)

LIST OF TABLES

1.0 SUMMARY

This report describes the results of a 20-month program designed to investigate parameters which effect the foreign object damage resulting from ingestion of birds into fan blades of a QCSEE-type engine and to design, fabricate, and impact test QCSEE fan blades which show improvement in FOD resistance relative to existing blades. In order to accomplish these objectives, two phases of effort were accomplished. In the first phase, strain-gage-instrumented QCSEE-type fan blades were single-blade impacted in a Whirligig facility at selected impact conditions using small RTV projectiles while the resulting dynamic strains in the blades were recorded. Nine instrumented impacts were conducted. The mass of the impacting projectile was small [14 to 28 gm. (1/2 to 1 ounce)] in order to ensure elastic behavior in the blades and the strain gages. The impact strain data was also compared to results obtained from a finite element computer program. In the second phase of the program, four improved QCSEE-type fan blades were designed, fabricated and impact tested. A pin root attachment concept was also investigated from an impact standpoint in this phase.

In the first phase of the program, it was found that, in general, for the small objects used, the strains in the blade are proportional to the mass of the impacting object and the square of the relative velocity component normal to the blade at the impact location. These parameters can be further combined into an average or nominal force normal to the blade at the impact location. In general, the finite element computer program gave results that compare well with the test data. In the second phase of the program, the four improved blades exhibited substantial improvement in FOD resistance relative to former designs.

2.0 INTRODUCTION

Over the last several years, General Electric has been conducting a continuous effort under NASA-sponsored and other related programs directed at improvement of composite blade foreign object impact damage resistance. Field service reports for both commercial and military operations indicate the severity of the FOD problem. High incident rates of bird strikes occur, particularly during takeoff and landing phases of the flight envelope. Of the incidents listed, a fairly high percentage cause damage to the engine.

Engine FOD capability requirements are quantatively defined by FAA specifications. The QCSEE engine will be required to absorb the impact of 16 starlings, eight 0.68 kg (1.5 lb) birds or one 1.8 kg (4 lb) duck. To satisfy these specifications, it will be necessary for the engine to sustain little or no damage during starling ingestion, to be able to maintain 75 percent engine thrust following the eight 0.68 kg (1.5 lb) bird ingestions, and to have a safe engine shutdown with all damage being contained within the engine casing following a 1.8 kg (4 lb) bird ingestion.

In order to maintain engine thrust after starling or 0.68 kg bird impacts, rotor unbalance must be held to a low value. This requirement makes it manditory that fan blades exhibit little or no loss of material when subjected to up to 0.68 kg bird impacts.

QCSEE single-blade Whirligig impact testing conducted in 1974 revealed that the candidate fan blade exhibited unacceptable local impact damage. For a 0.91 kg (2 lb) bird impact at takeoff conditions, the blade lost over 60 percent of its original weight and was completely delaminated. An extensive posttest failure analysis of the impacted blade was conducted to gain insight into the failure characteristics of the blade. Among the items analyzed were high speed motion pictures of the impact, dye penetrant inspection, ultrasonic inspection and scanning electron micropscopy of the damaged blades. The general conclusion reached from the data was:

- The blades failed because of the low interlaminar shear strength of the materials used. This was, in turn, caused by the low bond strength between the untreated graphite and Kevlar fibers and the resin.

To improve the impact resistance of the QCSEE-type blades, the current program, which was already underway, was redirected in July, 1975. The original program was intended to develop a pin root attachment concept as a backup to the circular keyhole/outsert attachment used on the QCSEE blade. Since the pin root attachment had been designed and hardware procurement already was underway when the redirection occurred, the pin root concept was carried through into the current program and a pin root blade was fabricated and impact tested.

The purpose of the redirected program was two fold:

- To investigate the effect of various impact parameters such as fan speed, bird slice weight, span, and incidence angle on the impact severity due to bird strikes.

- To design, fabricate, and whirligig impact test four new types of blade designs to evaluate their impact resistance relative to existing blades. All blades were fabricated using existing QCSEE blade tooling, thus geometry was constant.

To accomplish the first objective, a series of existing QCSEE composite blades were whirligig tested at various impact conditions. Three of these blades were instrumented with strain gages.

Those impact parameters that most greatly affect FOD to composite fan blades were defined based upon data generated in this test series. A finite element computer program was also utilized to calculate the strain at the locations where strain gages were installed on the blade. Comparisons between the strains from the computer model and the test data were made.

The second objective was accomplished through the design of the internal laminate configuration, fabrication, and testing of a series of four QCSEE-type composite fan blades. Each of these blades incorporated different materials and/or laminate designs that were expected to have a positive influence on FOD tolerance improvement. Specimen testing of various materials and layup configurations was conducted to help define improved material systems to be used in the blades. All blades were designed to meet frequency, stability, and strength criteria required for satisfactory engine operation. One blade of each of the four designs was fabricated. The tooling for molding these blades was the same tooling as that used for the QCSEE variable pitch fan blades (Reference 1).

Each of the four blades was impact tested in the whirligig facility. All blades were tested using the same slice size, incidence angle and relative velocity. velocity.

3.0 EVALUATION OF IMPACT PARAMETERS

To establish those parameters which have the greatest influence on blade impact damage and FOD resistance, a series of "same-design" composite blades supplied by the QCSEE program were whirligig tested at various impact conditions. Three of these blades were instrumented with strain gages.

The impact slice sizes were small [14 to 18 grams (1/2 to 1 ounce)] to assure blade response would be elastic and to avoid destruction of the strain gages. A finite element computer program was also utilized to calculate the strain at the locations where strain gages were installed on the blade. Comparisons between the strains from the computer model and the test data were made.

3.1 BLADES USED

The four blades used for this test series were preliminary QCSEE UTW composite blades as fully described in Reference 1. The blade configuration is shown in Figure 1. The blade molded configuation consisted of a solid composite airfoil and staight bell-shaped composite dovetail. The molded blade leading edge was slightly reduced in thickness along the entire span to allow space for nickel plate leading edge protection. The correct aerodynamic airfoil profile was established when the nickel plate was installed. An aluminum outsert was bonded to the dovetail to provide a bearing surface at the blade/trunnion interface. This circular outsert concept permits the blade to rotate about the root upon sufficienlty high impact forces, thereby absorbing some of the impact energy.

A summary of the aero blade parameters is presented in Table I. The blade chord, maximum thickness, stagger angle, and camber are plotted as a function of blade span in Figures 2, 3, 4, and 5, respectively.

The airfoil definition is described by 15 radially spaced airfoil cross sections which are stacked on a common axis. These are shown along with details of the blade cross sections in Figure 6. Each section location corresponds to the like designated elevation defined on the blade, Figure 1. The dotted portion of the leading edge defines the aero profile and the solid inner portion describes the molded composite cross section.

The material and ply arrangement for the QCSEE composite blades is based on previous development efforts which led to the selection of a combination of fibers in a single blade to provide the proper frequency responses to satisfy STOL engine conditions. Figure 7 shows the general ply shapes, layup arrangement, fiber orientations and material in each ply of the blade. Figure 8 shows a trimetric view of the general arrangement

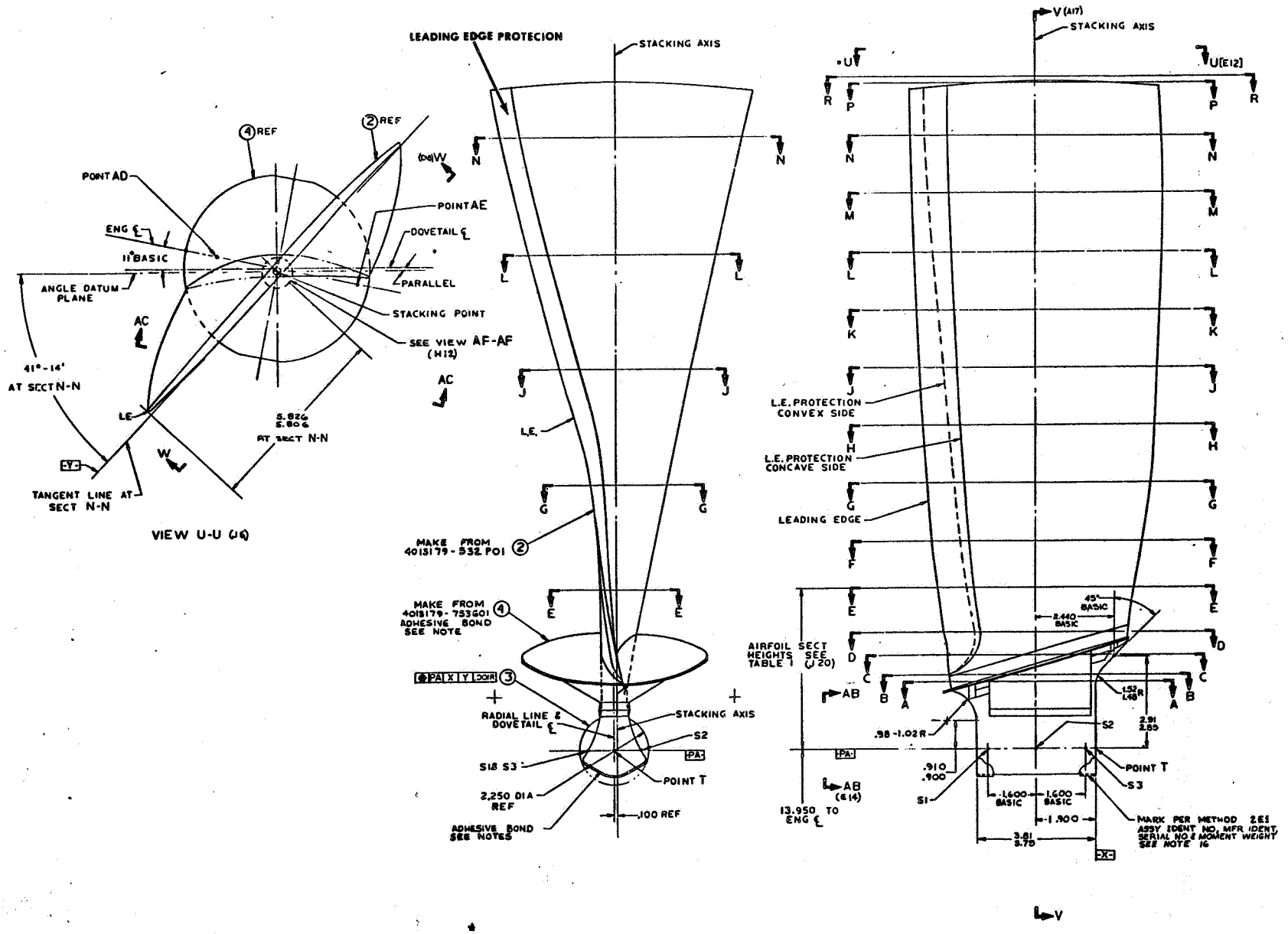

Figure 1. UTW Composite Fan Blade.

Table I. QCSEE UTW Composite Fan Blade Design Summary.

Aero Definition	
Tip Speed	306 m/sec (1005 ft/sec)
Tip Diameter	180 cm (71 in.)
Radius Ratio	0.44
Number of Blades	18
Bypass Pressure Ratio	1.27 Takeoff
Aspect Ratio	2.11
Tip Chord	30.3 cm (11.91 in.)
Root Chord	14.8 cm (5.82 in.)
T_M Root	1.92 cm (0.76 in.)
T_M Tip	0.91 cm (0.36 in.)
Root Camber	66.2°
Total Twist	45°
Solidity	
Tip	0.95
Root	0.98

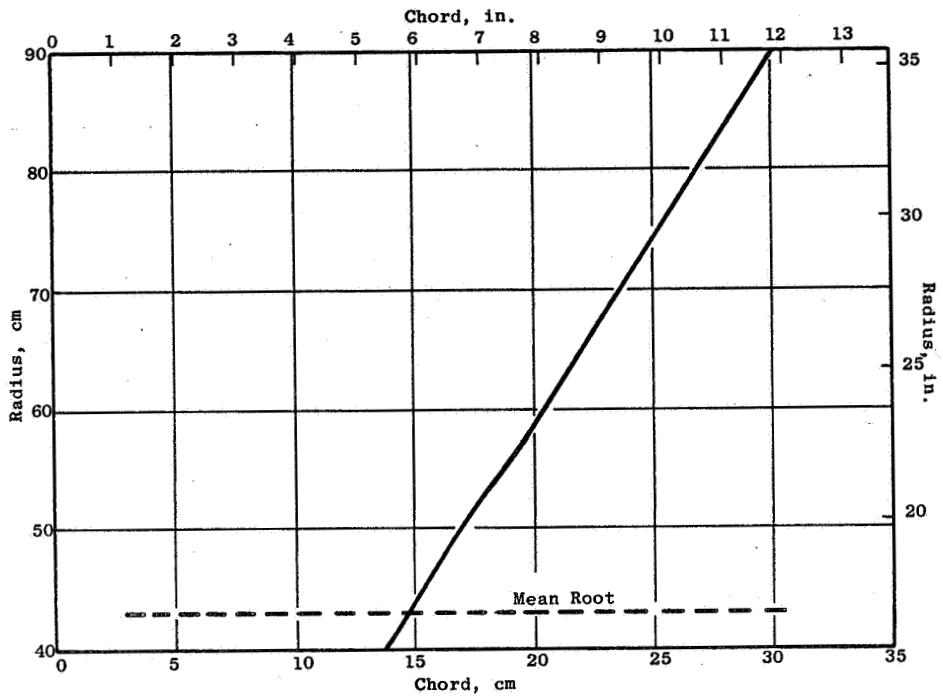

Figure 2. UTW Blade Chord Radial Distribution.

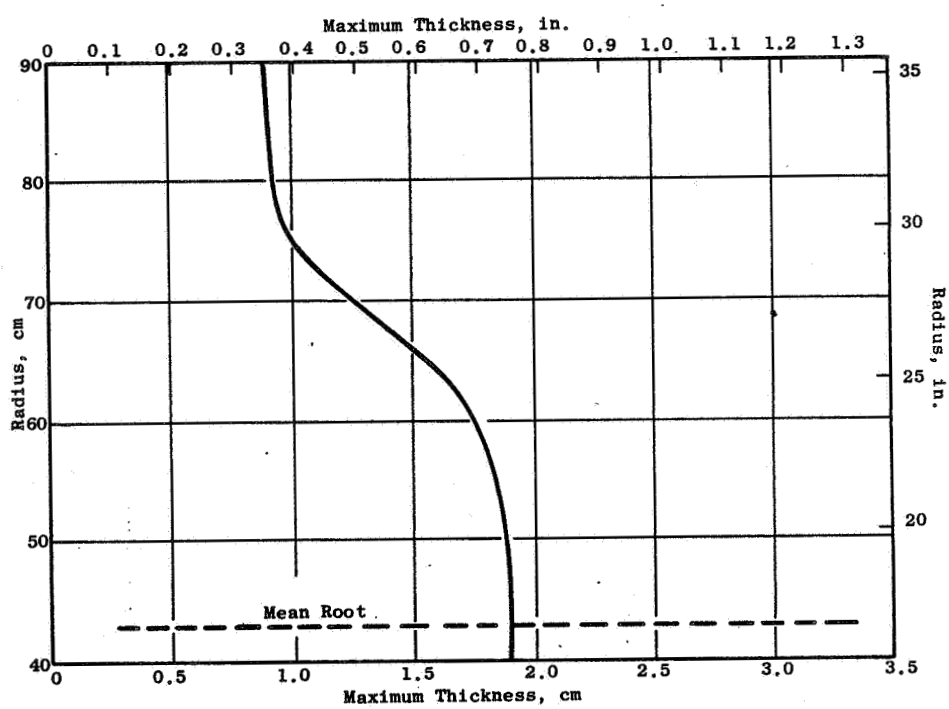

Figure 3. UTW Blade Max. Thickness Radial Distribution.

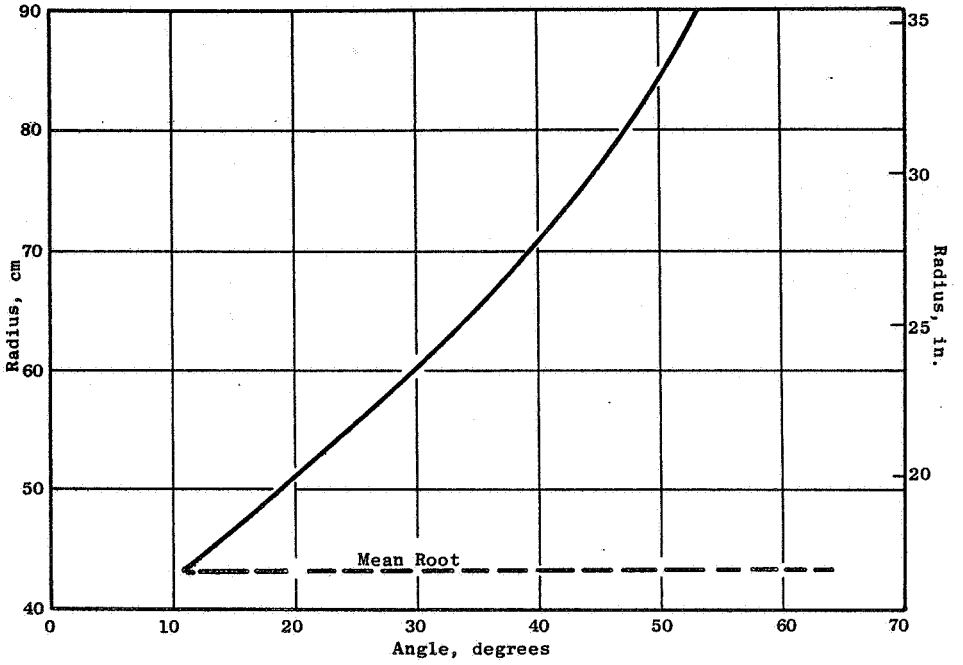

Figure 4. UTW Blade Stagger Angle Radial Distribution.

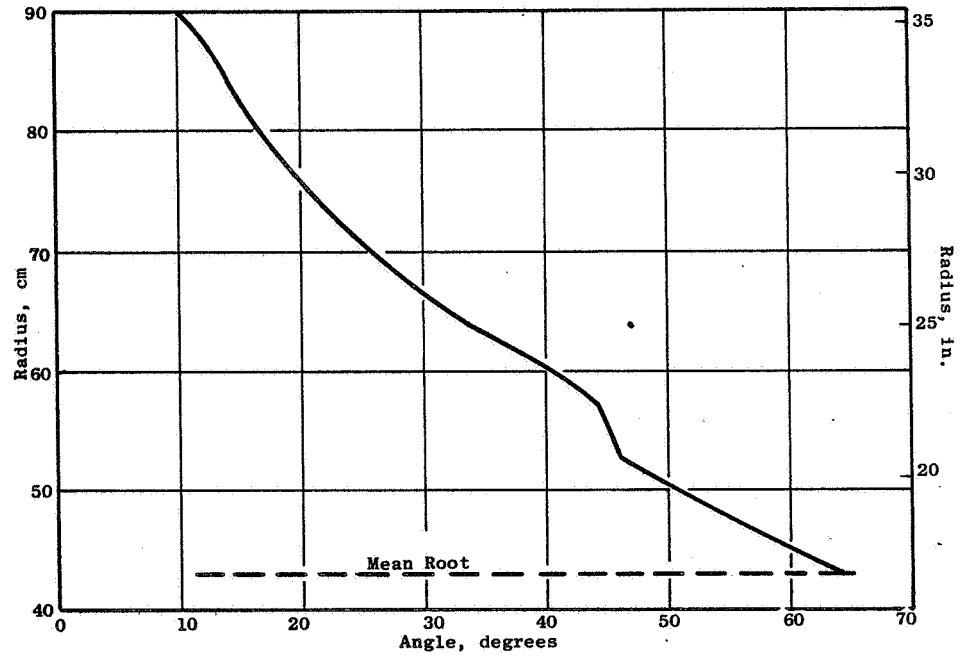

Figure 5. UTW Blade Camber Angle Distribution.

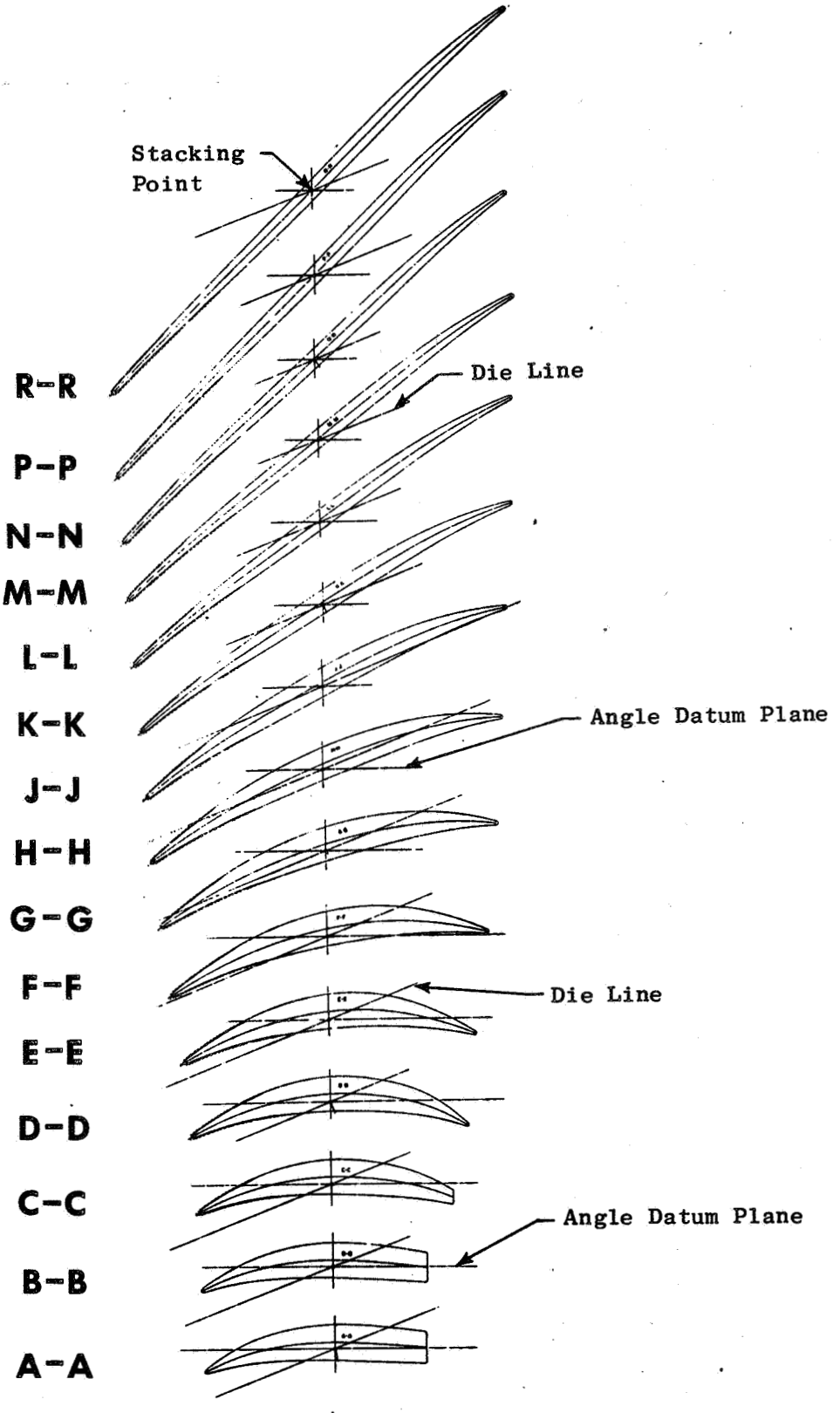

Figure 6. Blade Airfoil Sections.

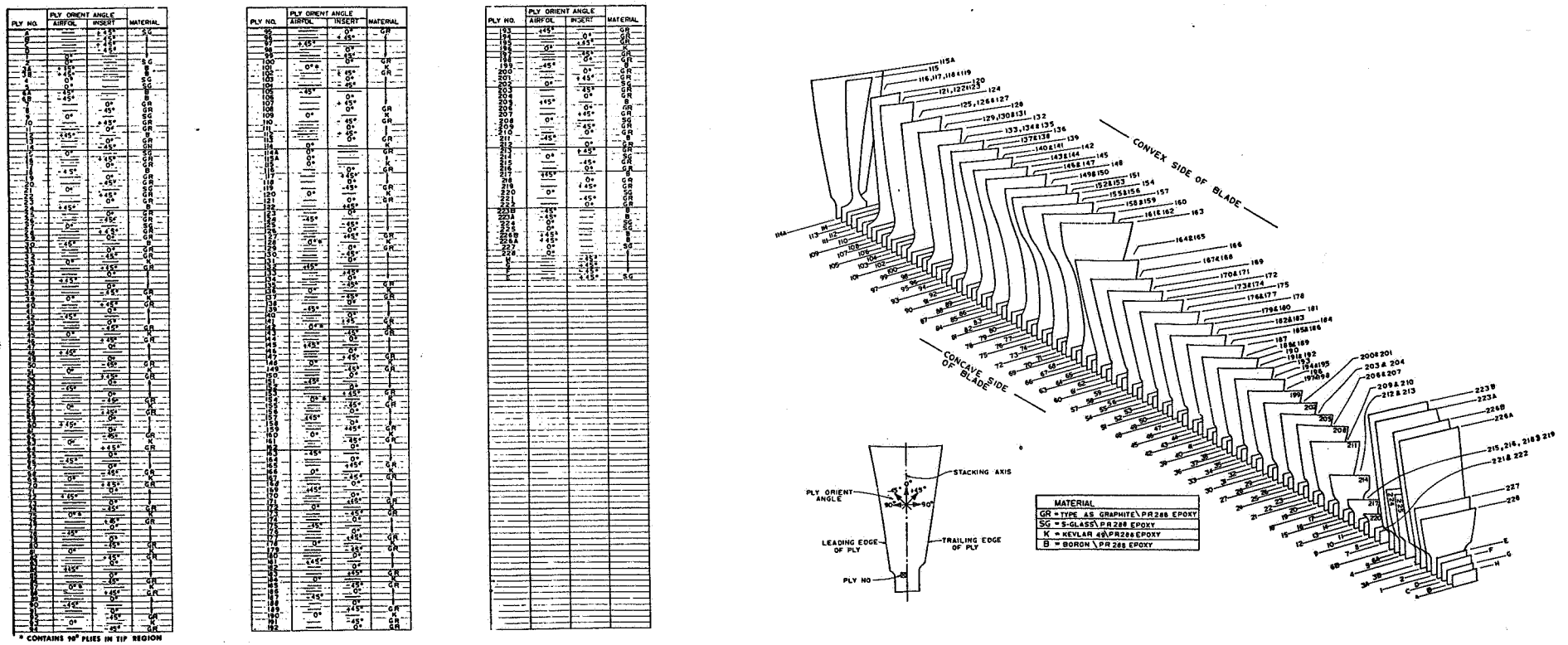

Figure 7. Ply Layup and Material Arrangement.

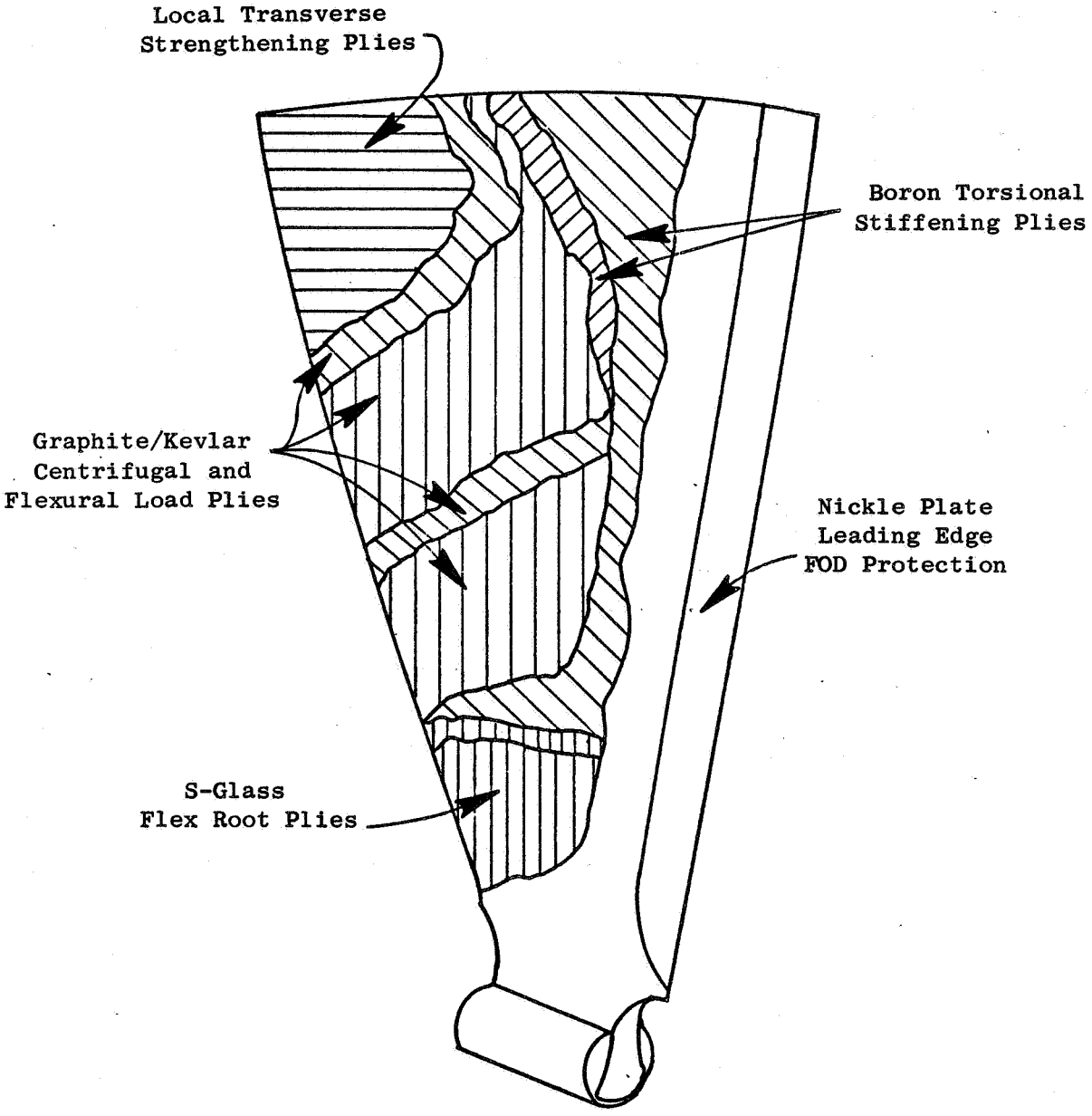

Figure 8. QCSEE UTW Composite Blade.

of the plies in the blade. Torsional stiffening plies in the airfoil region of the blade are oriented at ± 45 degrees to provide the shear modulus required for a high first torsional frequency. These plies contain boron towards the outer surfaces of the blade and graphite in the inner regions. Plies of Kevlar-49 are interspersed throughout the blade with their fibers being oriented in the longitudinal direction of the blade. Several Kevlar-49 plies in the tip region of the blade are oriented at 90 degrees to the longitudinal axis to provide chordwise strength and stiffness to the blade. S-glass plies are included on the surface of the blade in the root region for increased root flexibility.

The resin system used is a product of the 3M Company and is designated as PR288. Material properties for the various fibers and the resin used are shown in Table II.

A summary of the blade frequencies and weights for the specific blades used for this testing are shown in Table III.

Figure 9 presents the strain gage map used. Blades QP010, QP013, and QP014 were instrumented and strain data were recorded for the first nine tests. Gage locations were selected to correspond to the centers of the elements in the finite element computer model to allow direct comparison between test and analysis (Figure 10).

The strain gage used was an FAE-125-35-S6E. This gage, purchased from BLH, Inc., was selected because of its good elongation properties. It is a 0.32 cm (1/8 inch) long gage made of Constantan 400 foil and has an elongation capability of three to five percent. The dynamic capability of this gage has been demonstrated on previous programs to be well over 20 kHz.

The cement, BR610 a standard strain gage cement, was purchased from W.T. Bean, Inc., and is rated between three and seven percent elongation depending on test conditions. It is a thermosetting epoxy and requires a heat cure of two hours at 135° C (275° F) minimum.

The jumper wires and lead wires were standard Teflon-coated stranded copper. The jumpers were 36 AWG; the leadout wire was 30 AWG.

The lead wires on the blade airfoil were held down with "Metlbond 329". This is a thermosetting metal-filled epoxy on a synthetic fiber cloth carrier. The cure temperature was 135° C (275° F) for 1.5 hours minimum.

Readout was on a constant DC voltage bridge balance circuit with a five VDC supply. Output was recorded on magnetic tape at a speed of 152 cm/sec (60 in./sec). Strain data versus time was then transferred to graphical form for analysis.

3.2 TEST APPARATUS

The facility, shown schematically in Figure 11, consists of a 0.75 Mw (1000 horsepower) drive motor, a variable-speed output magnetic clutch, a

Table II. Composite Material Properties.

	AU PR288 Graphite	PR288 Boron	PR288 S-Glass	PR288 Kevlar 49
Fiber Volume, Percent	60	55	60	60
Elastic Modulus, 10^6N/cm^2 (10^6 psi) (0° Orientation)	11.9 (17.2)	20.0 (29.0)	5.9 (8.5)	7.6 (11.0)
Elastic Modulus, 10^6N/cm^2 (10^6 psi) (90° Orientation)	1.1 (1.6)	1.2 (1.8)	0.8 (1.1)	0.6 (0.8)
Elastic Modulus, 10^6N/cm^2 (10^6 psi) (0/22/0/-22 Orientation)	9.5 (13.8)	11.7 (17.0)	4.7 (6.8)	5.9 (8.6)
Shear Modulus, 10^6N/cm^2 (10^6 psi) (0/22/0/-22)	1.1 (1.6)	1.9 (2.7)	0.6 (0.9)	0.6 (0.93)
Density, G/cm^3 (lb/in^3)	1.5 (0.056)	1.9 (0.070)	2.0 (0.072)	1.4 (0.050)
Tensile Strength, kN/cm^2 (ksi) (0°)	138 (200)	138 (200)	138+ (200+)	138 (200)
Tensile Strength, kN/cm^2 (ksi) (0/22/0/-22)	95 (138)	95 (138)	95+ (138+)	95 (138)
Flex Strength, kN/cm^2 (ksi) (0°)	193 (280)	---	---	62 (90)
Flex Strength, kN/cm^2 (ksi) (0/22/0/-22)	168 (244)	---	172 (250)	59 (85)
Shear Strength, kN/cm^2 (ksi) (0°)	7 (10)	7.6 (11.0)	8.1 (11.8)	3.4-7 (5-10)
Charpy Impact, m-N (ft-lb) (±10°)	20 (15)	10 (7.5)	47 (35)	23 (17)

Table III. Blade* Frequency Characteristics.

S/N	Measured Frequency, Hz					Weight,	
	1F	2F	1T	3T	2T	kg	lb
QP010	58	190	285	430	672	2.24	4.94
QP013	62	190	284	420	662	2.24	4.94
QP014	67	190	284	424	664	2.24	4.94

* Material AU/Boron/S-Glass/Kelvar

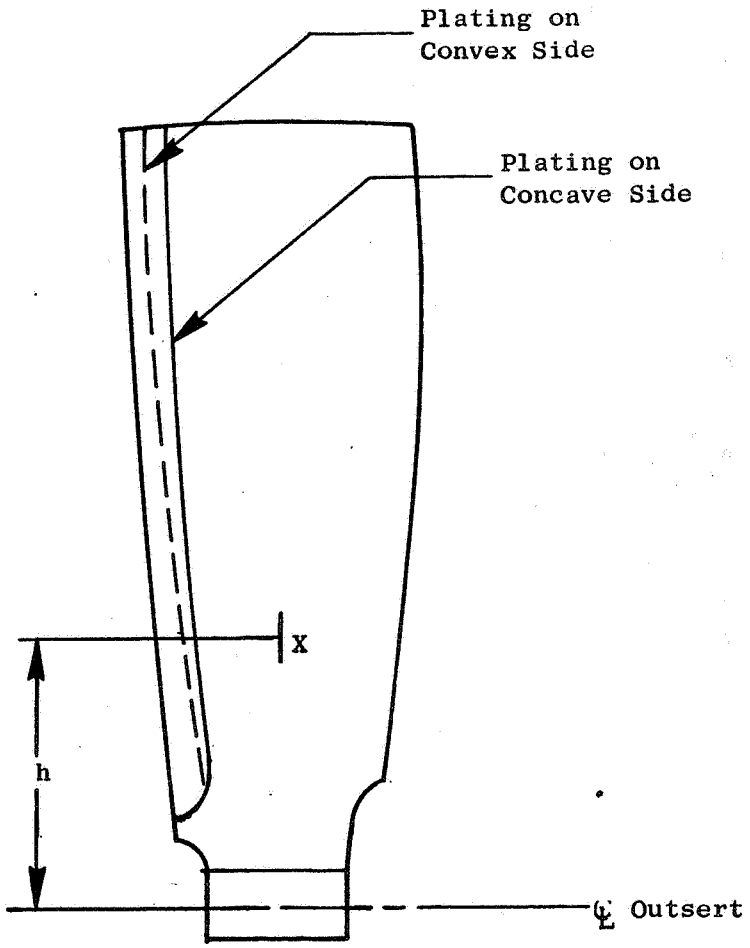

GAGE	h		X		SIDE	DIRECTION
	cm	in.	cm	in.		
1	43.26	17.03	6.20	2.44	CX	Radial
2	43.26	17.03	9.78	3.85		Chordal
3	38.51	15.16	5.66	2.23		Chordal
4	33.73	13.28	4.98	1.96		Radial
5	24.21	9.53	3.91	1.54		Chordal
6	24.21	9.53	7.09	2.79		Radial
7	19.43	7.65	3.68	1.45	CX	Radial
8	19.43	7.65	3.56	1.40	CV	Radial
9	19.43	7.65	6.71	2.64	CX	Chordal
10	19.43	7.65	6.53	2.57	CV	Chordal
11	4.45	1.75	.89	.35	CX	Radial
12	4.52	1.78	8.69	3.42	CX	Radial

CX - Convex Side
CV - Concave Side

NOTES: h, measured from outsert ℄
X, measured from blade leading edge except gages 11 and 12 measured from outsert leading edge

Each blade to be instrumented with 10 of the 12 gages in the table above. Omit 2 gages on each blade according to the table below.

Blade	Omit
QP010	8, 10
QP013	8, 10
QP014	1, 2

Figure 9. Blade Gage Map.

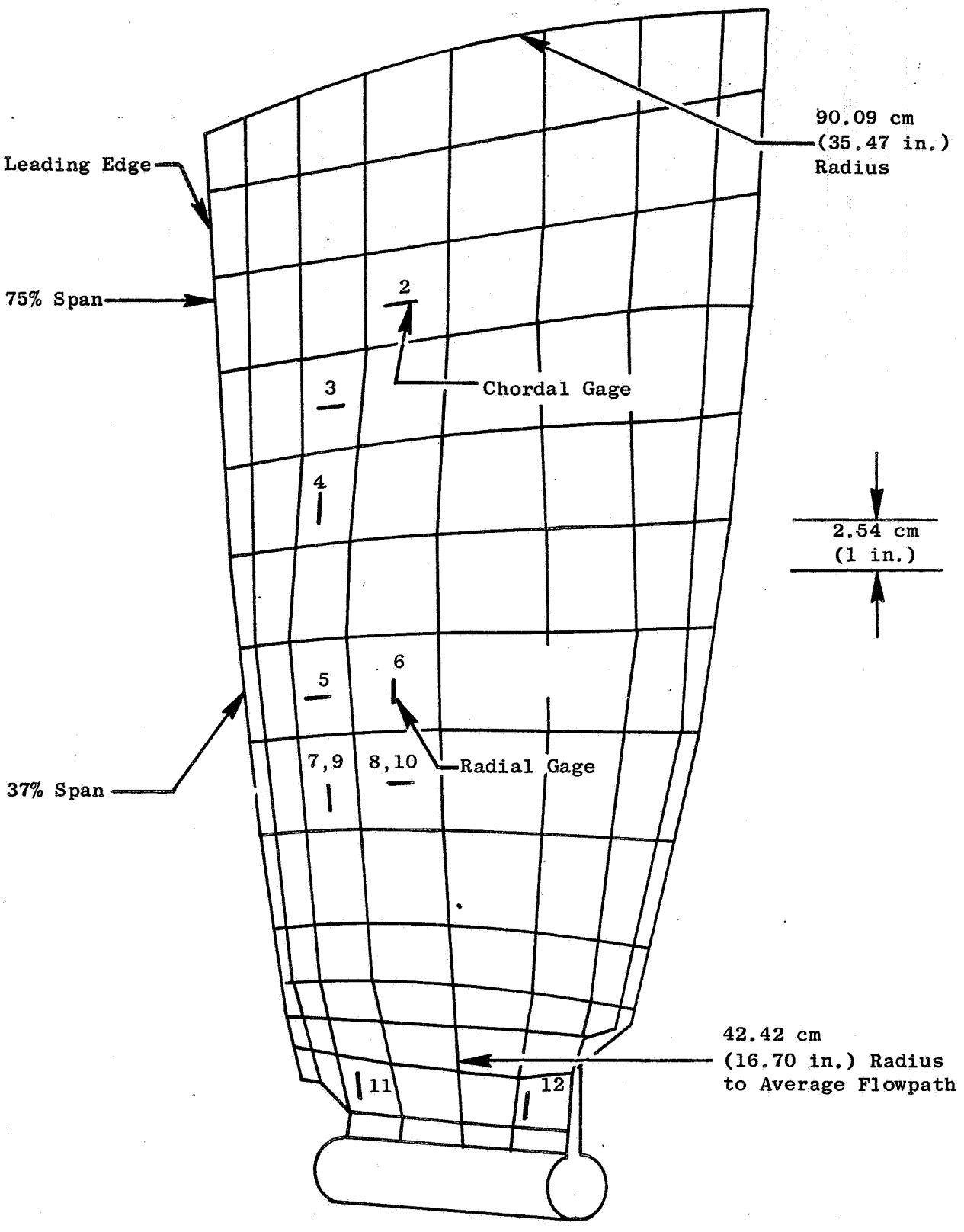

Figure 10. Strain Gage Map.

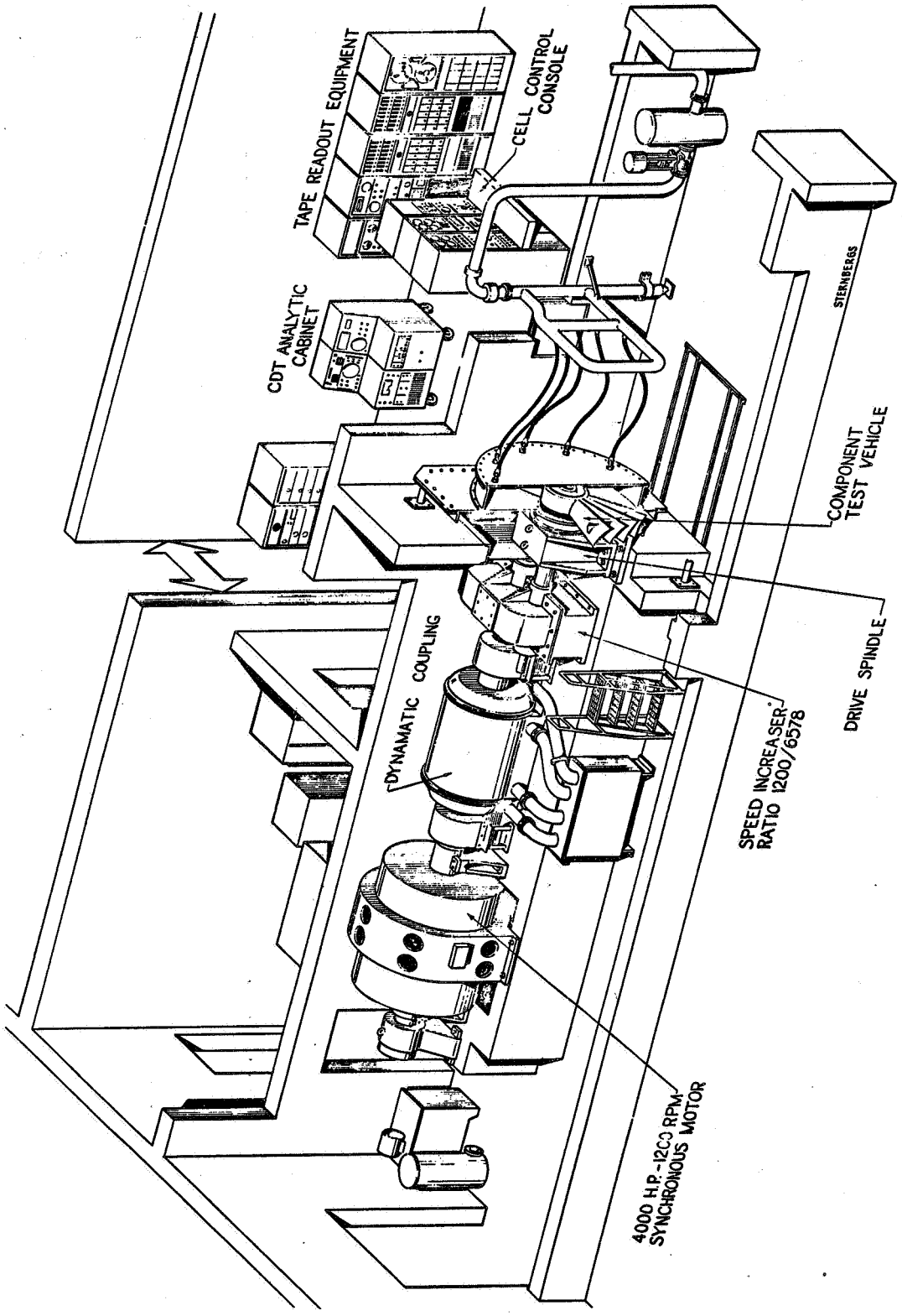

Figure 11. Whirligig Test Facility.

speed-increasing gearbox, and a horizontal drive spindle shaft to the rotor. The test setup was basically a standard TF39 fan package. The blade and rotor were enclosed in an environmental chamber to control the atmosphere and contain the debris. During testing, the chamber was filled with helium to lower the heat buildup caused by the rotating blade. Figure 12 presents a photograph of a blade installed in the facility.

The rotor was soft mounted to lessen possible rig damage should an unbalance occur. The disk was provided with two opposing spindles, one for the composite blade and the other for a counter weight. The blade spindle was positioned for proper incidence angle for impact. This is shown in Figure 13.

The environmental chamber is made with camera ports, located on both sides and directly in front of the rotor, to permit high speed motion pictures to be taken from several angles simultaneously. The blades and background are appropriately painted to reflect light and provide contrast for the movies.

The blades were impacted with simulated (RTV) birds injected into the path of the blade at the appropriate rotor speed. The density of the RTV material used was 673 kg/m^3 (42 lb/ft^3). The "Fixed Bird" technique is used to set the impact bite. This means that the bird is securely fixed to a mechanical system which inserts it at a set depth into the path of the rotating blade and retracts it after impact. Basically, the mechanism shown in Figure 14 consists of a cup (bird carrier) attached to the end of a spring-loaded shaft which is supported and free to slide in ball bushings. It is actuated by firing an explosive bolt which holds the shaft (and spring) in the retracted (cocked) position. The particular springs used provided a maximum stroke of 7.6 cm (3.0 in.) in 10 milliseconds. This yielded a maximum slice size of 6.35 cm (2.5 in.) allowing 1.25 cm (0.5 in.) clearance between blade and bird before impact.

To obtain the required slice, the explosive bolt must be fired when the rotor is at the required speed, but at an instant which will permit the blade to reach the impact point at the same time the bird reached the desired depth (full stroke). In addition, the camera and lights must be activated to record the event.

Figure 15 shows the block diagram of the firing system used to trigger the events and fire the bolt at the proper time. The operating sequence for the system is outlined below.

- The rotor speed signal is fed to a frequency counter. When the proper speed is reached, the cell operator turns on the spot-lights and activates the trigger switch, starting the cameras.
- When the control camera reaches operating speed, it trips a micro-switch which completes a circuit to permit the 1/rev signal to reach the delay unit. This signal also starts the firing of four sets of sequenced flash bulbs.

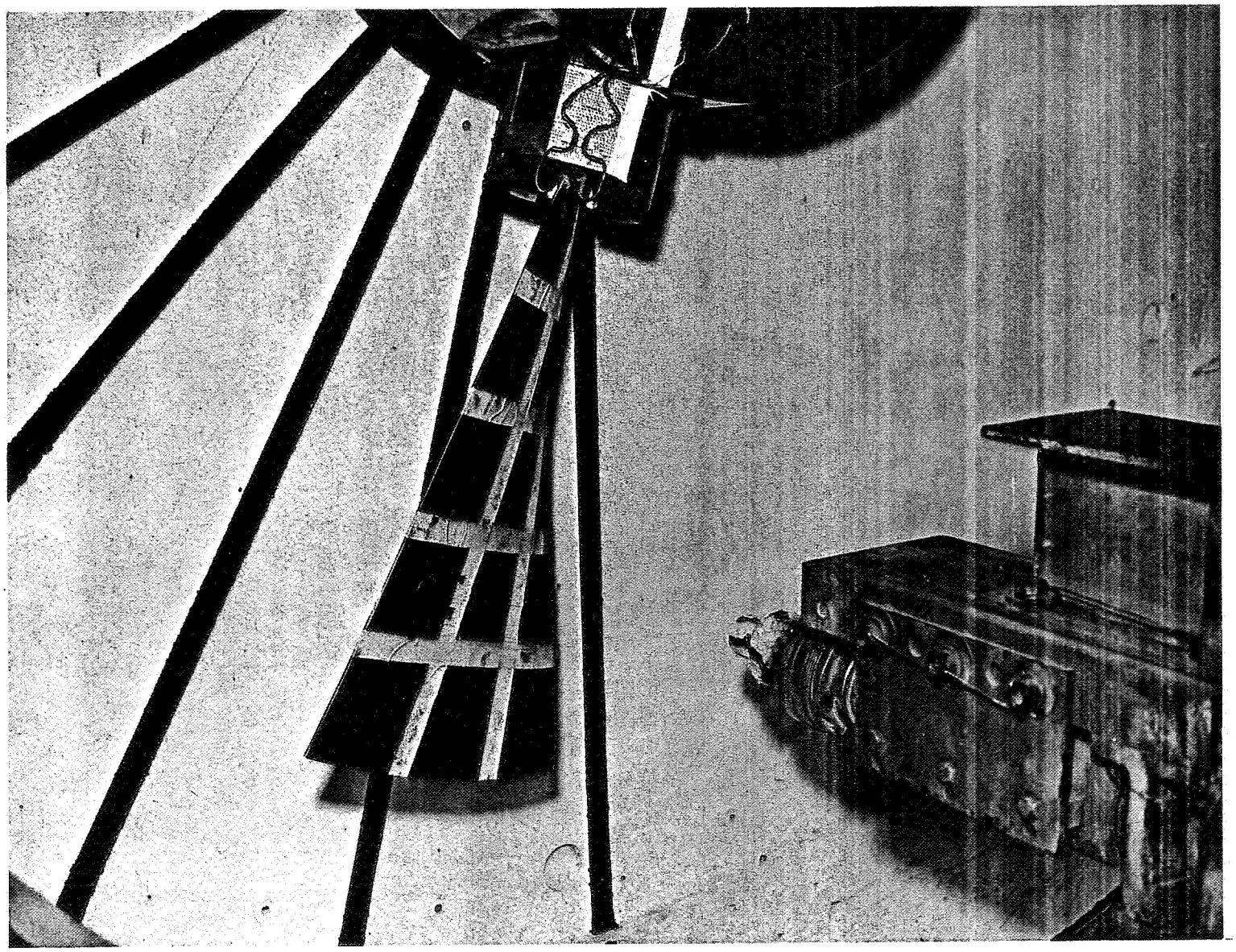

Figure 12. Task II Blade Installed in Whirligig Facility.

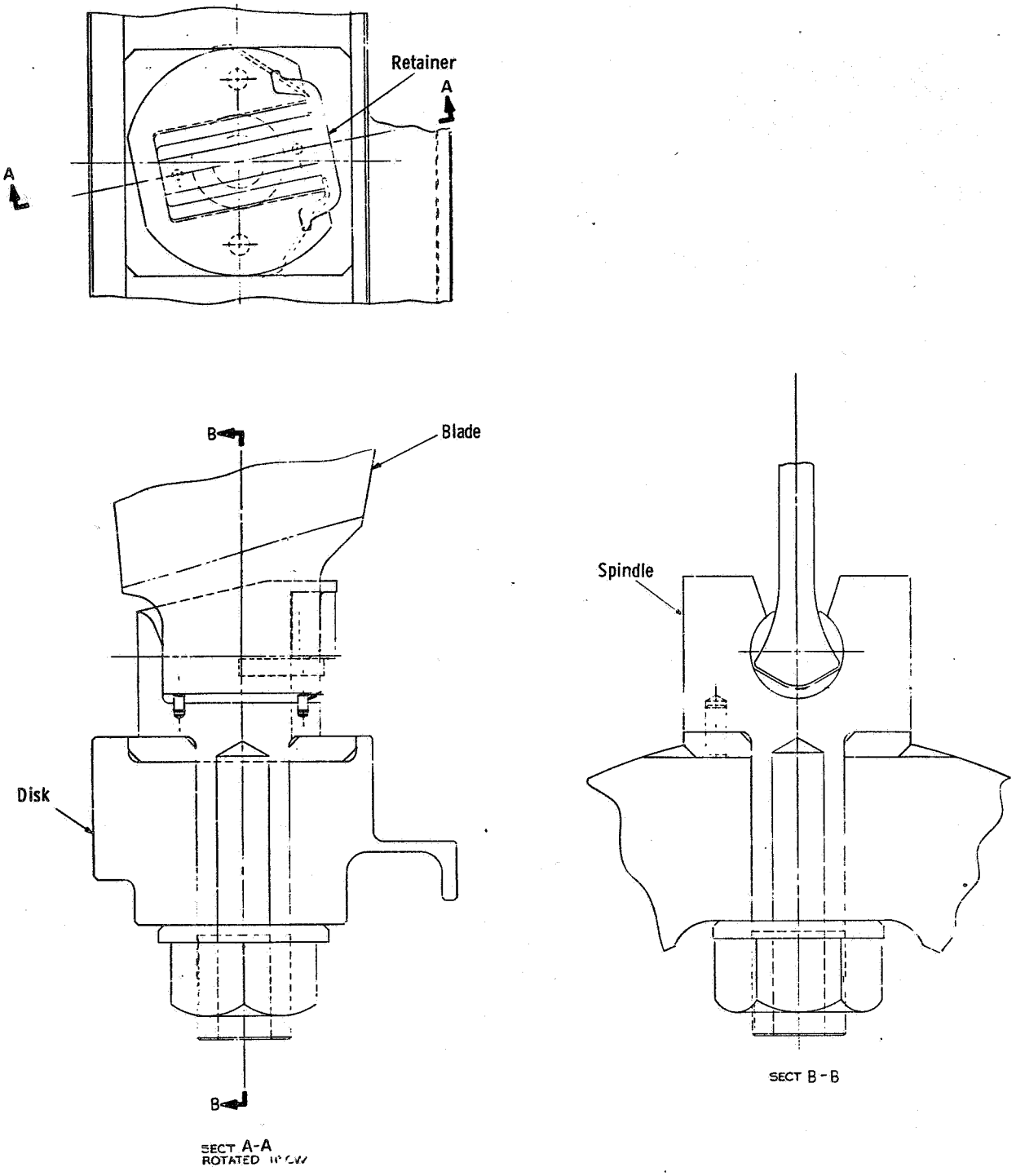

Figure 13. Whirligig Rotor Assembly, QCSEE Impact Tests.

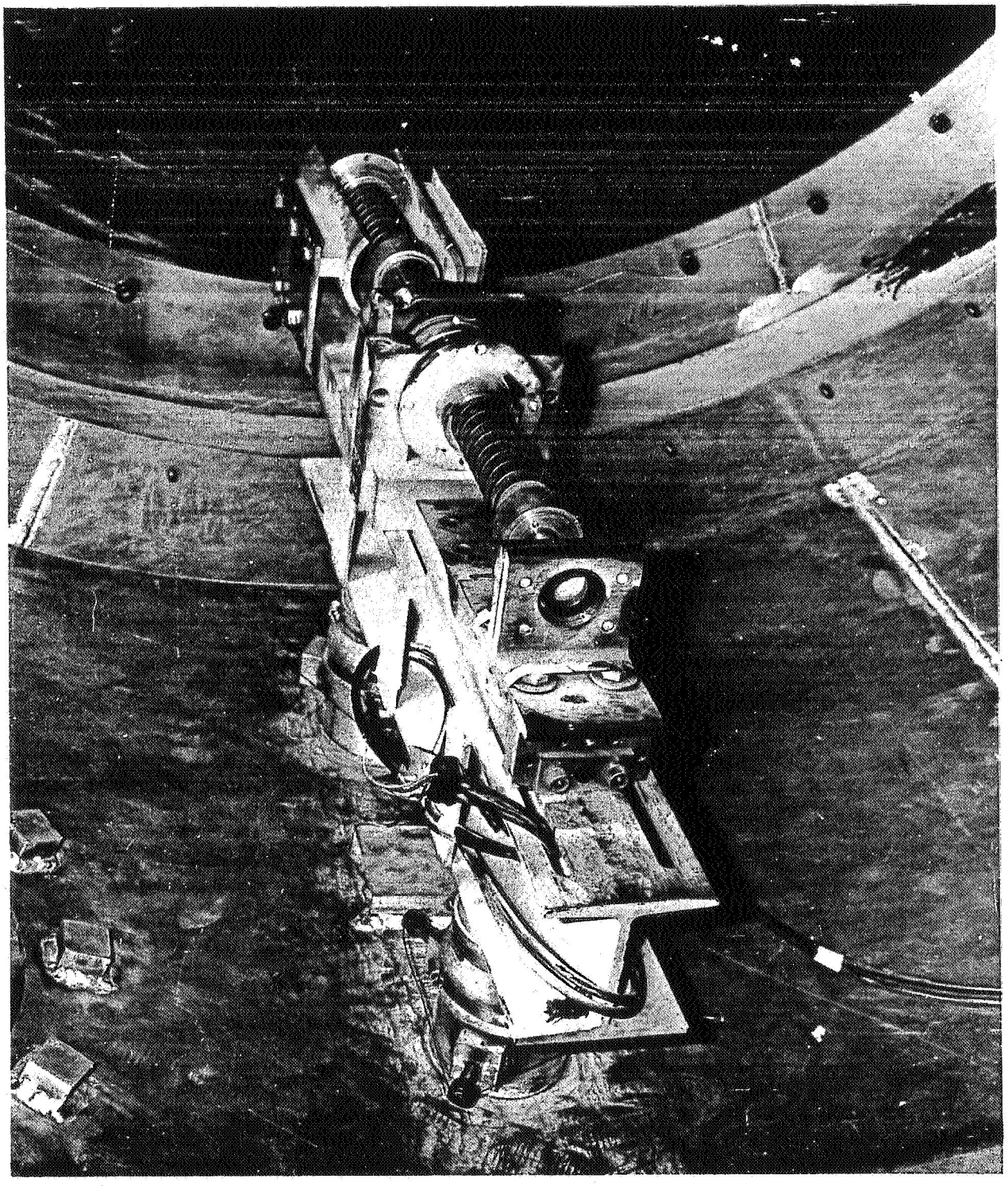

Figure 14. Bird Ingestion Mechanism for Single Blade Rotating Ingestion Testing.

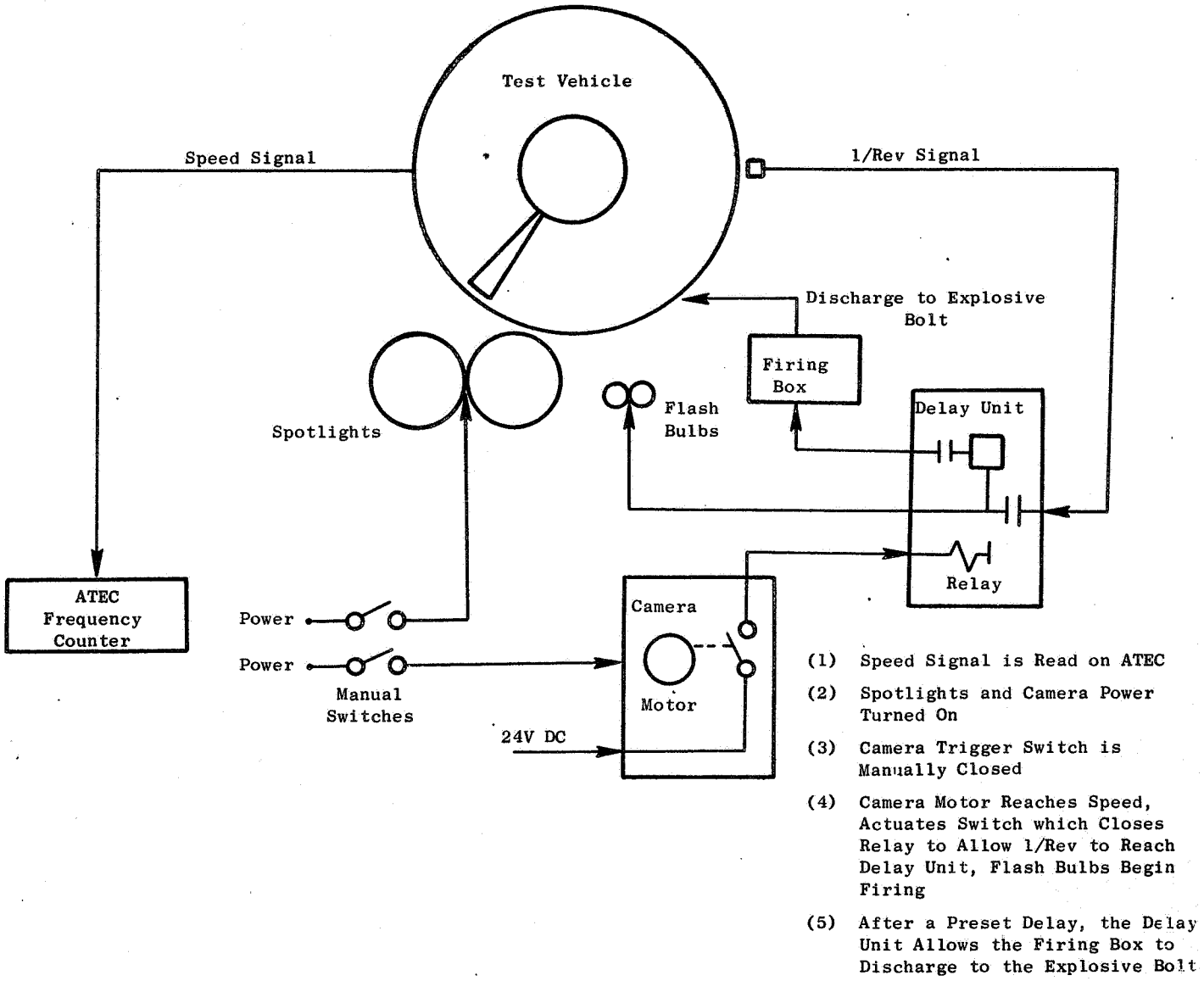

Figure 15. Firing Sequence, Whirligig Impact Tests.

- After a preset delay has occurred, allowing the flash bulbs to reach maximum lighting intensity, the delay unit discharges, causing the bolt to fire.

Experience has indicated that setup and operation for impact testing large composite blades in the soft mounted vehicle required that a large number of details, parameters and procedures be checked, logged and followed. Therefore, extensive use of check lists was made to insure that all preparations and setups are completed before each shot and that the established test procedure was followed. In addition, an engineering data sheet was included to be sure that pertinent data items were obtained.

3.3 TEST PLAN

Since the objective of the testing was to investigate the effects of various impact parameters on FOD to composite blades, a test plan was developed which varied the impact parameters in a systematic manner. Three of the four blades tested were strain gage instrumented in order to measure the strains resulting from the controlled impacts. This allows the relative importance of each parameter in terms of FOD resistance to be identified.

The impact parameters investigated are defined in Figure 16; they include total momentum (M_T), normal momentum (M_N), normal energy (E_N), transferred energy (E_T), and normal force (F_N). Total momentum (M_T) is defined as the mass of the bird sliced off (W_S) times the circumferential velocity of the blade at the impact location (V_{rel}). The normal momentum (M_N) is the component of momentum normal to the chord of the blade at the impact location, $W_S\ V_{rel}\ (\sin\theta)$. The normal energy ($E_N$) is the kinetic energy of the bird slice relative to the blade in a direction normal to the blade chord, $W_S\ (V_{rel}\ \sin\theta)^2/2$.

The transferred energy (E_T) is derived from conservation of momentum considerations assuming the blade and bird move as one body after impact, that is:

$$W_S\ V_{rel}\ \sin\theta = V_C\ (W_S + W_B)$$

where V_C = the combined velocity of blade and bird after imapct

W_B = effective mass of the blade

then $$V_C = \frac{V_{rel}\ (\sin\theta)\ W_S}{W_S + W_B}$$

then $E_T = (V_C^2/2)W_B$ = energy added to blade by bird strike so that

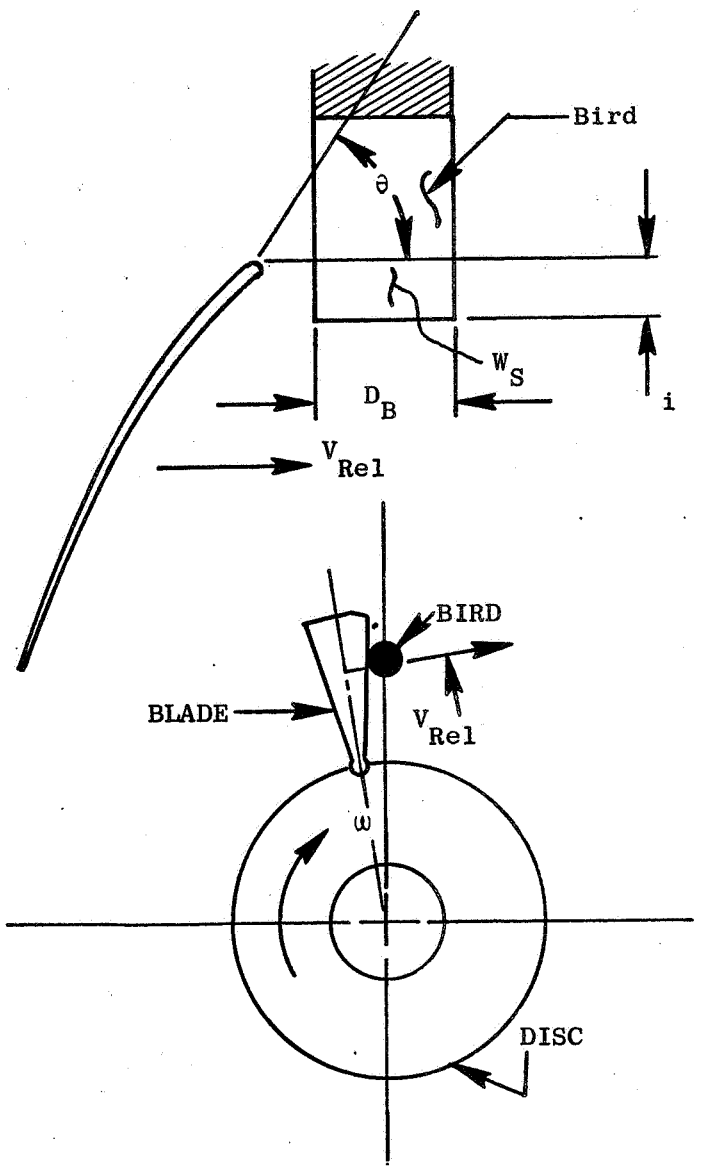

D_B = Bird Diameter

V_{Rel} = Relative Velocity

W_S = Slice Weight of Bird

W_B = Effective Blade Weight

i = Length of Bird Cut Off

θ = Incidence Angle

ω = Blade Rotational Speed

Total Momentum = $M = W_S V_{Rel}$

Normal Momentum = $M_N = W_S V_{Rel} \text{ Sin } \theta$

Normal Energy = $E_N = \dfrac{W_S (V_{Rel} \text{ Sin } \theta)^2}{2}$

Transferred Energy = $E_T = \dfrac{W_S (V_{Rel} \text{Sin } \theta)^2 X}{2} \dfrac{W_S W_B}{(W_S + W_B)}$

Normal Force = $F_N = \dfrac{W_S (V_{Rel} \text{Sin } \theta)^2}{2} \left(\dfrac{1}{D_B \text{ Cos } \theta} \right)$

Figure 16. Impact Parameters Investigated.

$$E_T = \frac{(V_{rel} \sin \theta)^2}{2} W_B \left(\frac{W_S}{W_S + W_B}\right)^2 = \frac{W_S (V_{rel} \sin \theta)^2}{2} \frac{W_S W_B}{(W_S + W_B)}$$

$$= E_N \left(\frac{W_S W_B}{(W_S + W_B)^2}\right)$$

The normal force (F_N) is calculated using a fluid dynamic analogy. That is, if the bird is assumed to have fluid-type properties under impact conditions, then ideally the impact force on the blade would be:

$$F_N = \Delta pA$$

where Δp = pressure difference

A = area

For the case of a cylindrical bird being sliced by the blade, the pressure component normal to the blade is $\Delta p = 1/2\ \rho\ V_N^2$ or $F = 1/2\ \rho\ V_N^2 A$.

The maximum contact area between the blade and bird would be an ellipse and would occur when the blade was half way through the bird:

$$A = \frac{\pi}{4} D_B \left(\frac{i}{\cos \theta}\right)$$

so that the normal force would be:

$$F_N = \frac{\rho (V_N)^2}{2} \frac{\pi}{4} \frac{D_B (i)}{\cos \theta}$$

noting that $W_S = \rho\left(\frac{\pi}{4}\right) D_B^2\ (i)$

$$F_N = \frac{W_S\ V_N^2}{2\ D_B \cos \theta}$$

Table IV presents the test schedule. The last five columns on Table IV present the variation of the impact parameters relative to run 1 on QP010 for the 75% span impacts. For the 37% span impacts the parameters are compared to run 5.

Table IV. Test Matrix.

Blade	Run	% Span	Incidence Angle (deg)	W_s gm (oz) Plan	D_B cm (in.)	RPM	$\frac{M_N}{M_{N_{Ref\ Plan}}}$	$\frac{E_N}{E_{N_{Ref\ Plan}}}$	$\frac{M_{Total}}{M_{Total_{Ref\ Plan}}}$	$\frac{E_{Transf}}{E_{Transf_{Ref\ Plan}}}$	$\frac{F_N}{F_{N_{Ref\ Plan}}}$
QP010	1	75	23	14 (0.5)	3.81 (1.5)	3200	1.0	1.0	1.0	1.0	1.0
	2	75	23	14 (0.5)	3.81 (1.5)	3800	1.19	1.42	1.19	1.42	1.42
	3	75	23	28 (1.0)	5.08 (2.0)	3200	2.0	2.0	2.0	4.0	1.5
	4	75	23	28 (1.0)	5.08 (2.0)	2260	1.4	1.0	1.4	2.0	0.75
QP013	5	37	40	14 (0.5)	3.81 (1.5)	3200	1.0*	1.0*	1.0*	1.0*	1.0*
	6	37	40	14 (0.5)	3.81 (1.5)	3800	1.19*	1.42*	1.19*	1.42*	1.41*
	7	37	40	28 (1.0)	5.08 (2.0)	3200	2.0*	2.0*	2.0*	4.0*	1.5*
QP014	8	75	33	14 (0.5)	3.81 (1.5)	3200	1.4	1.4	1.0	2.8	2.13
	9	75	33	14 (0.5)	3.81 (1.5)	3800	1.66	1.9	1.19	3.9	3.0

*Relative to 37% Span.

3.4 TEST RESULTS

3.4.1 Tabulation of Impact Parameters

The impact parameters studied are discussed in Section 3.3 of this report. The planned test conditions were shown in Table IV in Section 3.3, while the actual test conditions and the calculated values for the five impact parameters are listed in Table V. A comparison of the planned test parameters to the actual test parameters shows that the only item that varied significantly from the plan was the slice weight. In spite of this, there is sufficient variation in the impact parameters to allow parameter evaluation.

3.4.2 Presentation of Test Data

For each run made (see Table V), the dynamic strain data was recorded on tape and then played back with the strain response of each gage being presented versus time.

Figure 17 presents strain/time traces for several gages for the first shot 16.0 gram (0.563 ounce) slice at 3200 rpm. Figures 18, 19, and 20 present strain/time traces for three other shots relative to the first 16.0 gram (0.563 ounce) slice at 3200 rpm data. Several observations may be made from these comparative data:

- All the dynamic strain data appear to be of high quality with regard to repeatability, accuracy, and noise level.
- The strain waveforms for a given impact location tend to be independent of projectile variables. That is, the frequency of the waveforms are independent of projectile variables. However, when impacts at different spans are considered, shots 1 and 5 for example, Figure 21, the waveforms show dramatically different characteristics.
- Peak strain amplitudes in the impact region occur on the first cycle and are dependent on projectile variables.

The strain/time traces for all shots made are included in the Appendix for reference purposes. From the strain/time traces in the Appendix, values for first peak strain and maximum peak strain were tabulated and are shown in Tables VI and VII. Using this data and values for the impact parameters from Table VI, plots were made showing impact parameter versus first peak strain and impact parameter versus maximum peak strain for impacts at 75 percent span and impacts at 37 percent span.

Representative plots showing total momentum (M_T), normal momentum (M_N), and transferred energy (E_T) versus strain are shown in Figures 22 through 24. The data shown in these plots are for strain gages 2 through 7 and runs 1, 2, 3, 4, 8, and 9 which were 75 percent span impacts. From the data

Table V. Summary of Test Results.

Run	Slice wt, gm (oz)	% Span	V_{Rel} m/sec (ft/sec)	rpm	Deg., θ	M_T, N/sec (lb/sec)	$\frac{M_T}{M_T \text{ Ref}}$	M_N, N/sec (ft/sec)	$\frac{M_N}{M_N \text{ Ref}}$	E_T, J (ft-lb)	$\frac{E_T}{E_T \text{ Ref}}$	E_N, J (ft-lb)	$\frac{E_N}{E_N \text{ Ref}}$	F_N, N (lb)	$\frac{F_N}{F_N \text{ Ref}}$
1	16 (0.563)	75	262.1 (860)	3200	23	4.188 (0.94)	1.0	1.65 (0.37)	1.0	0.788 (0.581)	1.0	83.5 (61.6)	1.0	2384 (536)	1.0
2	17 (0.60)	75	310.9 (1020)	3808	23	5.29 (1.19)	1.26	2.05 (0.46)	1.24	1.266 (0.934)	1.61	125.8 (92.8)	1.51	3590 (807)	1.51
3	24 (0.84)	75	262.1 (860)	3195	23	6.27 (1.41)	1.5	2.45 (0.55)	1.49	1.763 (1.3)	2.24	124.9 (92.1)	1.5	2660 (598)	1.12
4	19 (0.67)	75	185.9 (610)	2260	23	3.51 (0.79)	0.84	1.38 (0.31)	0.84	0.553 (0.408)	0.70	49.5 (36.5)	0.6	1054 237	0.44
5	18 (0.63)	37	189.0 (620)	3202	40	3.60 (0.81)	1.0*	2.31 (0.52)	1.0*	1.249 (0.92)	1.0*	150.5 (111)	1.0*	5155 1159	1.0*
6	11 (0.39)	37	225.6 (740)	3797	40	2.62 (0.59)	0.73*	1.69 (0.38)	0.73*	0.658 (0.485)	0.53*	128.8 (95)	0.86*	4413 (992)	0.86*
7	21 (0.74)	37	189.0 (620)	3196	40	4.23 (0.95)	1.17*	2.71 (0.61)	1.17*	1.703 (1.256)	1.36*	174.9 (129)	1.16*	4484 (1008)	0.87*
8	14 (0.49)	75	262.1 (860)	3200	33	3.65 (0.82)	0.87	2.00 (0.45)	1.22	1.182 (0.872)	1.5	142.2 (104.9)	1.7	4444 (999)	1.86
9	12 (0.42)	75	310.9 (1020)	3804	33	3.74 (0.84)	0.89	2.00 (0.45)	1.22	1.228 (0.906)	1.56	172.2 (127)	2.1	5396 (1213)	2.26

*Relative to 37% span only.

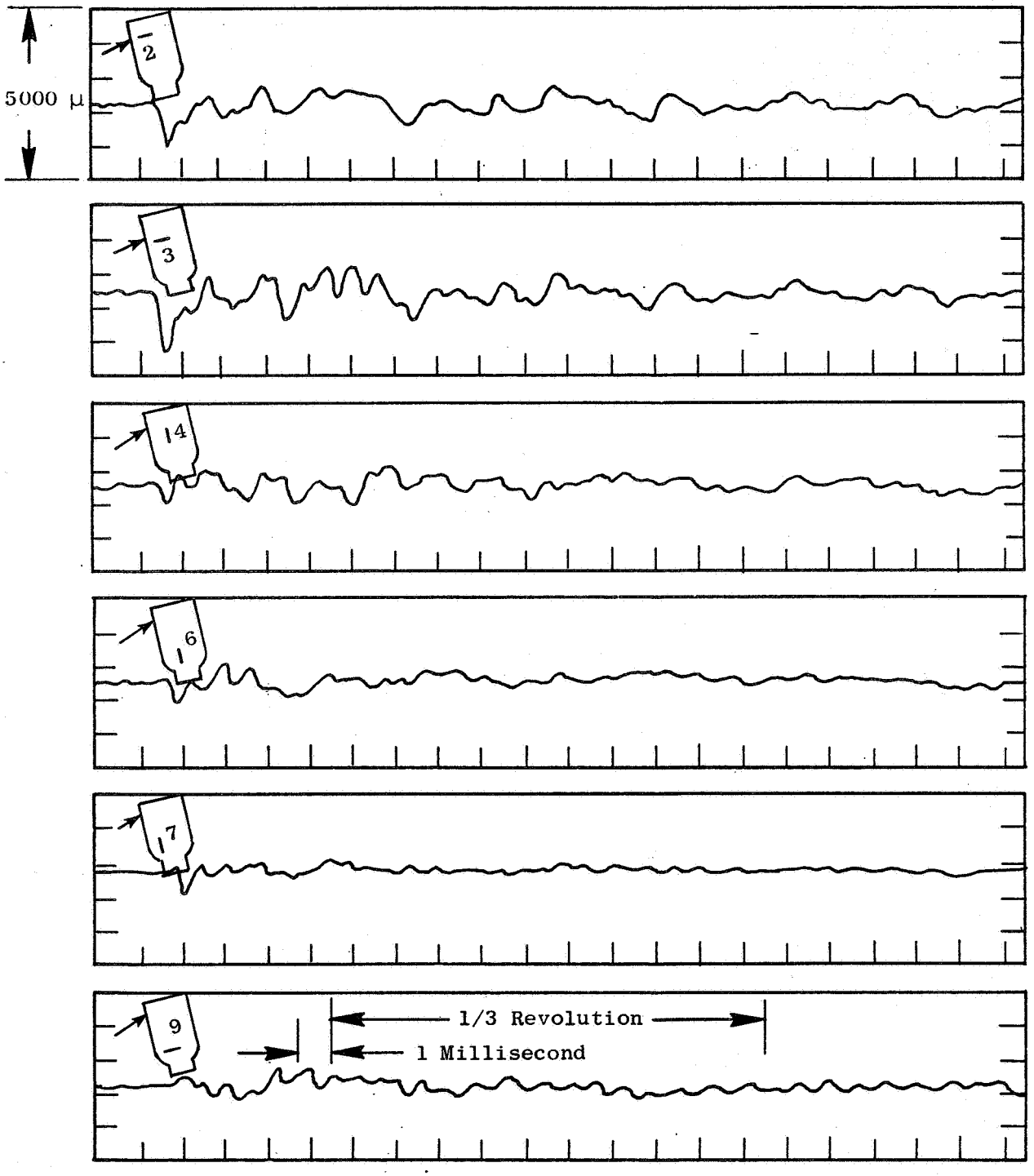

Figure 17. Typical Strain Gage Trace.

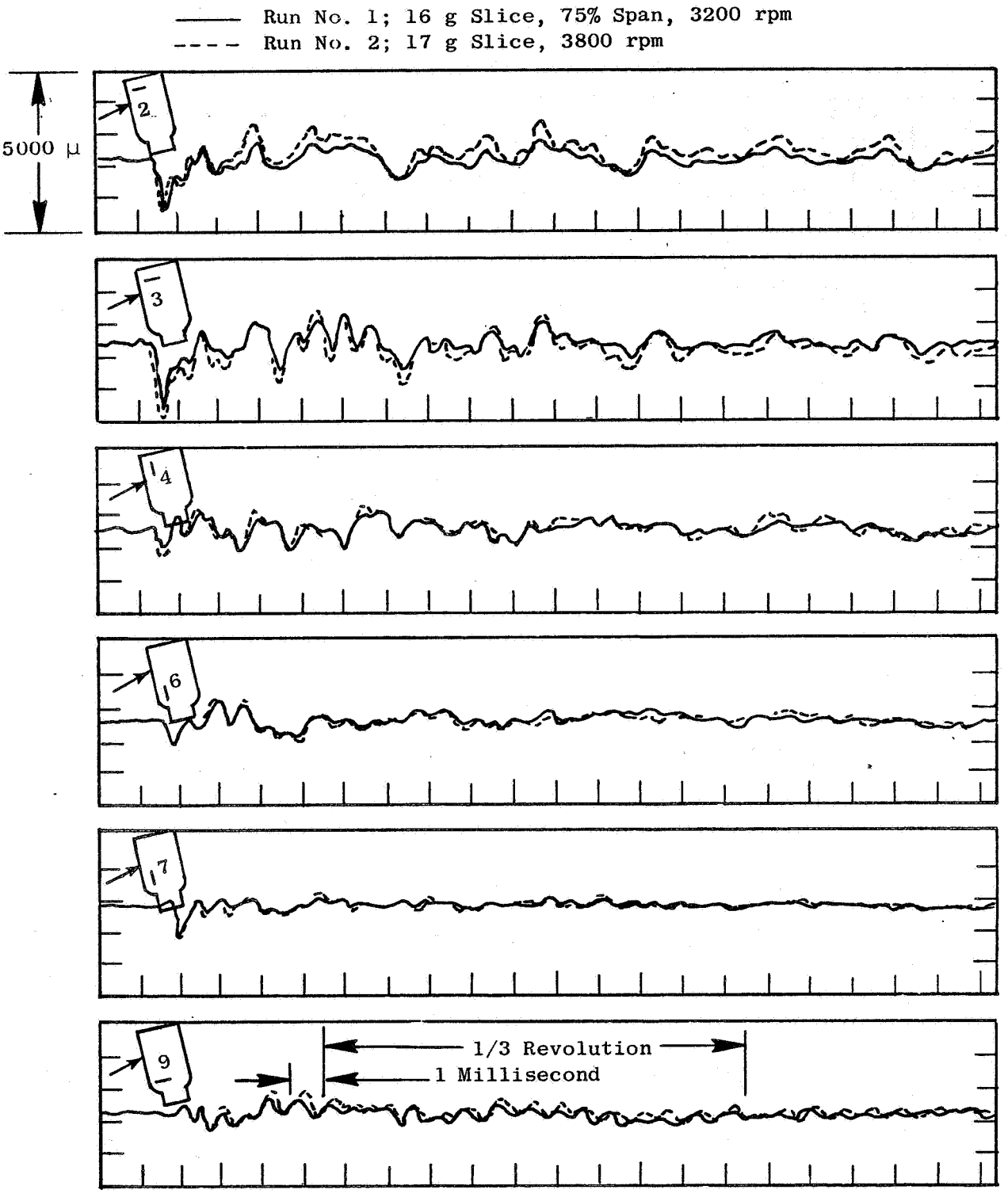

Figure 18. Run 2 Compared to Run 1.

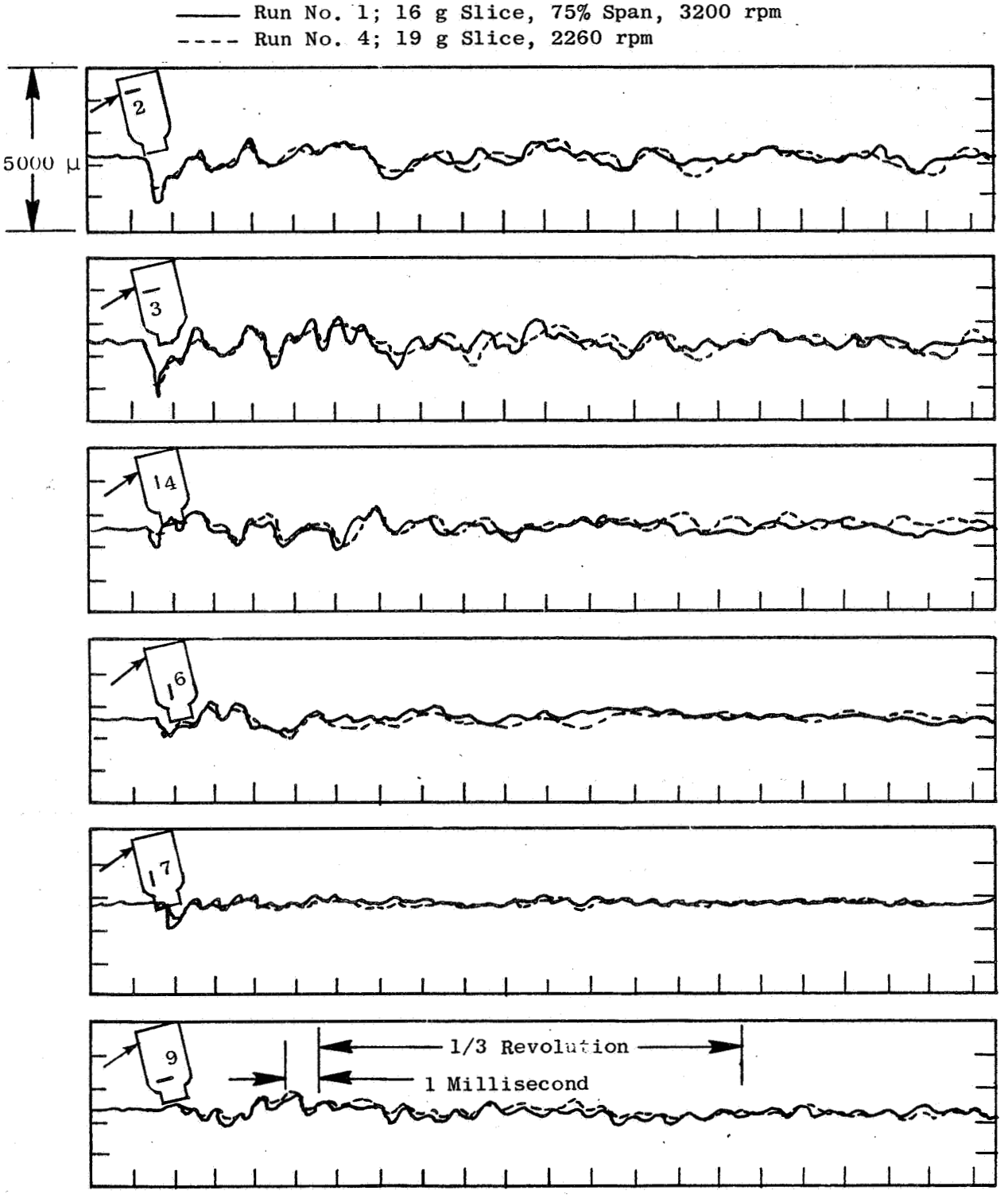

Figure 19. Run 4 Compared to Run 1.

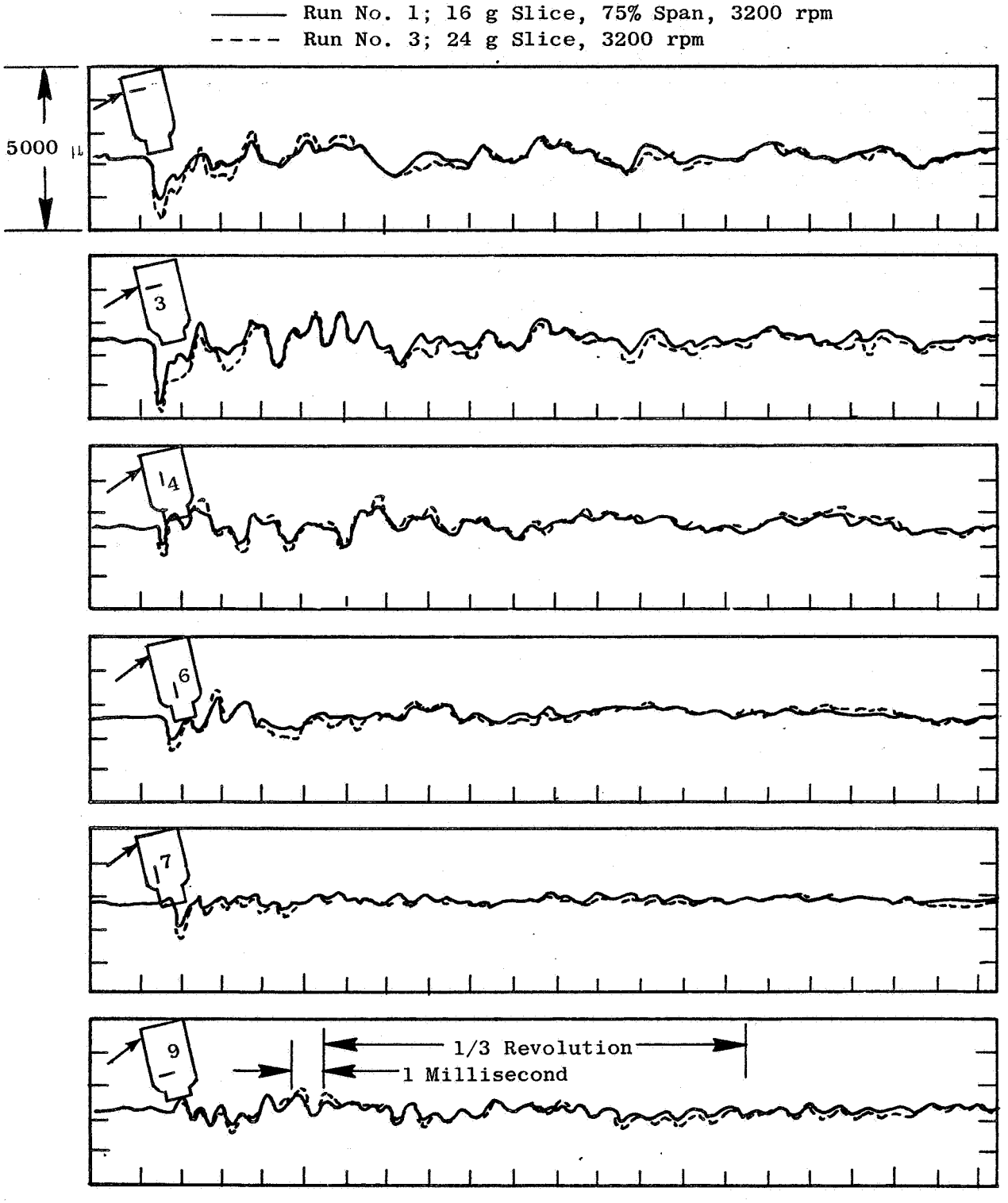

Figure 20. Run 3 Compared to Run 1.

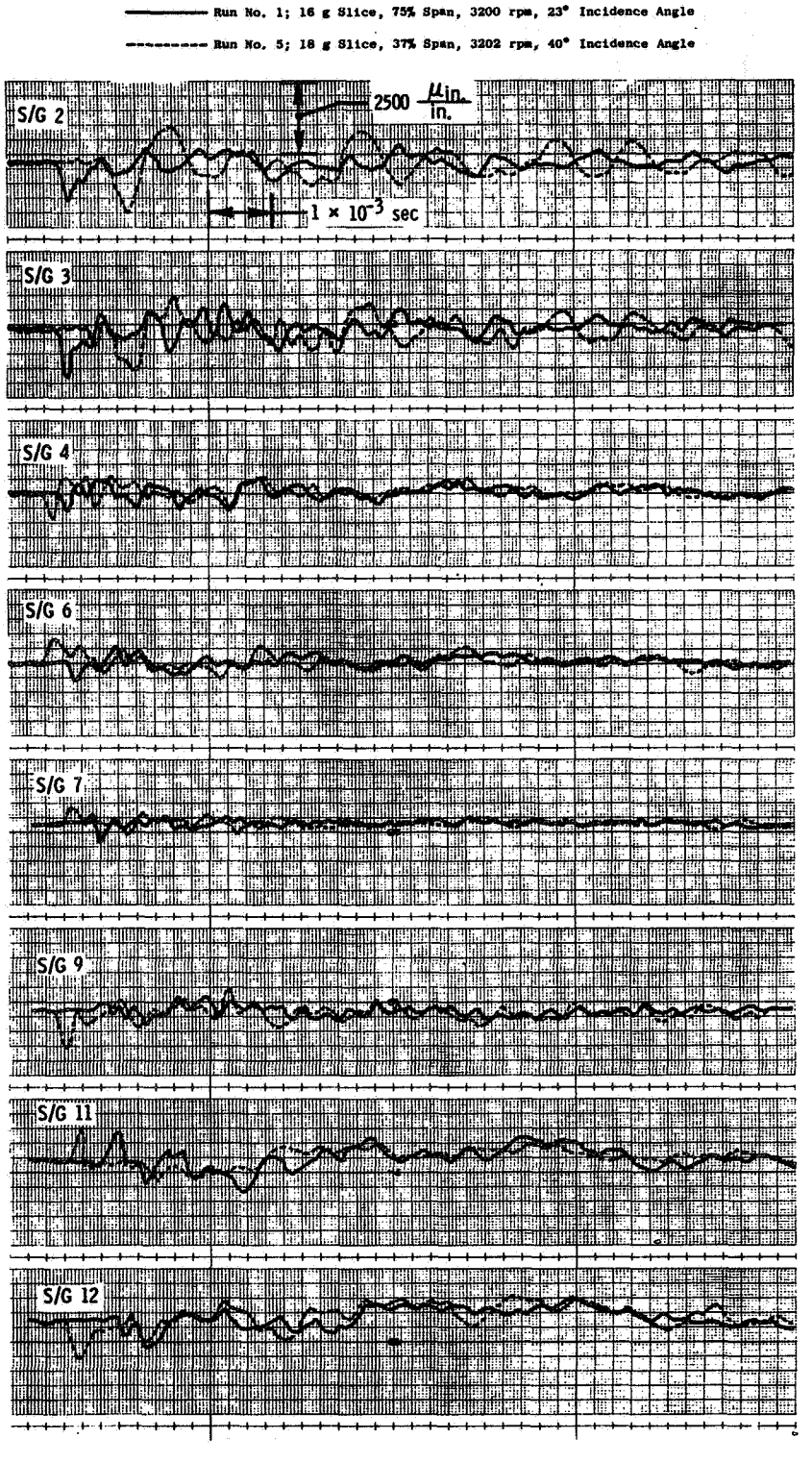

Figure 21. Comparison of Strains for Impacts At Two Different Spans.

Table VI. First Peak Strain.

Strain, (μ cm/cm)

Run	Gage										
	C[1] 2	C 3	R 4	5	R 6	R 7	8	C 9	10	R 11	R 12
1	1300	1650	550	-	600	650	-	250	-	1000	650
2	1900	2100	800	-	700	950	-	300	-	1050	1200
3	1900	2100	900	-	1000	1100	-	450	-	1400	1300
4	1000	1350	300	-	500	500	-	150	-	700	450
5	200	550	900	2400	800	650	-	1300	-	600	1350
6	100	400	700	2000	650	550	-	1050	-	500	1200
7	100	500	650	2400	900	700	-	1400	-	500	1400
8	-	2650	1300	900	950	1200	400	400	500	-	1200
9	-	2800	1300	900	1200	1400	500	350	600	-	1250

(1) C = strain gages located in chordal direction
R = strain gages located in radial direction

Table VII. Maximum Peak Strain.

Strain, μ cm/cm

Run	Gage										
	C[1] 2	C 3	R 4	5	R 6	R 7	8	C 9	10	R 11	R 12
1	1300	1650	650	-	600	650	-	450	-	1000	1000
2	1900	2100	800	-	700	950	-	700	-	1050	1200
3	1900	2100	900	-	1000	1100	-	700	-	1400	1300
4	1000	1350	700	-	600	500	-	550	-	800	1000
5	1700	1300	900	2400	800	650	-	1300	-	600	1350
6	1300	850	700	2000	650	550	-	1050	-	500	1200
7	1950	1400	650	2400	900	700	-	1400	-	500	1400
8	-	2650	1300	1550	950	1200	950	900	800	-	1200
9	-	2800	1300	1550	1200	1400	1100	950	900	-	1250

(1) C = strain gages located in chordal direction
R = strain gages located in radial direction

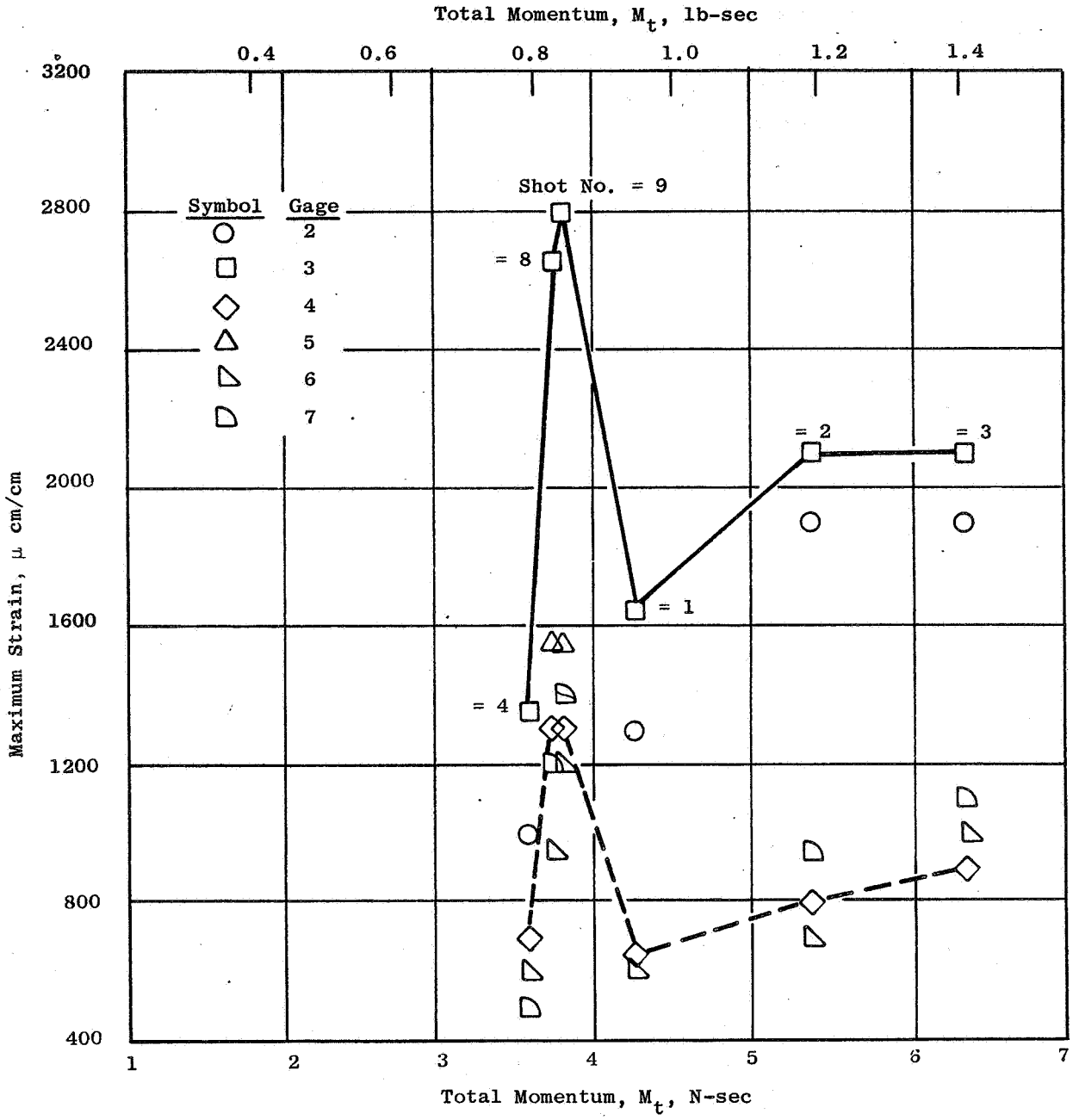

Figure 22. Strain Data Versus Total Momentum for 75% Span Impact Tests.

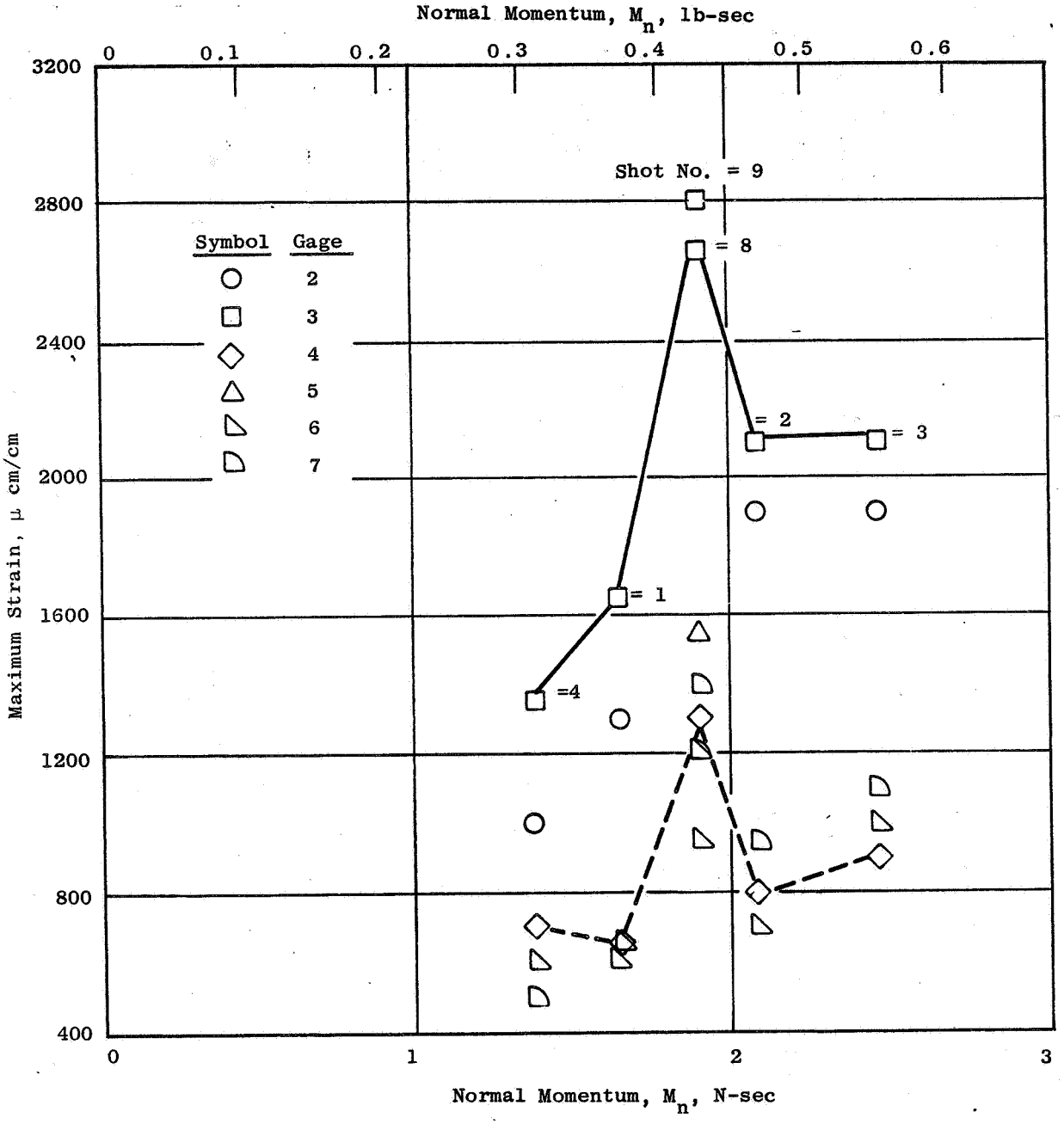

Figure 23. Strain Data Versus Normal Momentum for the 75% Span Impacts.

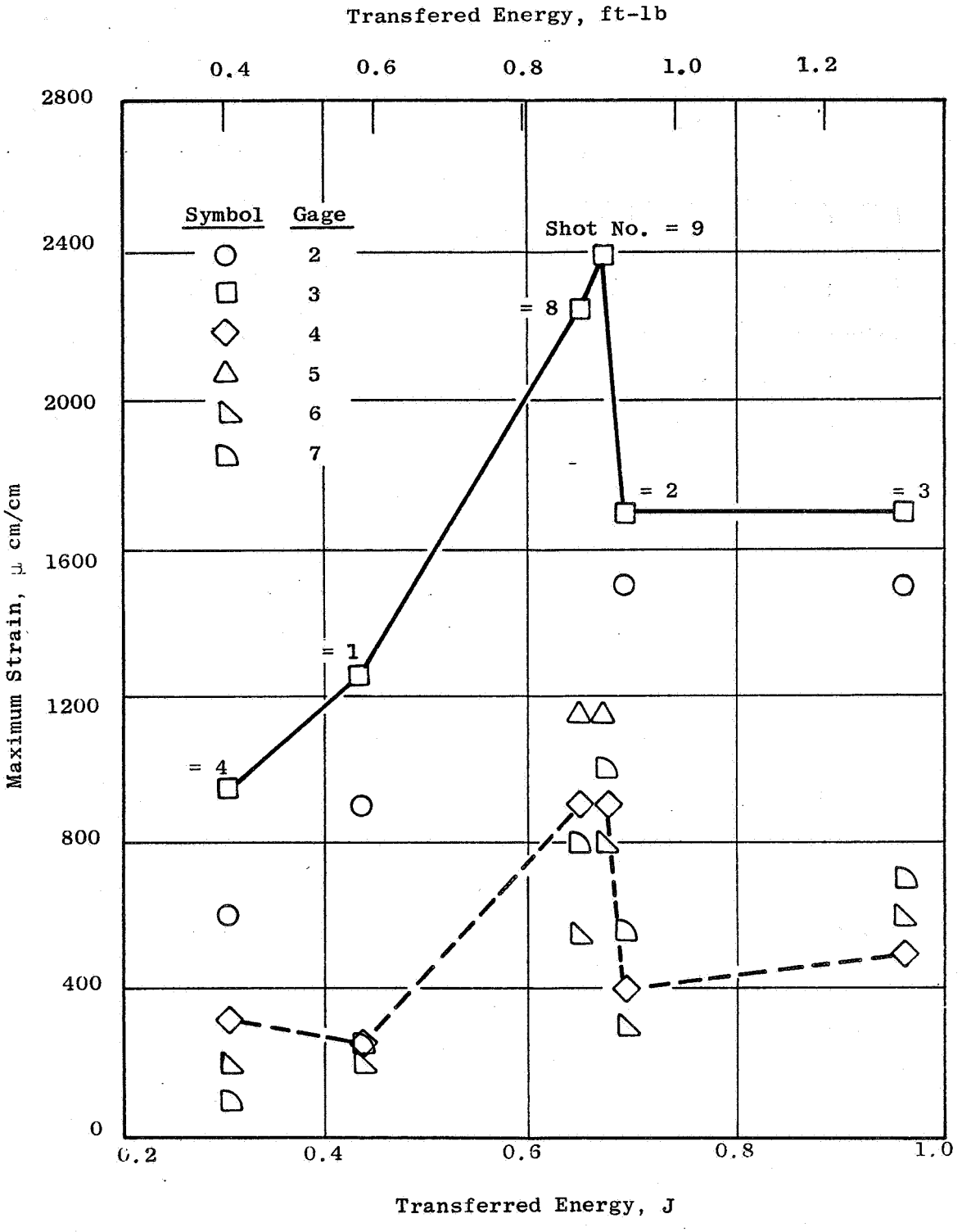

Figure 24. Strain Data Versus Transferred Energy for 75% Span Impacts.

shown for run numbers 1 through 4, it appears that these parameters (M_T, M_N, and E_T) account fairly well for changes in slice weight and rotor rpm. However, when the data from runs 8 and 9 are included, it becomes apparent that these parameters do not adequately account for a change in incidence angle since the primary difference between runs 1 to 4 and runs 8 and 9 was a change in incidence angle from 23 to 33 degrees.

Plots of strain data versus normal energy are shown in Figures 25 through 28. The normal energy parameter (E_N) appears to handle variations in slice weight, rotor rpm, and incidence angle better than the first three parameters studied, so additional effort was spent to determine how well the strain data correlates with E_N. A least squares curve fitting routine was used to plot straight lines through the data (and through the origin). The difference between the curve fit and the actual data was then plotted against normal energy. This is shown in Figures 29 and 30. From these plots, it can be seen that the strain data falls within ± 20 percent of a straight line curve fit when the low energy data is excluded. When the numerous possibilities for error are considered (stain gage variations, errors in strain gage readout, etc.), this type of correlation is encouraging.

Based on the success of the normal energy parameter in correlating the strain data, calculations were made using the normal force parameter which accounts for bird diameter as well as slice weight. These data were plotted against first peak strain data with the resulting plots shown in Figures 31 through 34. A straight line curve fit was made without forcing the data to pass through the origin. This was done on the assumption that the normal force does not account for all the forces which produce strain in the blade. The difference between the actual data and the curve fit is shown in Figure 35. This indicates that the strain data, in general, can be made to conform to a straight line when plotted against normal force when this line is not forced to pass through the origin. There are several possible explanations for the data not passing through the origin:

- There is a chordwise force not accounted for in the normal force parameter.
- Not all of the energy from impact is absorbed by the blade. Some is dissipated as heat energy and in deformation of the RTV bird.

In summary, it appears that based on the data obtained in this test series, the total momentum (M_T), the normal momentum (M_N), and the transferred energy (E_T) do not correlate the strain data when changes in incidence angle must be considered. The local energy (E_N) and normal force (F_N), however do account for changes in bird slice weight, relative velocity, and incidence angle for the same percent span. Further studies of the normal force parameter (F_N) brought some additional insight into the impact process. Though the data appears to vary in a linear manner with normal force, it is apparent that the normal force is not the only factor affecting the strain levels recorded. In order to completely describe the impact, more information has to be made available on the additional forces that are involved. The usefulness of either the local energy or the normal force parameters

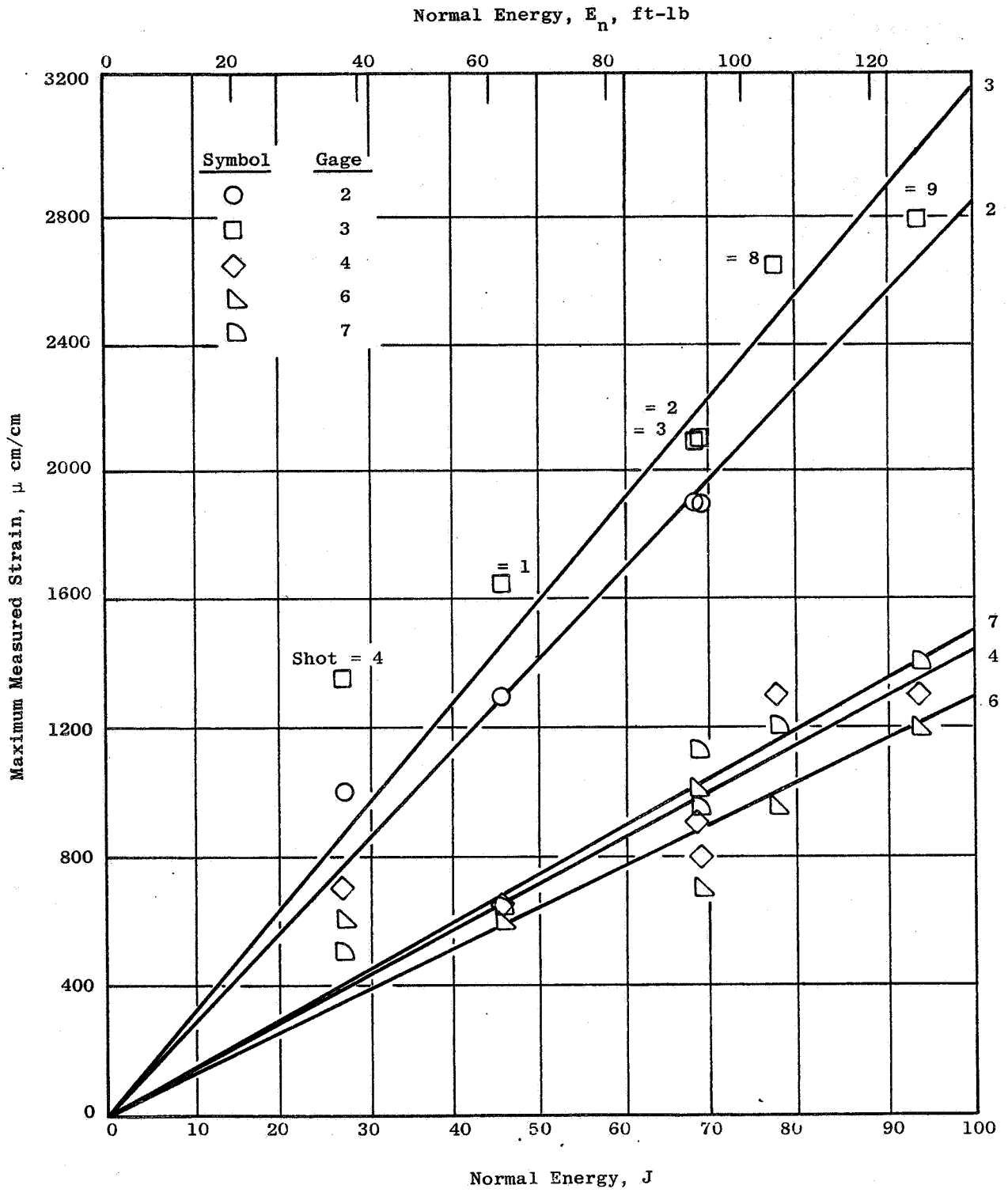

Figure 25. Maximum Strain Versus Normal Energy for 75% Span Impacts.

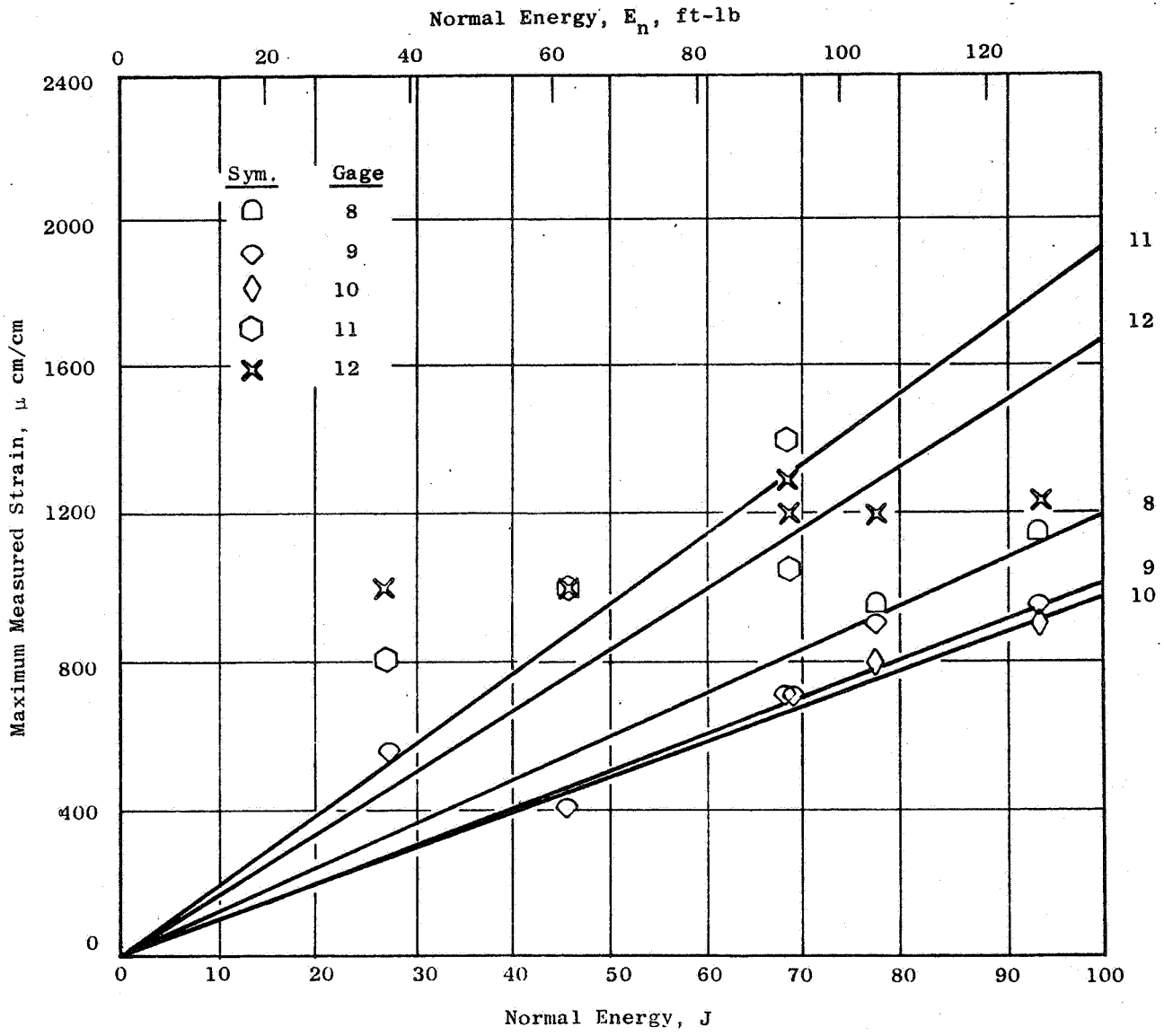

Figure 26. Maximum Strain Versus Normal Energy for 75% Span Impacts.

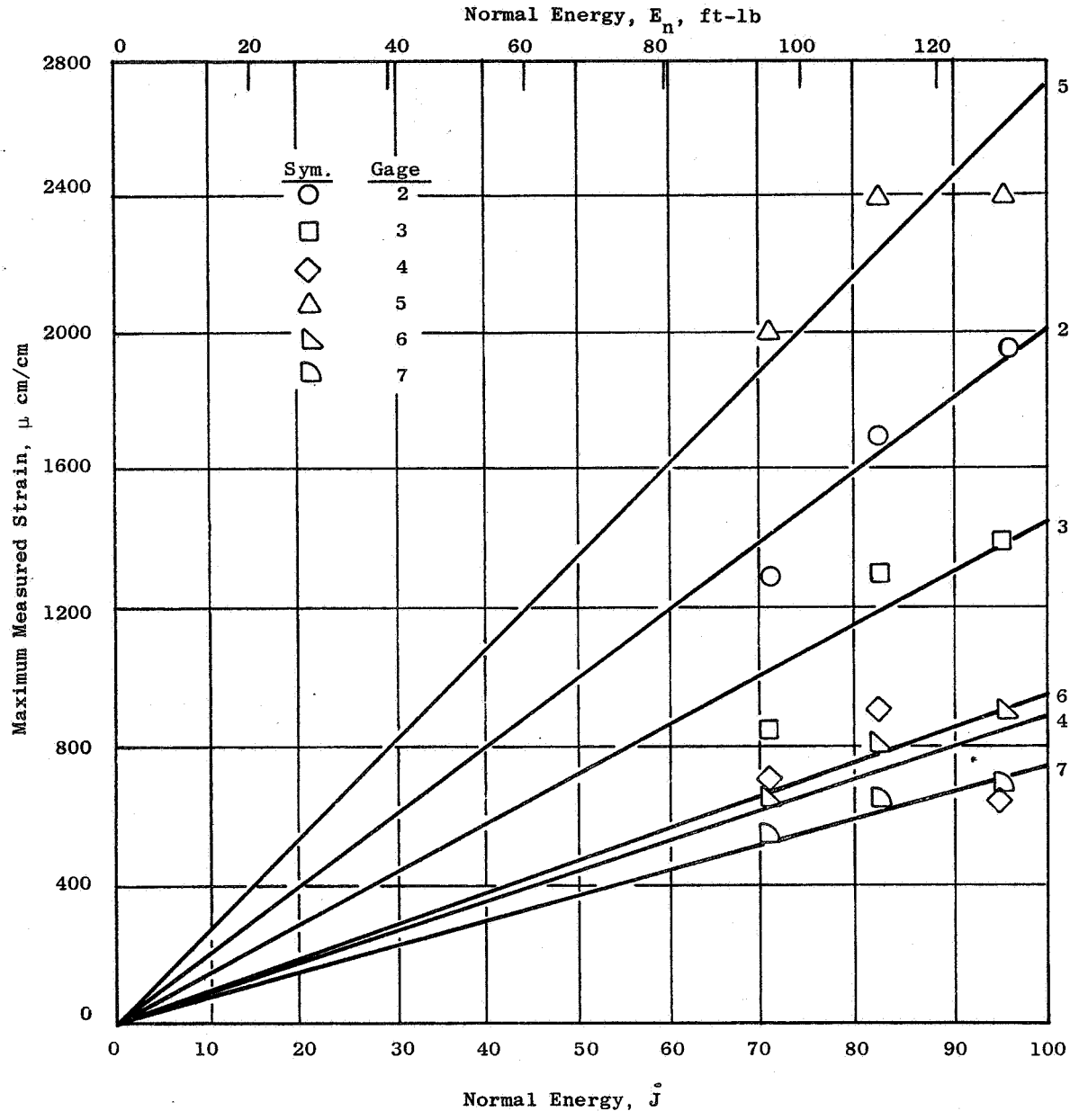

Figure 27. Maximum Strain Versus Normal Energy for 37% Span.

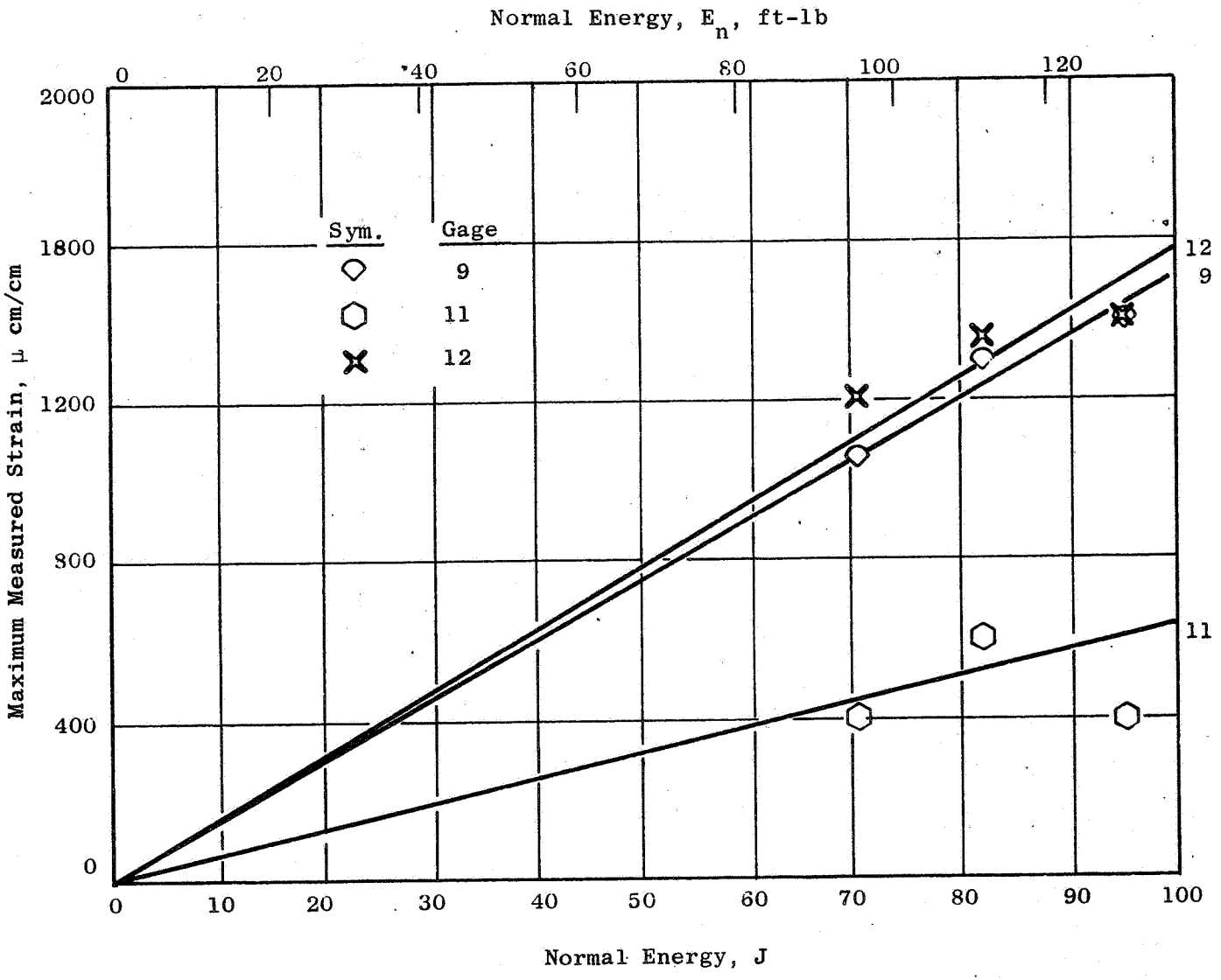

Figure 28. Maximum Strain Versus Normal Energy for 37% Span.

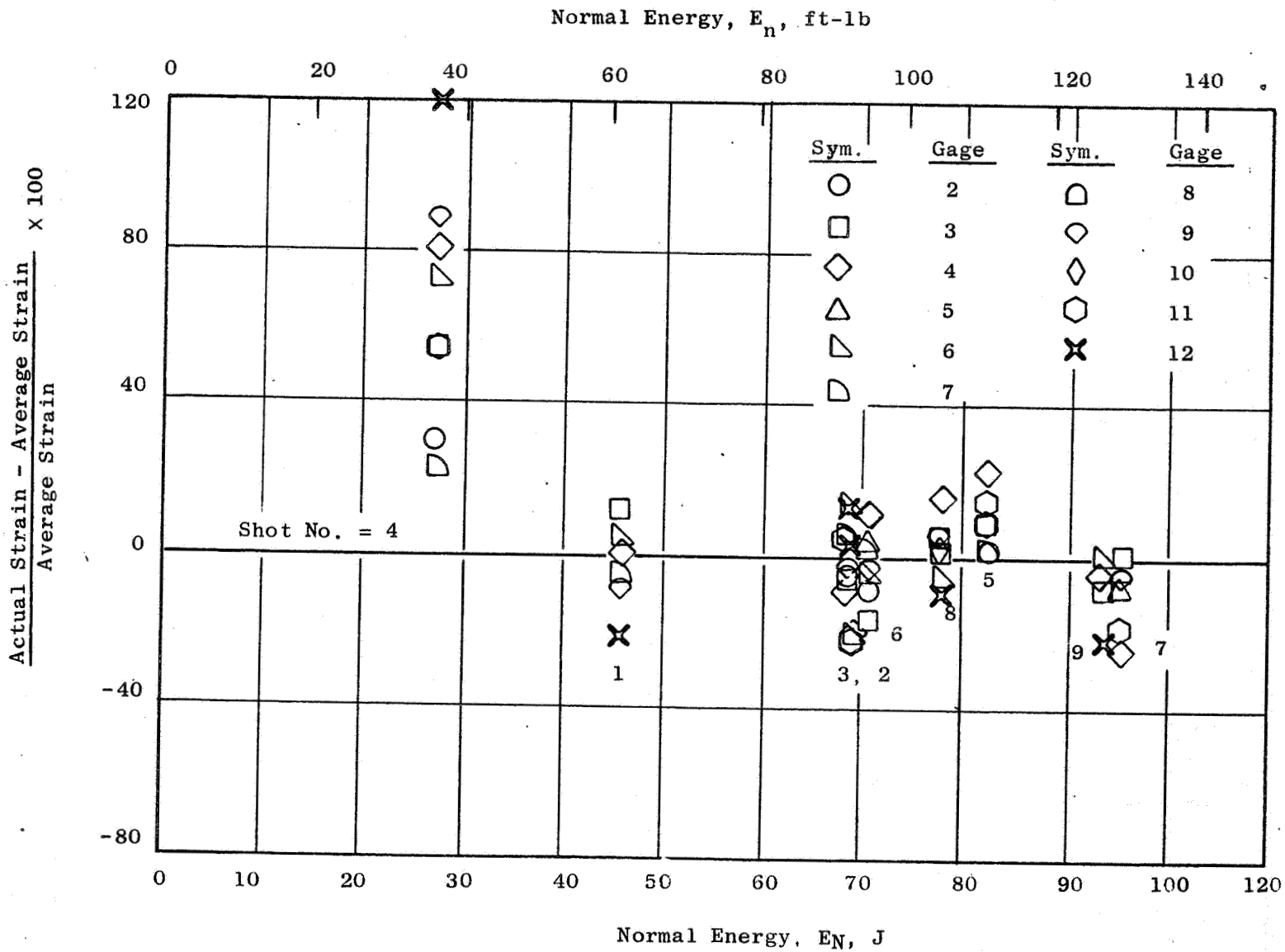

Figure 29. Normal Energy Versus Maximum Strain Correlation.

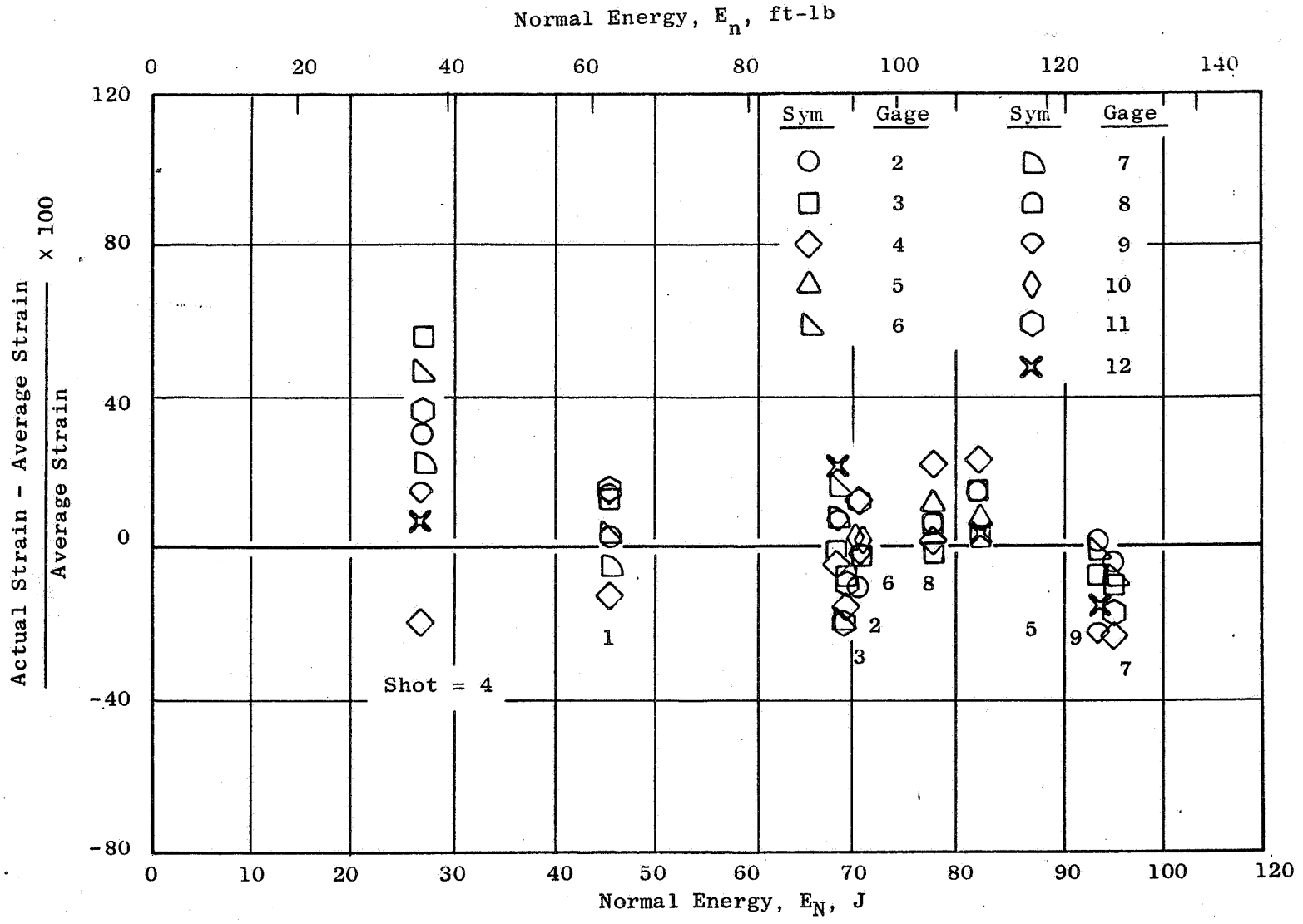

Figure 30. Normal Energy Versus Peak Strain on First Cycle.

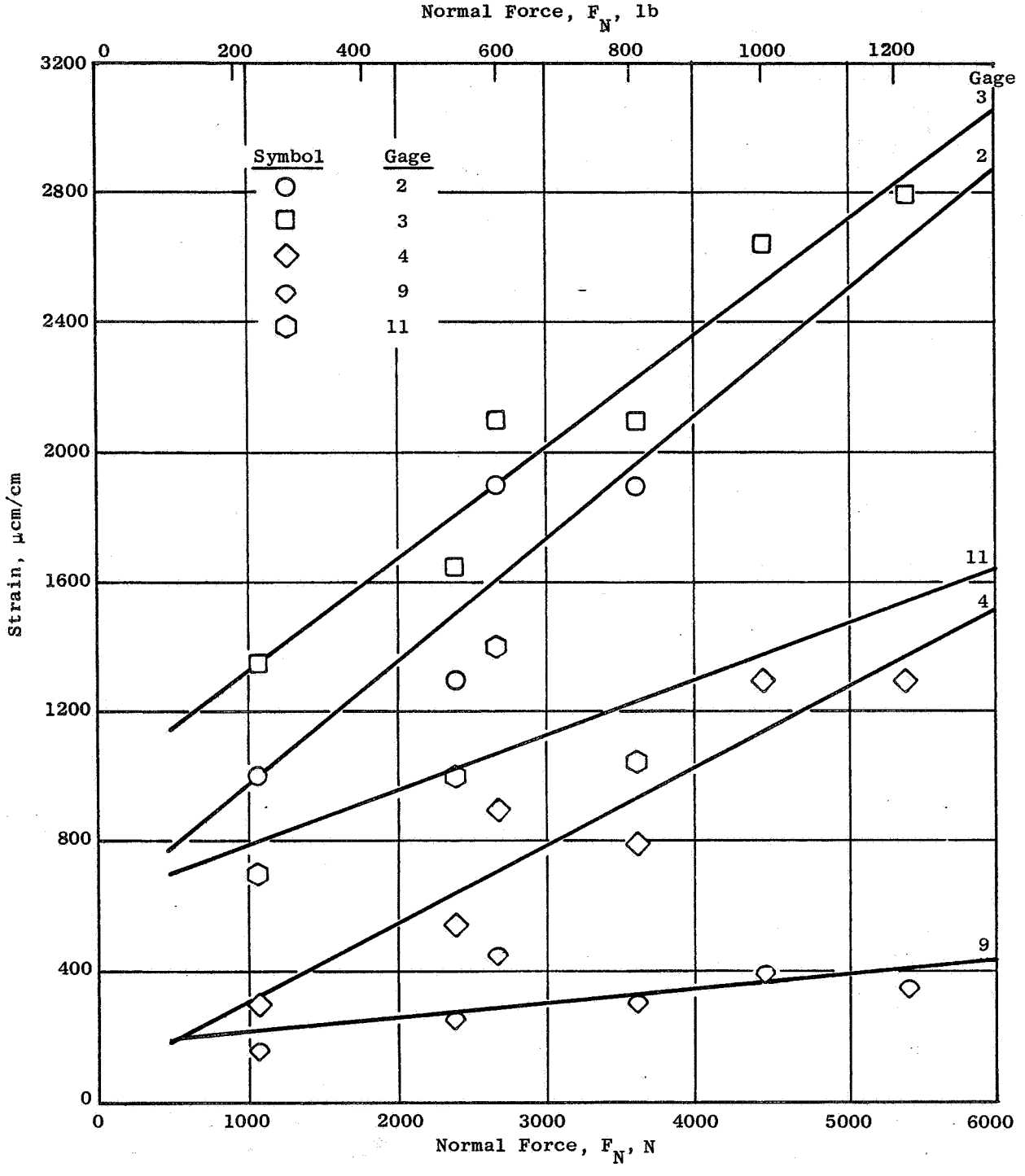

Figure 31. First Peak Strain Versus Normal Force for 75% Span.

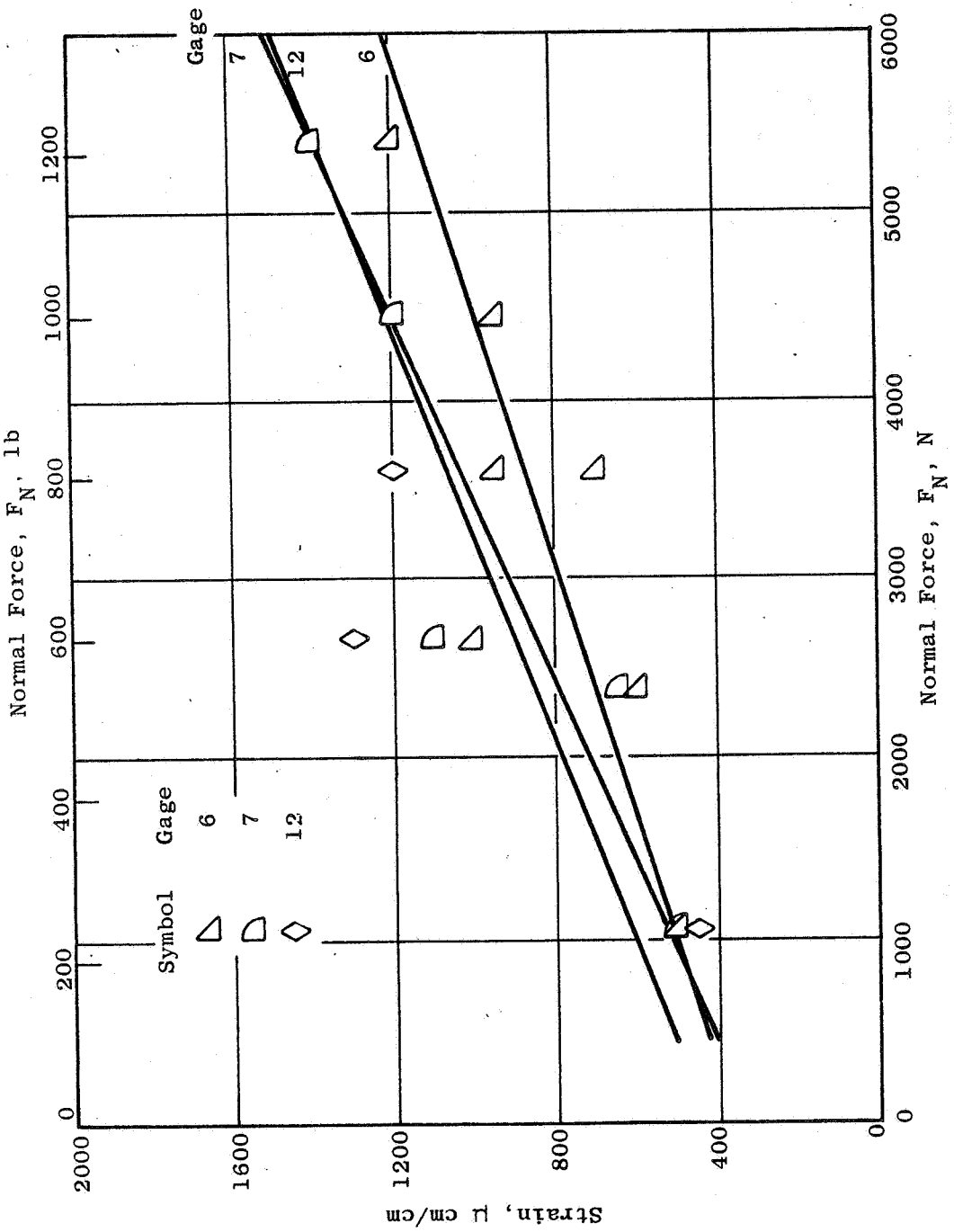

Figure 32. First Peak Strain Versus Normal Force for 75% Span.

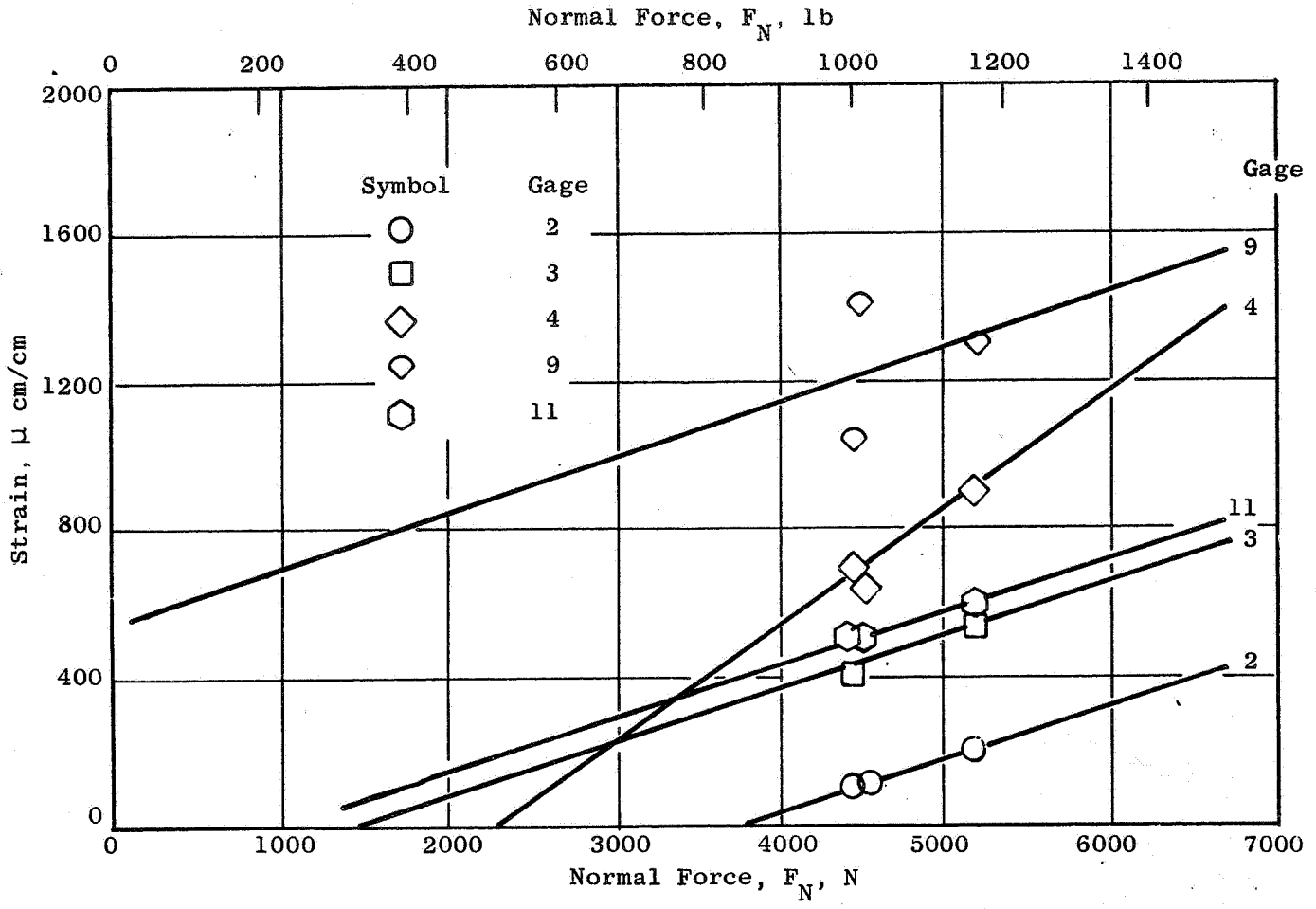

Figure 33. First Peak Strain Versus Normal Force for 37% Span.

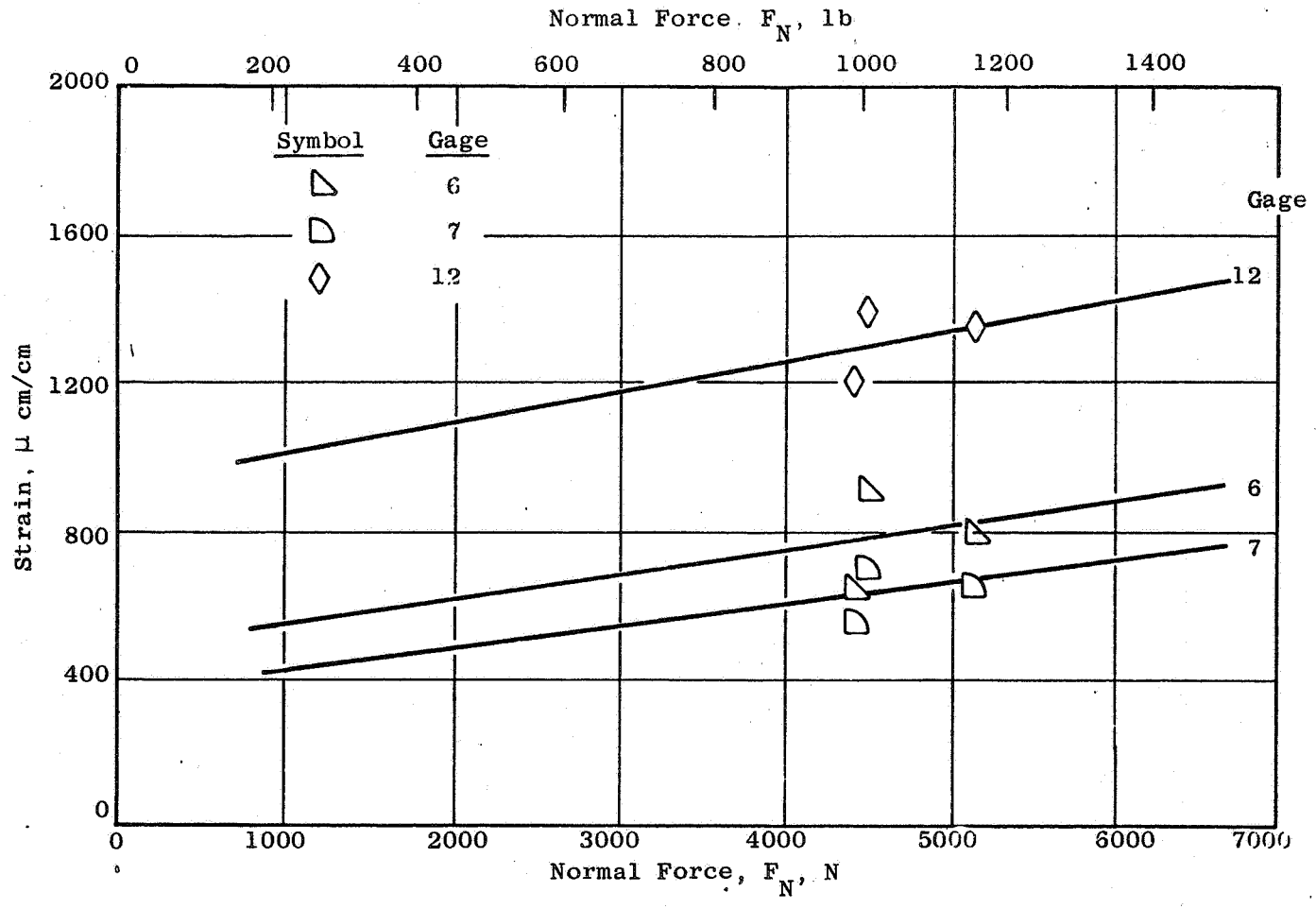

Figure 34. First Peak Strain Versus Normal Force for 37% Span.

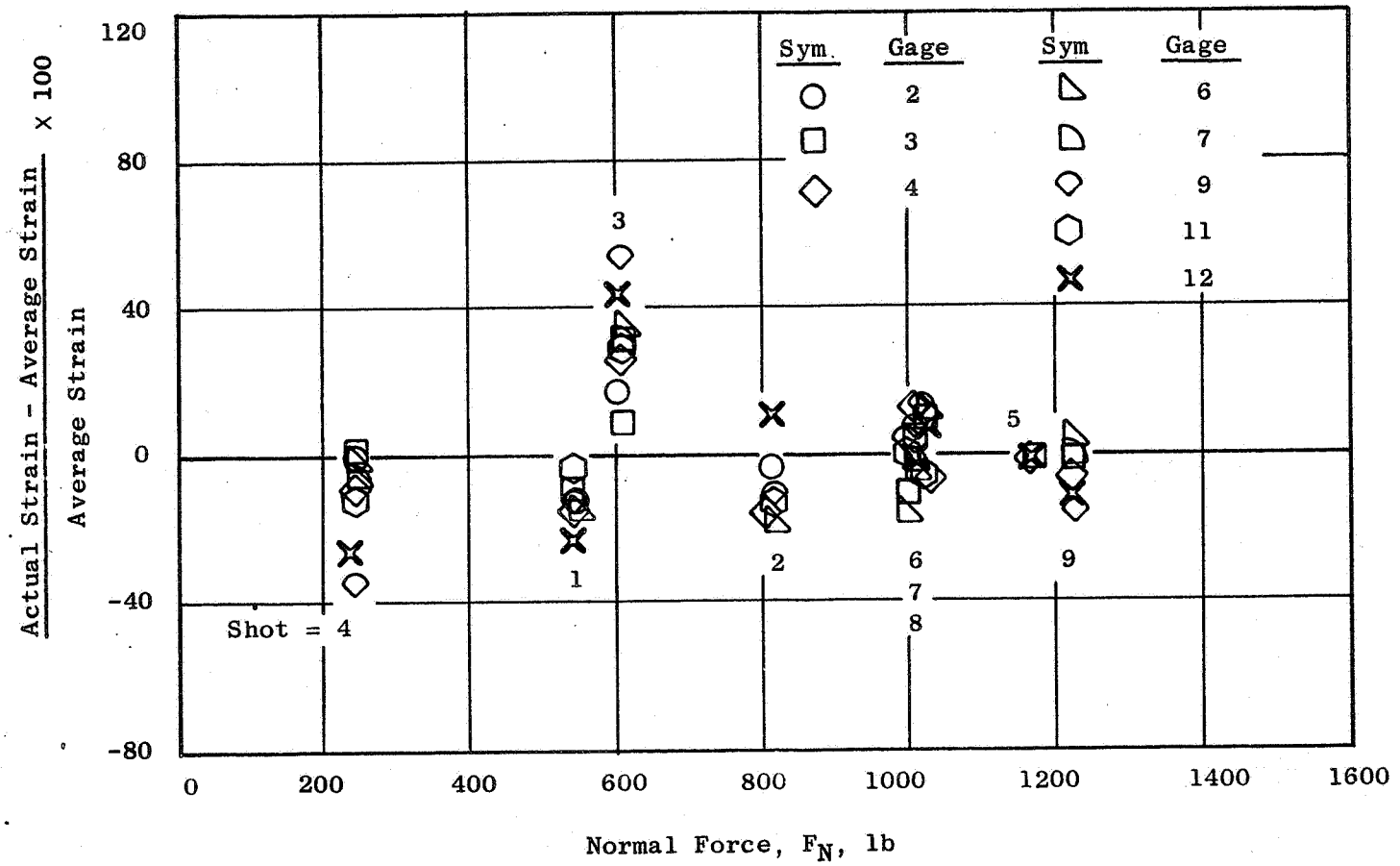

Figure 35. Normal Force Versus Peak Strain on First Cycle for 37% and 75% Spans.

is to allow the strains measured in low level impacts to be extrapolated to higher impact levels and so to predict the damage possibility, and to select potentially severe impact situations when new blade designs are being considered. The normal force parameter can also be used as a baseline approach to analytically modeling the bird/blade interaction.

3.4.3 Spectrum Analysis

To obtain information on the frequency and relative amplitude of the frequency response exhibited by a composite blade immediately following impact, a spectrum analysis was carried out on the strain gage response of two strain gages (numbers 3 and 4, see Figure 10). The strain gage response was obtained from the impact of QP014 at 75 percent span by a 14 gram (0.49 ounce) RTV bird at an incidence angle of 33 degrees with a rotor speed of 3200 rpm (Run No. 8). Strain gage numbers 3 and 4 were chosen since they were located near the impact, and one gage (No. 3) measured strains in the chordal direction while the other strain gage (No. 4) measured strains in the radial direction.

The response of strain gage No. 3 at impact and up to 0.05 seconds after impact is shown in Figure 36. From this figure, it can be seen that the initial response is of high amplitude and relatively high frequency which, after approximately 0.015 second, has become a steady 280 Hz response corresponding to the first torsional frequency of this blade. Also, note that the strain amplitude has decayed to 10 percent of the initial value after about 0.038 second. Figure 37 shows the relative amplitudes of frequencies between zero and 10,000 Hz for this first 0.05 second of the response. From this curve, it can be seen that the contribution from frequencies above 4000 Hz is negligible. Looking at the amplitudes of frequencies between zero and 2500 Hz (Figure 38), the three major frequencies are approximately 280 Hz, and 1157 Hz. Evaluation of the first 0.0125 seconds of gage response after impact produced the curve shown in Figure 39. From this curve, several observations can be made. In comparison to the longer (0.05 second) time span, it appears that the same frequencies are present but that the relative amplitudes have changed with a shift towards the higher frequencies. A further reduction in time span to 0.006 second produced the spectrum shown in Figure 40. This curve reveals that although the lower frequencies are still present, the predominant frequency in regard to amplitude is now about 1150 Hz.

The response of strain gage No. 4 was evaluated in a manner similar to the evaluation of strain gage No. 3. Figure 41 shows the strain gage response for the first 0.05 second after impact. Again, as with strain gage No. 3, there is an initial high amplitude response which quickly decays to a lower amplitude response. Looking at the amplitudes of the frequencies between zero and 10,000 Hz (Figure 42), the contribution from frequencies above 4000 Hz again is negligible. An evaluation of the frequencies between zero and 2500 Hz (Figure 43) reveals that the primary response frequencies are 80, 180, (corresponding approximately to the first and second flexural frequencies of the blade), 340, 1140, and 2400. Evaluation of the frequency

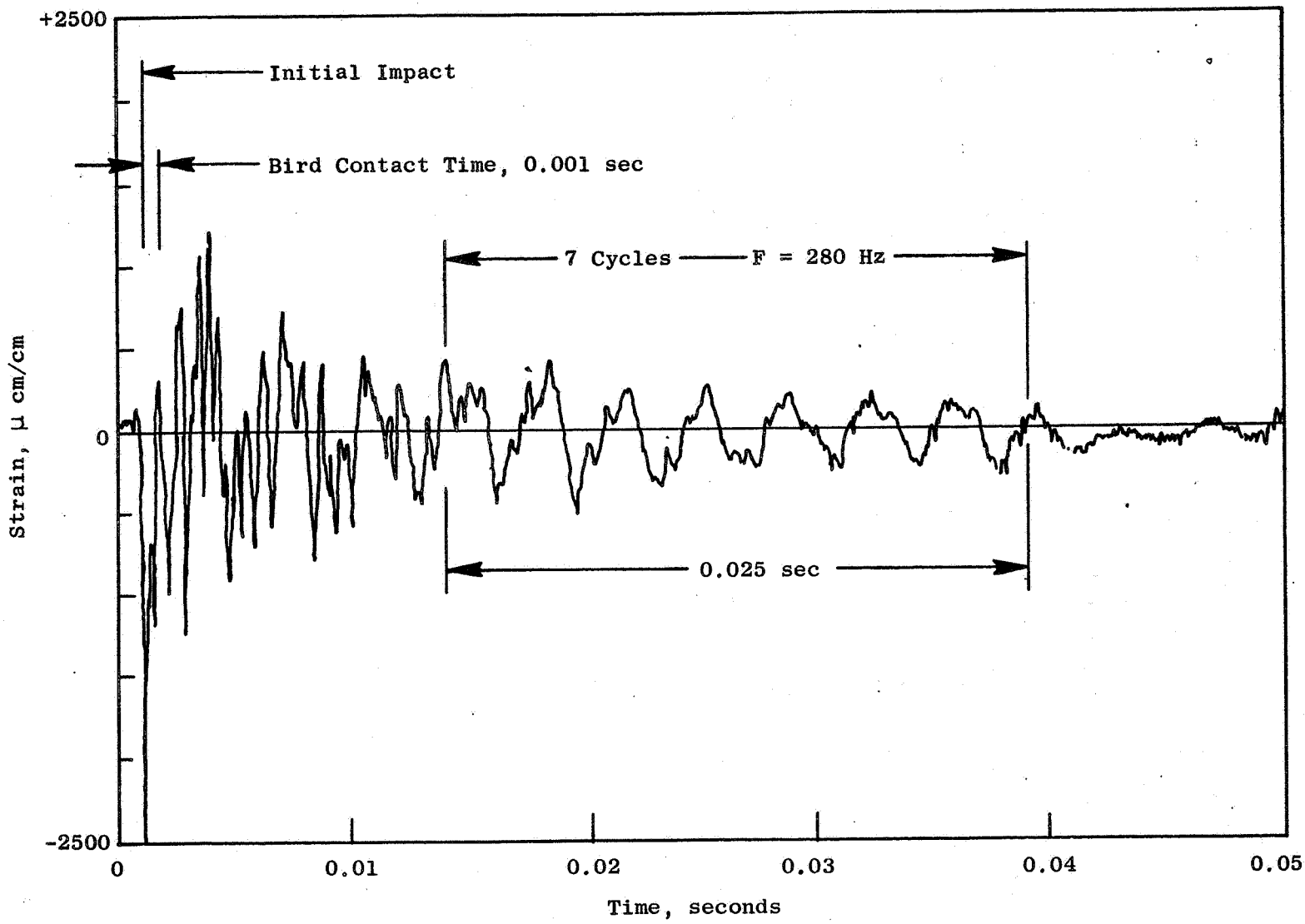

Figure 36. Strain Gage 3 Time Trace for Run 8.

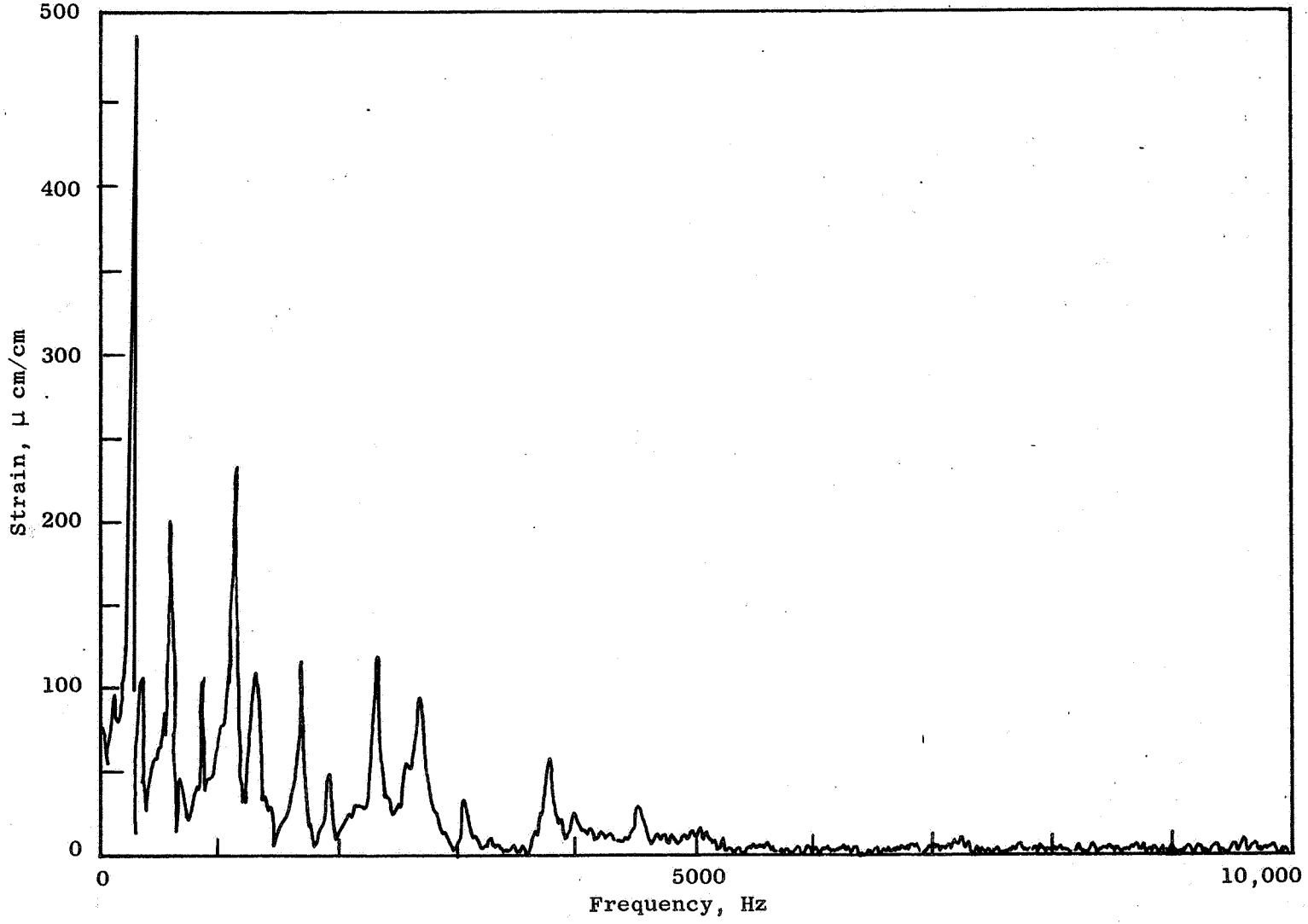

Figure 37. Frequency Spectrum for First 0.050 Seconds of Impact; Gage 3, Run 8.

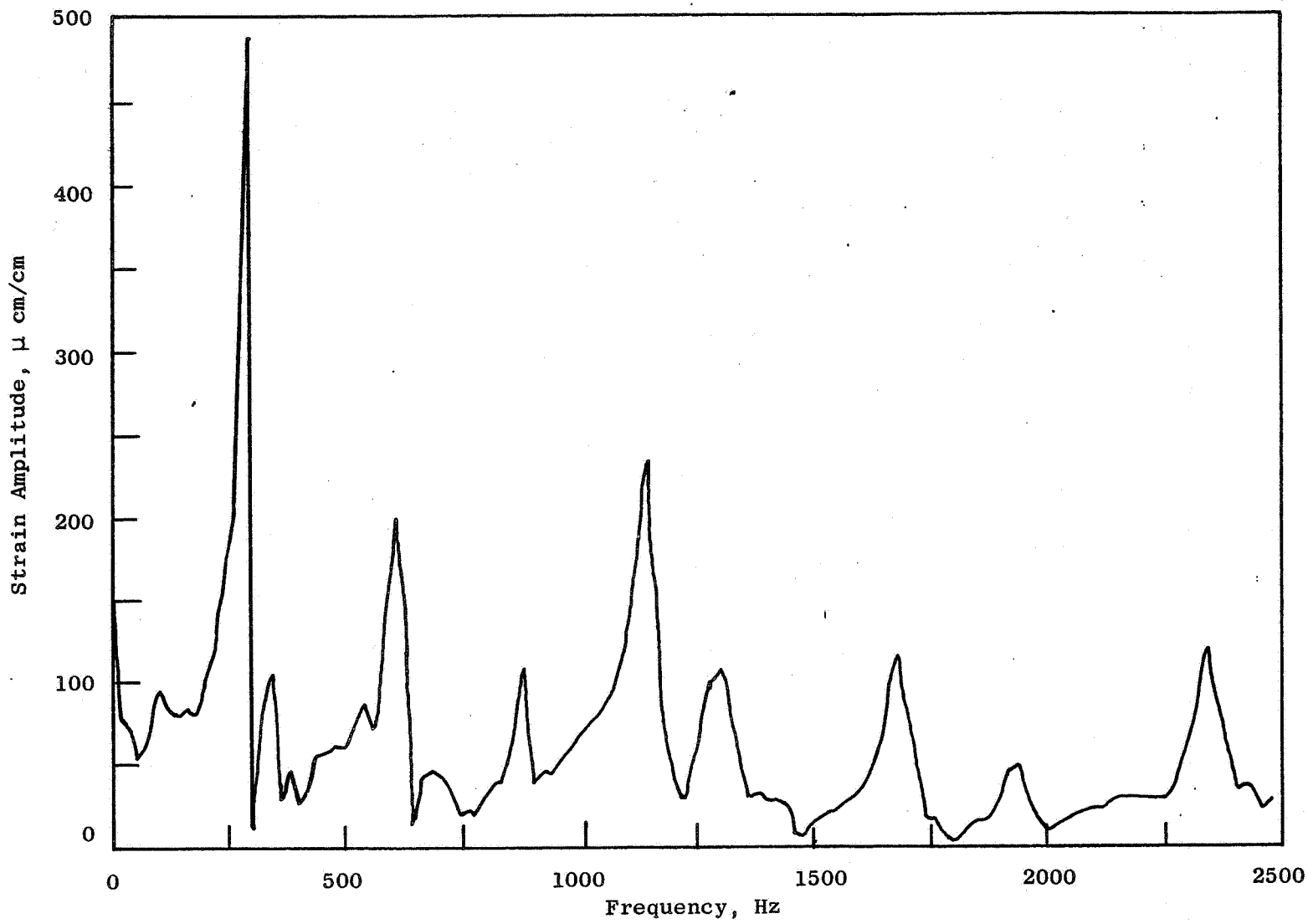

Figure 38. Frequency Spectrum for First 0.050 Seconds after Impact; Gage 3, Run 8.

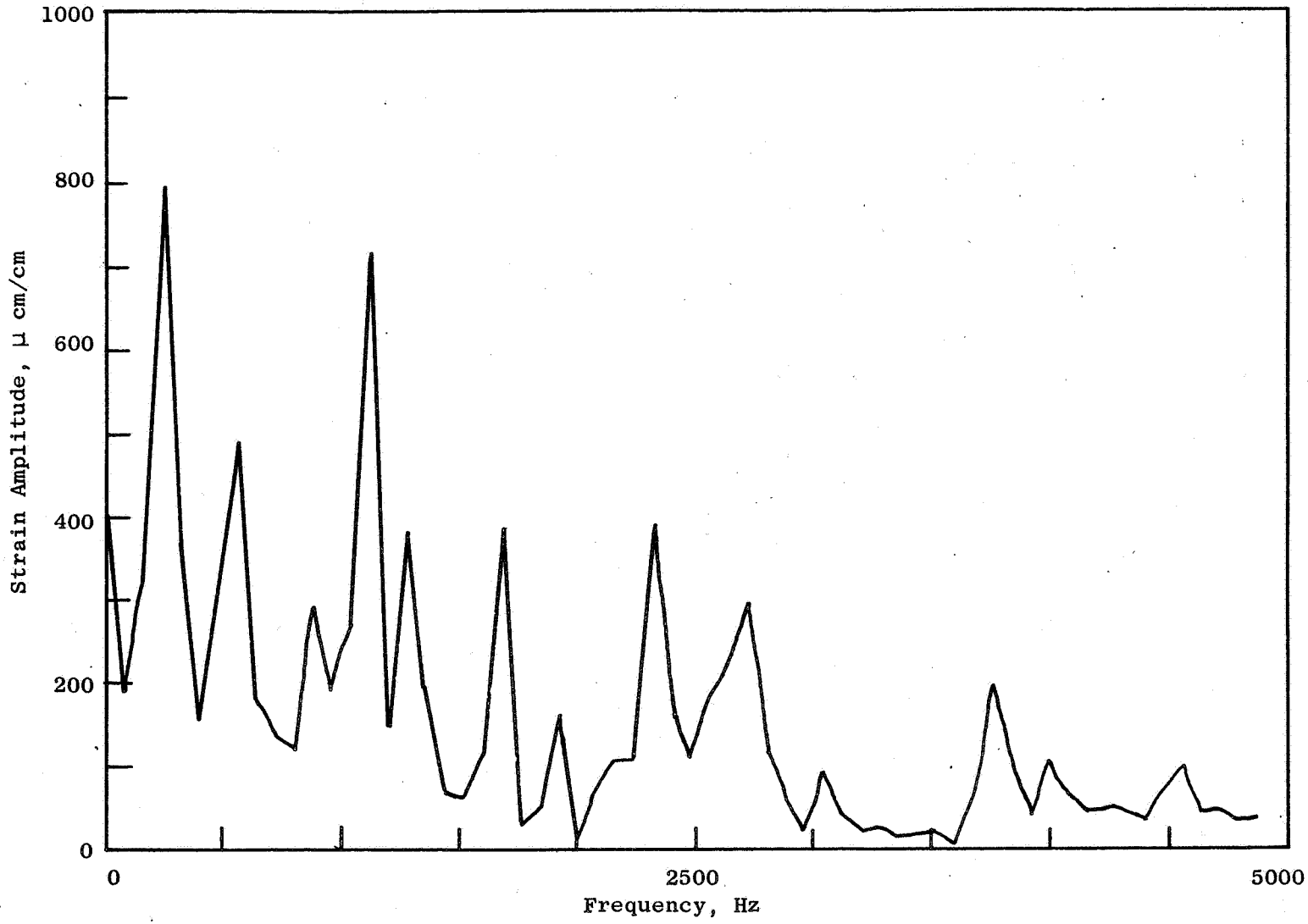

Figure 39. Frequency Spectrum for First 0.0125 Seconds After Impact; Gage 3, Run 8.

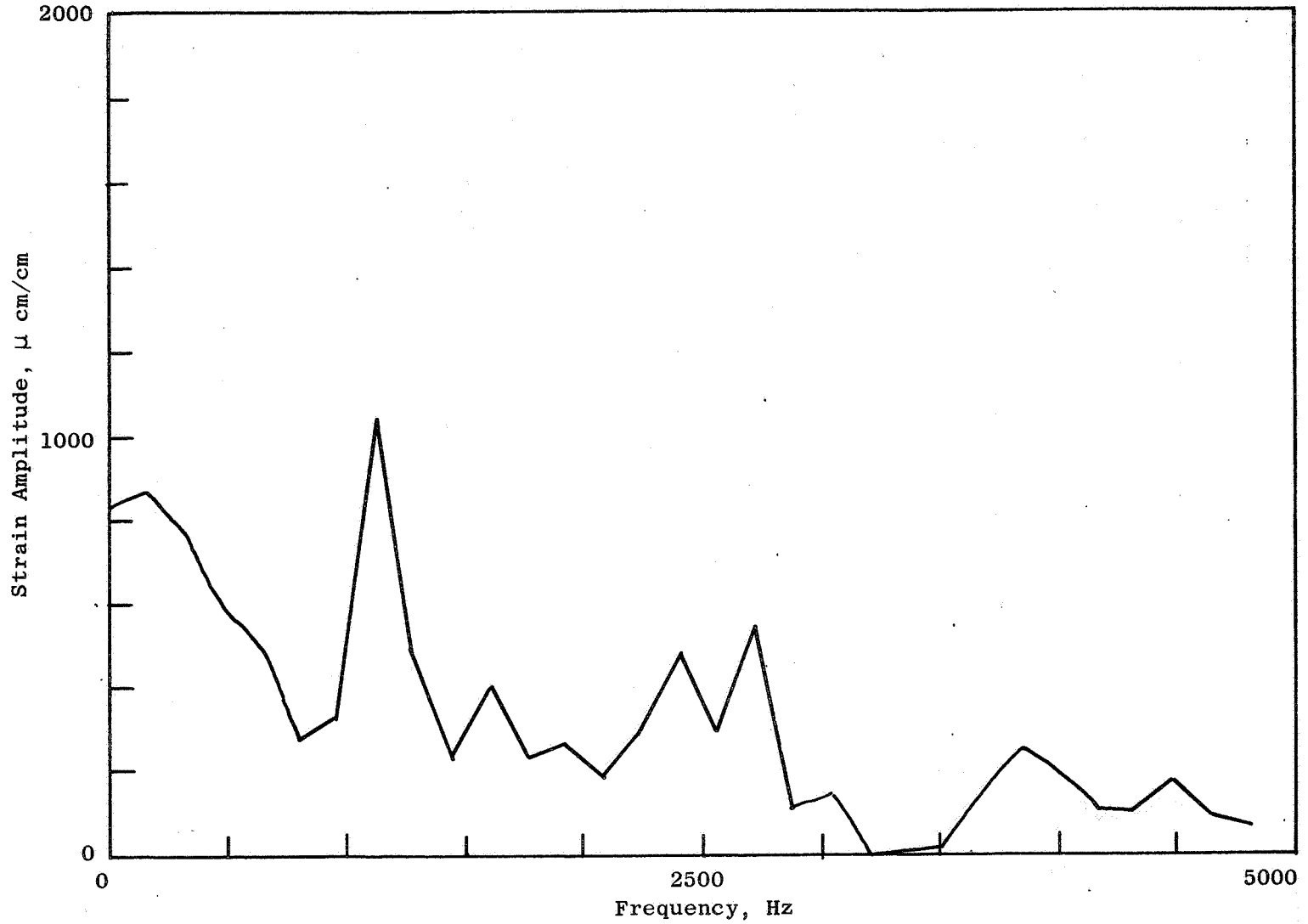

Figure 40. Frequency Spectrum for First 0.006 Seconds After Impact; Gage 3, Run 8.

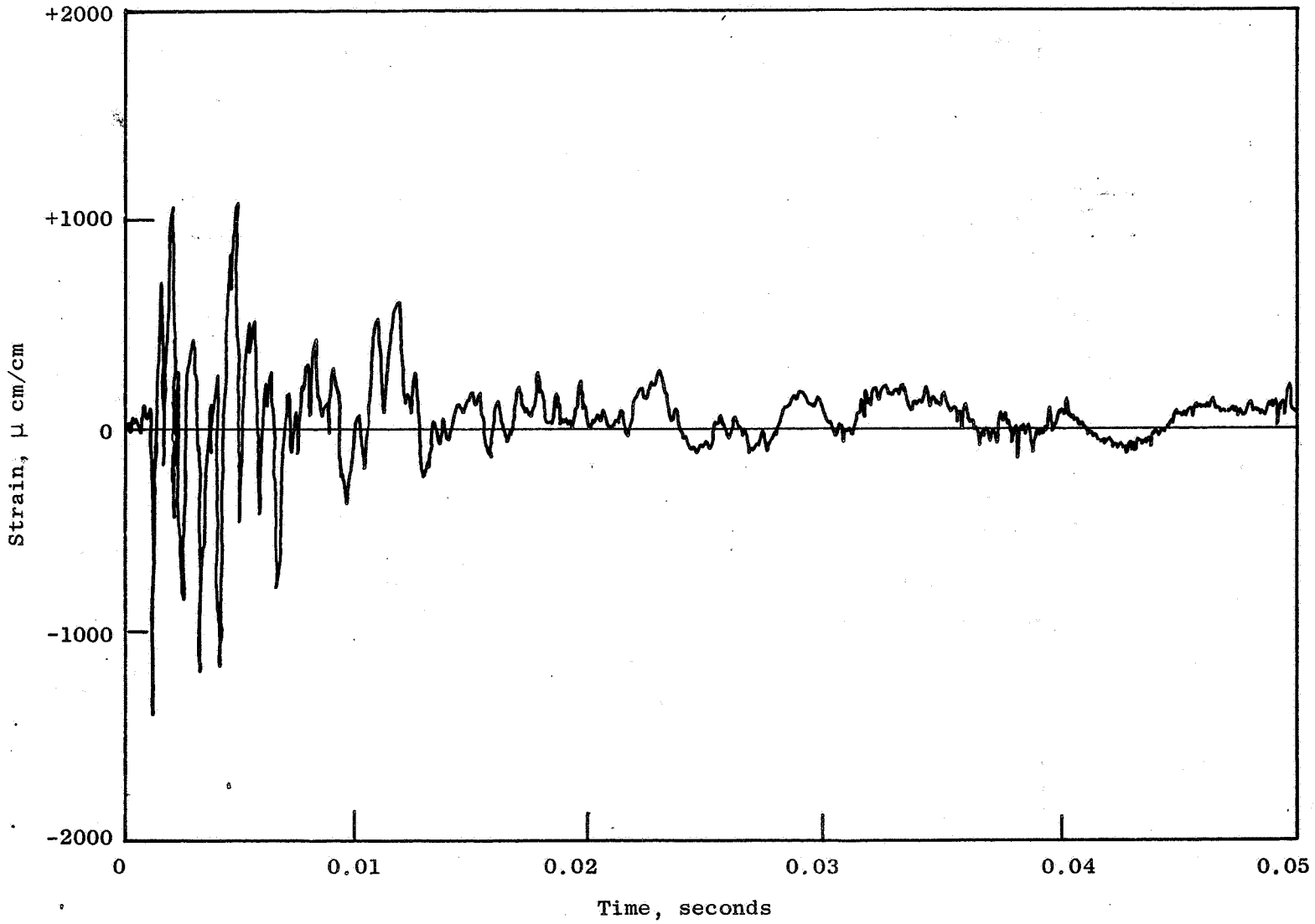

Figure 41. Strain Gage 4 Time Trace for Run 8.

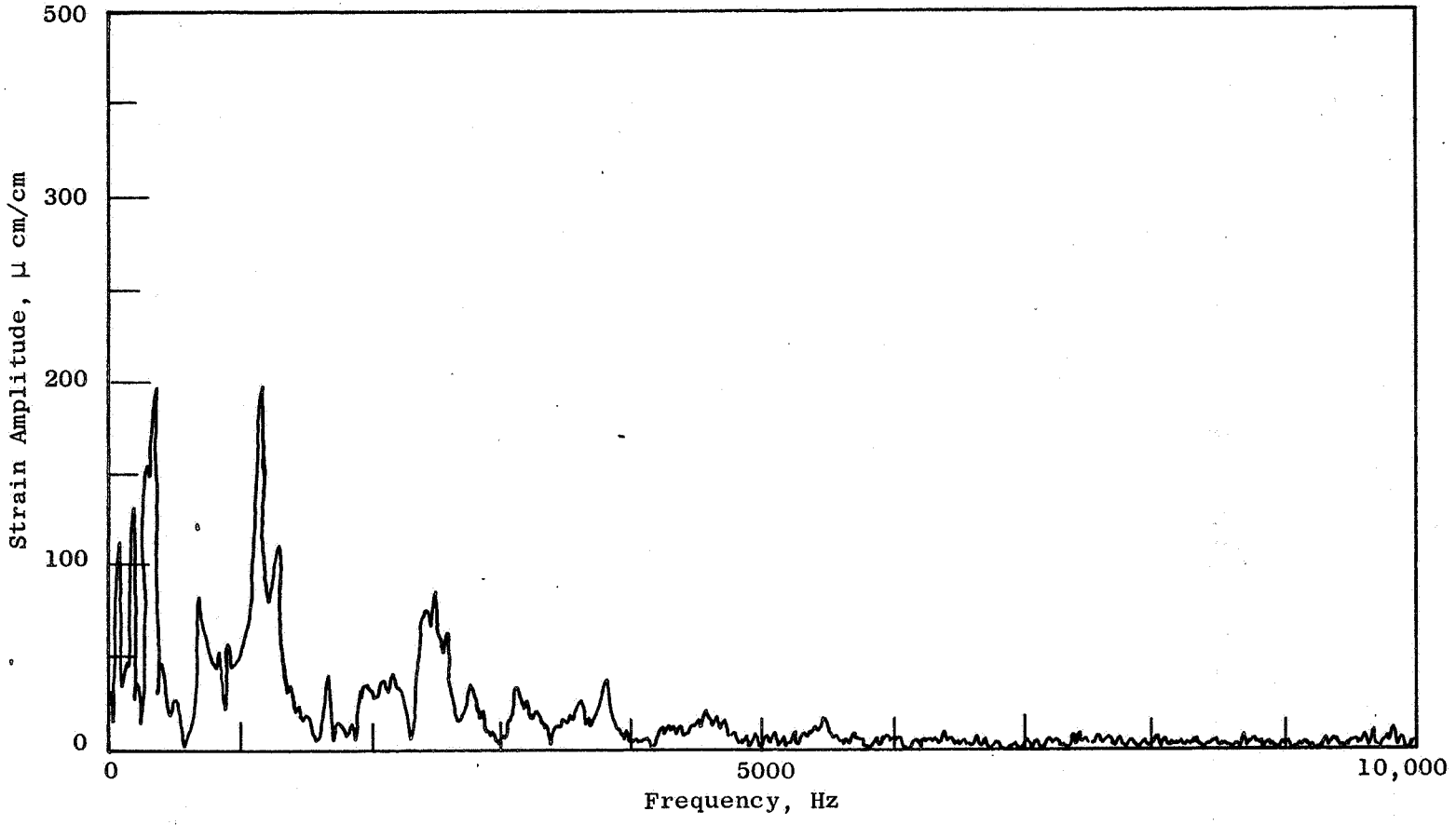

Figure 42. Frequency Spectrum for First 0.05 Seconds After Impact; Gage 4, Run 8.

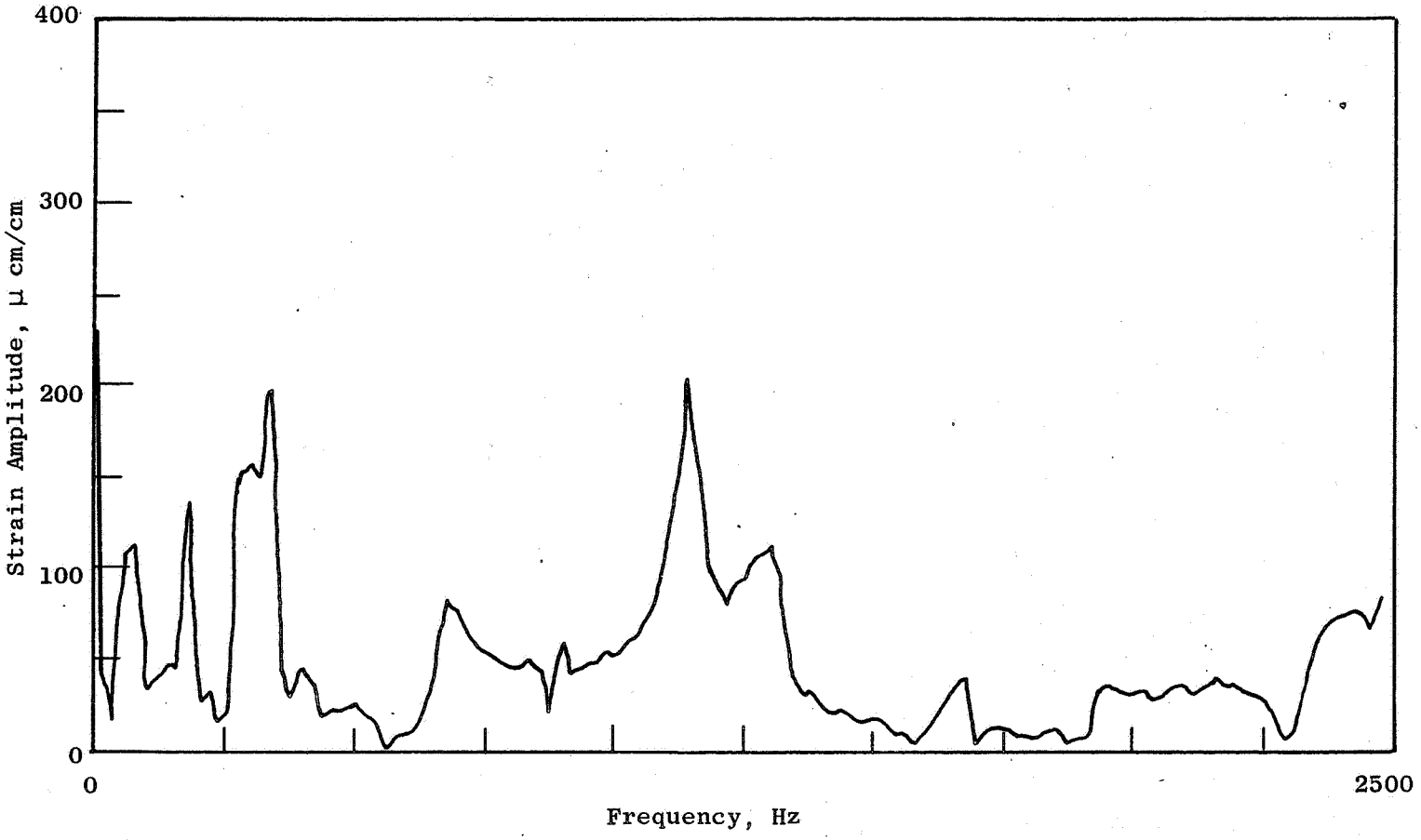

Figure 43. Frequency Spectrum for First 0.05 Seconds After Impact; Gage 4, Run 8.

spectrum obtained from the first 0.0125 second of the impact response (Figure 43) shows the two predominant frequencies to be 340 Hz and 1140 Hz with the higher frequency (2400 Hz) still present. The spectrum from the first 0.006 seconds of the impact (Figure 44) indicates the primary dominance, over this initial time span, of the 1140 Hz response with the 340 Hz and 2400 Hz frequencies still making a significant contribution.

In summary, the following observations may be made:

- For the longer time span (0.05 second), the impact response spectrum is composed primarily of the fundamental blade frequencies (first and second flexural for the radial gage No. 3 and first torsional for the chordal gage No. 4) along with a higher frequency (approximately 1150 Hz).

- As decreasing time spans (0.0125 and 0.006 second) closer to the impact time are evaluated, the fundamental frequencies decrease in amplitude and the higher frequency (approximately 1150 Hz) becomes predominant.

- For both strain gages No. 3 and No. 4, the contribution from frequencies above 4000 Hz is negligible.

- In terms of blade design for impact, these results indicate that any impact stress analysis must be capable of including blade frequencies much higher than the first few blade natural frequencies.

3.4.4 Test Data Comparison to Analysis

The QCSEE composite fan blade was analyzed using a parametric, 3-D, finite element, eigenvalue, and thermal stress computer program named PARA-TAMP-EIG. The program accounts for the inertial forces of rotation and vibration. In addition, the stiffening effect of rotation is taken into account. The program has the capability of giving directly the first eight modes, frequencies, and corresponding stress for a specified speed of rotation as well as the deflections and stresses in both stationary and rotating bodies. The program uses an eight-noded box element (Figure 46) to build up the stiffness and mass characteristics by Gaussian integration (Figure 47). Each box has 33 degrees-of-freedom: 24 corresponding to the three motions of each of the eight nodes; and nine internally eliminated to minimize strain energy. The program can handle 3-D-anisotropic material properties with the blade root restrained by both friction and springs and loads being applied by either distributed pressures or point forces.

The dynamic impact analysis of the QCSEE composite blade model (Figure 48) was performed using the frequencies, mode shapes, and relative stress distributions from the 3-D finite element program in combination with a recently programmed dynamic impact response computer program. This program

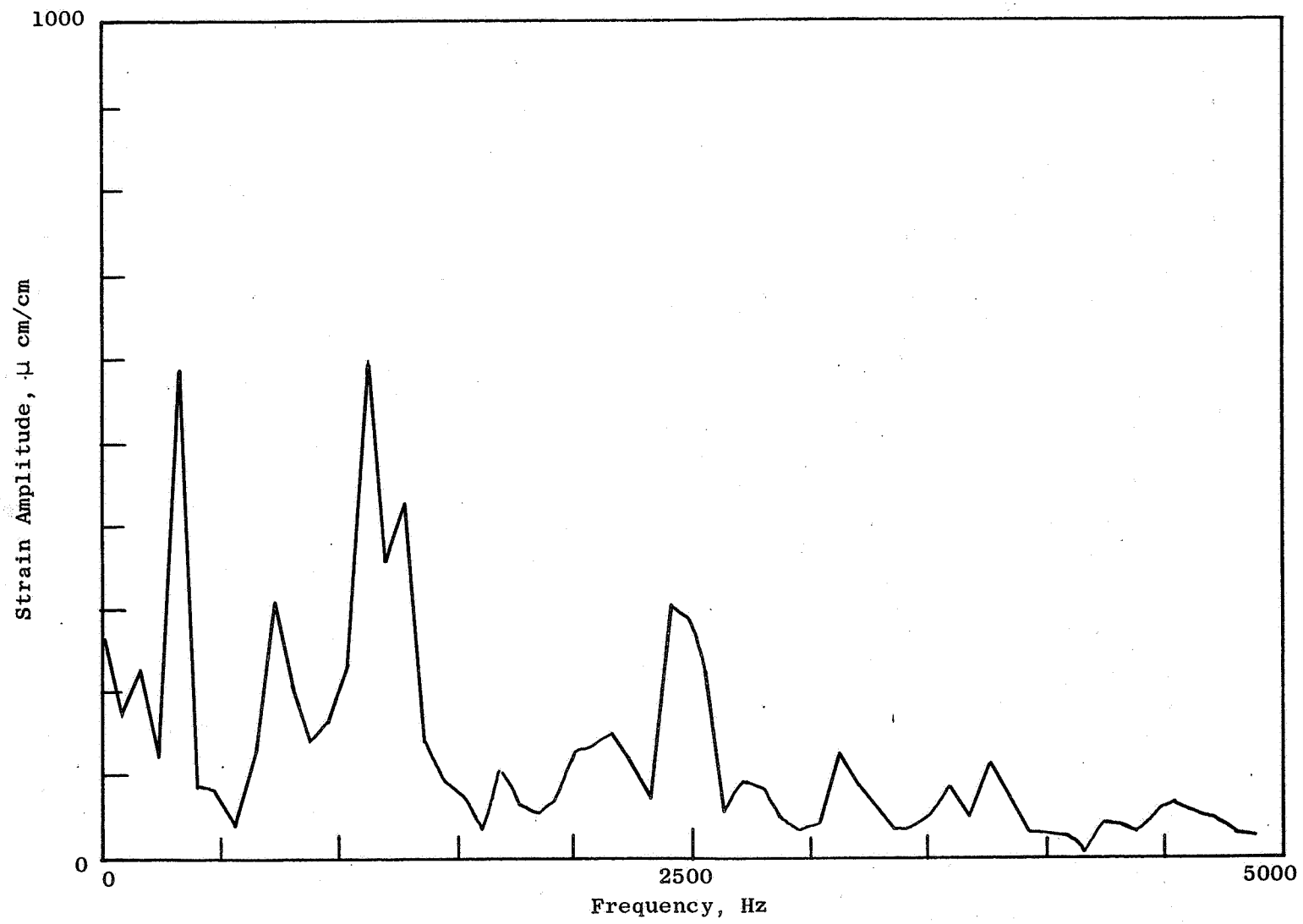

Figure 44. Frequency Spectrum for First 0.0125 Seconds After Impact; Gage 4, Run 8.

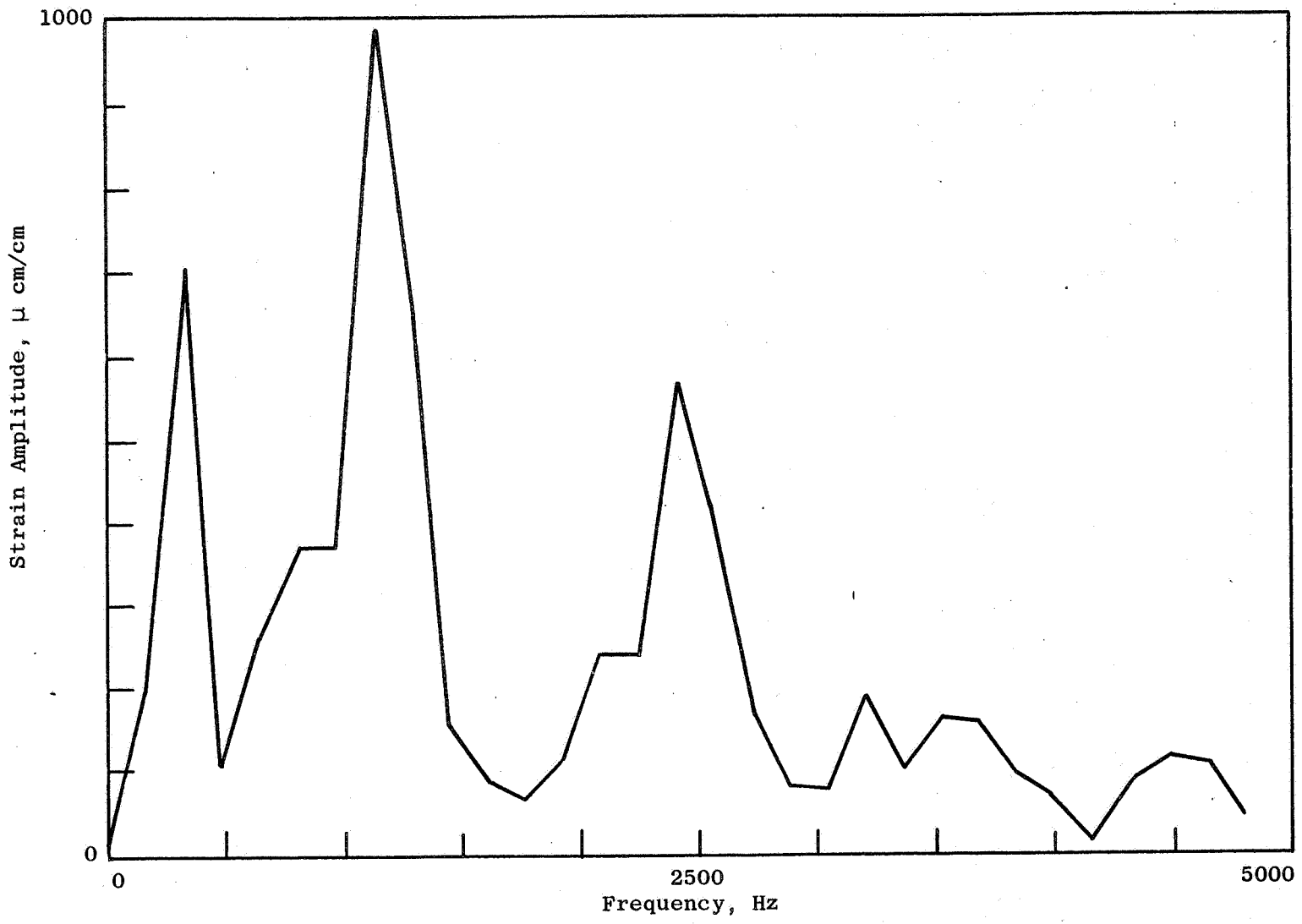

Figure 45. Frequency Spectrum for First 0.006 Seconds After Impact; Gage 4, Run 8.

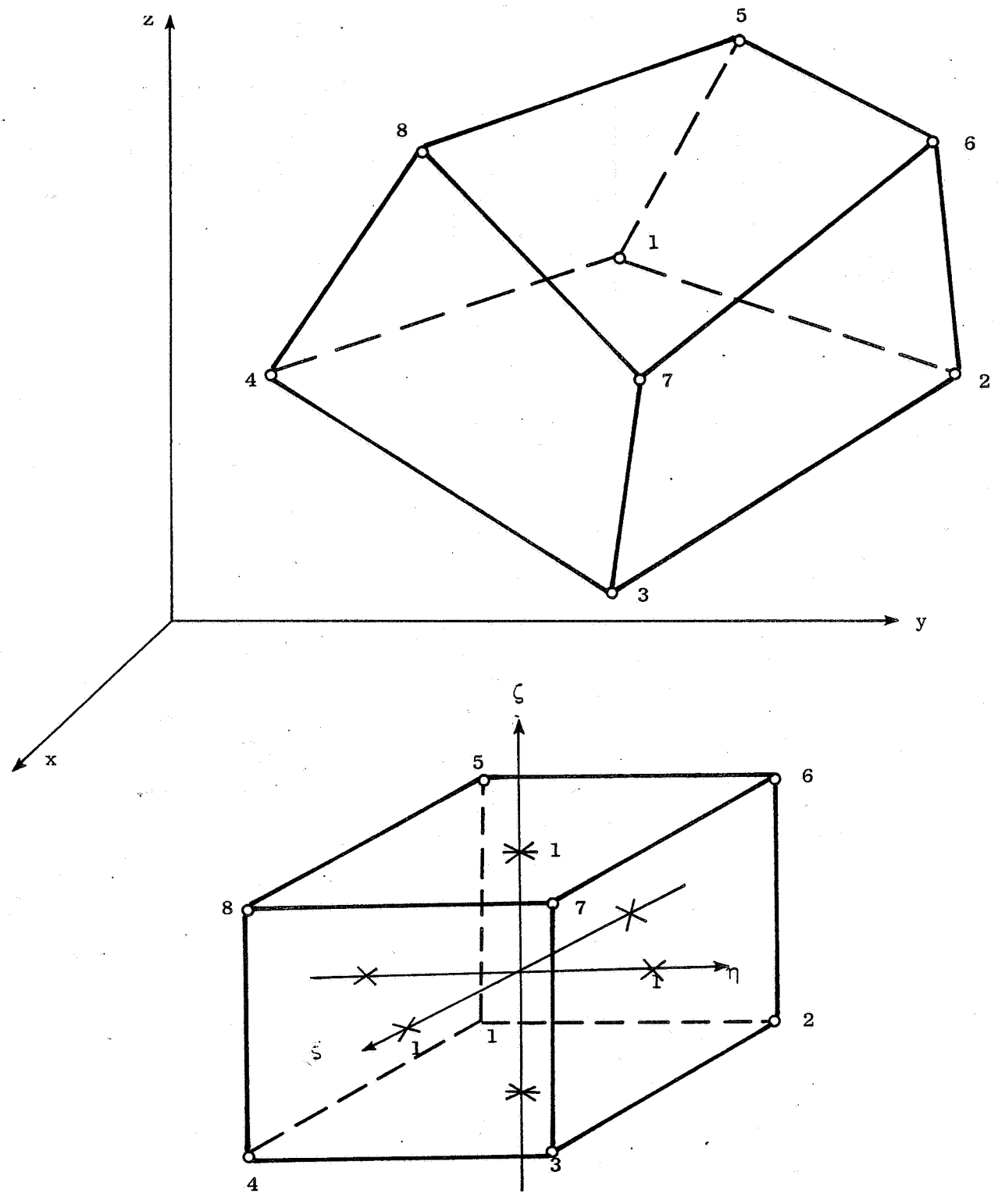

Figure 46. Isoparametric Representation of an Eight-Noded Element.

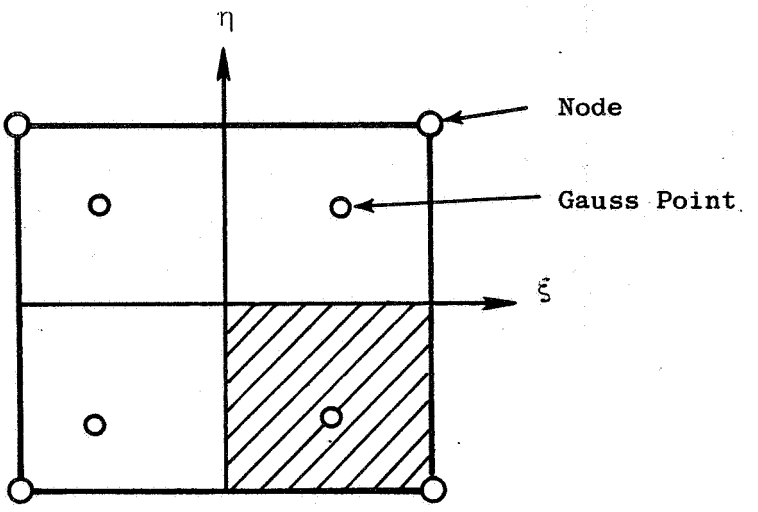

a) Isoparametric Space

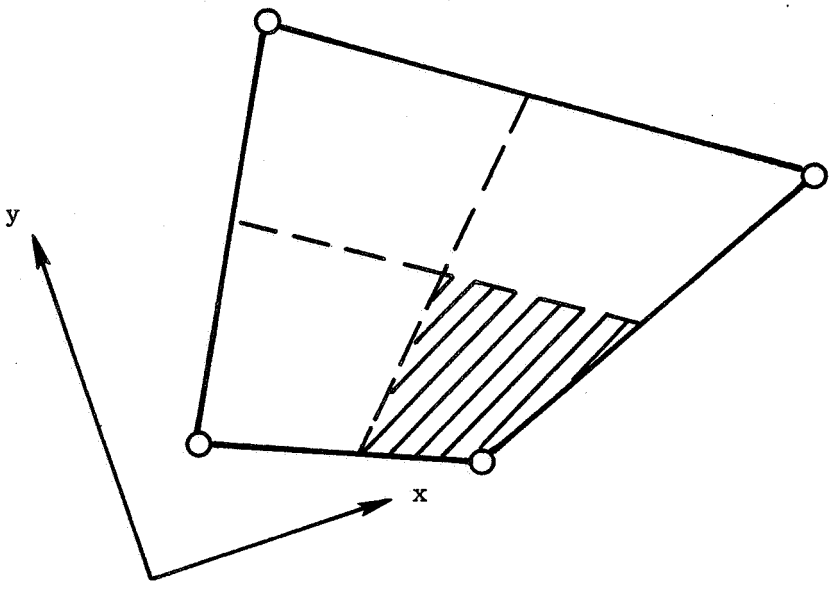

b) Cartesian Space

Figure 47. Gaussian Integration of Eight-Noded Box Element. Lumping the Mass at a Nodal Point. The Shaded Area Shows the Mass that is Lumped at the Adjacent Node.

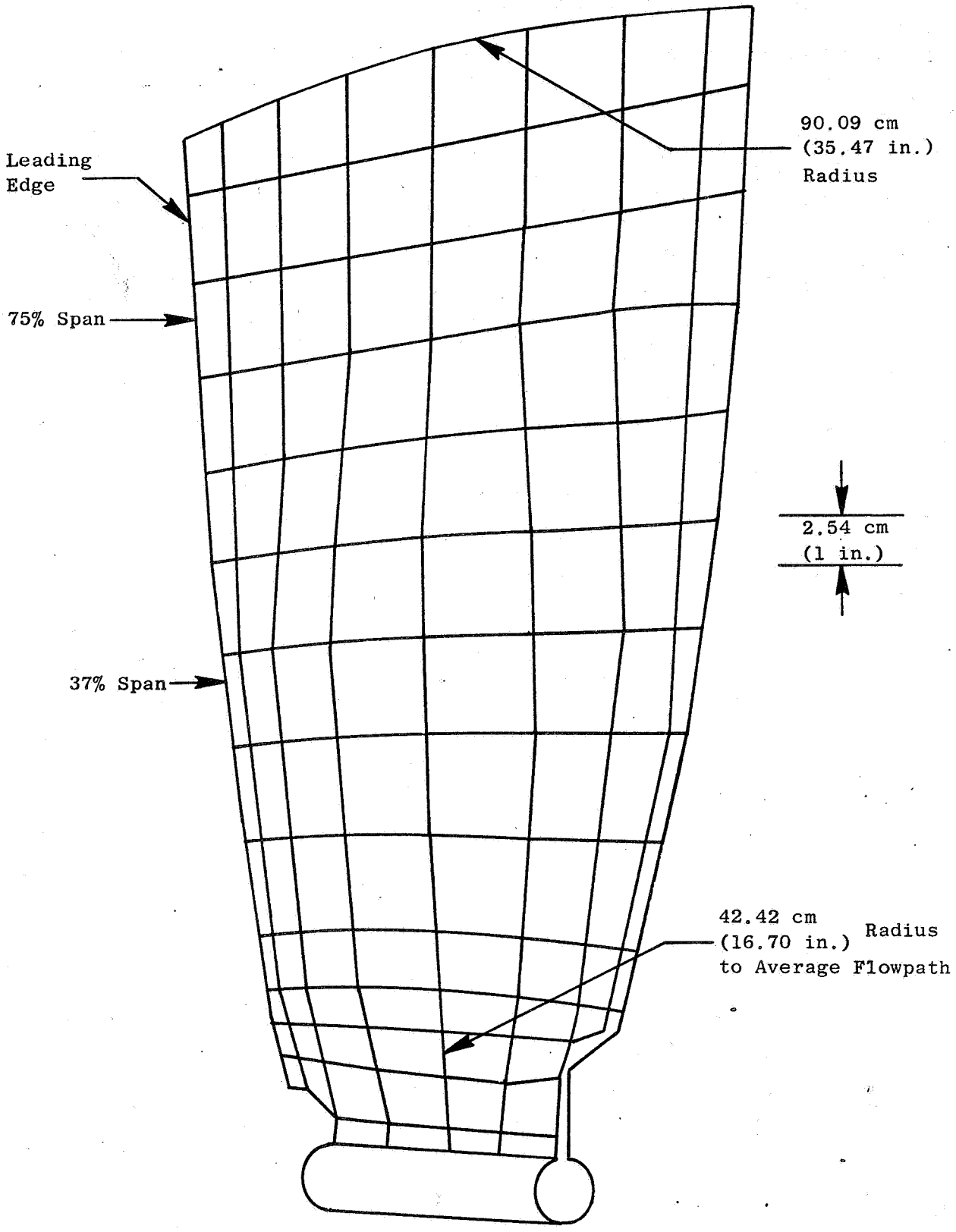

Figure 48. QCSEE Composite Blade Model.

was generated to consider a lumped mass, spring-damper system applied at the nodal points of the blade. The mass traverses the blade chord along the "bird wipe line" as shown in Figure 49. This analysis determines the interaction loads between bird and blade versus time, as shown in Figure 50.

Analytical predictions of impact strain versus time for run numbers 1, 5, and 8 were made using the PARA-TAMP-EIG finite element computer program (see Appendix I). A comparison of the waveforms obtained from analysis and test data for run No. 1 is shown in Figure 51. The following observations can be made from this comparison:

- The analytical response compares favorably with the test data for the initial peaks.
- The analytical model does not appear to damp out the strain levels when compared to the test data.

3.4.4.1 Analytical and Test Peak Strain Comparison

A comparison was made between strain data recorded during impact and analytical data obtained from the finite element computer program for the following cases:

Run No.	Blade Type	% Span	Slice Wt (gm)	rpm	Incidence Angle
1	QCSEE	75	16	3200	23°
5	QCSEE	37	18	3202	40°
8	QCSEE	75	14	3200	33°

Figure 10 shows the finite element model used in the analysis and the strain gage locations/type (radial or chordal). The same bird model and impact force versus time curve was used for all runs. The data utilized in the comparison was the first peak which occurred immediately following impact. For ease of comparison, the data was plotted as analytical strain minus test strain divided by maximum test strain for each strain gage. This is shown in Figure 52 for runs 1 and 8 and in Figure 53 for run 5.

From Figure 52, it can be seen that, in general, the analytical and test data agree within +25 percent and -12 percent. The largest error occurred at gage location number 12 for both run 1 and run 8. One possible reason for this larger error at this location is the relatively coarse finite element model in the root area of the blade.

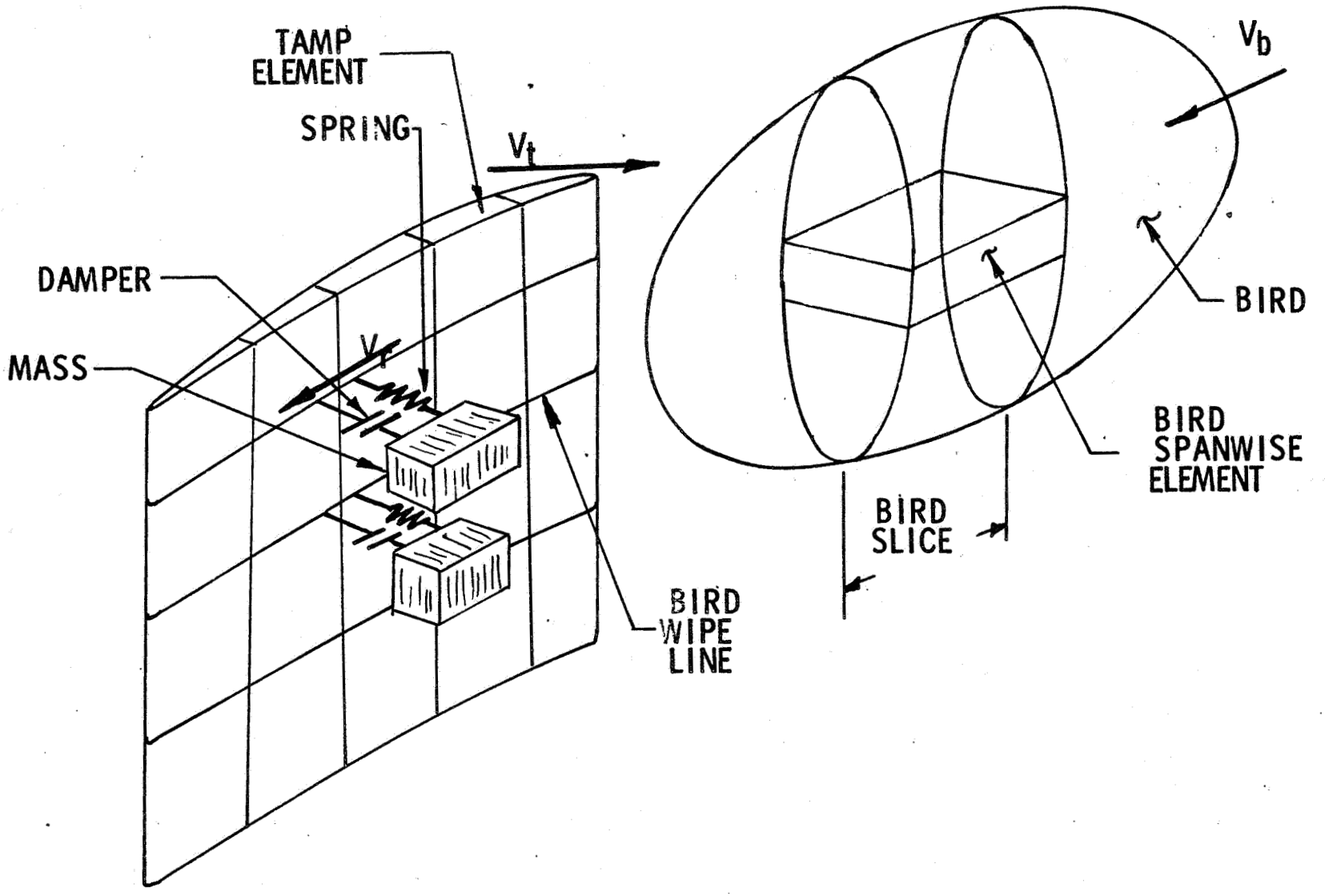

Figure 49. TAMP Bird Impact Analysis.

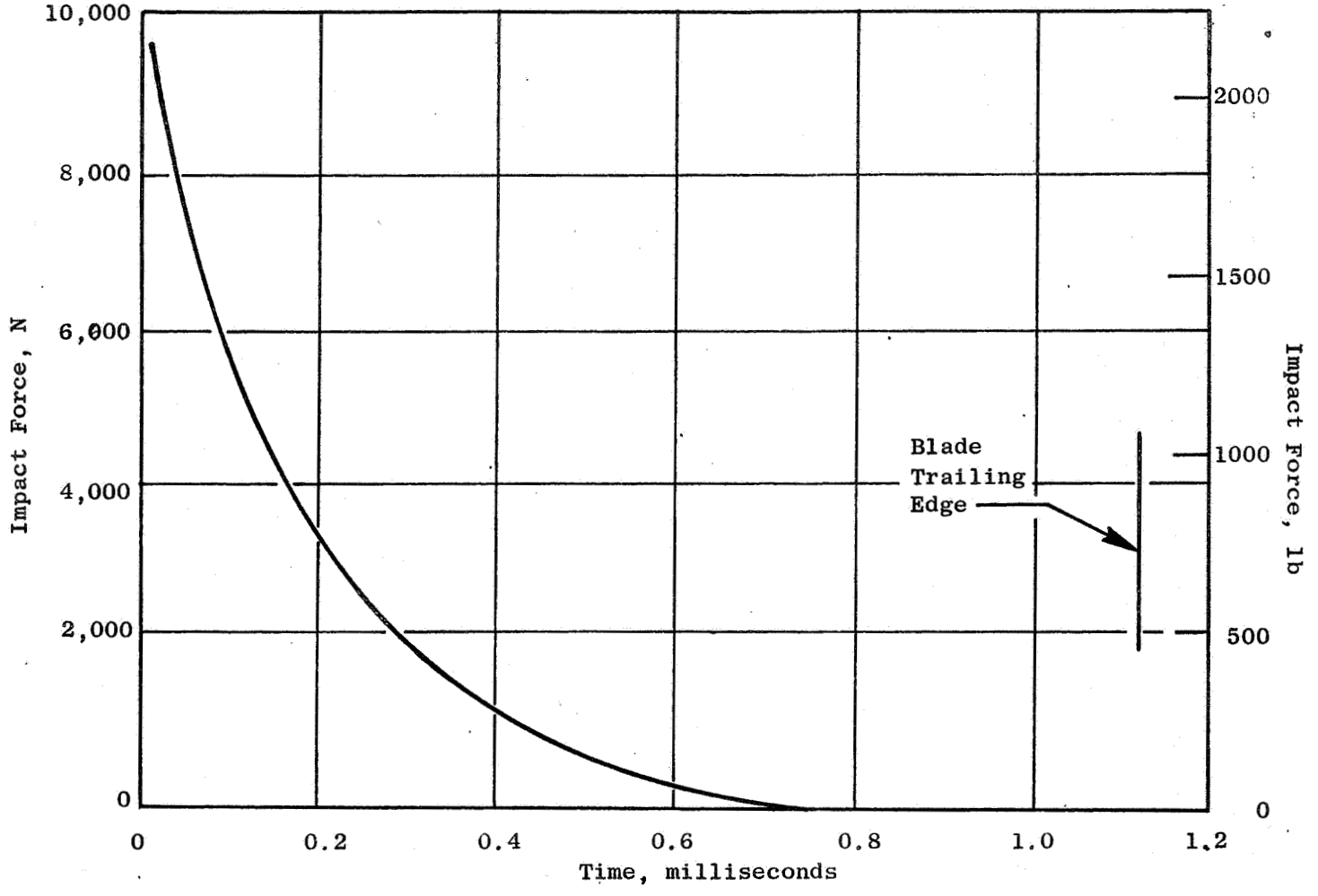

Figure 50. Analytical Force on Blade for Run 1.

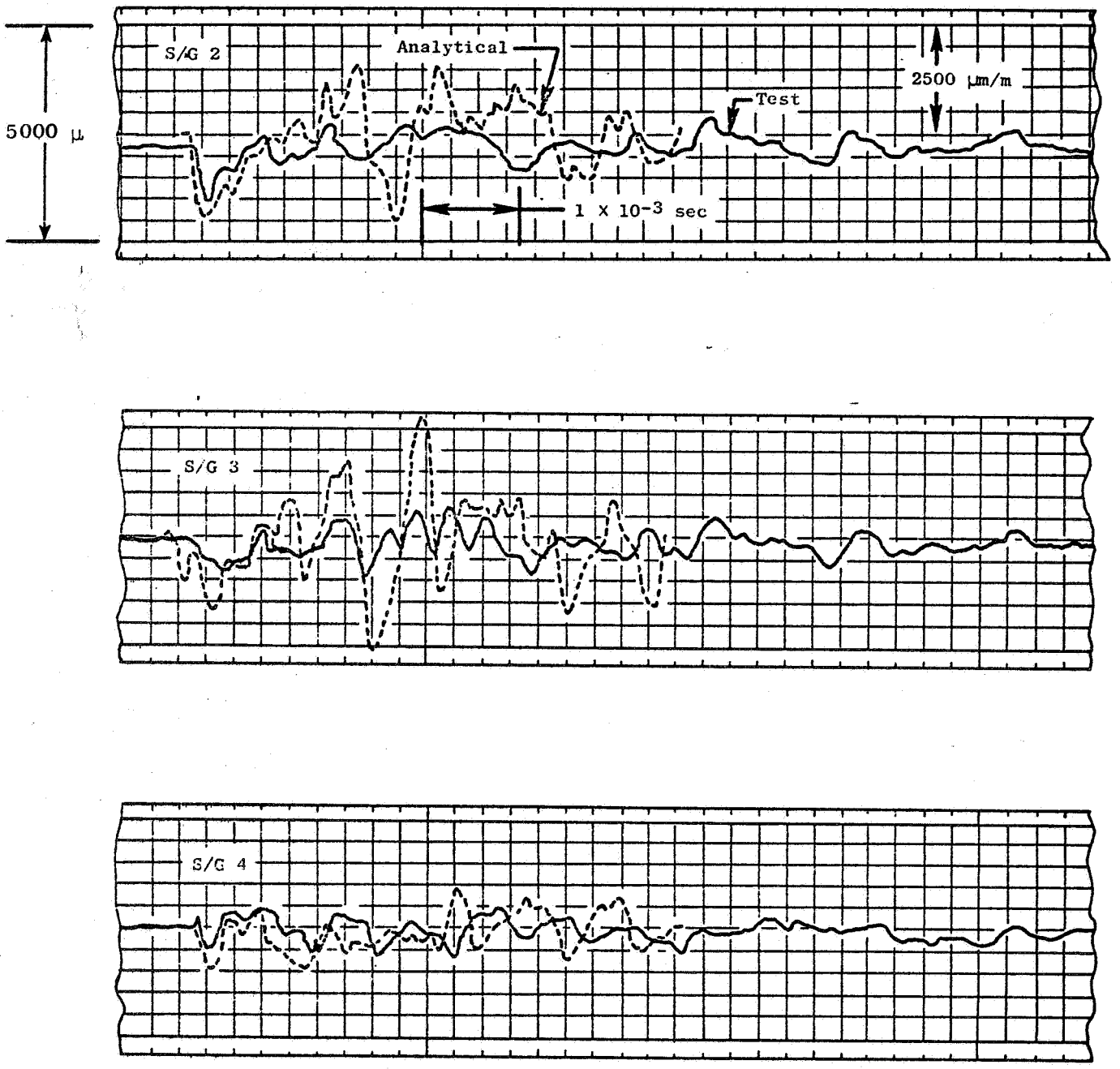

Figure 51. Analytical Predictions Versus Test; Run 1, Baseline Impact, 75% Span, 16 gram Slice, at 3200 rpm.

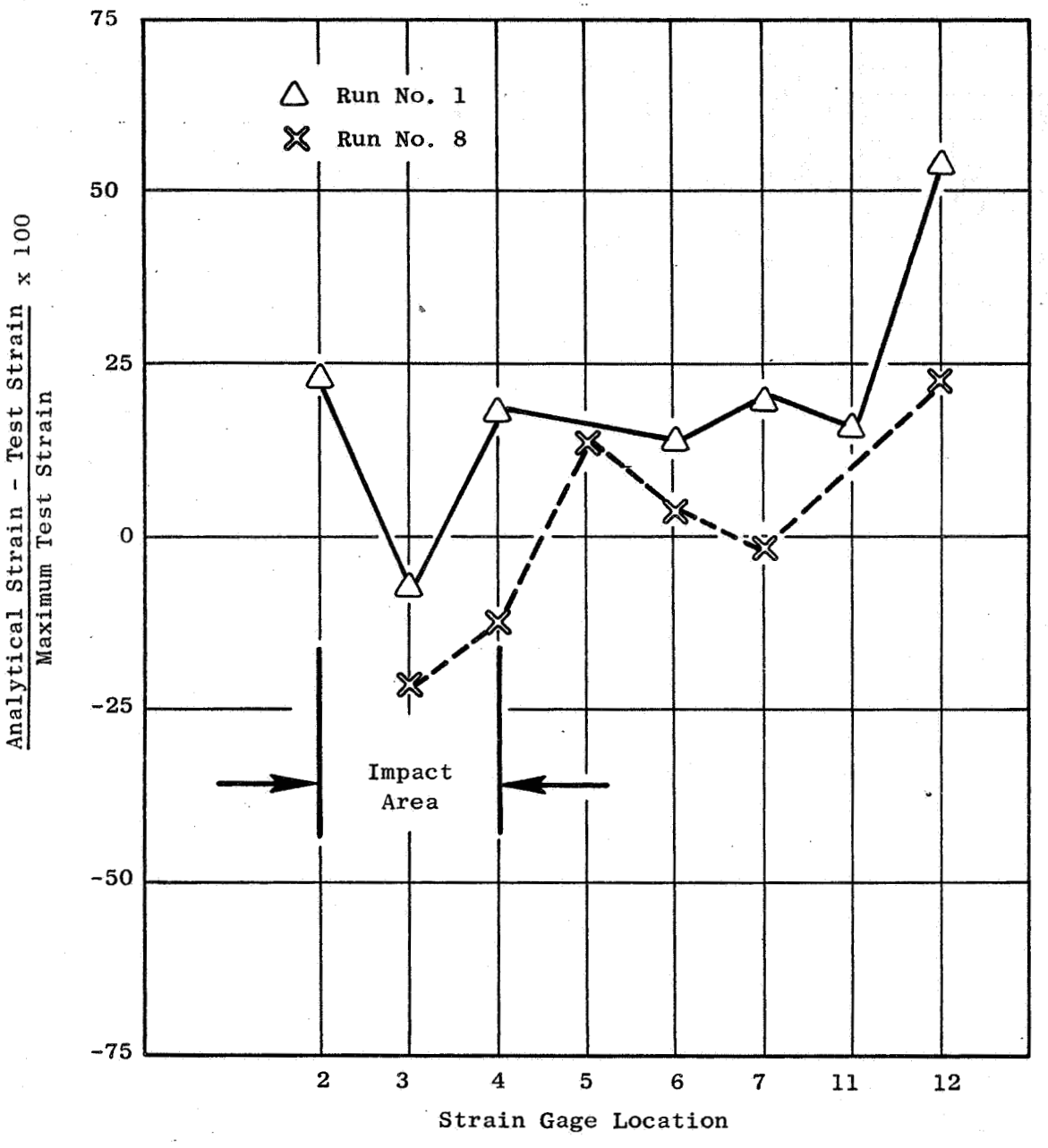

Figure 52. Analytical Strain Versus Test Strain Runs 1 and 8.

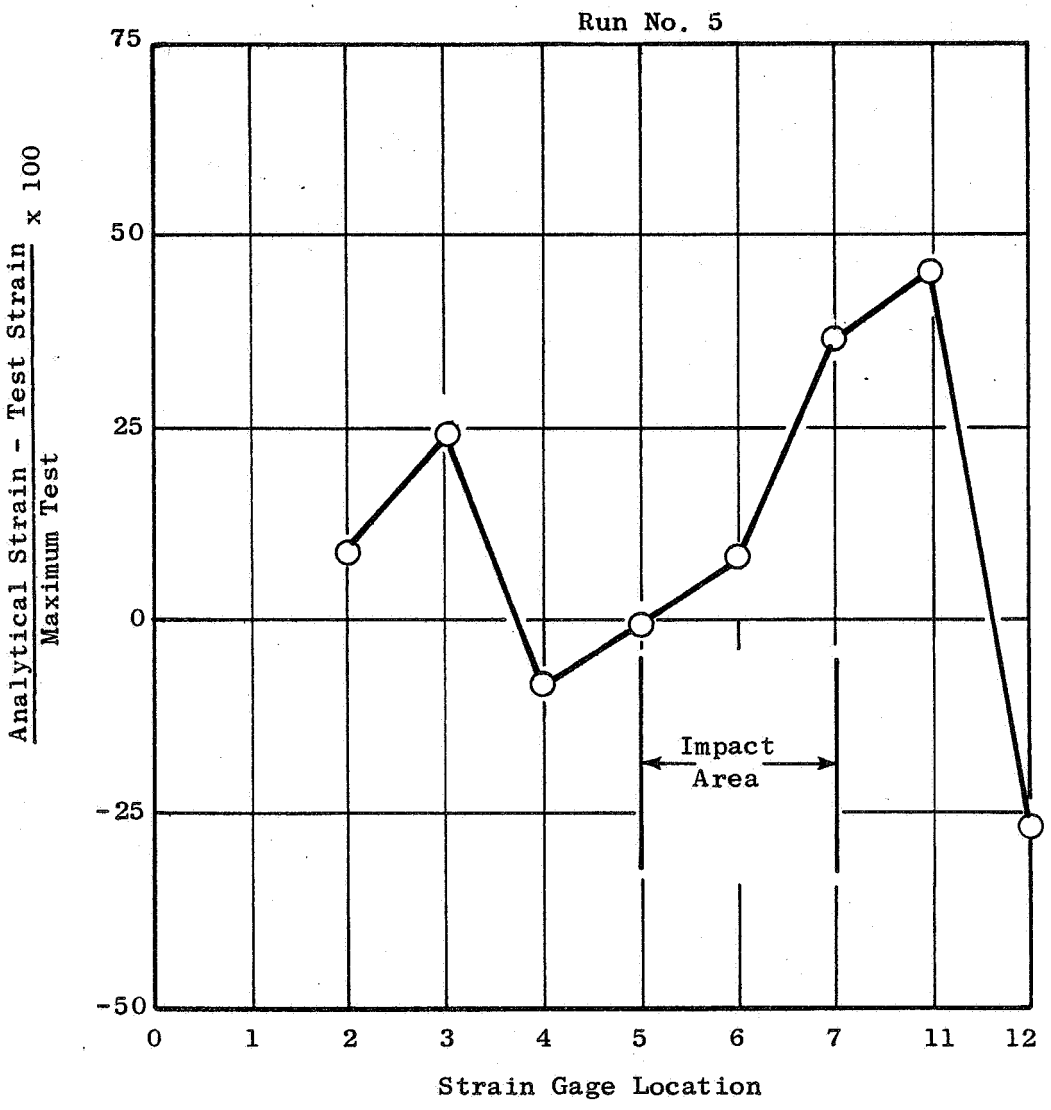

Figure 53. Analytical Strain Versus Test Strain Run 5.

The analytical versus test strain comparison for run number 5, shown in Figure 53, exhibits somewhat poorer agreement than for runs 1 and 8. This is a result of the fact that the impact occurred at 37 percent span, while the same bird properties (spring constant and damping characteristics) were used as had been used for the impacts at 75 percent span.

In summary, the comparison has shown good correlation between analytical strain and measured strain for the impacts and strain locations studied. In addition, it appears that with some additional work on the bird modeling even better agreement may be obtained between analytical and test data.

4.0 IMPROVED IMPACT RESISTANT BLADES

The objective of this phase of the program was to investigate the effectiveness of various material combinations and layup configurations on the improvement of FOD resistance of composite blades. This was accomplished through the design of the internal configuration, fabrication, and testing of a series of four fan blades.

Each of the blades was different in material and/or laminate design. Selection of design features was based on the results of specimen testing of various materials and layup configurations which was conducted. All blades were designed to meet frequency, stability, and strength criteria required for satisfactory QCSEE engine operation. These criteria are discussed in detail in Reference 2.

One blade of each of the four designs was fabricated. The tooling for molding these blades was the same tooling as that used for the QCSEE variable-pitch fan blades (Reference 3).

Blade quality was verified by a combination of quality control of materials and processes combined with nondestructive inspection of the finished blades, including frequency checks. Each of the four blades was then impact tested in the Whirligig facility. All blades were tested using the same object slice size, incidence angle, and relative velocity.

One existing QCSEE blade was modified to incorporate a pin root design. The effect of this attachment on impact resistance was also tested in the Whirligig.

4.1 MATERIALS SELECTION

As part of the development of improved impact resistant blades, it is necessary to assess various composite systems and laminate configurations. It was the purpose of this portion of the program to fabricate and test a series of composite specimens to establish the advantages of different laminate configurations and material combinations. Test specimens were used as a screening tool for evaluating and determining what material combinations and layup configurations were to be used for fabrication of the improved composite fan blades. In addition, if necessary, specimens were fabricated and tested to provide data for the actual materials, ply configurations, and processes used in each composite blade fabricated and impact tested. For each material or ply combination, testing consisted of two tests each of short beam shear, flatwise tensile and charpy impact.

An additional part of this effort was to evaluate fabrication processes as they relate to the mechanical properties of fabricated parts. To accomplish this, specimens were taken from actual blades after impact test and subjected to test. This permitted assessment of the properties achieved under the actual conditions of molding temperature, time, and pressure from a blade relative to properties from simple panels.

Figure 54 presents a drawing of the configurations used for the test specimens. For each material/ply combination, all specimens were cut from a single flat molded panel. These test panels were 2.54 cm × 22.9 cm × 1.0 cm (1 in. × 9 in. × .4 in.) in size and were molded using the same schedule used on blades. This involves two hours at 110° C (230° F) and one hour at 177° C (350° F).

Specimens for longitudinal short beam shear strength, flatwise tensile strength, and charpy impact strength were machined from the panels in accordance with Figure 55. In general, the longitudinal direction in the panels corresponds to the radial direction in a blade. In addition, a sample was taken from each panel for chemical analysis. The mechanical property tests were conducted at room temperature.

Six configurations were initially identified for test panel evaluation. The basic material combinations used in these configurations are listed in Table VIII. The orientation of the respective plies is representative of the tip portion of QCSEE-type composite blades. Figure 56 presents the detailed ply layups used for two typical panels. The layups were selected because they represent a cross-section of the state of the art for current composite blade use.

Panel 1 simulates the configuration of the preliminary QCSEE blades discussed in Section 3.1. Panel 2 is the same as Panel 1 except the AU-type graphite is replaced by AS-type graphite; this configuration simulates the the QCSEE engine blades reported in Reference 2. Panel 3 was the same as Panel 2 except the Kevlar material was replaced by S-glass.

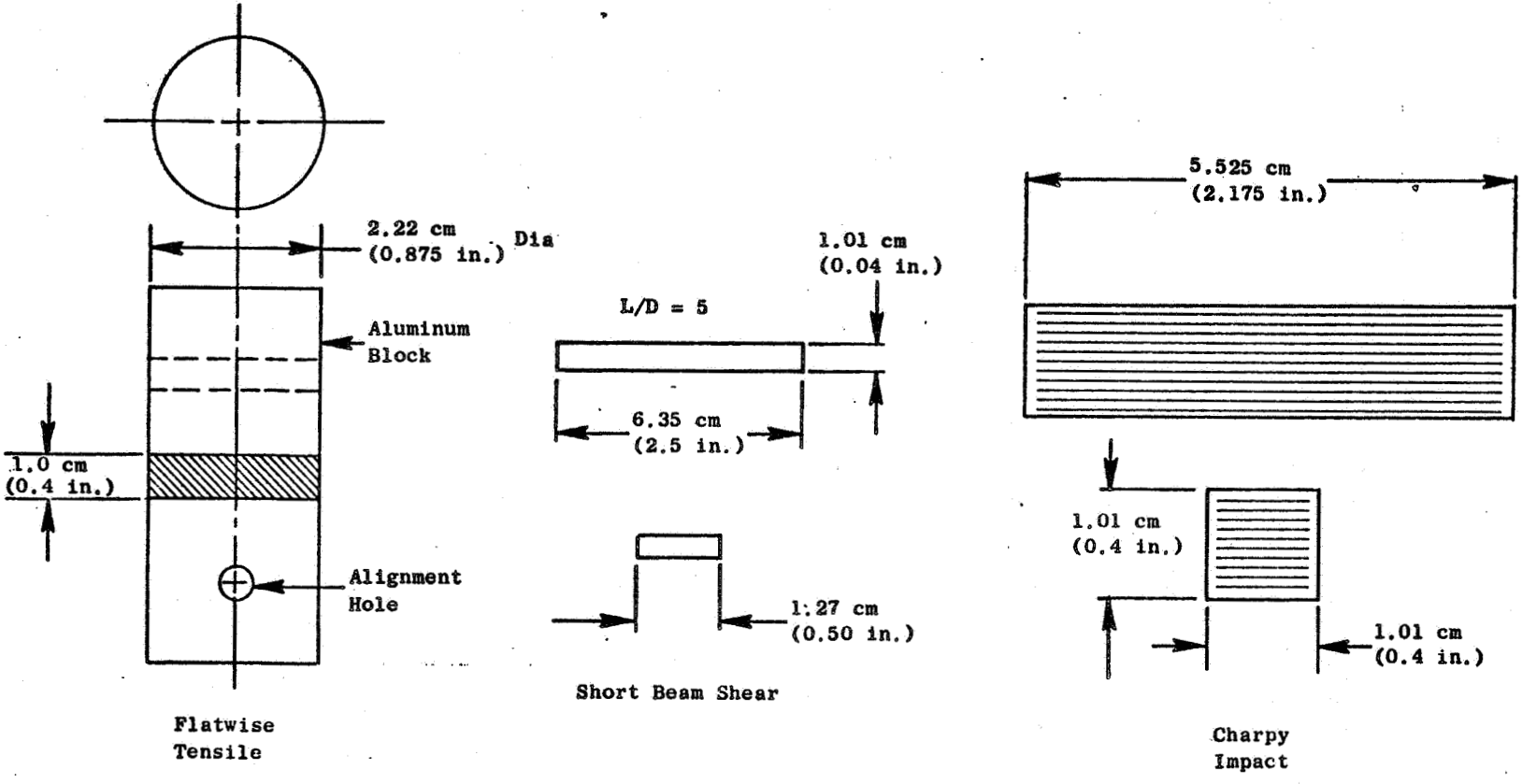

Figure 54. Test Specimen Configurations.

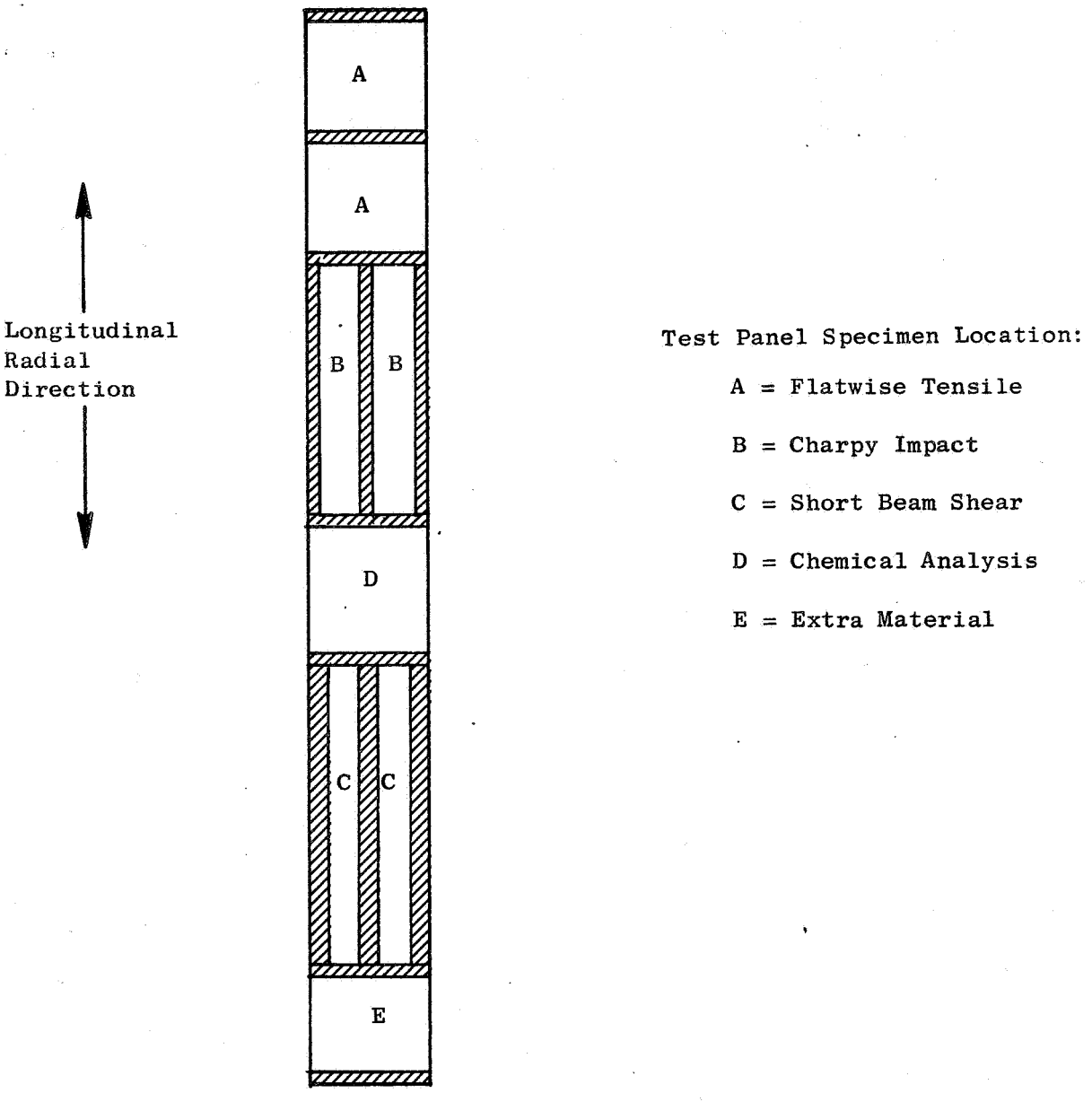

Figure 55. Test Specimen Location in Molded Panel.

Table VIII. Definition of Original Panel Fiber/Resin Systems.

Panel	Material	Orientations	Comments
1	AU/S-Glass/Boron/Kevlar	0 ± 45	Preliminary Design QCSEE Blade Configuration Interply
2	AS/S-Glass/Boron/Kevlar	0 ± 45	Panel Above with AS Replacing AU - Interply
3	AS/More S-Glass/Boron/ No Kevlar	0 ± 45	Above Panel with S-Glass Replacing Kevlar - Interply
4	80 AS/20 S-Glass	0 ± 35	Intraply Type Design
5	80 AS/20 S-Glass/Boron	0 ± 35	Intraply Type Design
6	T300/PR288/S-Glass	0 ± 35	Intraply Type with Alternate Graphite/Resin System

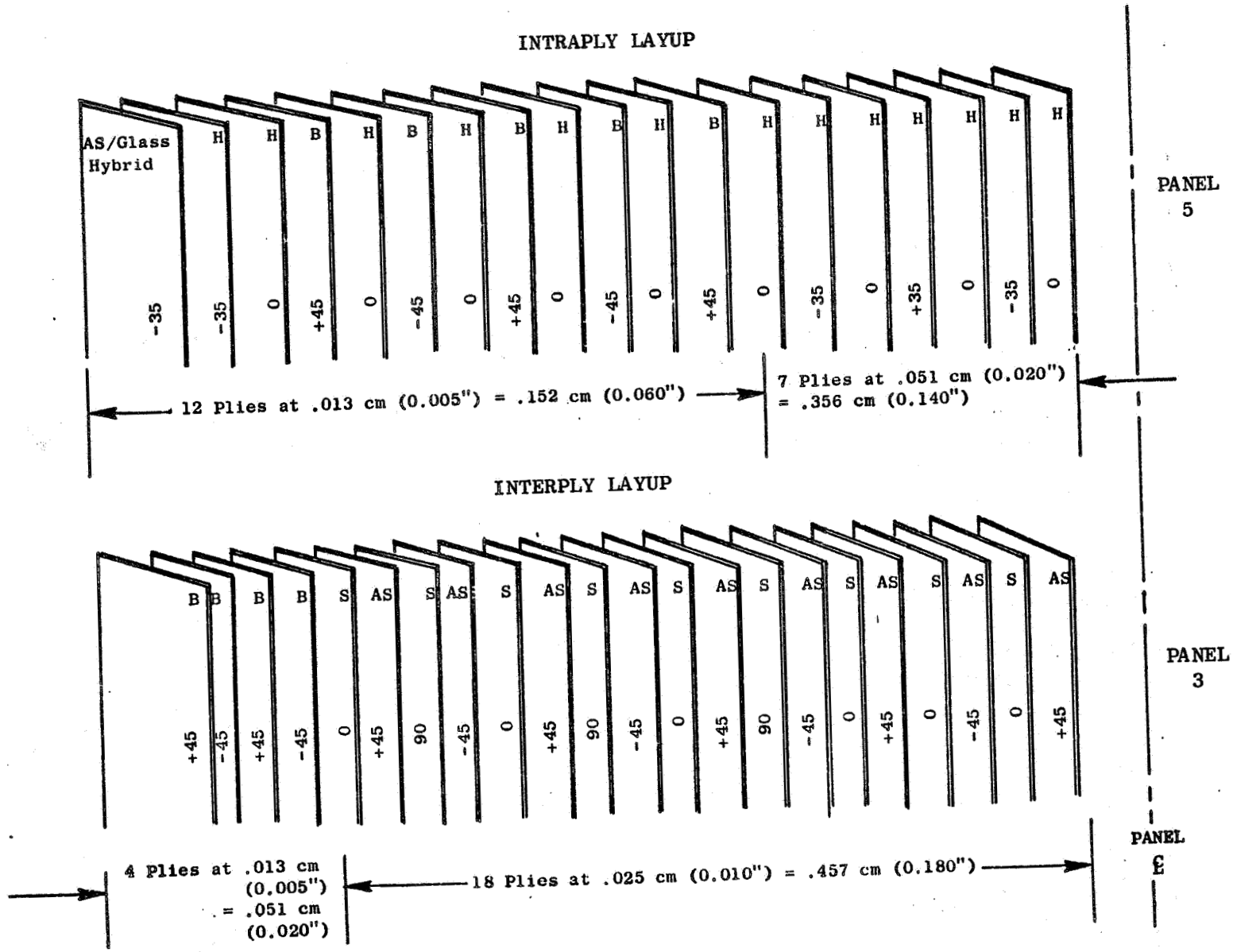

Figure 56. Typical Half-Panel Layups.

Panel 4 is different in three ways from the first three panels. The layup orientation is ± 0° ± 35° instead of ± 0° ± 45°, the plies are 0.05 cm (20 mils) thick instead of 0.025 cm (10 mils) thick, and the material is an intraply or striped hybrid. Intraply hybrids have both AS and S-glass included in the same ply. On the other hand, in Panels 1, 2, and 3, each ply is either all graphite, all Kevlar or all S-glass (interply hybrid). All the intraply material used was 80 percent graphite and 20 percent S-glass by fiber volume.

Panel 4 had no boron plies on the outside, while Panel 5 had boron plies at ± 45° orientation. In actual blades, boron is sometimes required to meet blade natural frequency requirements. Panel 6 was the same as Panel 4 except an alternate graphite (T300) replaced the AS material.

Table IX presents the results of the tests. There appeared to be no significant differences in the flatwise tensile properties of all six configurations. The data from five of the configurations were within 2.5 percent; 23 MN/m^2 (3380 psi). Short-beam shear strengths, on the other hand, showed a range from 27.6 MN/m^2 (4010 psi) to 74.0 MN/m^2 (10,730 psi). The replacement of low shear type AU graphite in Panel 1 with type AS in configuration 2 showed no effect on the shear strength of the overall composites. Examination of the specimens revealed that, in both cases, failure occurred in the low shear strength Kevlar plies. Configurations 4, 5, and 6 produced the highest shear values. These materials averaged 150 percent greater strength than the first two configurations.

There appear to be no differences in the charpy impact test panel data between Configurations 1 and 2 as a result of changing the graphite fiber from untreated type AU to surface-treated type AS. Both panels contained approximately the same fiber volume ratio of 5 percent boron, 27 percent Kevlar, and 26 percent graphite. Configuration 3, which had an intermediate shear strength of 51.0 MN/m^2 (7400 psi), had the highest charpy impact strength of all the candidates with a value of 39.9 N-m (29.4 ft-lb). This can be attributed to the high percentage of S-glass in the composite (26.4 percent). Furthermore, with S-glass having a rather high specific gravity (2.49 g/cm^3), the Configuration 3 panel had the highest density of the candidates (1.777 g/cm^3). The remaining three systems, which constitute the "high shear" materials, had charpy impact strengths of around 27.1 N-m (20 ft-lb). The volume of S-glass fiber in these configurations remained fairly constant, 11.7 ± 1.0 percent. Figure 56 presents the short-beam shear and charpy data for all six configurations in graphical form. Figures 58 through 63 present photos of the cross section of each panel.

At the conclusion of this test series, the following conclusions were made:

1. The flatwise tensile strengths of all panels was essentially equal.

Table IX. Test Panel Data for Materials Screening Study.

Configuration	Materials	Flat. Tensile Strength, MN/m^2 (psi)	SBS Strength, MN/m^2 (psi)	Charpy Impact Strength, N-m (ft-lb)	Density g/cm^3	Fiber Vol., %	Voids, %
1	Boron Kevlar Type AU Graphite	19.2 (2790)	29.6 (4290)	18.4 (13.6)	1.52	5.0 27.7 26.2	0.6
2	Boron Kevlar Type AS Graphite	18.8 (2720)	27.6 (4010)	18.6 (13.7)	1.510	5.1 26.5 25.8	1.2
3	Boron Type AS Graphite S-Glass	19.1 (2770)	51.0 (7400)	39.9 (29.4)	1.777	5.8 24.2 26.4	1.8
4	AS(80)/ S-G1(20)	19.2 (2790)	74.0 (10,730)	29.4 (21.7)	1.659	45.2 12.7	0.4
5	AS(80)/ S-G1(20) Boron	23.3 (3380)	68.2 (9890)	26.0 (19.2)	1.680	39.1 10.8 7.0	1.9
6	T300(80)/ S-G1(20)	18.9 (2740)	72.0 (10,440)	29.0 (21.4)	1.628	46.1 11.3	0.0

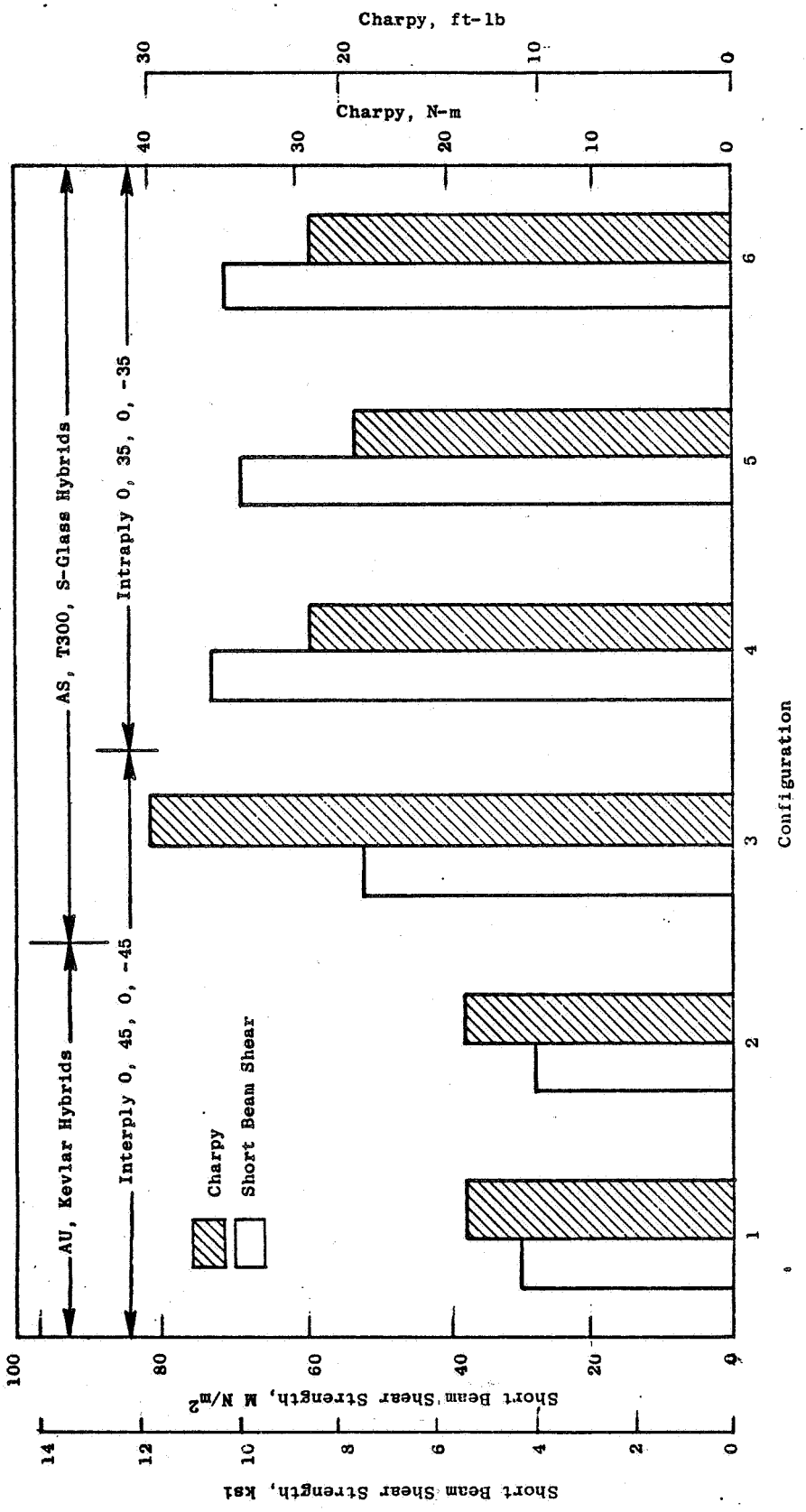

Figure 57. Test Panel Data Evaluation.

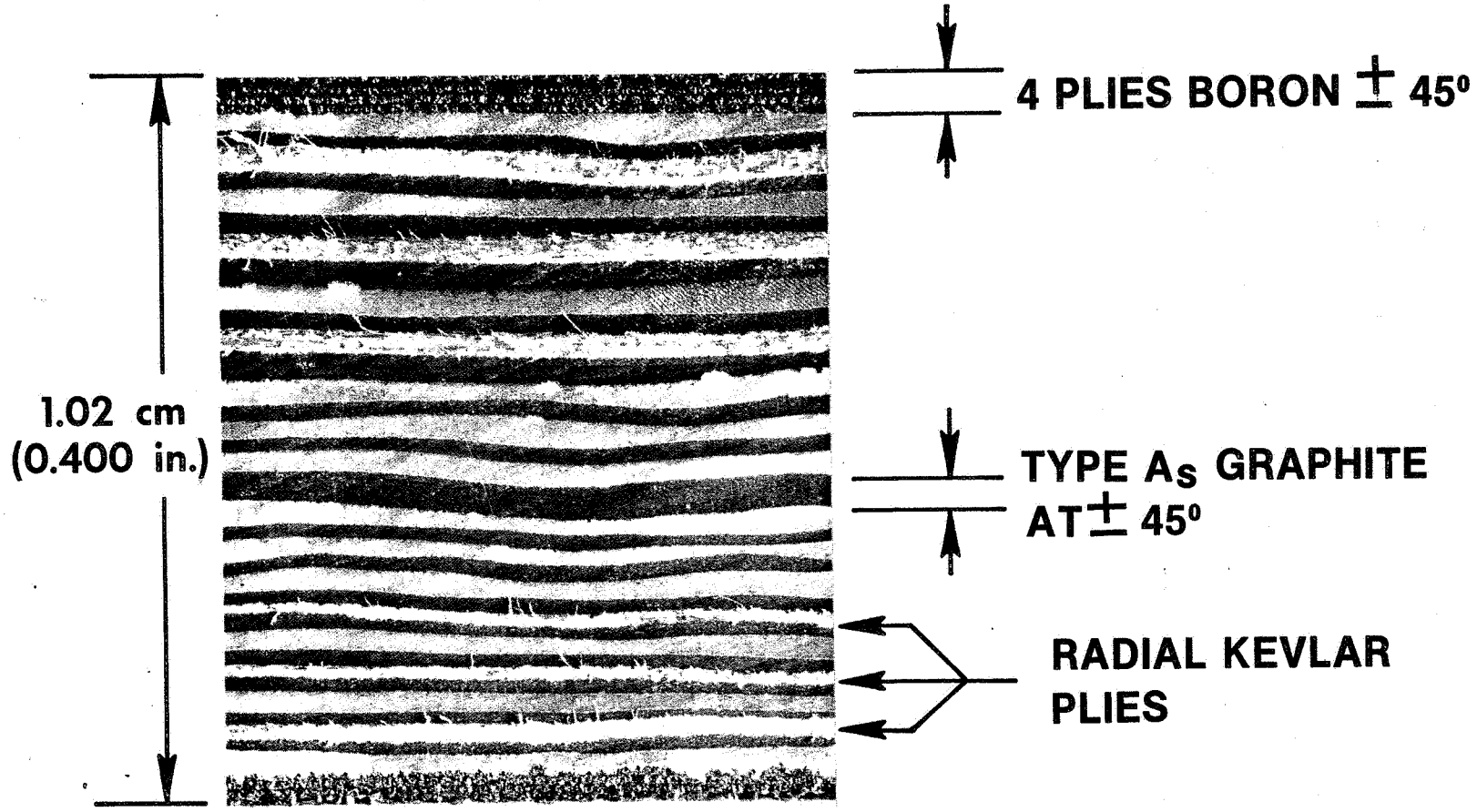

Figure 58. Cross Section of Test Panel Representing Current QCSEE Blade.

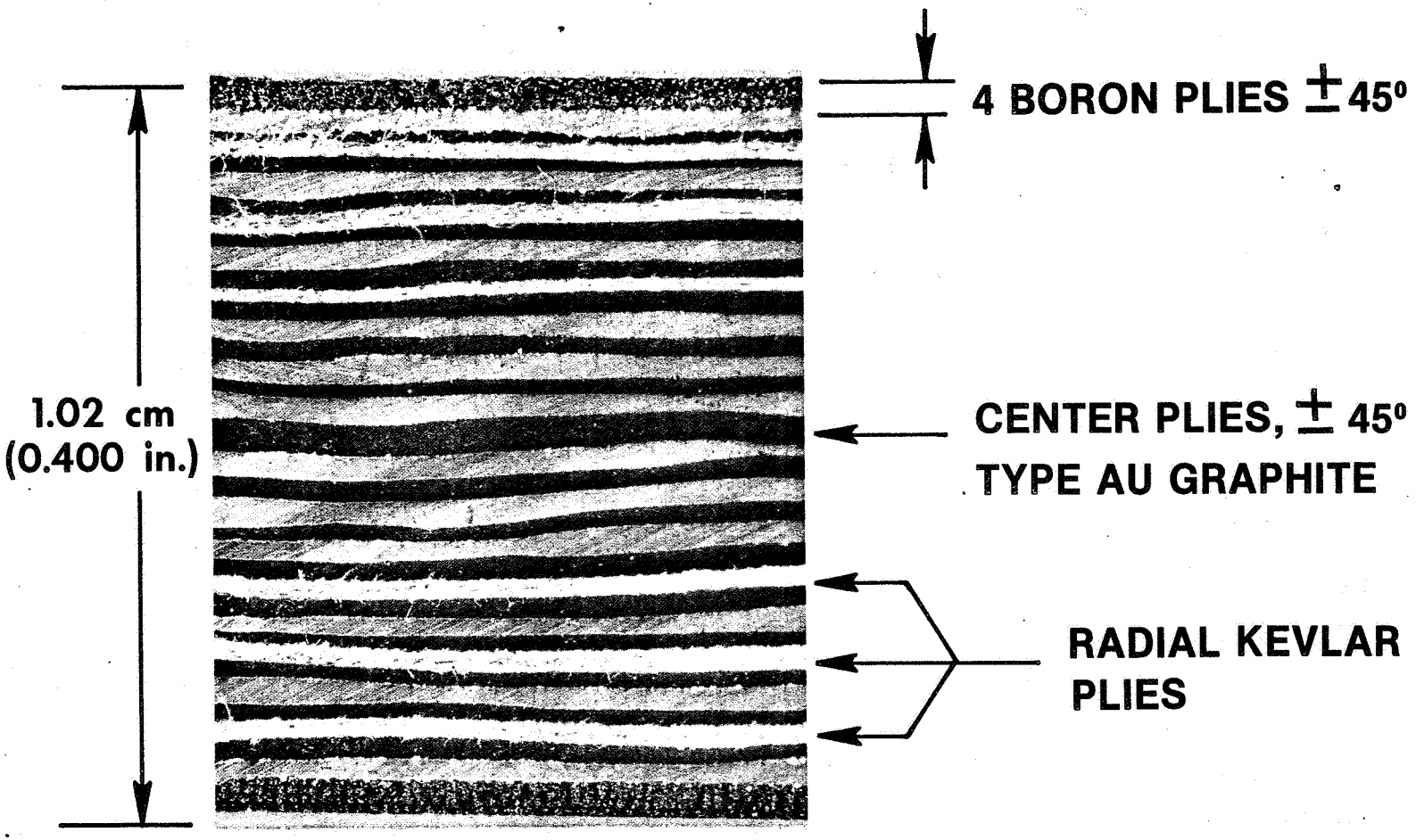

Figure 59. Cross Section of Test Panel Representing Task II Blades.

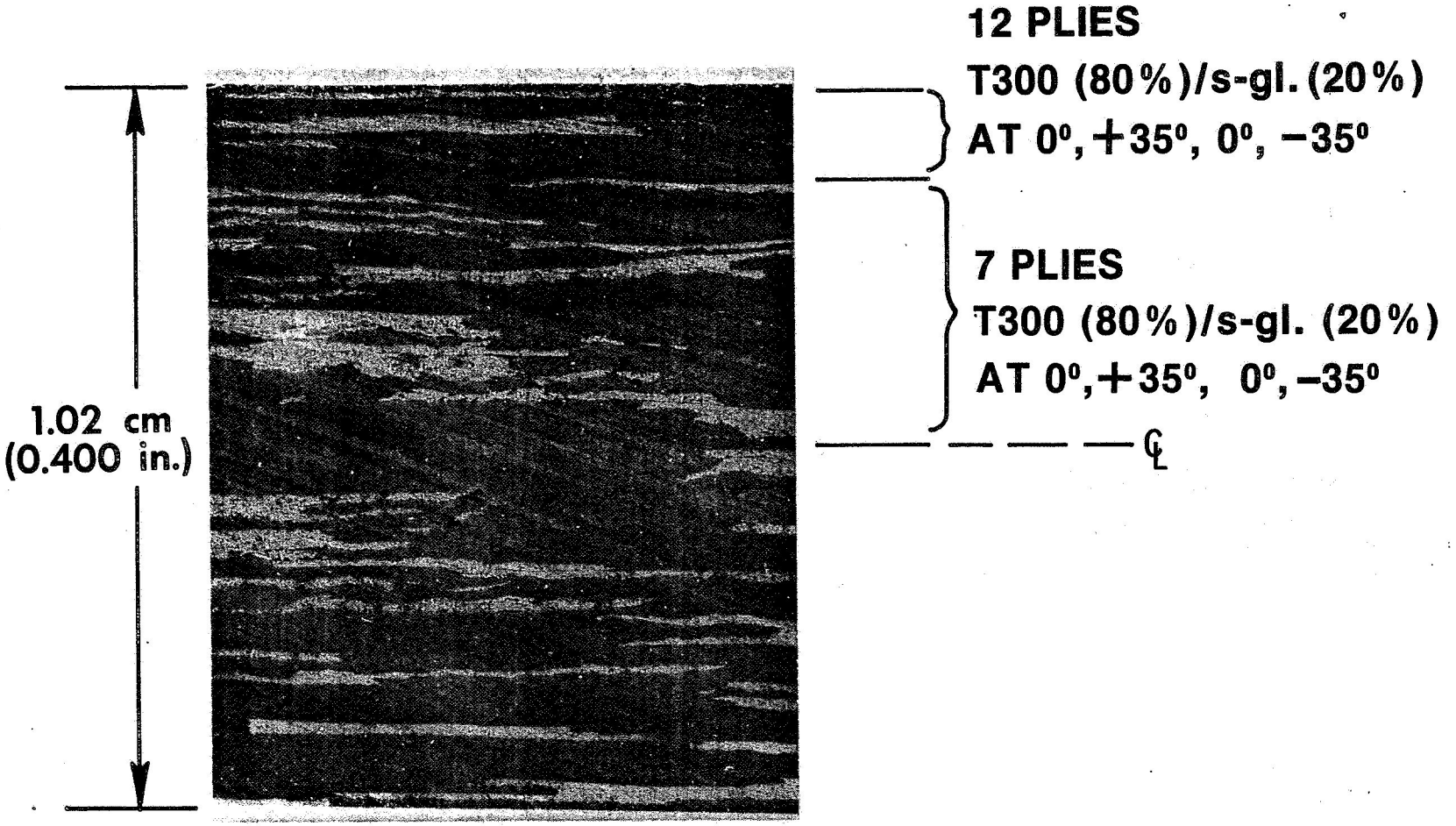

Figure 60. Cross Section of Test Panel Representing Standard Layup with T300 Graphite.

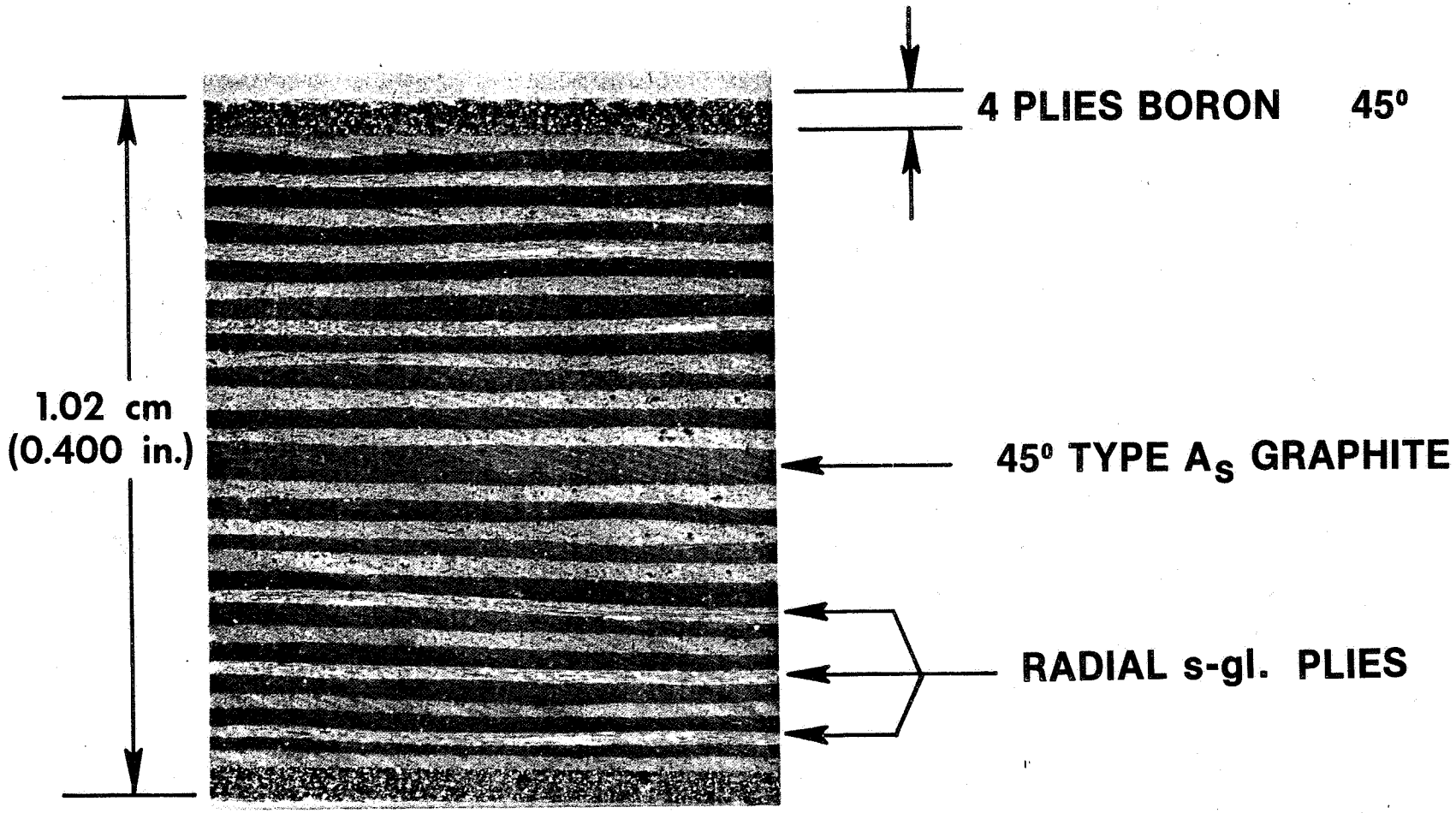

Figure 61. Cross Section of Test Panel Representing Current QCSEE with S-Glass Replacing Kevlar.

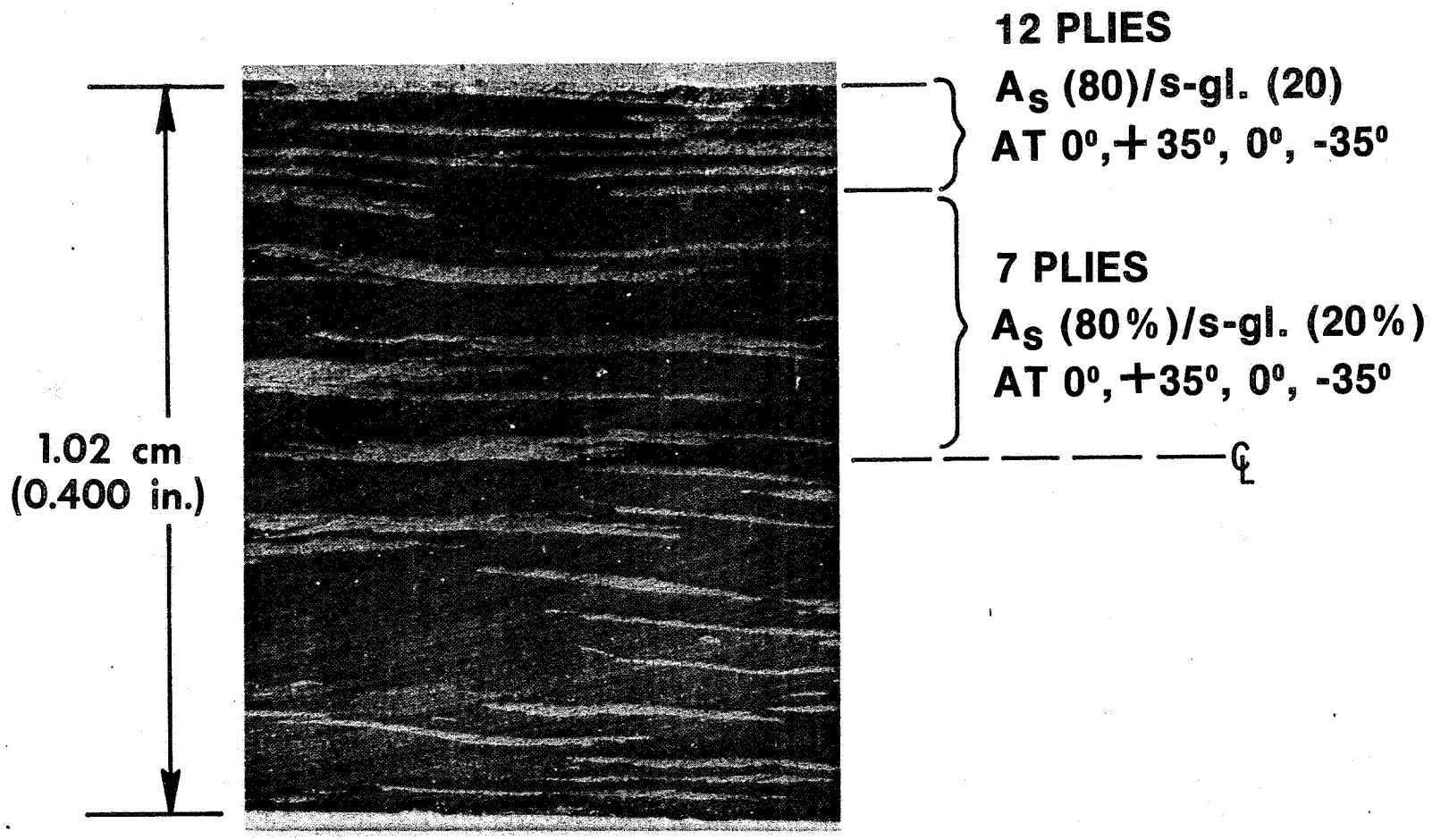

Figure 62. Cross Section of Test Panel Representing Standard Layup.

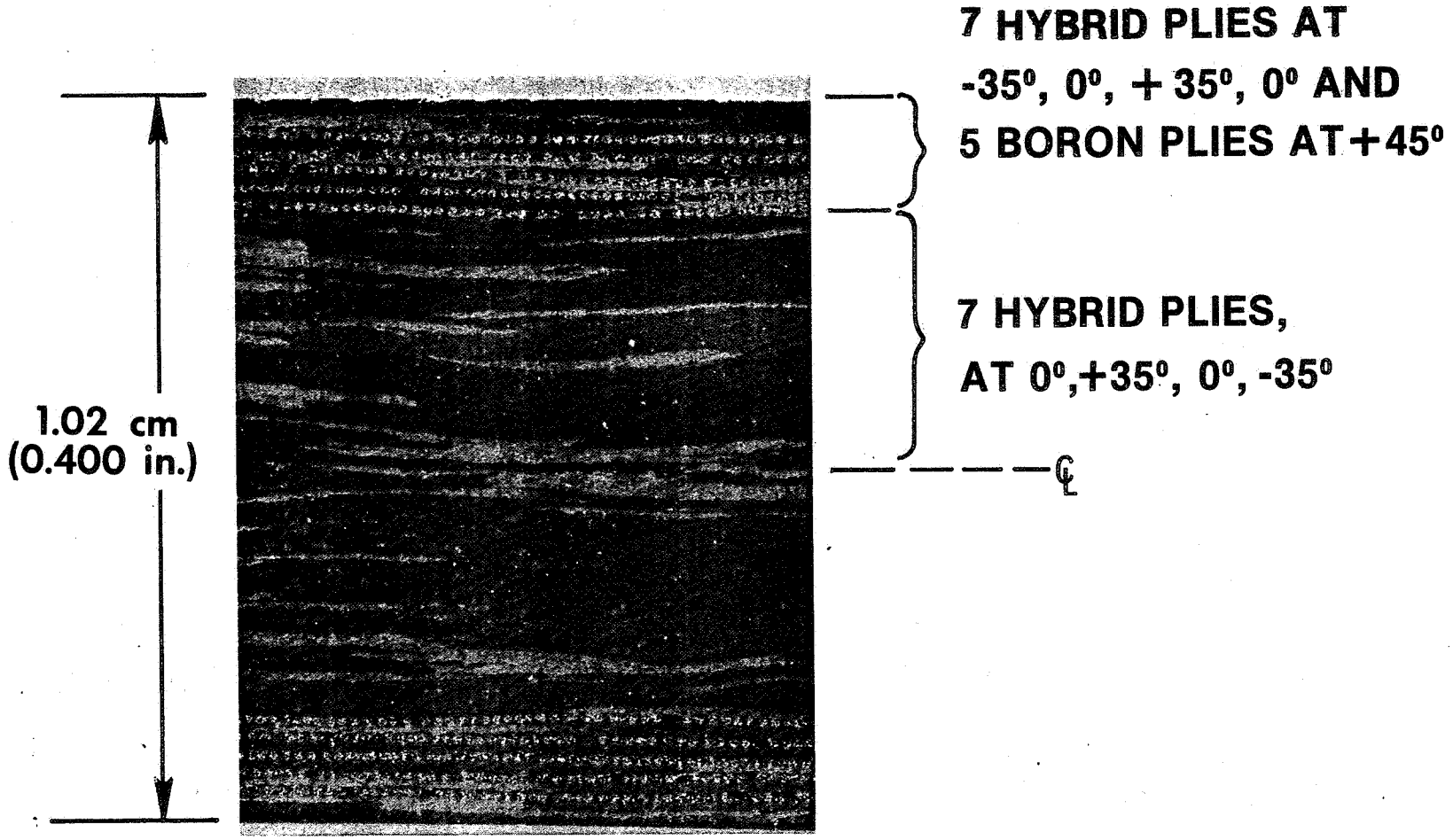

Figure 63. Cross Section of Test Panel Representing Standard Layup with Boron Added.

2. The panels containing Kevlar produced low short-beam shear and charpy values relative to the panels containing S-glass.

3. Replacing the untreated graphite (AU) with surface-treated graphite (AS) did not improve short-beam shear or charpy values when Kevlar was present; the Kevlar being the weak link.

4. The intraply hybrid panels (4, 5, 6) having a ± 0° ± 35° orientation have higher short-beam shear values than the comparable interply hybrid panel (3) having ± 0° ± 45° orientation. This is probably due to the lower ply orientation angle.

5. The panel with a high percentage of S-glass had the highest charpy value.

6. All three of the intraply panels had essentially the same properties.

Based on the above conclusions and other ongoing studies, additional panel tests were conducted.

1. Panel 7 AS/S-glass panel representative of AS/S-glass interply plus boron with ± 0° ± 45° orientation having 20% S-glass plies (versus 45% for Panel 3) (Figure 64).

2. Panel 8; AS/S-glass panel as above with ± 0° ± 35° orientation. This panel offers a direct comparison to Panel 5 relative to interply versus intraply material (Figure 65).

These panels had short-beam shear strengths of 41.4 MN/m^2 (6000 psi) and 46.2 MN/m^2 (6700 psi), respectively, which compare to previously tested values of 51.0 MN/m^2 (7400 psi) for a ± 0° ± 45° panel with a higher percentage of S-glass (Panel 3) and 68.9 MN/m^2 (10,000 psi) for 80 AS/20 S-glass panels (4, 5, and 6) which were otherwise similar to the current panels.

From the results of these two panel tests, the following conclusions were drawn:

- Reducing the amount of S-glass in Panel 7 relative to Panel 3 resulted in a 19 percent loss in short-beam shear strength.

- The interply panel had 32 percent lower short-beam shear strength than the similar intraply panel. For this reason, more emphasis in the remainder of the program was placed on the intraply material.

A wedge-shaped panel representative of the blade leading edge region was fabricated to evaluate the effect of placing an adhesive layer down the center of the lay-up, Figure 66. The objective of this study was to use the adhesive to fill in the triangular regions at the ends of the plies

C-2

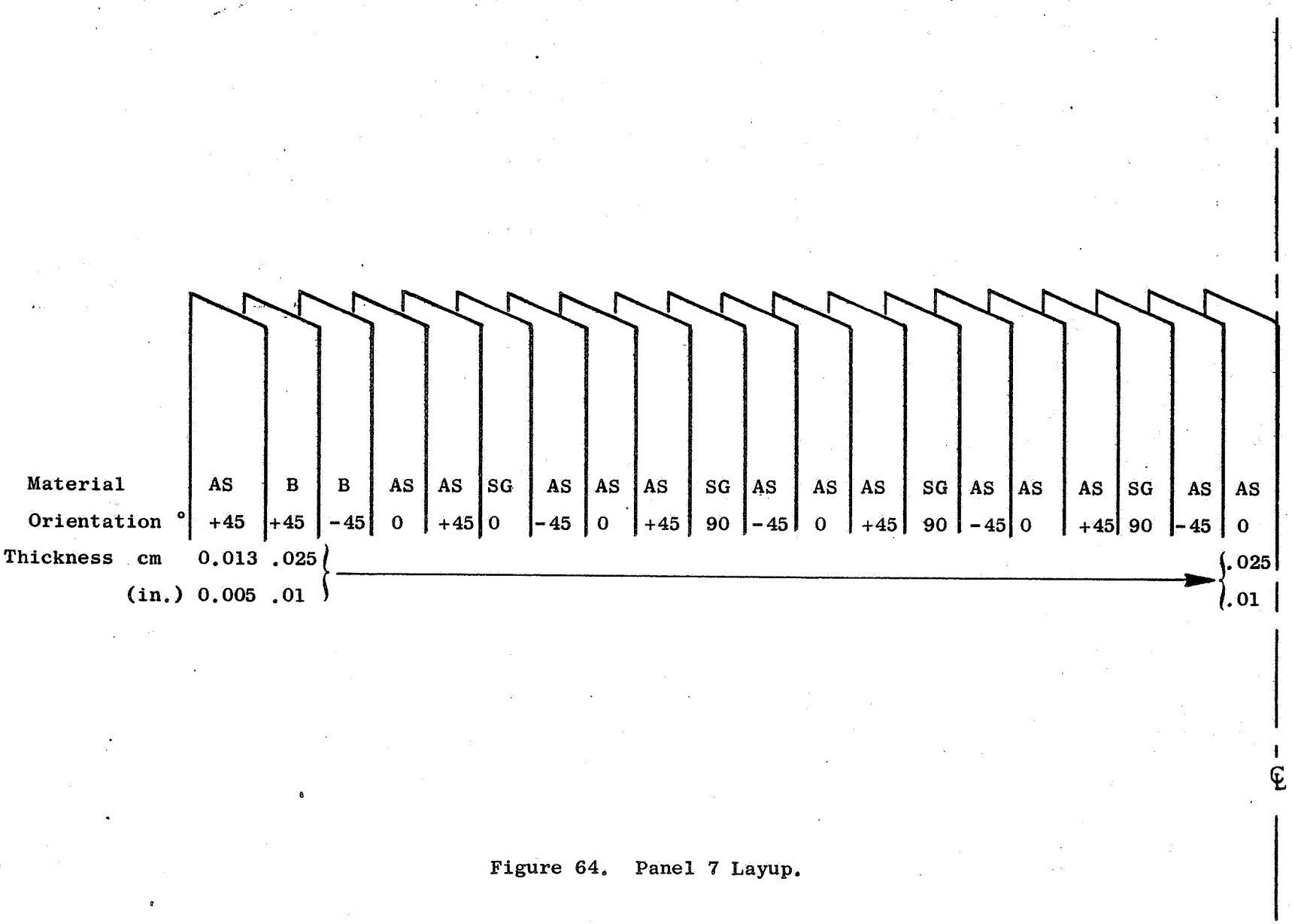

Figure 64. Panel 7 Layup.

- Panel 8 with Interply Material at 0, +35, 0, -35

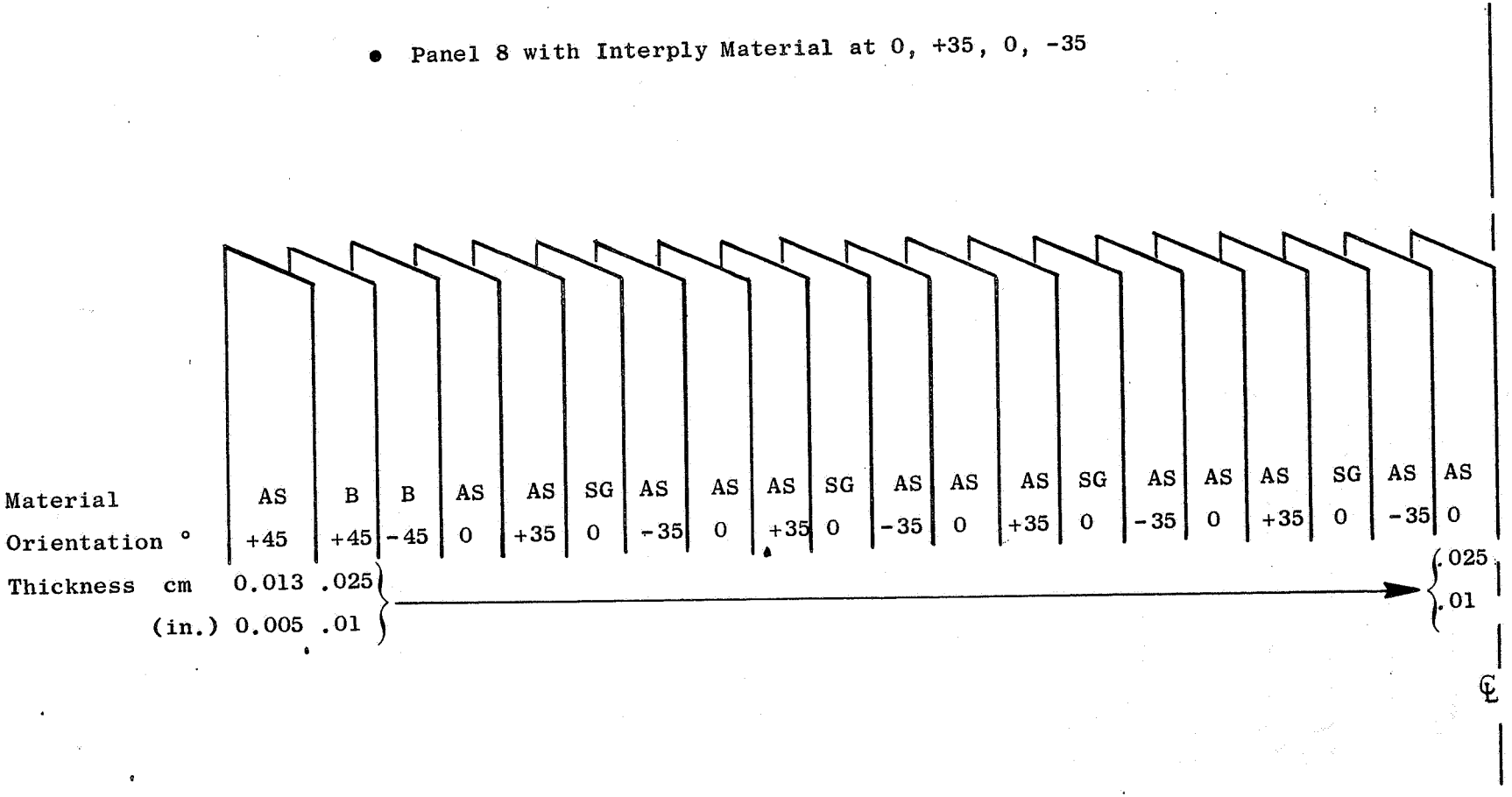

Figure 65. Panel 8 Layup.

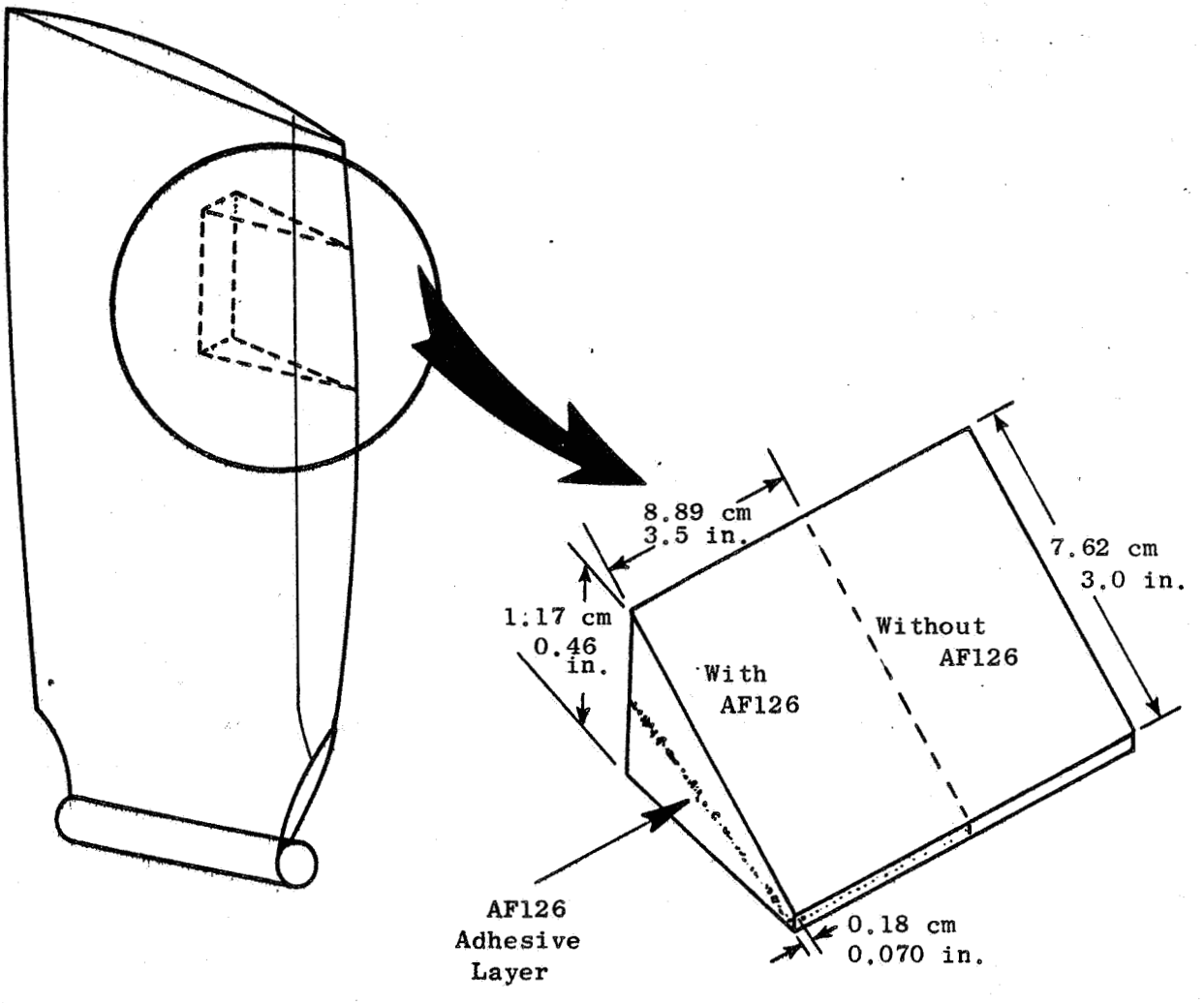

Figure 66. AF126 Adhesive Panel.

which exist in an actual blade and thereby to potentially improve the shear strength at this location. Short-beam shear specimens were tested at an L/d ratio of 5:1. The data showed no improvement in shear strength by using the AF126 layer; however, examination of the specimens revealed that failures occurred in the outer plies and not the center. The failures were of a tensile nature rather than shear. Additional specimens were then tested using L/d ratios of 3:1 and 2:1. After testing a single specimen at 3:1 and examining the specimen, the failure mode was still tensile. The remaining specimens were then tested at 2:1. Still, failure did not occur along the center plane and no differences were noted in test data values. In addition, due to the tapered nature of the specimens, testing of the specimens in the short-beam shear setup was difficult because the panel tended to slide when the load was applied. In view of the above difficulties, it was not possible to reach any definite conclusions relative to the adhesive core panel. In an actual blade with a complex molding, improvement by this technique might offer some advantages.

A test panel was also fabricated to evaluate chordwise shear properties with ply "shingling" angles of 5, 10, and 15 degrees. The theory being that if the plies run across the neutral axis, the shear strength should be improved over the case where the plies run parallel to the neutral axis. Two short-beam shear specimens at each angle were machined and tested at room temperature using a 5:1 L/d ratio. Like the tapered panels, these specimens failed in bending instead of shear. In order to solve this test problem, more specimens were fabricated with reinforcing outer plies to improve the bending strength. Figure 67 shows a sketch of these panels. Results of the tests are as follows:

Angle	Shear Strength NM/m^2 (psi)	
0°	60.0	8700
5°	62.1	9000
10°	55.8	8100
15°	58.6	8500

These results show that shingled angles do not significantly decrease or increase the shear strength of flat panels. Shingled plies however, may offer the potential for improved blade strength by eliminating the potentially weak center ply ends characteristic of conventional blade layups.

Following impact testing of the four blades fabricated from selected material configurations described in Section 4.5, two blades were sectioned and short-beam shear and flatwise tensile specimens were obtained. The specimens were obtained from an undamaged area of the blade about four inches above the outsert near the center of the blade. Table X shows a comparison of the values from the original panel data and the specimens

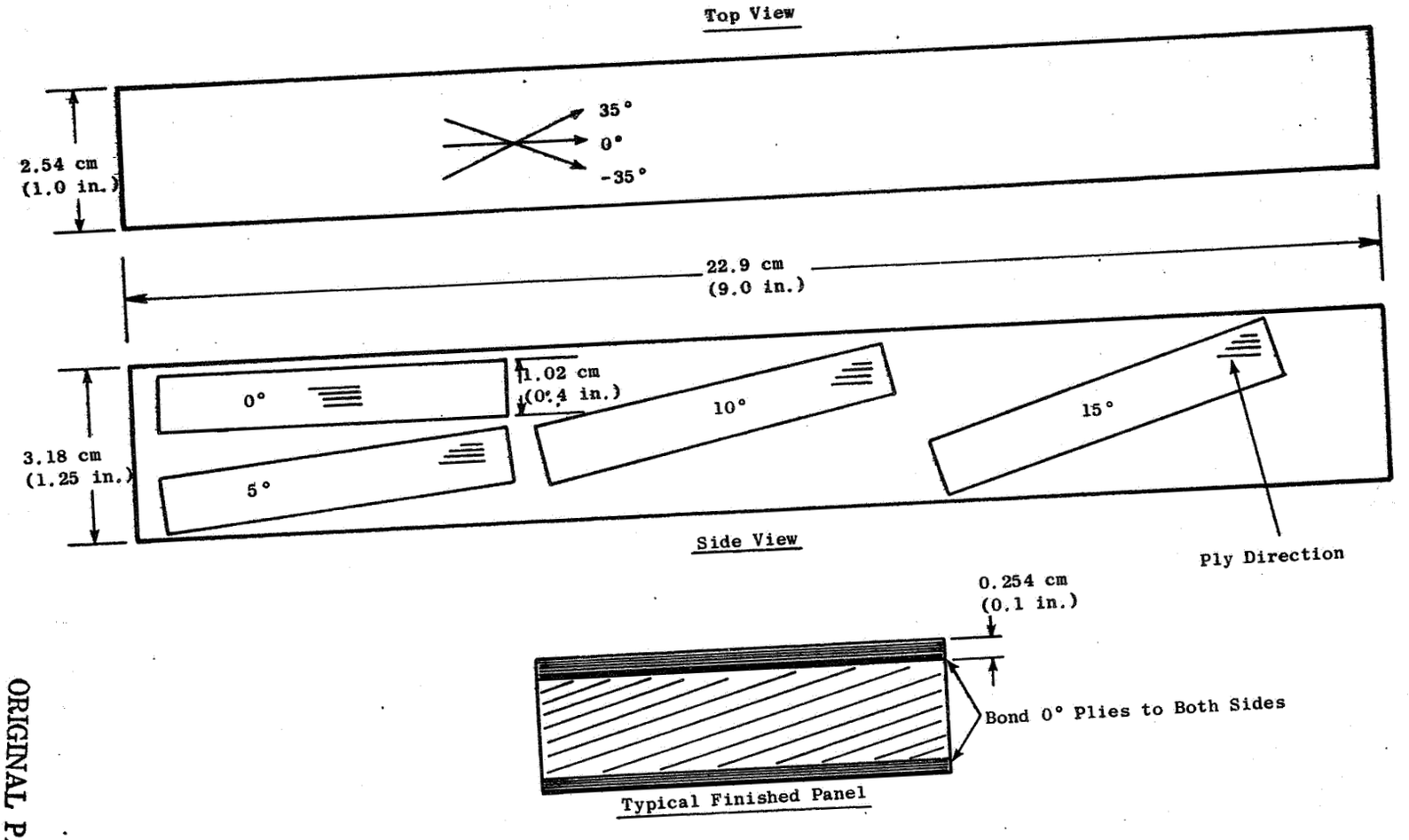

Figure 67. "Shingling" Radial Test Panel.

taken from the blades. As can be seen, the specimens obtained from the blade exhibited as good, or better, flatwise tensile and short-beam shear strengths as the panels. This result shows that the material properties in a complex molded blade are as good as a simple panel in the location where the blade specimens were obtained.

Table X. Blade/Panel Material Property Comparison.

Blade	Short-Beam Shear MN/m^2 (psi)		Flatwise Tensile MN/m^2 (psi)	
	Panel	Blade	Panel	Blade
PQP003	68.2 (9890)	86.9 (12,800)	23.3 (3380)	27.7 (4020)
PQP006	68.2 (9890)	86.9 (12,800)	23.3 (3380)	22.3 (3230)

4.2 BLADE DESIGN

4.2.1 Pin Root Blade Design

One of the objectives of the program was to design and test a blade with a pinned root attachment and to determine if a blade with such an attachment offered improvement in its resistance to foreign object damage.

A pinned root blade would be expected to provide an advantage in foreign object damage resistance since the blade attachment would have less frictional moment resistance to rotation because of the small pin diameter as compared to the relatively large diameter of the outsert used on blades with keyhole type attachment. Under high centrifugal loading, the large contact forces on a keyhole outsert have the potential of restricting rotation of the outsert to such an extent that the blade bending stresses in the root of the blade might exceed the blade's strength and result in fracture or delamination. Another advantage of a pin root attachment is that with special "tuning" the blade's first flexural frequency can be designed to vary proportionally to the blade's speed thus avoiding first flexural frequency crossover of the 1/rev line. First flexural frequency crossover of this engine excitation condition can sometimes restrict operational capabilities.

The pin root attachment hardware design is shown in Figures 68 through 71 and is shown installed on a QCSEE blade in Figures 72 and 73. The attachment consists of a titanium slotted hub which encompasses the composite blade's dovetail and extends radially inward to connect with a clevis and pin attachment. The hub contains two slots which match two clevis lugs attached to a trunnion which extends through the disk. This provides three lugs in the hub. A 2.22 cm (7/8 inch) diameter pin provides the load

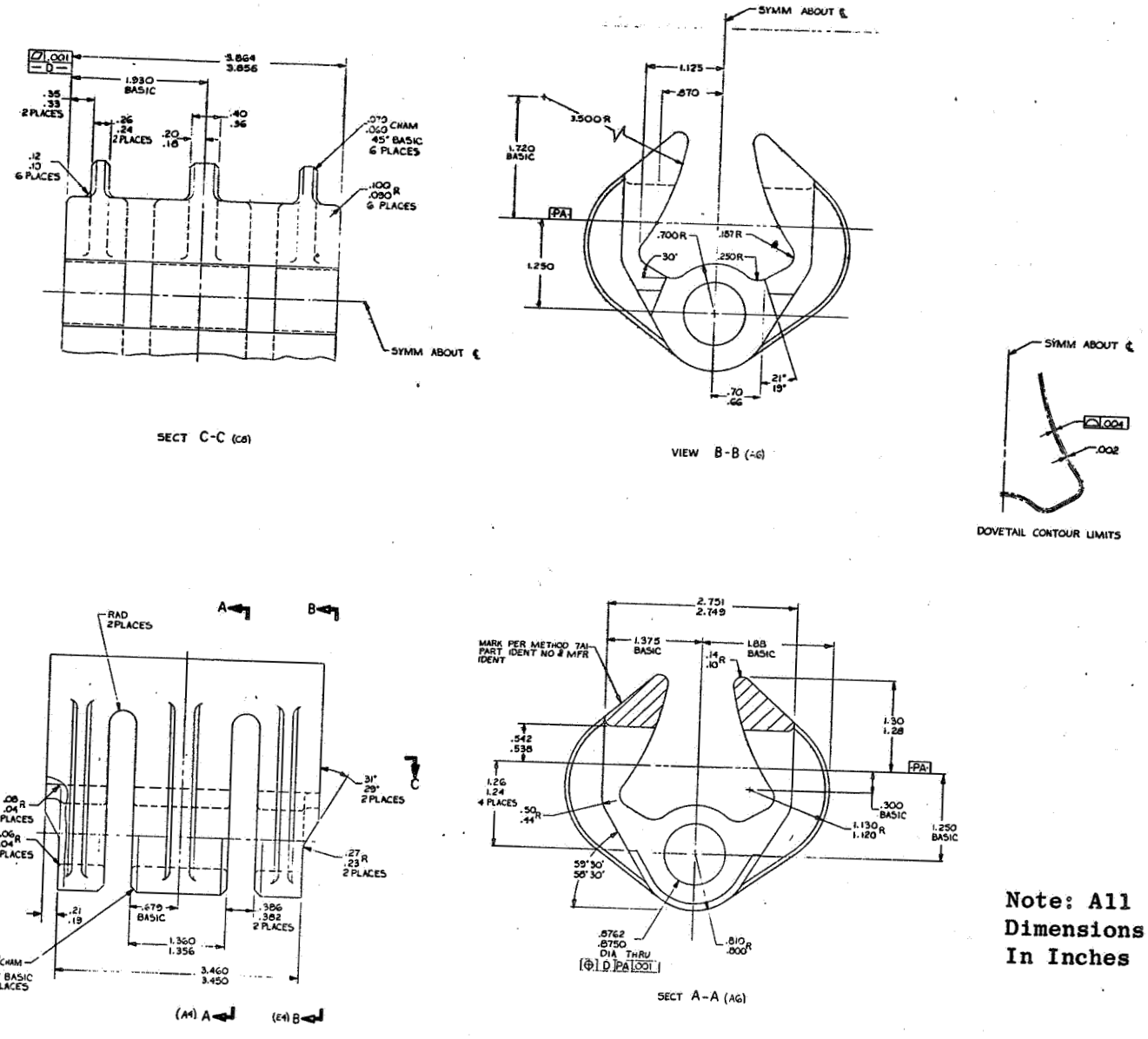

Figure 68. Pin Root Dovetail Outsert.

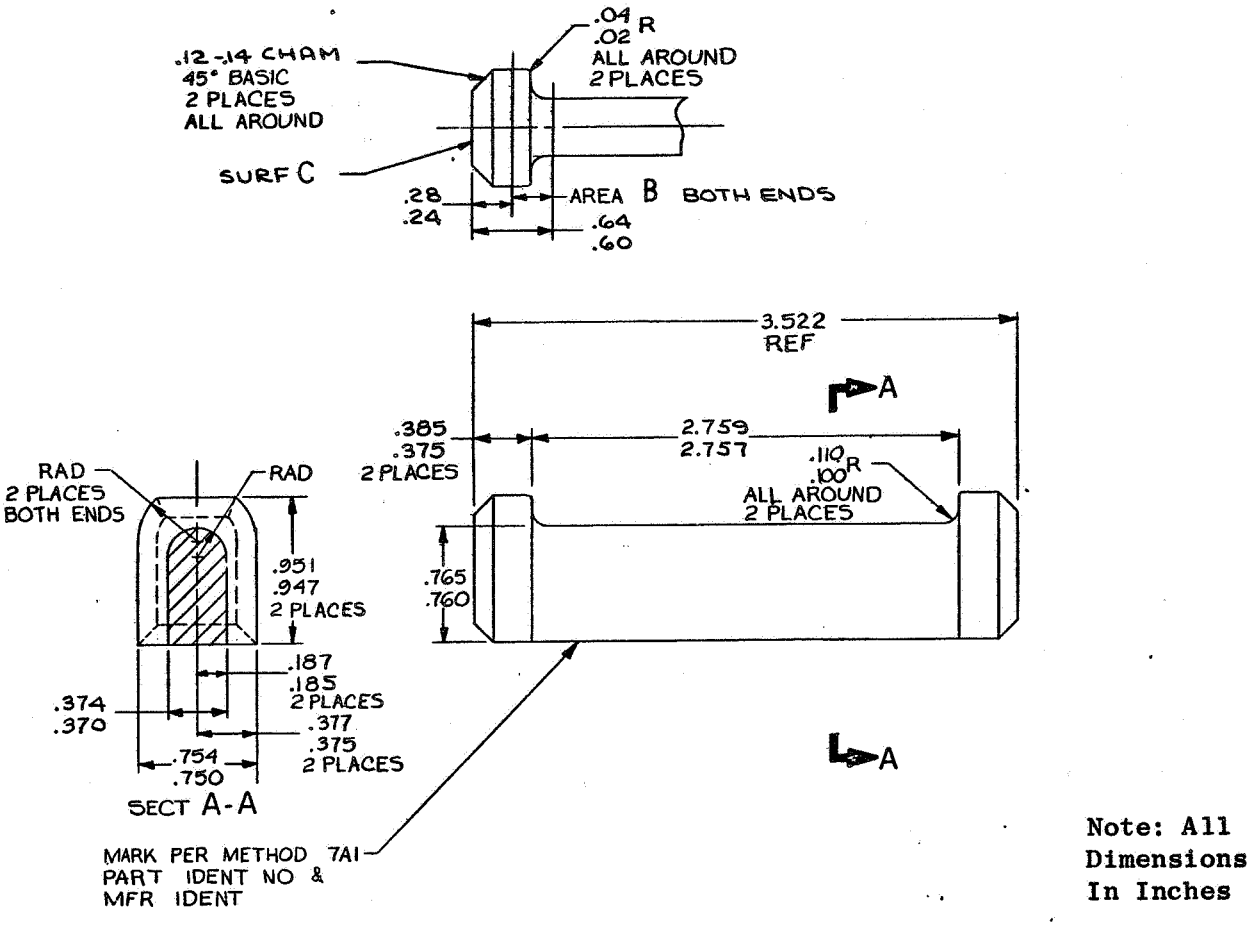

Note: All Dimensions In Inches

Figure 69. Pin Root Dovetail Tie Bar.

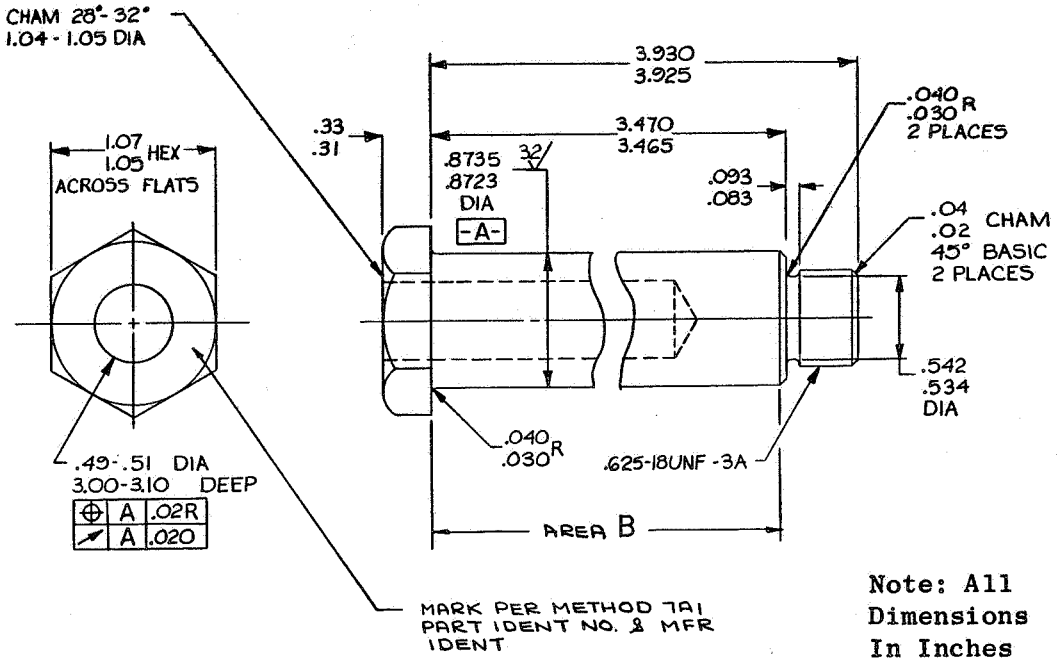

Figure 70. Pin Root Dovetail Bolt Clevis.

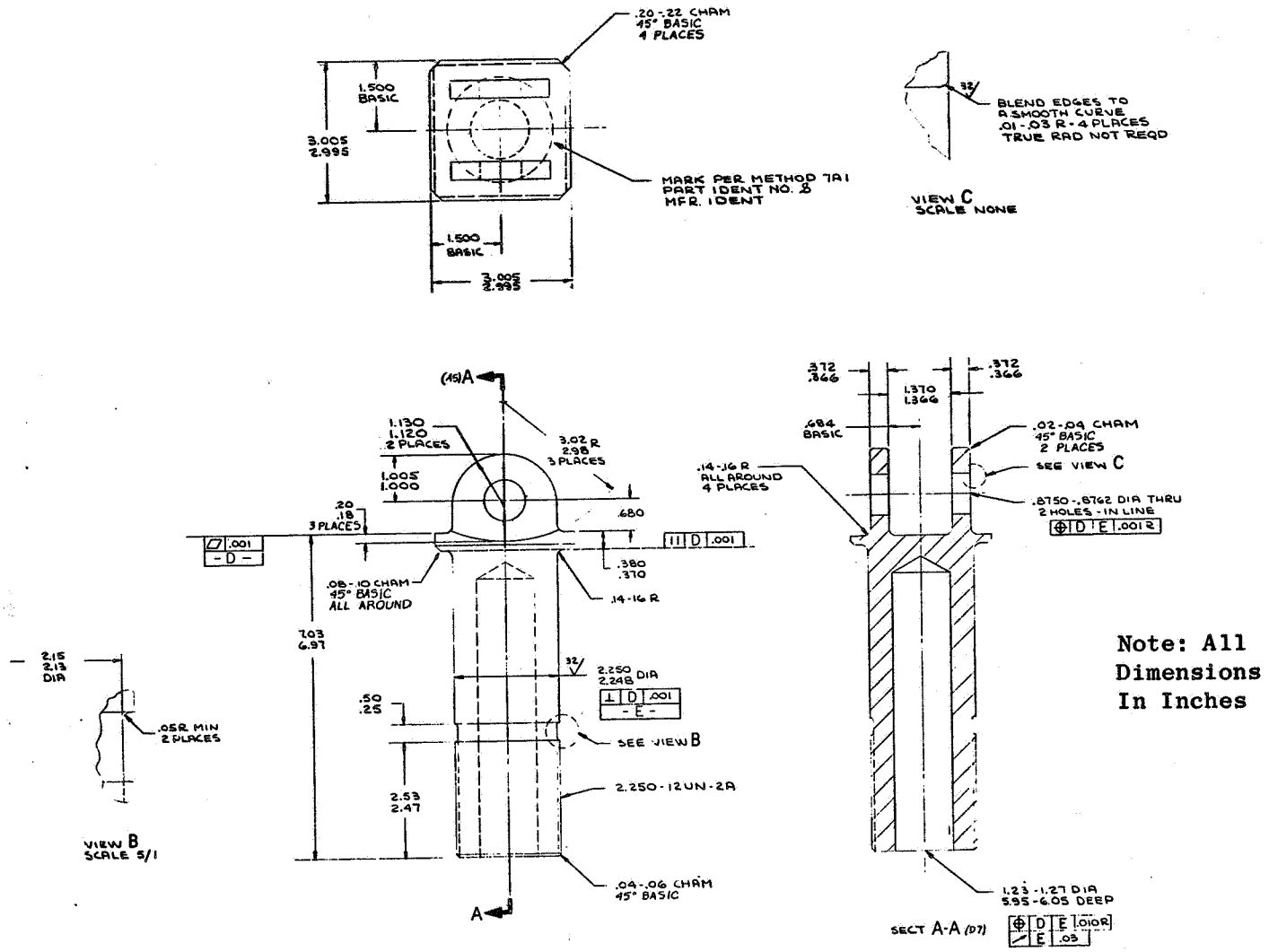

Figure 71. Pin Root Dovetail Spindle.

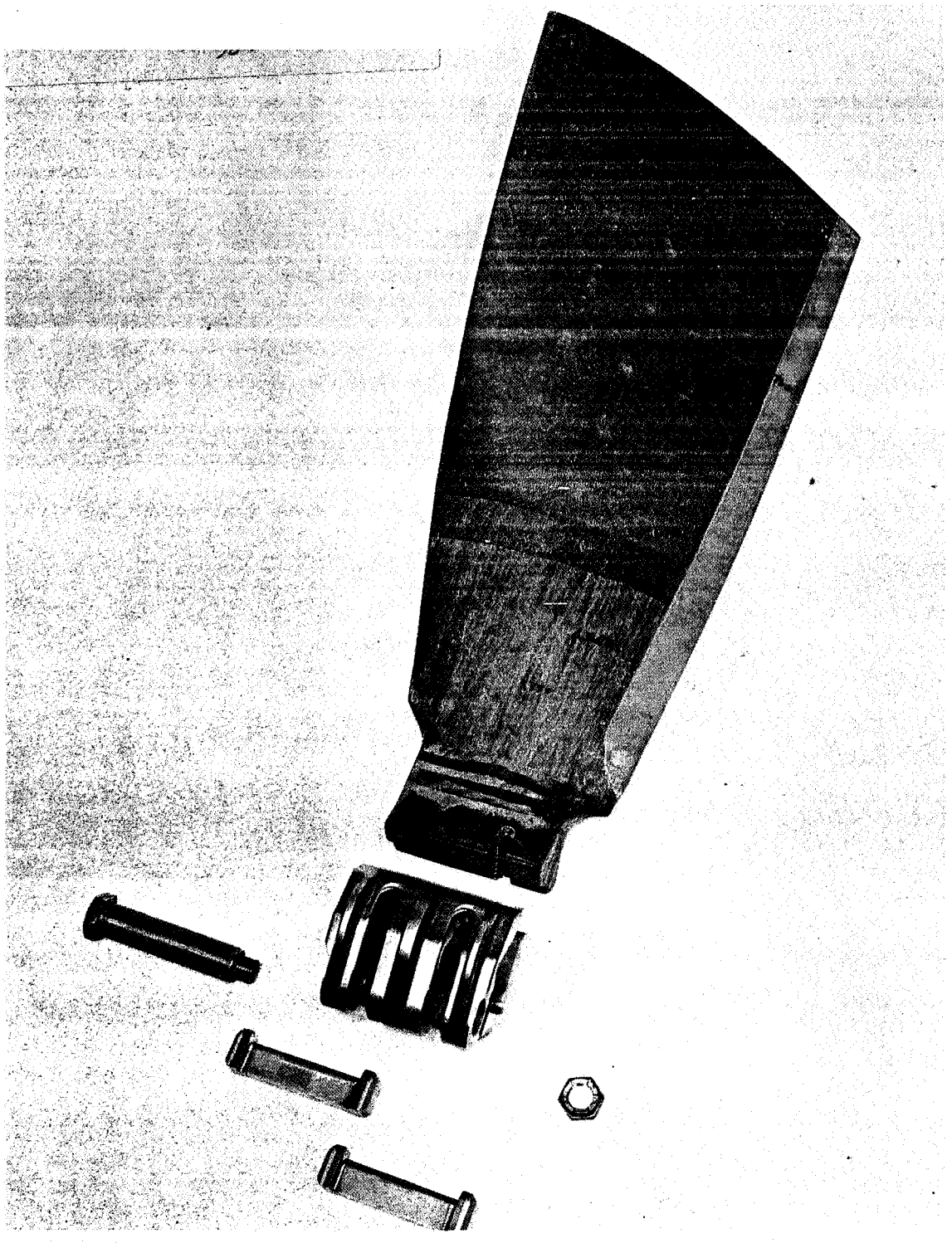

Figure 72. Pin Root Blade Parts. Note: Only One of the Two Required Slots has Been Machined in Blade Shown.

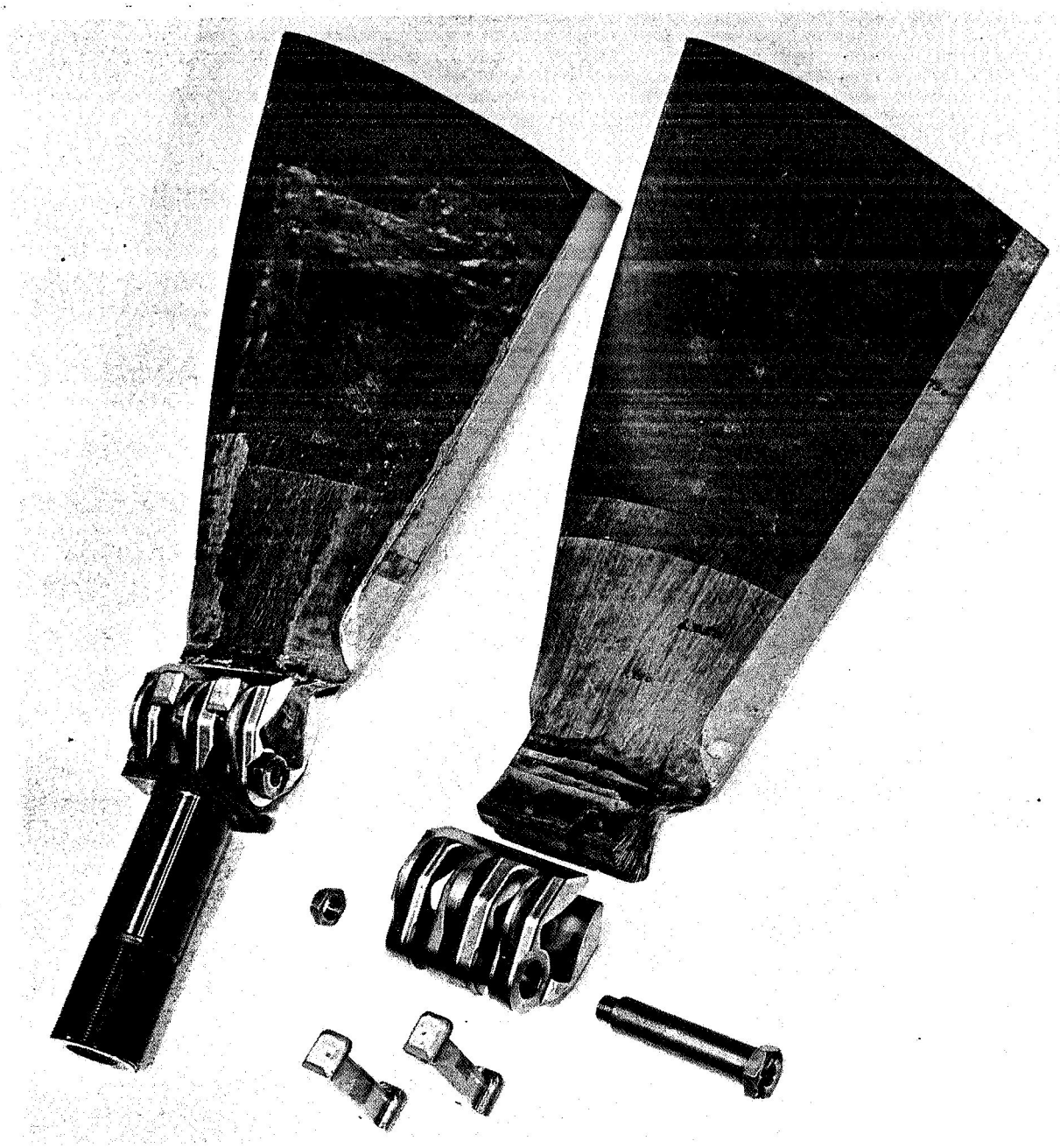

Figure 73. Pin Root Blade Parts and Assembled Blade. Note: Only One of Two Required Slots has Been Machined on Unassembled Blade.

transfer and locks the assembly together. The pin is retained by a 1.59 cm (5/8 inch) lock nut.

Blade radial loading introduces large lateral or transverse loading in the dovetail. This is counteracted by a combination of ribs which extend down each of the three lugs on the hub and two steel internal tie bars which fit in the two slots in the hub, immediately above the trunnion clevis lugs. The blade is slotted up through the dovetail to provide clearance for the two tie bars. The attachment assembly consisting of blade, tie rods, and hub is integrally bonded together. When fitted together with the trunnion clevis, pin, and lock nut, the blade and tie rods become doubly secured and cannot separate, even in the event of a debond.

The design is based on using a blade with the configuration of the QCSEE design molded blade (Reference 2) with the dovetail machined to accommodate the pin root attachment hardware. The machined dovetail for this configuration has a slightly greater width and chord length than the QCSEE blade and has two 0.95 cm (3/8 inch) wide longitudinal slots extending from the bottom of the dovetail upward approximately 3.2 cm (1-1/4 inch). The greater width and chord length of the dovetail result in the same average operating stress levels as the unslotted QCSEE dovetail.

The tested configuration actually consisted of a machined QCSEE preliminary blade (Reference 1) removing its keyhole type outsert, and slotting this to fit the attachment hardware. This provided a somewhat shorter chord length and less dovetail on the attachment. Analysis showed that this was acceptable for a demonstration test.

4.2.2 Improved Impact Resistant Blade Design

In this part of the program, four QCSEE blades with improved impact resistance were designed. The same external geometry as the QCSEE engine blades was used since the same die was used to mold the blades. The blades were designed to have acceptable frequency characteristics and weight. The candidate fibers and the selected resin and their properties for blade fabrication are shown in Table XI.

The following specific considerations were used in the design of the blades:

- From the panel tests discussed in Section 4.1, the Kevlar hybrid material was eliminated from consideration due to low short-beam shear and charpy values relative to the S-glass hybrids.

- Boron plies were necessary on the outside of the blade to obtain sufficiently high first torsion frequency.

Table XI. Candidate Materials.

Fibers	Source	Tensile Strength MN/m^2 (ksi)	Youngs Modulus MN/m^2 (ksi)	Density g/cm^3 ($lb/in.^3$)
AS Graphite	Hercules	2827 (410)	207 (30)	1.78 (0.064)
S-Glass	Ferro	3447 (500)	86 (12.5)	2.49 (0.090)
Kevlar	Dupont	2758 (400)	138 (20)	1.45 (0.052)
Boron	Avco	2758 (400)	379 (55)	2.63 (0.095)
PR288 Resin	3M	69 (10)	3 (0.5)	1.27 (0.046)

- From the panel test results, the intraply hybrids exhibited higher radial interlaminar shear strength than the interply hybrids and were, therefore, considered to be the favored candidate material.

Table XII presents a summary of the concepts considered. Configuration A is the QCSEE engine blade (Reference 2) and was included for reference only.

Configuration B is the same as A except the Kevlar has been replaced directly with S-glass. This substitution results in a shear strength increase of 85 percent and a charpy impact increase of 45 percent over the Configuration A.

Configuration C utilizes intraply material and the standard layup configuration similar to that used on the F103 blade (Reference 3). A schematic comparison of the QCSEE and standard layups is shown in Figure 74. The layup orientation angles were also changed to ± 0° ± 35° versus the ± 0° ± 45° layup orientations used on QCSEE.

Configuration D was the same as C except a 0.025 cm (0.010 in.) strip of AF126 adhesive was added along the centerline of the blade. The objective of the adhesive strip was to improve the shear strength at the center where the ply ends meet and where the shear stress is highest under impact.

Configuration E uses the 80 AS/20 S-glass intraply material like C and D and the QCSEE layup like B.

Configuration F is similar to C but uses a "one-sided layup", shown in Figure 75. This type layup would eliminate the resin-rich area at the center of the blade; however, warping and blade distortion might occur [due to thermal effects] during blade molding.

Configuration G is similar to F except the plies would be "shingled" or rotated as shown in Figure 76. This blade might have even more severe thermal problems than F.

Configuration H, as shown in Figure 77, has an integral Titanium leading edge spar which would transition into a pin-root-type dovetail. The remainder of the airfoil would be composite material. This configuration has been named the TICOM concept. This blade should offer significant impact improvement. Manufacturing complexities, however, made fabrication of this blade beyond the scope of this program.

After a detailed review of the above candidates including all the variables listed in Table XII, Configuration B, C, D, and E were selected for fabrication and impact testing. For manufacturing purposes, these blades were renamed PQP003, PQP004, PQP006, and PQP005, respectively. The detailed layup sequence and materials for each of these blades are shown in Figures 78 through 81.

Table XII. Blade Candidates.

Configuration	Material/Layup	Radial Strength MN/m^2 (ksi)	Radial Interlaminar Shear Strength MN/m^2 (ksi)	Charpy NM (ft-lb)	Frequencies - Hz At 100% Speed		Estimated Weight kg (lb)	Fabrication Problems	Impact Advantages
					1st Flex	1st Torsion			
A. Current QCSEE	36% AS at ± 45° 39% Kevlar at 0° 12-1/2% S-Glass at 0° 12-1/2% Boron at ± 45°	834 (121)	27.5 (4.0)	18.6 (13.7)	88	282	2.6 (5.8)	None	Baseline
B. QCSEE Without Kevlar	23% AS at 0° 38% AS at ± 45° 27% S-Glass at 0° 12% Boron at ± 45°	779 (113)	51.0 (7.4)	27.1 (20)	86	276	2.8 (6.1)	None	o 85% Shear Strength Increase o 45% Charpy Increase
C. Standard Layup and Intraply Material	40% 80 AS/20 S-Glass at 0° 40% 80 AS/20 S-Glass at ± 35° 10% AS at ± 35° 10% Boron at ± 45°	745 (108)	73.8 (10.7)	25.8-29.8 (19-22)	89	278	2.7 (6.0)	None	
D. Configuration C with Adhesive Core	(Same as C., Above)	745 (108)	73.8 (10.7)	-	89	278	2.7 (6.0)	None	Improved Shear
E. QCSEE Layup with Intraply Material		779 (113)	51.0 (7.4)	25.8-29.8 (19-22)	85	275	2.8 (6.1)	None	Improved Shear
F. One Sided Layup	(Same as C., Above)	745 (108)	73.8 (10.7)	-	89	278	2.7 (6.0)	Moderate	Improved Shear
G. Shingled Layup	(Same as C., Above)	745 (108)	73.8 (10.7)	-	-	-	2.7 (6.0)	High	Improved Shear
H. T1COM	Titanium Spar 80 AS/ 20 S-Glass at 0 + 35, 0, -35	-	414-483 (60-70)	-	85-98	265-280	-	Beyond Program Scope	

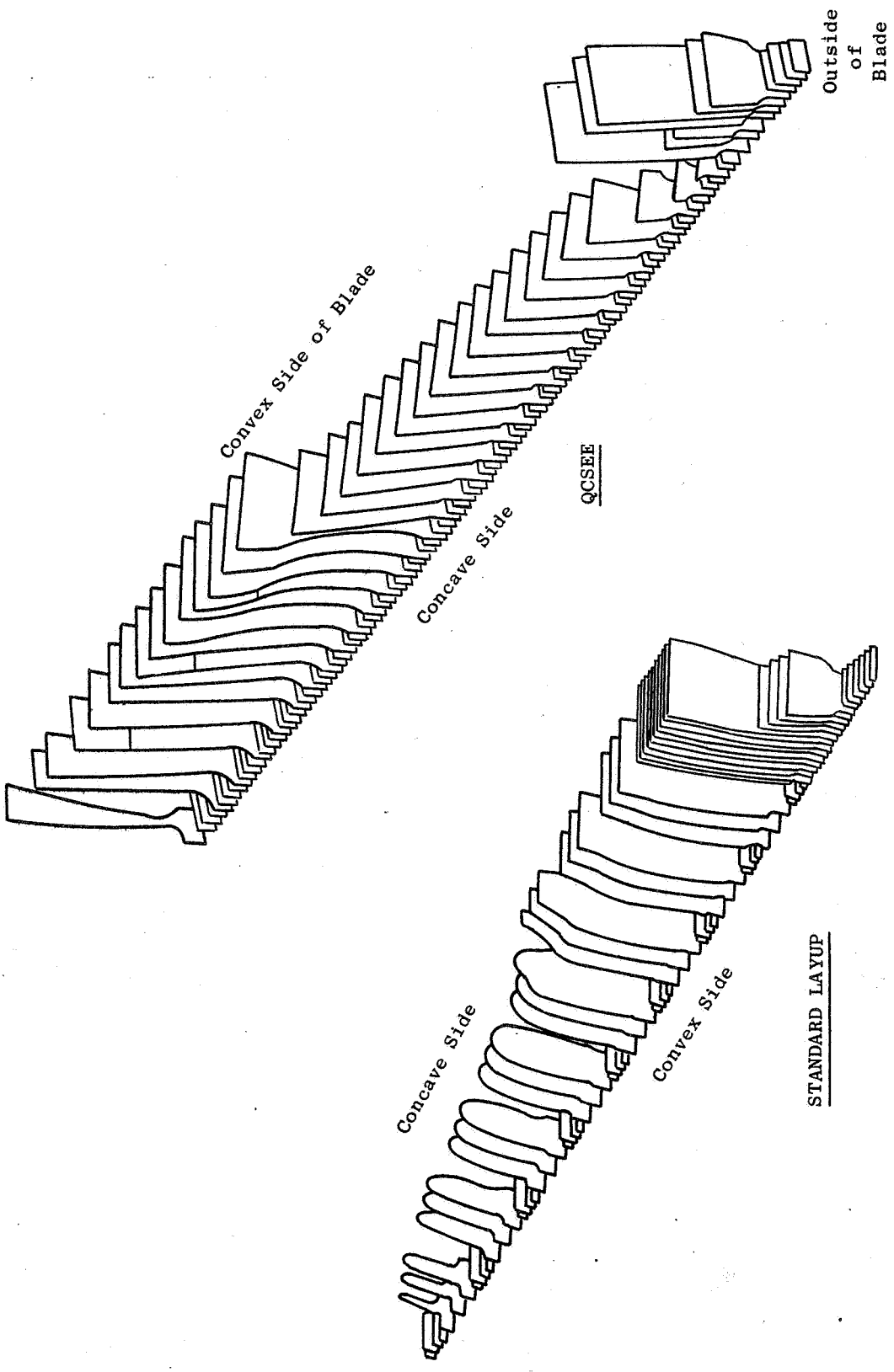

Figure 74. Schematic of QCSEE and Standard Layups.

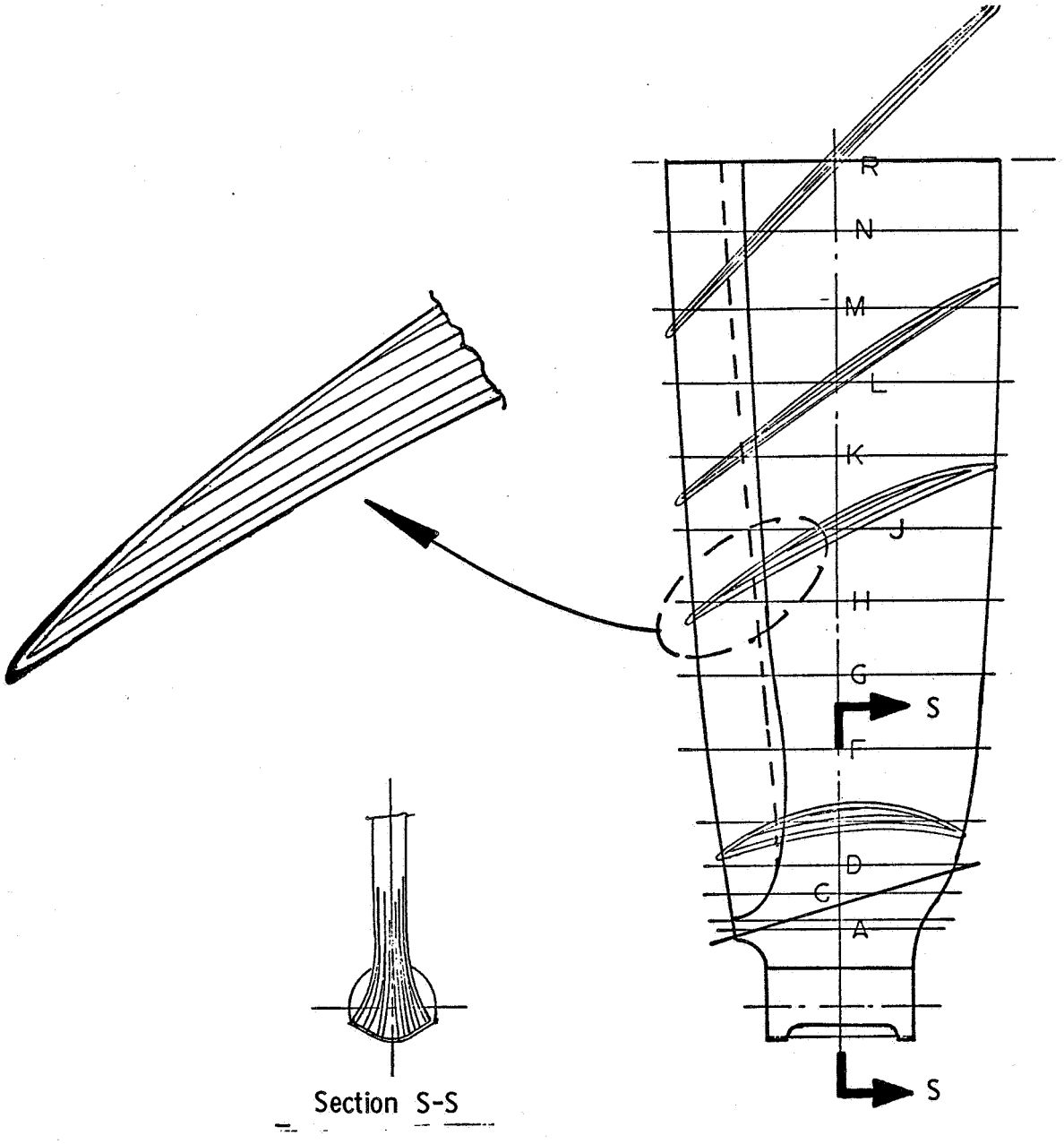

Figure 75. One Sided Layup.

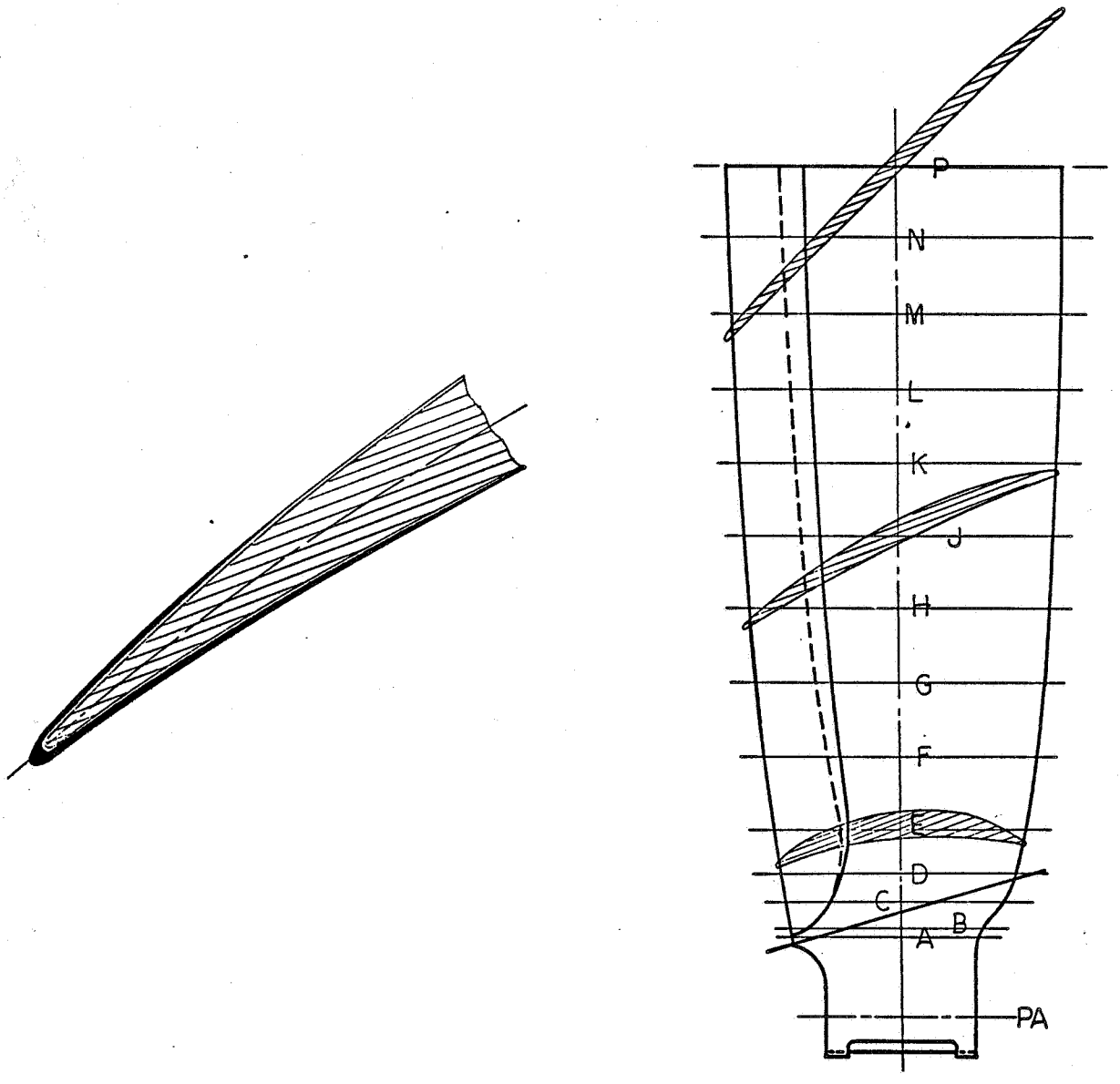

Figure 76. Singled Layup.

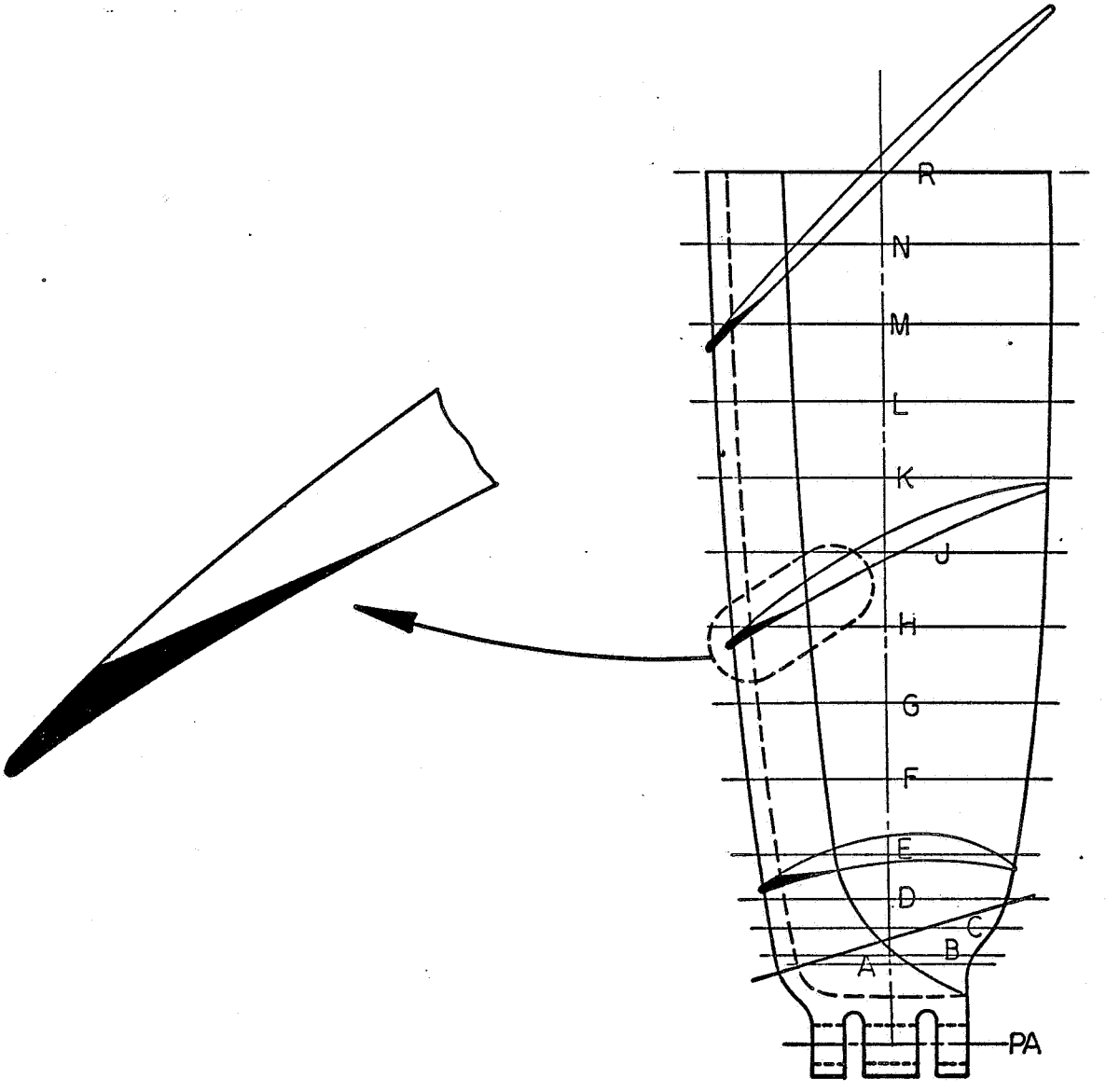

Figure 77. TICOM.

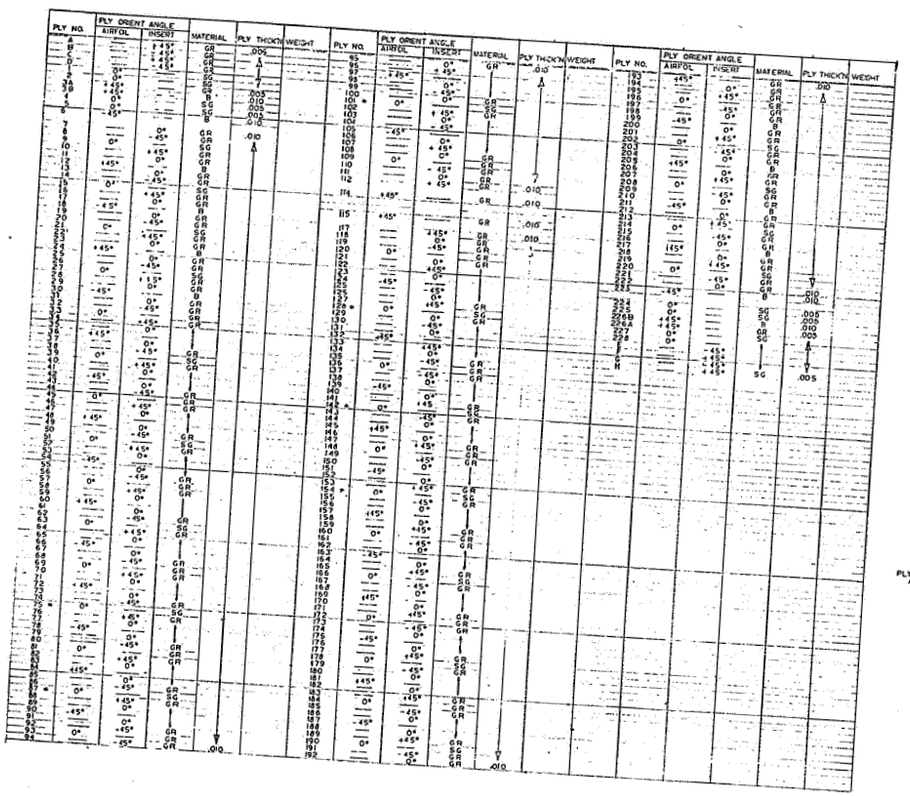

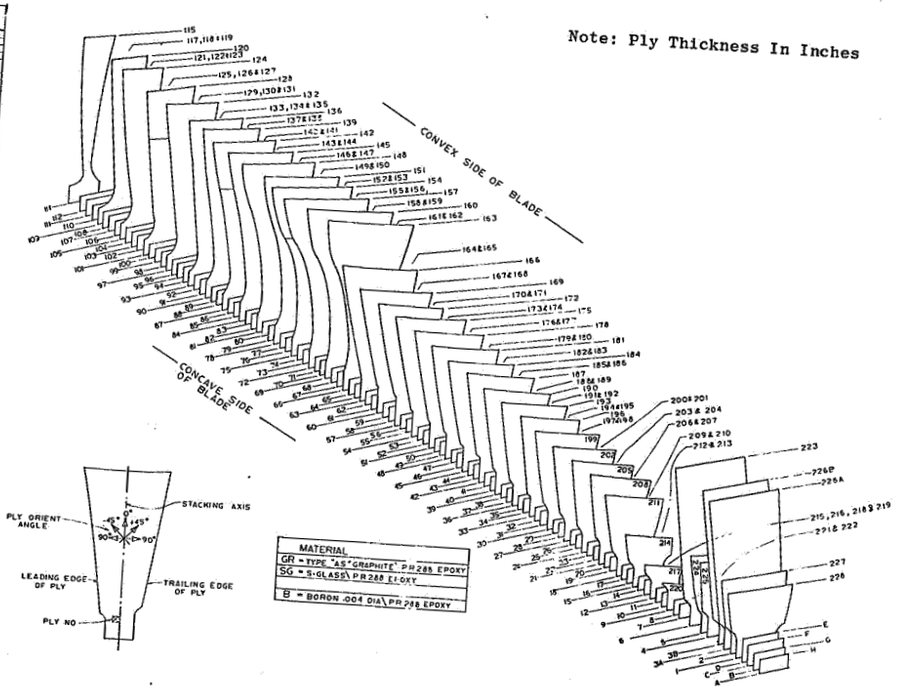

ORIGINAL PAGE IS
OF POOR QUALITY

Figure 78. Layup Sequence for Blade PQP003.

FOLDOUT FRAME 1

FOLDOUT FRAME 2

PLY NO		PLY ORIENT ANGLE		MATERIAL	PLY THICKNESS	WEIGHT
CONCAVE	CONVEX	AIRFOIL	INSERT			
A	E		+ 45°	80AS 20 SG	.005	
B	F		- 45°			
C	G		+ 45°			
D	H		- 45°			
1	201	0°		SG		
2	200	0°				
3	199	0°				
4	198	0°				
5	197	+ 45°		80AS 20SG		
6	196	+ 45°		B	.010	
7	195	0°		80AS 20SG	.005	
8	194	- 45°		B	.010	
9	193		-45°	80AS 20SG		
10	192		0°			
11	191		+45°			
12	190	0°			.005	
13	189		0°		.010	
14	188		- 45°			
15	187		0°			
16	186	+ 45°		B		
17	185		+45°	80AS 20SG		
18	184		0°			
19	183		-45°			
20	182	0°			.005	
21	181		0°		.010	
22	180		+45°			
23	179		0°			
24	178	- 45°		B		
25	177		- 45°	80AS 20SG		
26	176		0°			
27	175		-45°			
28	174	- 45°			.005	
29	173		0°		.010	
30	172		+ 45°			
31	171		0°			
32	170	- 35°			.020	
33	169		-45°		.010	
34	168		0°			
35	167		+45°			
36	166	0°			.020	
37	165		0°		.010	
38	164		-45°			
39	163		0°			
40	162		+ 45°			
41	161	+ 35°			.020	
42	160		0°		.010	
43	159		- 45°			
44	158		0			
45	157		+ 45°			
46	156	0°			.020	
47	155		0°		.010	
48	154		+45°			
49	153		0°			
50	152		-45°			
51	151	- 35°			.020	
52	150		0°		.010	
53	149		+ 45°			
54	148		0°			
55	147		- 45°			
56	146	0°			.020	
57	145		0°		.010	
58	144		-45°			
59	143		0°			
60	142		+45°			
61	141	+ 35°			.020	
62	140		0°		.010	
63	139		- 45°			
64	138		0°			
65	137		+ 45°			
66	136	0°			.020	
67	135		0°		.010	
68	134		+45°			
69	133		0°			
70	132		-45°			
71	131	- 35°			.020	
72	130		0°		.010	
73	129		+ 45°			
74	128		0°			
75	127		- 45°			
76	126	0°			.020	
77	125		0°		.010	
78	124		-45°			
79	123		0°			
80	122		+45°			
81	121	+ 35°			.020	
82	120		0°		.010	
83	119		- 45°			
84	118		0°			
85	117		+ 45°			
86	116	0°			.020	
87	115		0°		.010	
88	114		+ 45°			
89	113		0°			
90	112		-45°			
91	111	- 35°			.020	
92	110		0°		.010	
93	109		+45°			
94	108		0°			
95	107		-45°			
96	106	0°			.020	
97	105		0°		.010	
98	104		+45°			
99	103		0°			
100	102		-45°			
101		0°			.020	

Note: Ply Thickness In Inches

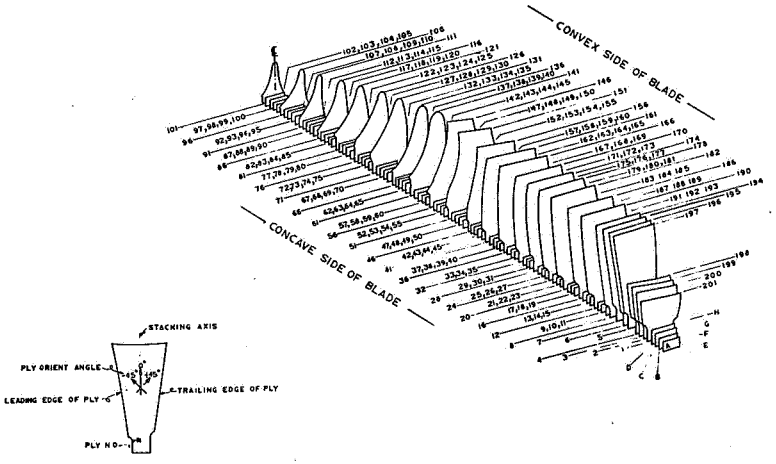

Figure 79. Layup Sequence for Blade PQP004.

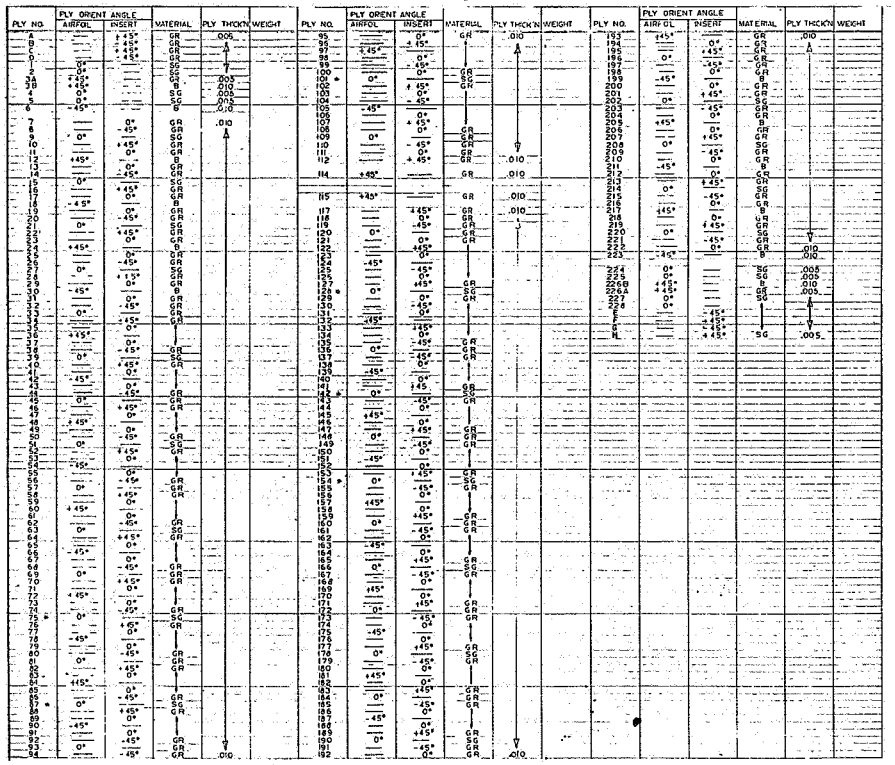

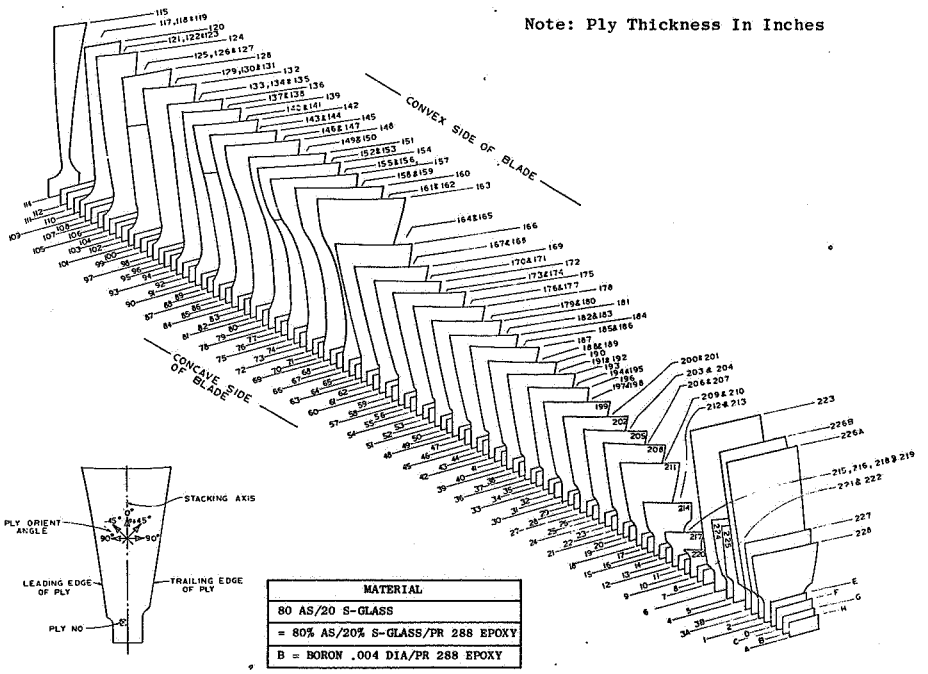

Figure 80. Layup Sequence for Blade PQP005.

PLY NO CONCAVE	PLY NO CONVEX	PLY ORIENT ANGLE AIRFOIL	PLY ORIENT ANGLE INSERT	MATERIAL	PLY THICKNESS	WEIGHT
A	E		+45°	6OAS|20SG	.005	
B	F		-45°			
C	G		+45°			
D	H		-45°			
1	201	0°		SG		
2	200	0°				
3	199	0°				
4	198	0°				
5	197	+45°		6OAS|20SG		
6	196	+45°		B	.010	
7	195	0°		6OAS|20SG	.005	
8	194	-45°		B	.010	
9	193		-45°	6OAS|20SG		
10	192		0°			
11	191		+45°			
12	190	0°			.005	
13	189		0°		.010	
14	188		-45°			
15	187		0°			
16	186	+45°		B		
17	185		+45°	6OAS|20SG		
18	184		0°			
19	183		-45°			
20	182	0°			.005	
21	181		0°		.010	
22	180		+45°			
23	179		0°			
24	178	-45°	45°	B		
25	177			6OAS/20SG		
26	176		0°			
27	175		-45°			
28	174					
29	173		0°	6OAS/20SG	.010	
30	172		+45°			
31	170	-35°			.020	
32	171		0°		.010	
33	169		-45°			
34	168		0°			
35	167		+45°			
36	166	0°			.020	
37	165		0°		.010	
38	164		-45°			
39	163		0°			
40	162		+45°			
41	161	+35°			.020	
42	160		0°		.010	
43	159		-45			
44	158		0			
45	157		+45°			
46	156	0°			.020	
47	155		0°		.010	
48	154		+45°			
49	153		0°			
50	152		-45°			
51	151	-35°			.020	
52	150		0°		.010	
53	149		+45°			
54	148		0°			
55	147		-45°			
56	146	0°			.020	
57	145		0°		.010	
58	144		-45°			
59	143		0°			
60	142		+45°			
61	141	+35°			.020	
62	140		0°		.010	
63	139		-45°			
64	138		0°			
65	137		+45°			
66	136	0°			.020	
67	135		0°		.010	
68	134		+45°			
69	133		0°			
70	132		-45°			
71	131	-35°			.020	
72	130		0°		.010	
73	129		+45°			
74	128		0°			
75	127		-45°			
76	126	0°			.020	
77	125		0°		.010	
78	124		-45°			
79	123		0°			
80	122		+45°			
81	121	+35°			.020	
82	120		0°		.010	
83	119		-45°			
84	118		0°			
85	117		+45°			
86	116	0°			.020	
87	115		0°		.010	
88	114		+45°			
89	113		0°			
90	112		-45°			
91	111	-35°			.020	
92	110		0°		.010	
93	109		+45°			
94	108		0°			
95	107		-45°			
96	106	0°			.020	
97	105		0°		.010	
98	104		+45°			
99	103		0°			
100	102		-45°			
101		0°			.020	
101A			AF126 ADHESIVE		.010	

Note: Ply Thickness In Inches

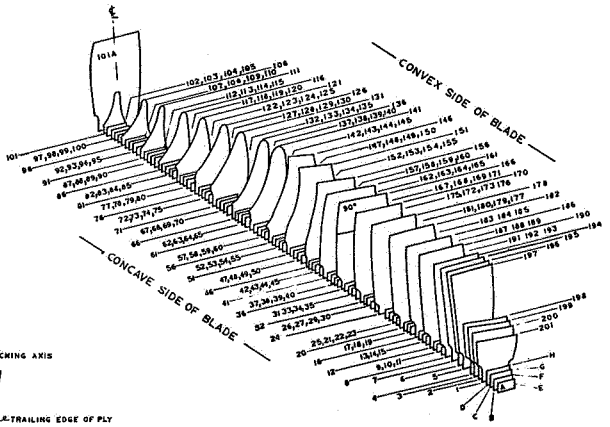

Figure 81. Layup Sequence for Blade PQP006.

Selection of these blade designs permitted the following thorough evaluation of several material and layup variations.

- PQP003 and PQP005 provided direct comparison of the interply and intraply material in an otherwise identical layup.
- PQP004 and PQP005 provided direct comparison between the standard layup and the QCSEE layup using the same intraply material.
- PQP004 and PQP006 allowed evaluation of the adhesive layer concept in otherwise identical blades.

4.3 BLADE FABRICATION

To assure production of high quality blades, a quality control procedure was established. The following paragraphs describe the methods used to assure the required blade-to-blade consistency. All the materials used were procured to General Electric specifications.

An established quality control plan for inspecting incoming epoxy prepregs at General Electric was employed on all materials procured under this program. This plan, which establishes the requirements and methods for selecting satisfactory prepreg material for use in composite blade molding activities, includes the following operations:

1. Checking inventory of incoming material and vendor's certifications for completeness and reported conformance to specification requirements
2. Logging in each lot and roll received
3. Visual inspection of workmanship
4. Sampling of material and verification of compliance with specification requirements, including physical properties, reactivity, and mechanical properties of a molded panel from each combination of fiber and resin batch
5. Handling, storage, and reinspection of out-of-date materials
6. Disposition of materials which fail to meet specification requirements.

Special material properties which were measured and compared to vendor-reported data on each prepreg lot are given below:

Prepreg Data	Laminate Data
Fiber, g/m^2 (Weight of fiber per m^2 of lamina area)	Flexure strength at room temperature, 394 K (250° F)
Resin, g/m^2 (weight of resin per m^2 of lamina area)	Flexure modulus at room temperature, 394 K (250° F)
Solvent content of prepreg, % weight	Shear strength at room temperature, 394 K (250° F)
Gel time, minutes at 383 K (230° F)	Fiber content, volume %
	Resin content, volume %
Visual discrepancies	Voids, volume %
	Density, g/cm^3

The basic sequence of operations involved in molding the QCSEE-type composite blades is outlined below:

1. Cut out and lay up the individual plies.

2. The fully assembled mold tool was heated to the prescribed temperature in the press such that all sections of the die were maintained at a uniform temperature.

3. The press was opened and release agent was applied to the mold cavity surfaces and any excess removed.

4. The assembled blade preform was loaded into the heated mold cavity.

5. The press was closed at a fast approach speed until the top and bottom portions of the mold engaged.

6. An intermediate closing speed was selected for preliminary debulking of the blade preform.

7. The dies continued to close at a preselected, slow rate. The movement continued until the die was closed and the prescribed molding load/pressure attained. Figure 82 shows a typical rate of closure and load application curve for molding a composite blade with a gel time of 60 ± 5 minutes at the constant molding temperature 383 K (230° F).

8. The press was opened and the blade molding was rapidly transferred into the postcure oven, thus, preventing thermal contraction stresses from being set up in the part. The blade was allowed to hang freely in the postcure oven for the predetermined process time necessary to achieve full material properties.

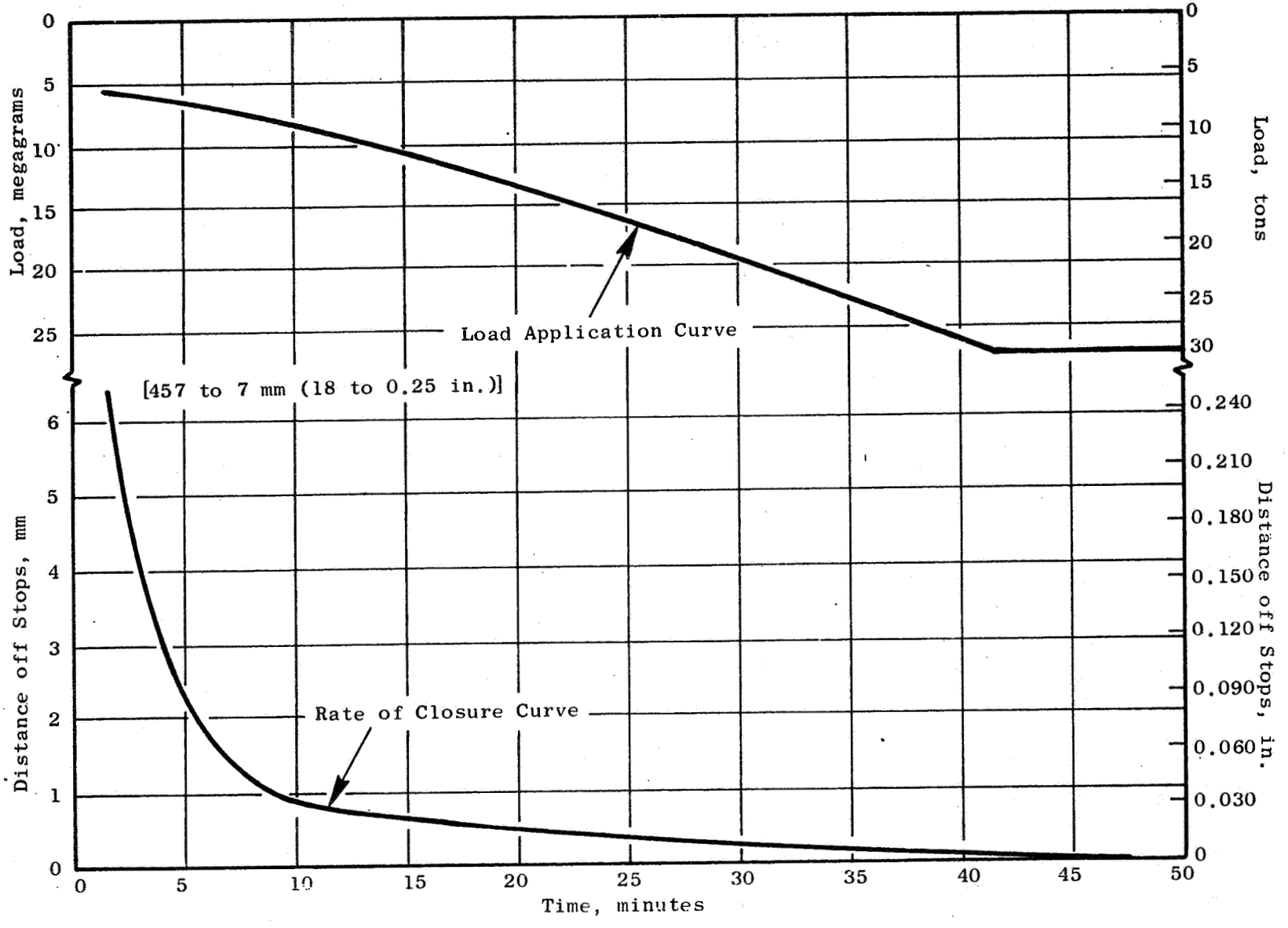

Figure 82. Molding Procedure for PR 288/Type AU Blade with Gel Time at 124° K (230° F).

After removing the blades from the postcure oven and trimming the resin flash, the following inspection operations were carried out:

1. Measurement and recording of molded weight, volume, and density.

2. Recording of surface defects in sketch form and by photographs taken of both sides of the blade.

3. Dimensional inspection and recording of the root and tip maximum dimensions.

Although the blade form was molded well within the desired envelope tolerances, it was extremely difficult to mold the dovetail profile to the accuracy required. As a result, dovetail profiles were final machined to size. A nickle plate leading edge protection system was also applied to the blades. The principal finishing operations performed on the blades are listed below:

1. Dovetail machining
2. Application of wire mesh to leading edge
3. Application of nickle plating to wire mesh
4. Trimming blade to length and tip forming

All blade specimens were subjected to through-transmission ultrasonic C-scan (TTUCS) inspection before and after testing in addition to holographic and root dye penetrant inspection.

The C-scan inspection technique, shown in Figure 83, is basically a measurement of sound attenuation due to both absorption and scattering. The through-transmission approach (as opposed to pure pulse-echo or reflection-plate pulse-echo/transmission approaches) provides for a more efficient energy transfer with a minimal influence of test equipment configuration or material/component shape. The scanner contour follows the airfoil with a master/slave servomechanism. Even so, the attenuation values must be referenced to a specific ply stackup and process sequence employed in the manufacture of each component.

High-resolution scanning (75 lines per inch for 15,000 units of data per square inch), combined with 10 shades-of-gray (5 percent of 95 percent on the Oscilloscope) recording on dry facsimile paper, provides an "attenugraph" image which is read much in the same manner as a radiograph.

The laser holographic facility, Figure 84, was also used to inspect the blades molded during this program. It is highly versatile in that the optical devices may be positioned to accommodate a variety of object types and fields of illumination on panels, blades, and other contoured components. Interferometry relies on secure blade fixturing and consistently reproducible stressing for the second exposure of a double-exposure hologram. Typical interferograms are presented in Figure 85.

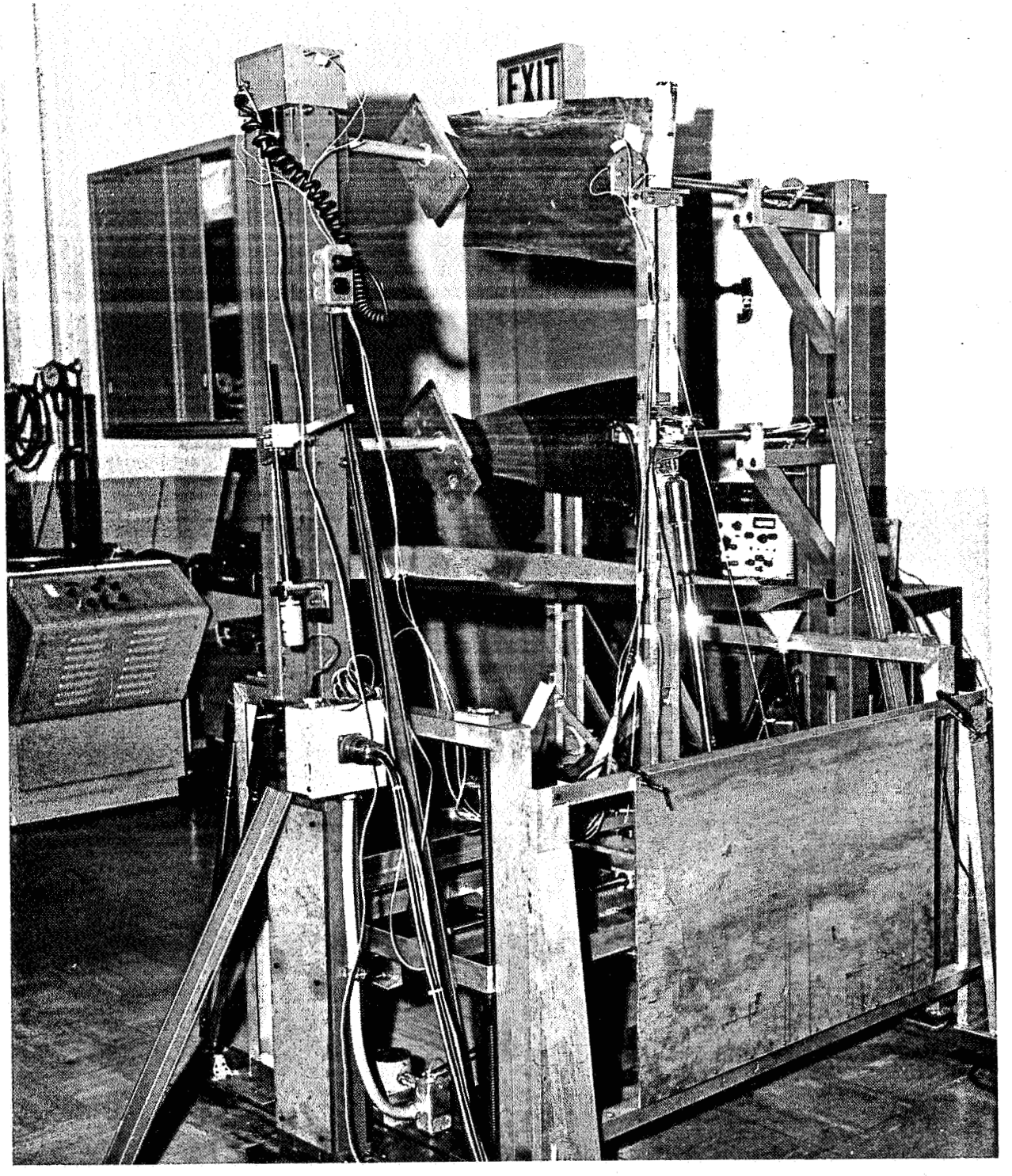

Figure 83. Test Technique for Ultrasonic C-Scan of Composite Blades.

Figure 84. Laser Holographic Facility.

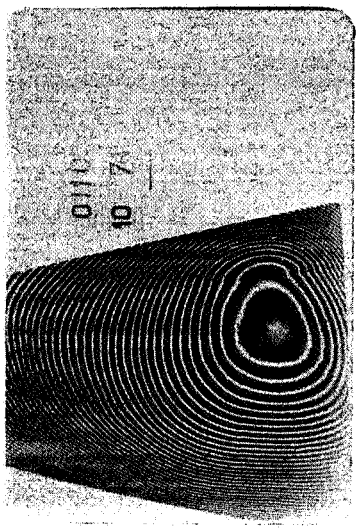

(a) Concave - Tip
No Discontinuity

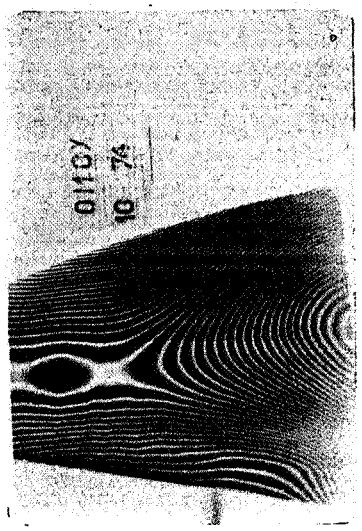

(b) Convex - Tip
No Discontinuity

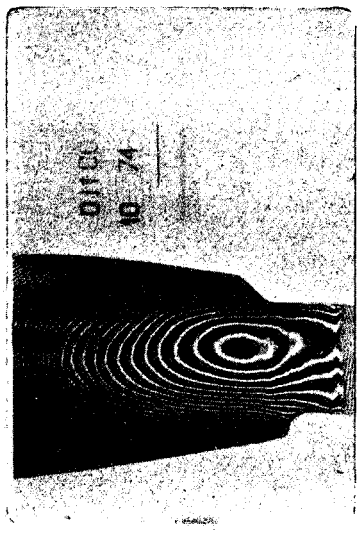

(c) Concave - Root
Slight Discontinuity Due to Ply Slippage

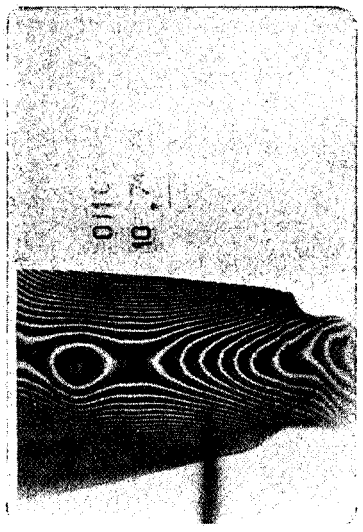

(d) Convex - Root
No Discontinuity

Figure 85. Holographic NDT of QCSEE Blade.

Dye penetrant inspection of the dovetail area was performed on each of the blades. This test was used to detect surface-connected root delaminations in the machined dovetail. The dye penetrant check also gives qualitative indications of root zone porosity.

The four blades fabricated were thoroughly nondestructively tested as described above. Their quality was judged to be acceptable for test.

4.4 IMPACT TEST PLAN

The same facility and procedures used for the testing described in Section 3.2 and 3.3 were used in this testing except no strain gages were used. Table XIII presents the test plan. The pin root blade was impacted at 23 degrees incidence with an objective 241 gram (8.5 ounce) slice weight. An identical blade but with a keyhole outsert was also tested at this condition.

The four improved blades were impacted at the same condition [33 degree incidence angle and 340 gram (12 ounce) slice weight] that resulted in serious damage to an early QCSEE blade, which had suffered over 60 percent weight loss and 100 percent airfoil delamination.

4.5 TEST RESULTS AND DISCUSSION OF RESULTS

4.5.1 Pin Root Blade Test

The first blade tested in this test series was the pin root blade discussed in Section 4.2.1 which was otherwise identical to a keyhole outsert blade previously tested. Results of the keyhole blade showed no weight loss and 75 percent delamination of the airfoil at 23 degree incidence angle at 3200 rpm and 241 gram (8.5 ounce) slice.

Before impact testing, the pin root blade was run up to 3800 rpm (117 percent of mechanical design), to demonstrate overspeed capability. Following this test, a delamination in the composite dovetail was detected. No damage was detected on previous runs at 3200 rpm. Figure 86 shows a photograph of the delamination at the leading edge using die penetrant. Figure 87 shows the extent of the delamination as defined by ultrasonic inspection; the area below the white ticked line representing the area of delamination. After a review of the extent of the delamination, it was decided to proceed with the impact test of the blade. Since the damage was confined to the root area of the blade, the ability of the airfoil portion of the blade to absorb the impact should be unchanged. Therefore, any impact advantage associated with the pin root concept could still be identified.

Table XIII. Test Matrix.

Blade	Shot	Incidence Angle (deg)	Slice Weight gms (oz)	rpm	Relative Velocity m/sec (ft/sec)	Bird Diameter cm (in.)
PQP010	14	23	241 (8.5)	3200	262 (860)	14.0 (5.5)
Pin Root	1	23	241 (8.5)	3200	262 (860)	14.0 (5.5)
PQP003	2	33	340 (12)	3320	271 (890)	14.0 (5.5)
PQP004	3	33	340 (12)	3320	271 (890)	14.0 (5.5)
PQP005	4	33	340 (12)	3320	271 (890)	14.0 (5.5)
PQP006	5	33	340 (12)	3320	271 (890)	14.0 (5.5)

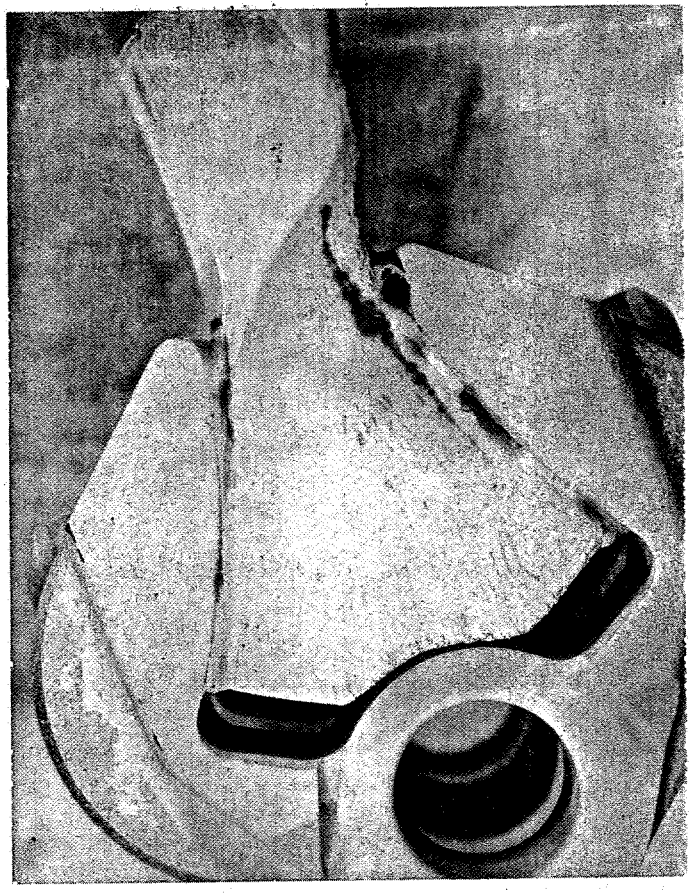

Figure 86. Pin Root Blade Root Delamination, Leading Edge.

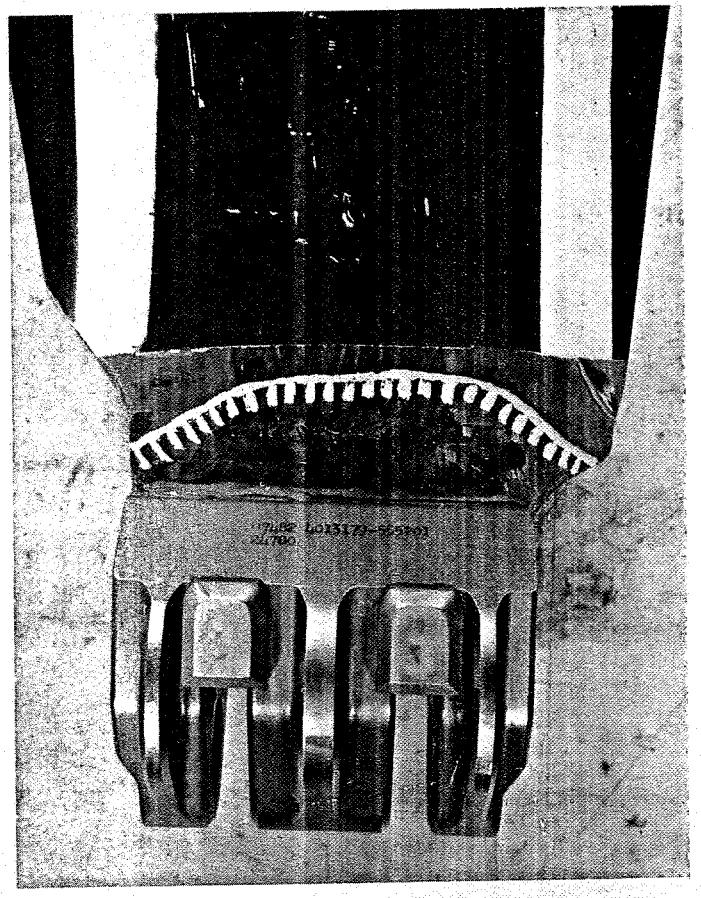

Figure 87. Pin Root Blade Root Delamination, Unbonded Area.

The AU/Kevlar blade equipped with a pin root was then impact tested. Figure 88 shows this blade after impact. This blade was tested at 3200 rpm and 23 degrees incidence angle with an objective slice of 241 grams (8.5 ounces). Analysis of the high speed movies showed that an initial slice of about 227 grams (eight ounces) was achieved with no weight loss to the blade. However, on the third and fourth revolutions after the initial impact, additional impacts occurred. The total slice size was 510 grams (18 ounces). The secondary impacts occurred for two reasons: (1) when the blade rotates about the pin, it moves axially outward toward the bird since the pin is oriented off the axial direction to set the 23 degree incidence angle, and (2) the injector oscillates after firing so that the bird is again close to the blade after two or three revolutions.

Analysis of the high speed movies was conducted to find the blade rotation for the pin root and keyhole blade. Although the initial slice weight of the pin root blade cannot be determined with great accuracy, it is felt it was not substantially different from the keyhole blade value of 241 grams (8.5 ounces). Comparisons of the rotation characteristics of the two blades is shown in Figure 89.

As can be seen from the figure, the pin root blade rotated to an initially higher angle than the keyhole blade, about 11 degrees versus five to six degrees. Also, the pin root blade rotation damped out much more slowly than the keyhole blade; this is due to the reduced friction associated with the pin. These data show that the pin root concept might be helpful for a particular blade design if the blade root was susceptible to root failure upon impact since the pin root has low resistance to rotation.

4.5.2 Improved Blades Test

Prior to impact testing, all four improved blades were bench frequency checked. Table XIV shows the frequency results. The range of the frequencies for the QCSEE preliminary blade described in Section 3.1 are also included for reference. As predicted, all four improved blades exhibit acceptable frequency characteristics from an engine installation standpoint. The weight of each blade prior to test is also shown. The weight of the improved blades are slightly higher than the QCSEE blade due essentially to the replacement of the Kevlar with heavier S-glass. Table XV presents the results of the impact test for the four blades in terms of the percentage of blade weight that was lost due to the impact and the percentage of the airfoil that was delaminated. The area delaminated was measured by an ultrasonic C-scan of the blades after impact. This technique, discussed in Section 4.3, is able to identify areas of delamination even if only one or two plies are delaminated.

Due to unavoidable variation in the timing and injector mechanism, it is not possible to achieve exactly the same slice size on each shot. For this reason, it is necessary to compare the data using results of the impact parameter investigation discussed in Section 3. Figures 90 and 91

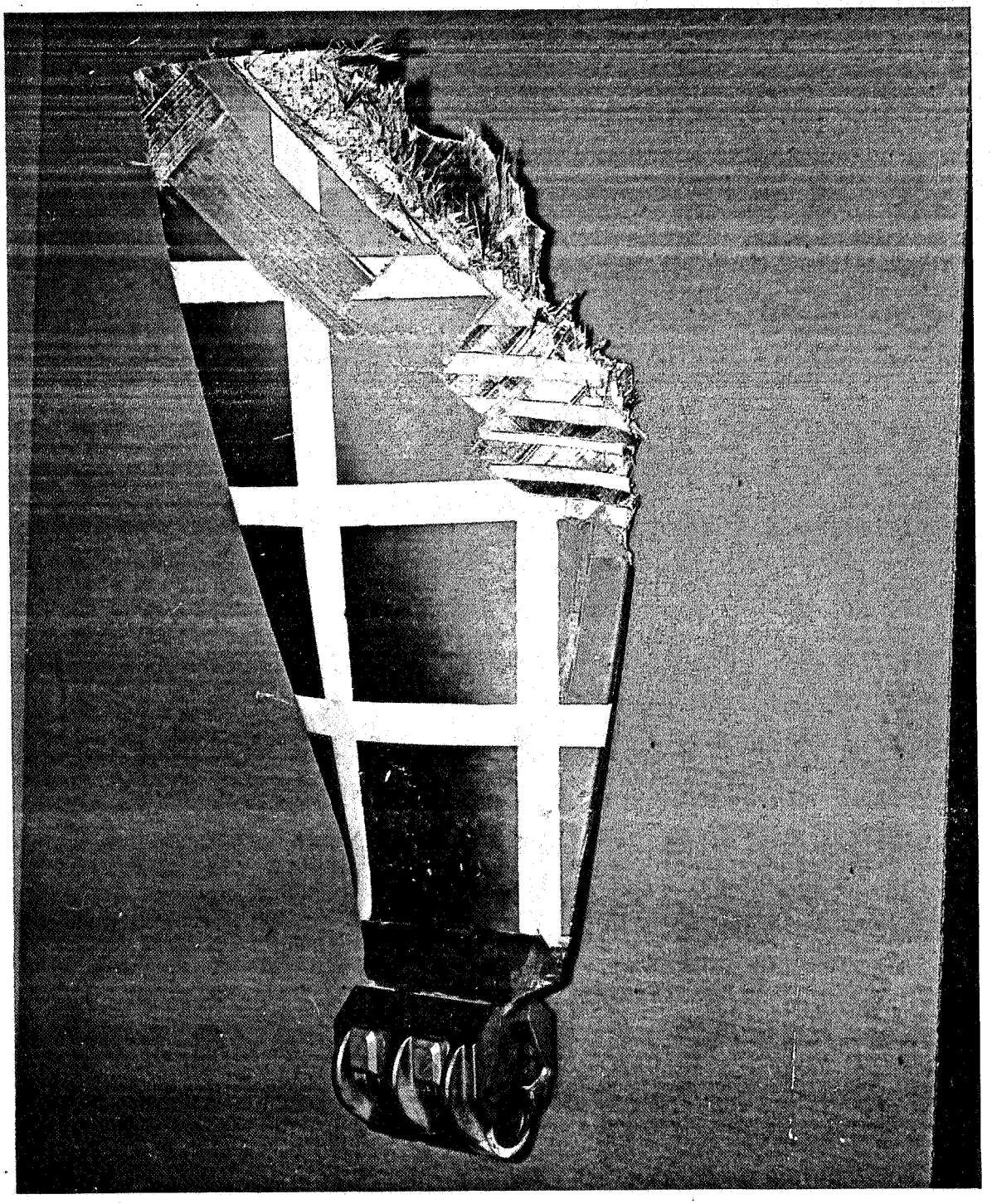

Figure 88. Pin Root Blade after Impact.

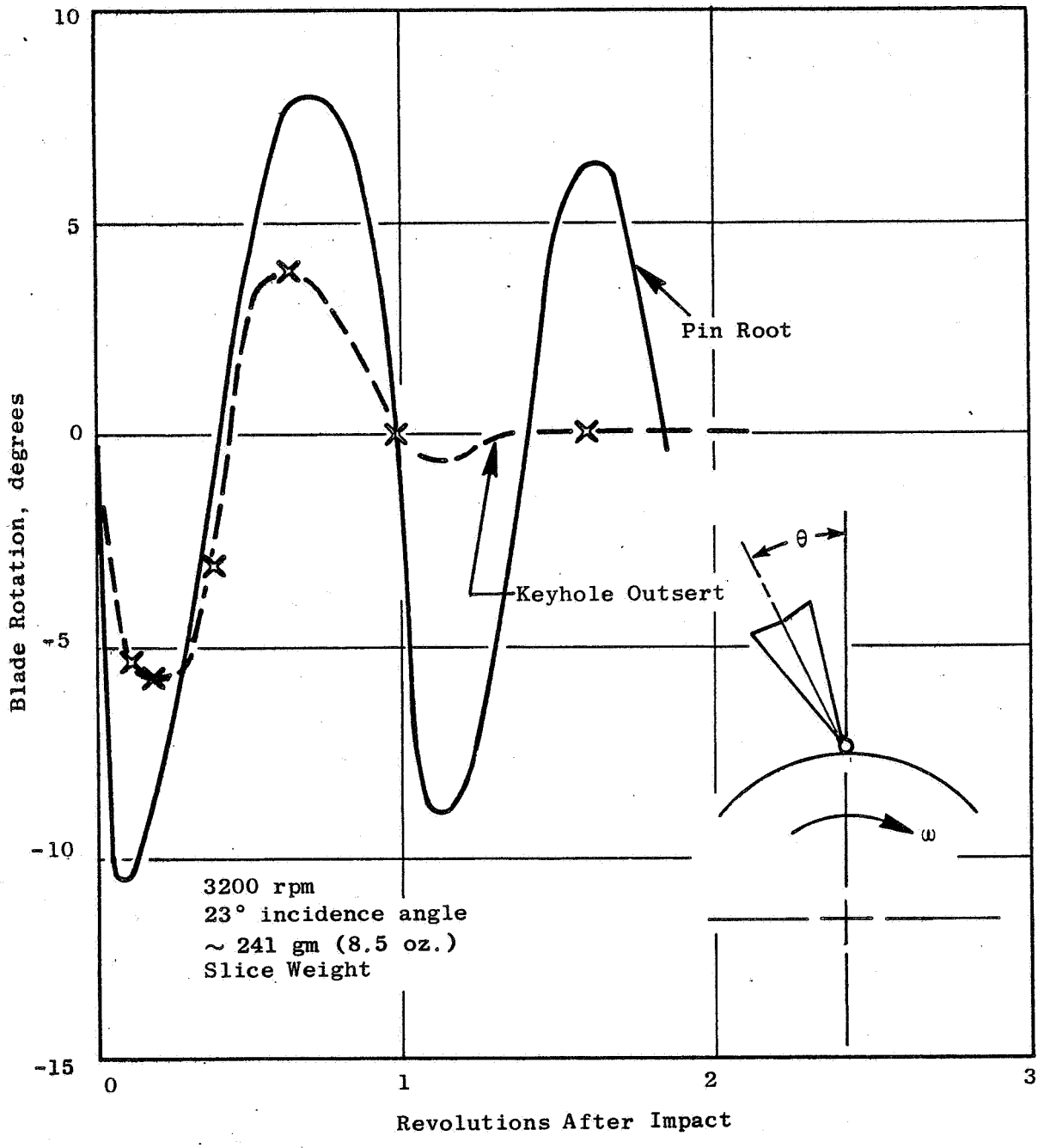

Figure 89. Rotation after Impact for Pin Root and Keyhole Outserts.

Table XIV. Bench Frequency Summary.

Blade	Description	Frequency, Hz		
		1st Flex	2nd Flex	1st T.
QCSEE Preliminary Blades	AU/Kevlar interply + Boron QCSEE type layup at 0° ± 45° orientation	58-67	190-192	284-288
PQP003	Same as above with AS/S-Glass + Boron	58	180	272
PQP004	80 AS/20 S-Glass intraply + Boron F103 Type layup (standard) at ± 0° ± 35° orientation	62	196	276
PQP005	Same as PQP003 except uses 80 AS/20 S-Glass intraply (striped) material	63	186	274
PQP006	Same as PQP004 except has AF126 Adhesive strip down center of blade	63	192	274

Table XV. Whirligig Impact Test Results, 33° Incidence Angle at Takeoff Engine Conditions.

Blade	Slice Wt W_s		Original Blade Weight		Percent Wt Loss W/W (%)	% Airfoil Area Delaminated
	g	oz	kg	lb		
PQP003	82	2.9	2.41	5.31	0	10
	482	17.0	2.41	5.31	26	81
PQP004	363	12.8	2.41	5.31	15	68
PQP005	232	8.2	2.44	5.37	14	94
PQP006	369	13.0	2.44	5.37	25	66

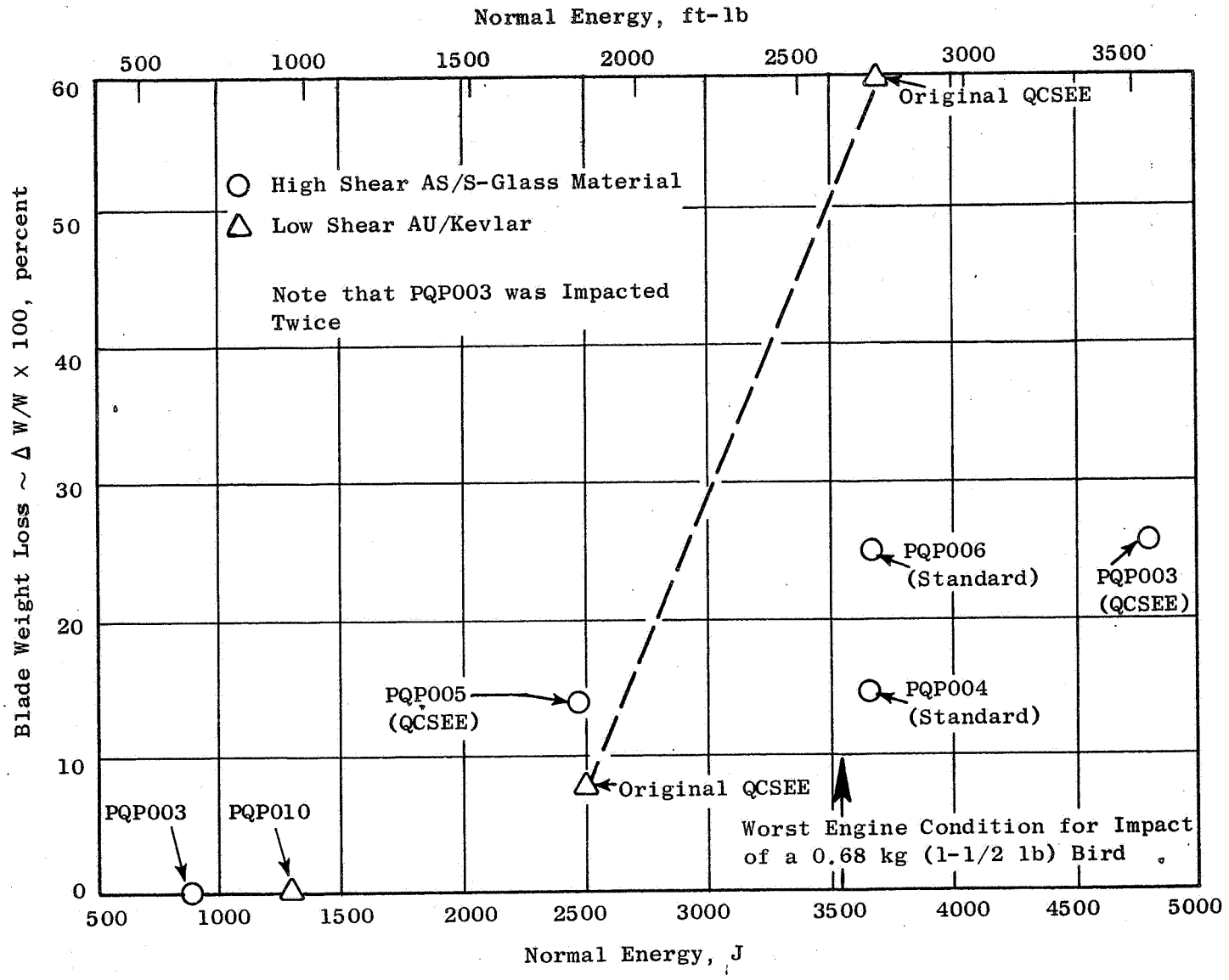

Figure 90. Blade Weight Loss for 75% Span Impact Tests.

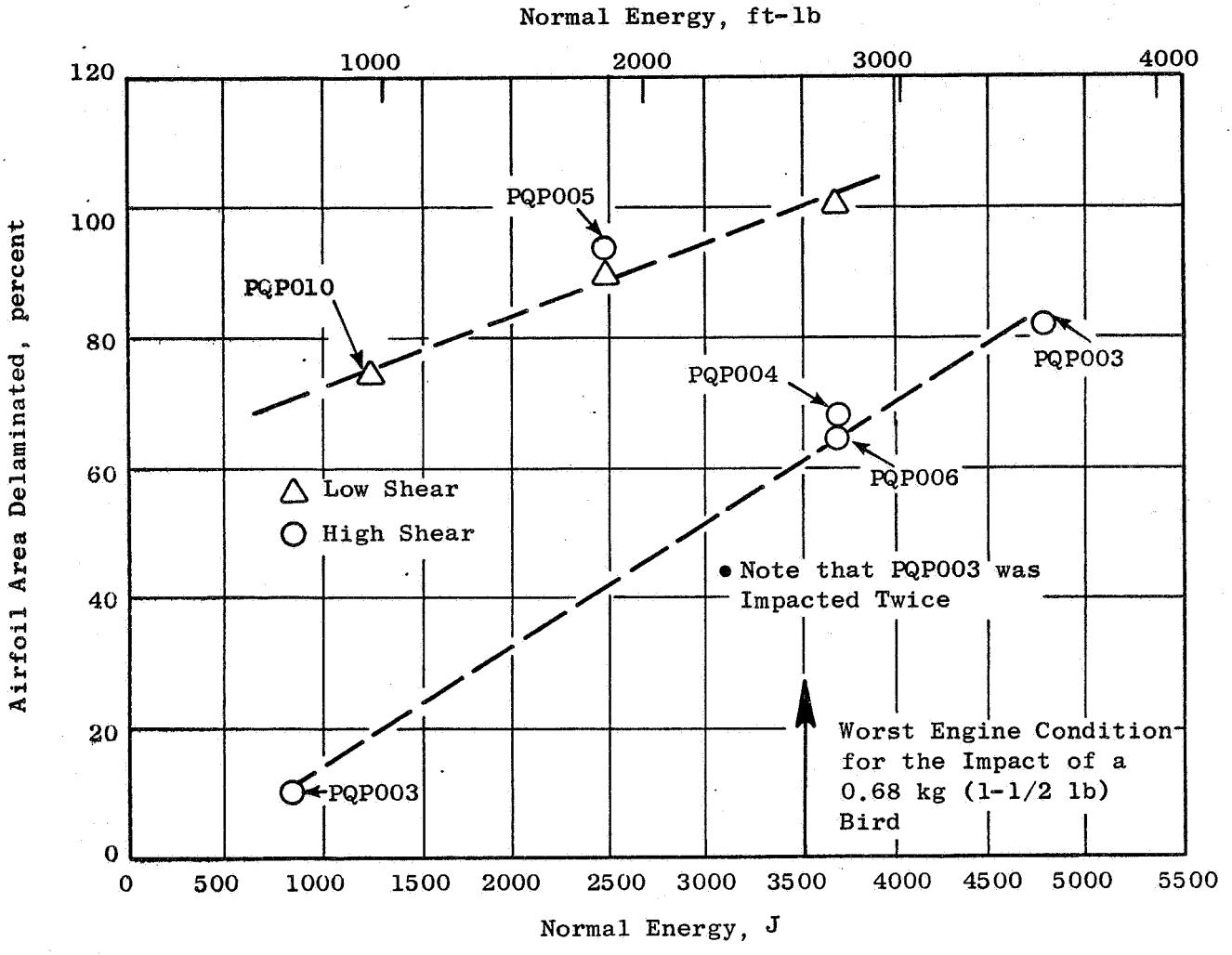

Figure 91. Airfoil Area Delaminated.

present the weight loss and area delaminated in graphical form versus the normal energy parameter, E_N, which is described in Sections 3.3 and 3.4. The results of testing on the original QCSEE blade in 1974 and the test conducted in conjunction with the pin root blade test are also shown for comparison. Note that blade PQP003 was also impacted with an 82 grams (2.9 ounce) slice. This was due to a malfunction in the injector mechanism, however, since the blade was not severely damaged, it was retested as shown. Also shown on Figures 90 and 91 is the normal energy at takeoff for a 0.68 kg (1-1/2 pound) bird impact. Photographs of the concave and convex side of each blade after impact are presented in Figures 92 through 99. Based on the data presented above, the following conclusions have been drawn:

- For the impact of a 0.68 kg (1-1/2 pound) bird at takeoff engine conditions, the improved blades with high shear materials show substantial improvement in FOD capability. The new blades exhibit a weight loss of 15 to 25 percent versus over 60 percent for the low shear material blades and an area delamination of 65 to 70 percent versus 100 percent for the low shear strength blades.

- On a weight loss basis, the standard-type and the QCSEE-type layups show about the same FOD tolerance. That is the blades having a standard layup (PQP004 and 006) and the blades having a QCSEE layup (PQP003 and 005) exhibited similar weight loss characteristics when impacted by RTV birds weighing between 200 to 500 grams.

- Observation of the failed blades suggests the standard-type layups PQP004 and 006 appear to lose a region at the leading edge tip when impacted, whereas blade PQP003, having the QCSEE design, lost the entire outer portion of airfoil. At lower span impacts, this characteristic of the QCSEE layup could result in worsened FOD capability relative to the standard layup.

- Adding a layer of AF126 adhesive along the center of the blade did not improve or lessen impact resistance.

- From an overall standpoint, the standard layup with intraply material appeared to offer the best FOD capability of any of the other candidates for the limited testing conducted.

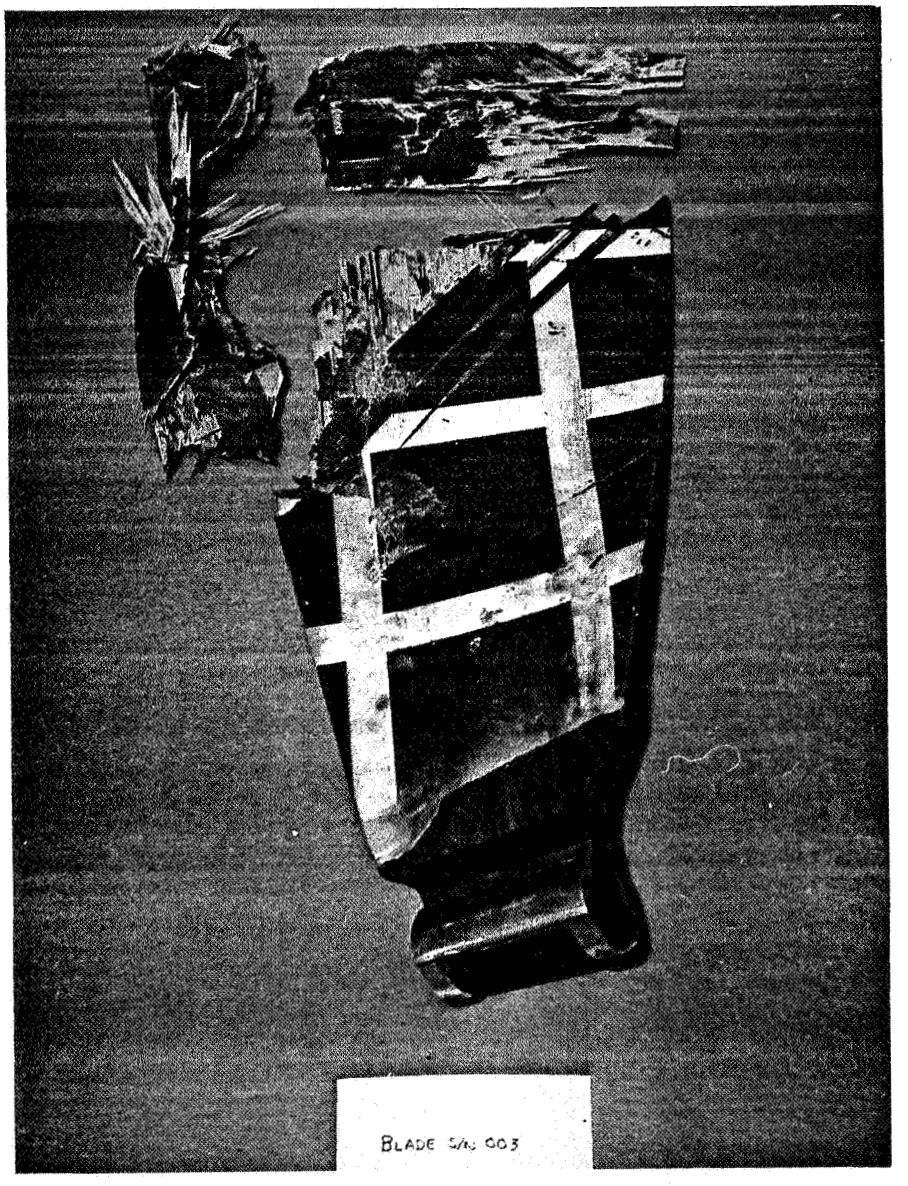

Figure 92. Blade PQP003 Concave Side after Impact.

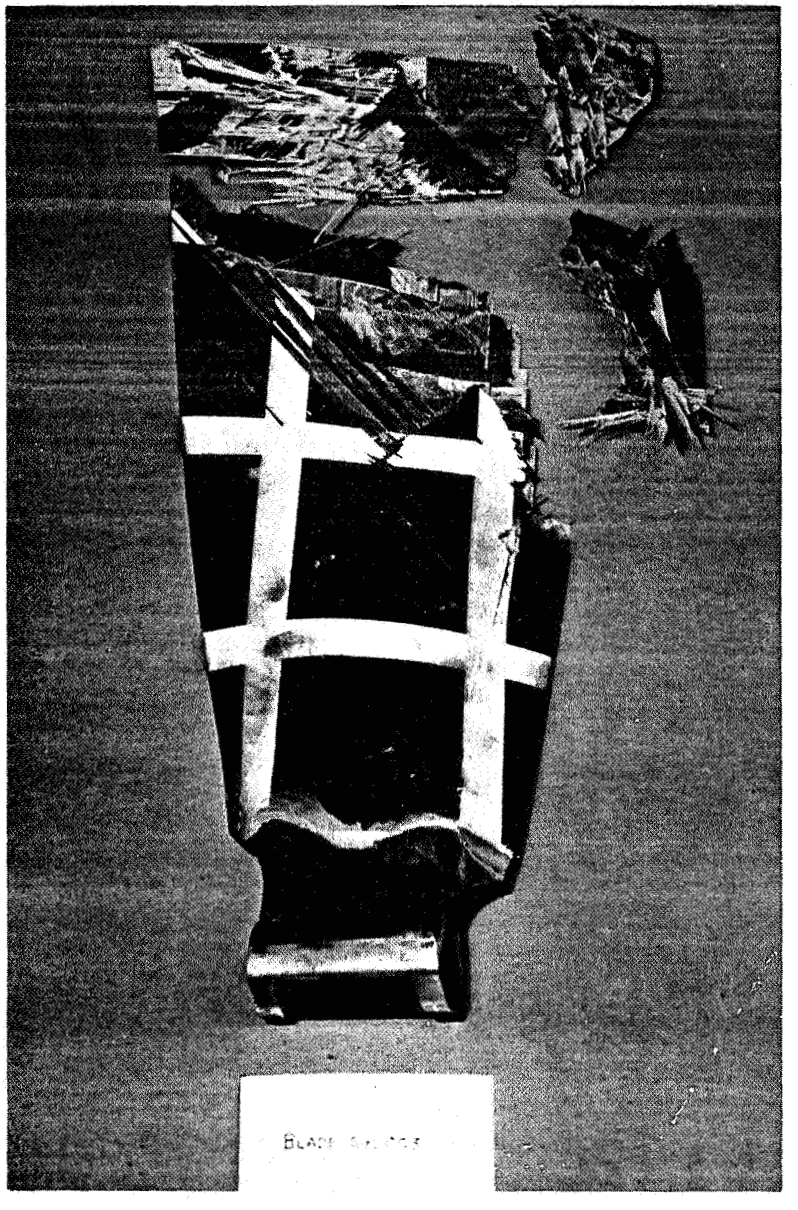

Figure 93. Blade PQP003 Convex Side after Impact.

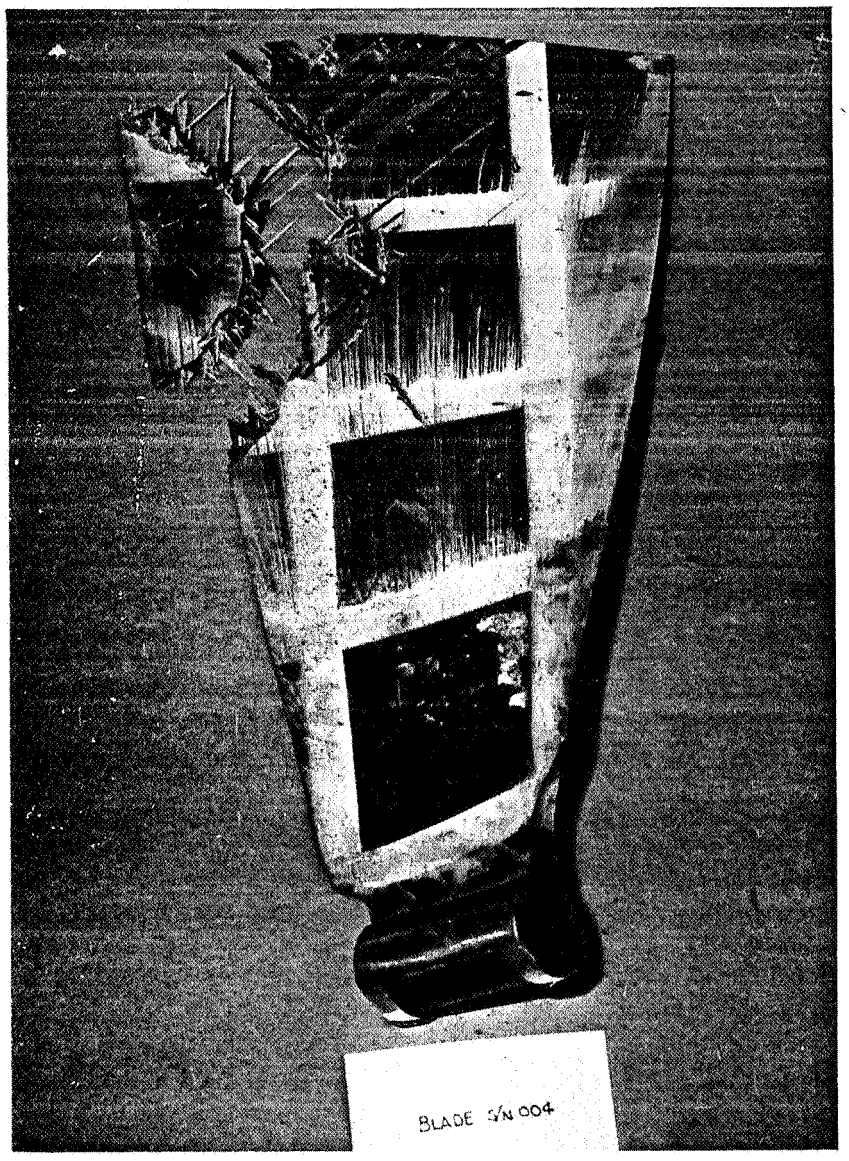

Figure 94. Blade PQP004 Concave Side after Impact.

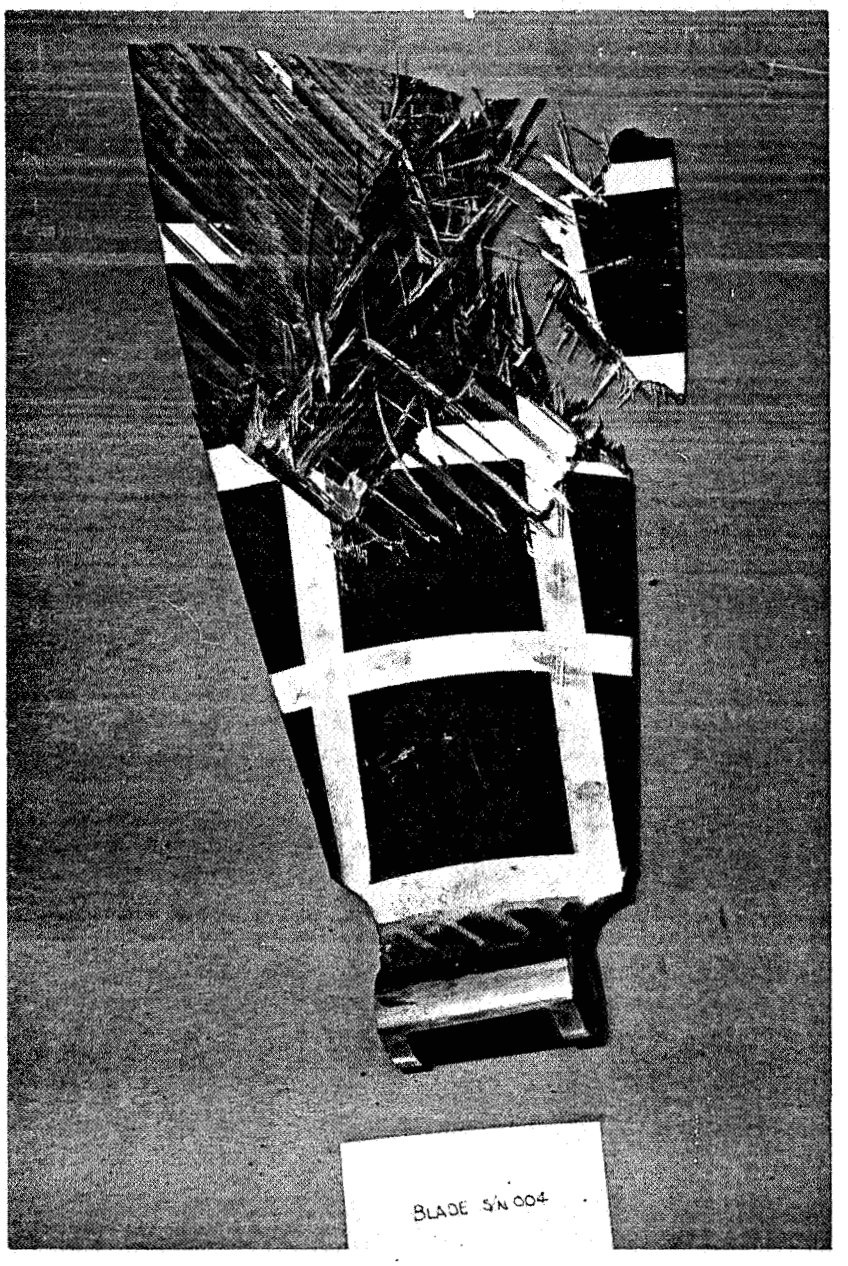

Figure 95. Blade PQP004 Convex Side after Impact.

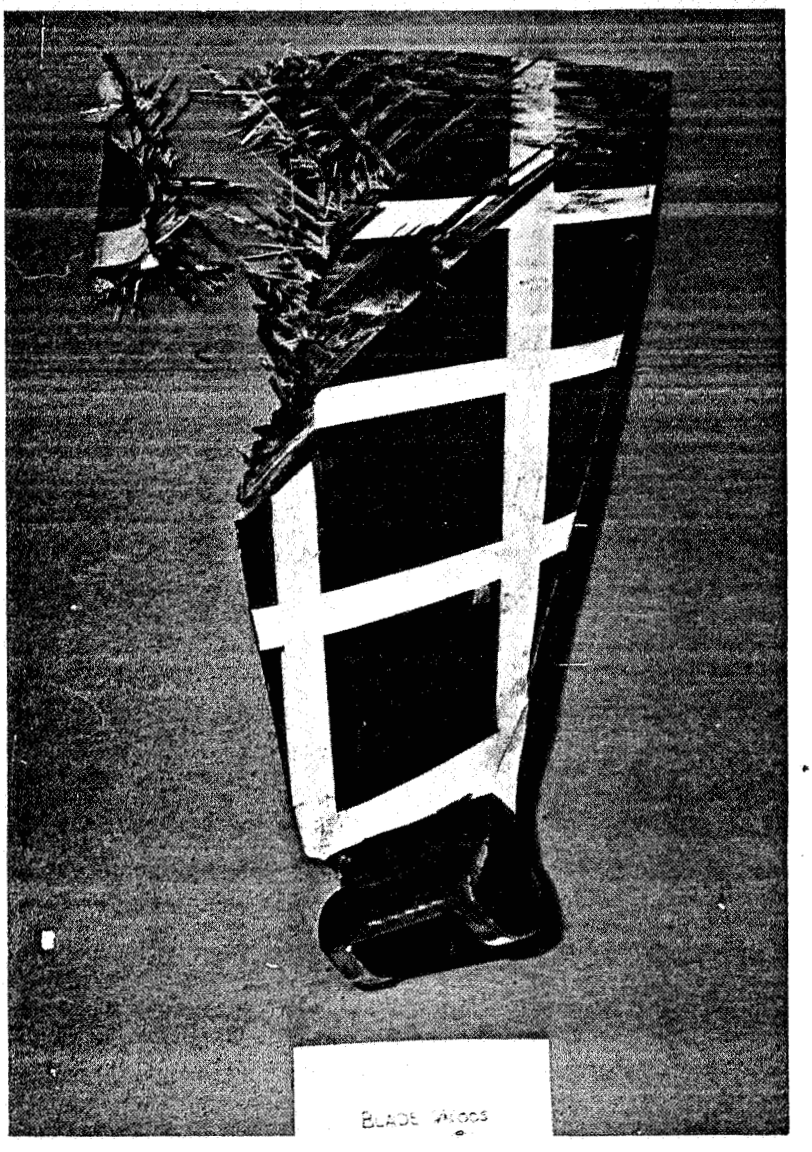

Figure 96. Blade PQP005 Concave Side after Impact.

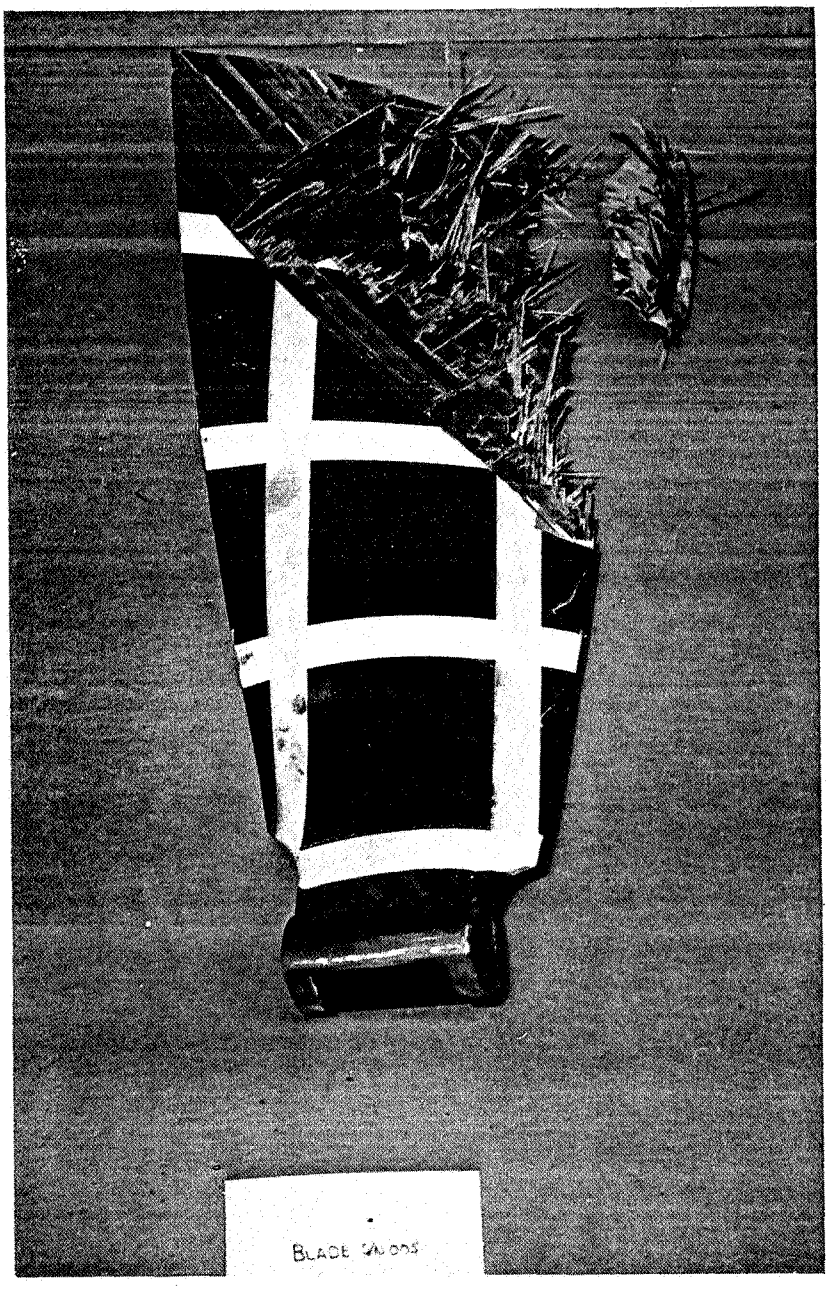

Figure 97. Blade PQP005 Convex Side after Impact.

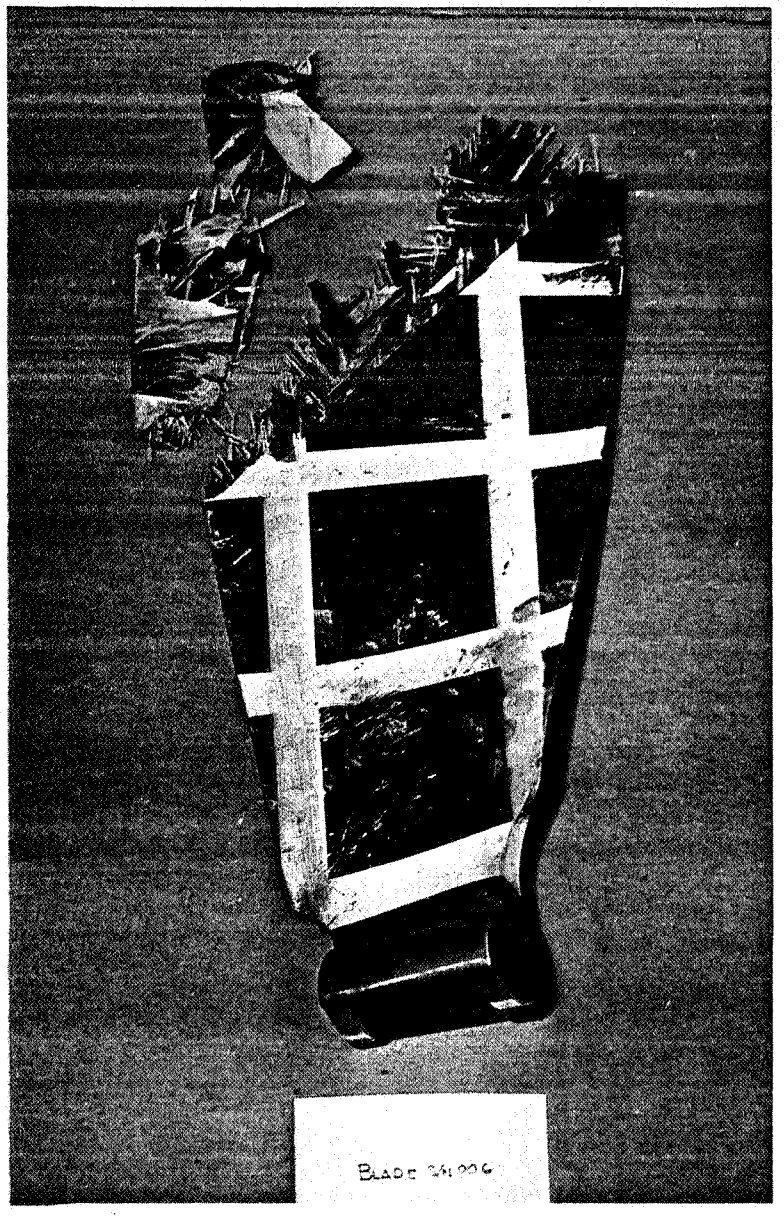

Figure 98. Blade PQP006 Concave Side after Impact.

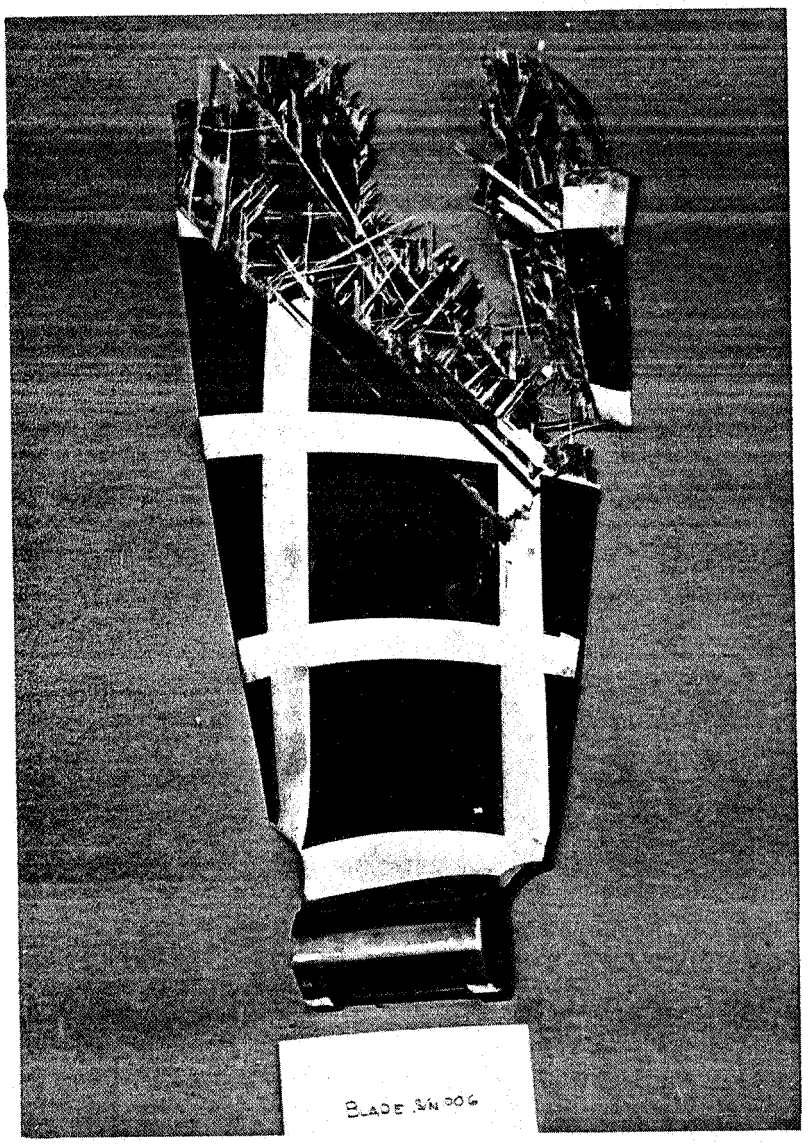

Figure 99. Blade PQP006 Convex Side after Impact.

5.0 CONCLUSIONS

This report has presented the results of a 20-month program designed to investigate parameters which effect the foreign object damage resulting from ingestion of birds into fan blades of a QCSEE-type engine; and to design, fabricate, and impact test QCSEE fan blades which show improvement in FOD resistance relative to existing blades. To accomplish the first objective, strain gage instrumented QCSEE-type fan blades were single-blade impacted in a Whirligig facility at selected impact conditions using small RTV projectiles while the resulting dynamic strains in the blade were recorded. In the second phase of the program, four improved QCSEE-type fan blades were designed, fabricated, and impact tested. A pin root attachment concept was also investigated from an impact standpoint in this phase. Based on the results of this program, the following conclusions have been reached:

Evaluation of Impact Parameters

- Excellent quality strain data was obtained during the testing.
- Varying the impact parameters investigated effected the amplitude of the resulting strain/time trace, but did not substantially effect the frequency of the wave. However, changes in the impact span changed both the amplitude and frequency of the waveforms.
- In the area of impact, the maximum strain occurs on the first cycle of the stress wave after impact.
- Frequencies up to 4000 Hertz contribute to the strain response for the small impacts studied.
- The kinetic energy of the bird normal to the blade chord and the normal force correlate the strain data well for the range of impact parameters studied.
- A finite element computer program gave excellent agreement with the test data for the impacts studied.

Improved FOD Resistant Blades

- A blade using a pin root attachment rotated more upon impact than a similar blade with a keyhole outsert, and the blade oscillations damped out much more slowly than for the keyhole design.

- AU/Kevlar and AS/Kevlar have a low interlaminar shear strength of about 30 MN/m^2 (4 ksi) in panel tests relative to AS/S-glass panels which have about 10 MN/m^2 (10 ksi) shear strength.

- For the impact of a 0.68 kg (1-1/2 pound) bird at takeoff engine conditions, the improved blades with high shear materials show substantial improvement in FOD capability relative to the older blade designs. The new blades exhibit a weight loss of 15 to 25 percent versus over 60 percent for the low shear material blades and an area delamination of 65 to 70 percent versus 100 percent for the old low shear strength blades at this impact condition.

6.0 REFERENCES

1.0 "Quiet Clean Short-Haul Experimental Engine (QCSEE) Under-the-Wing Engine Composite Fan Blade Preliminary Design Test Report," NASA CR-134846.

2.0 "Quiet Clean Short-Haul Experimental Engine Composite Fan Blade Design," NASA CR-134840.

3.0 C.T. Salemme and G.C. Murphy, "Low Cost FOD Resistant Organic Matrix Fan Blades," Report Number IR-413-4 (VII).

7.0 APPENDIX

The following 18 figures present the strain gage test data as measured for Runs 1 to 9 as discussed in Section 3.0. For all gages, tension is up the scale and compression is down the scale.

Run No. 1

16 gm Slice
75% Span
3200 rpm
23° Incidence Angle

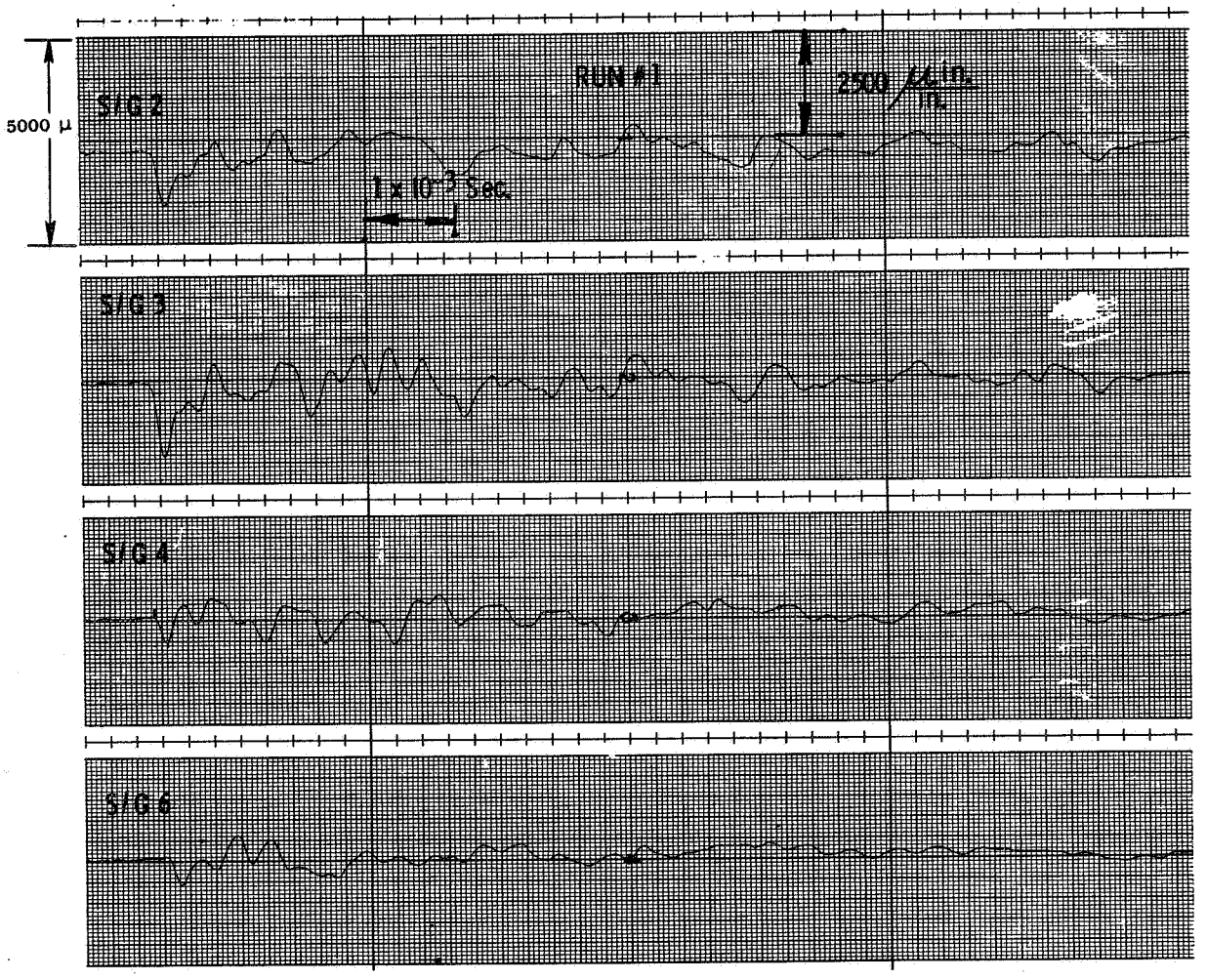

Run No. 1 (Concluded)

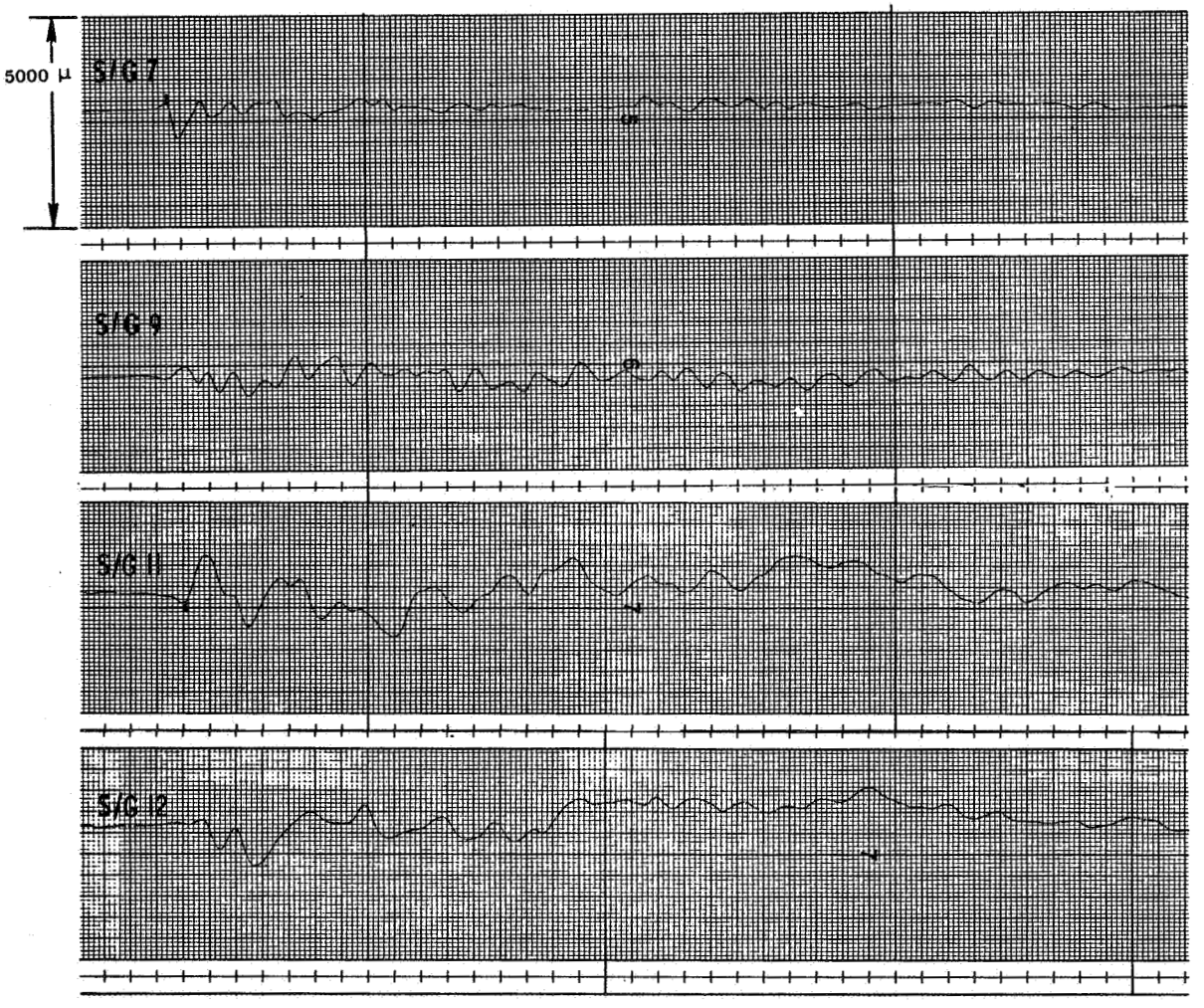

Run No. 2

17 gm Slice
75% Span
3808 rpm
23° Incidence Angle

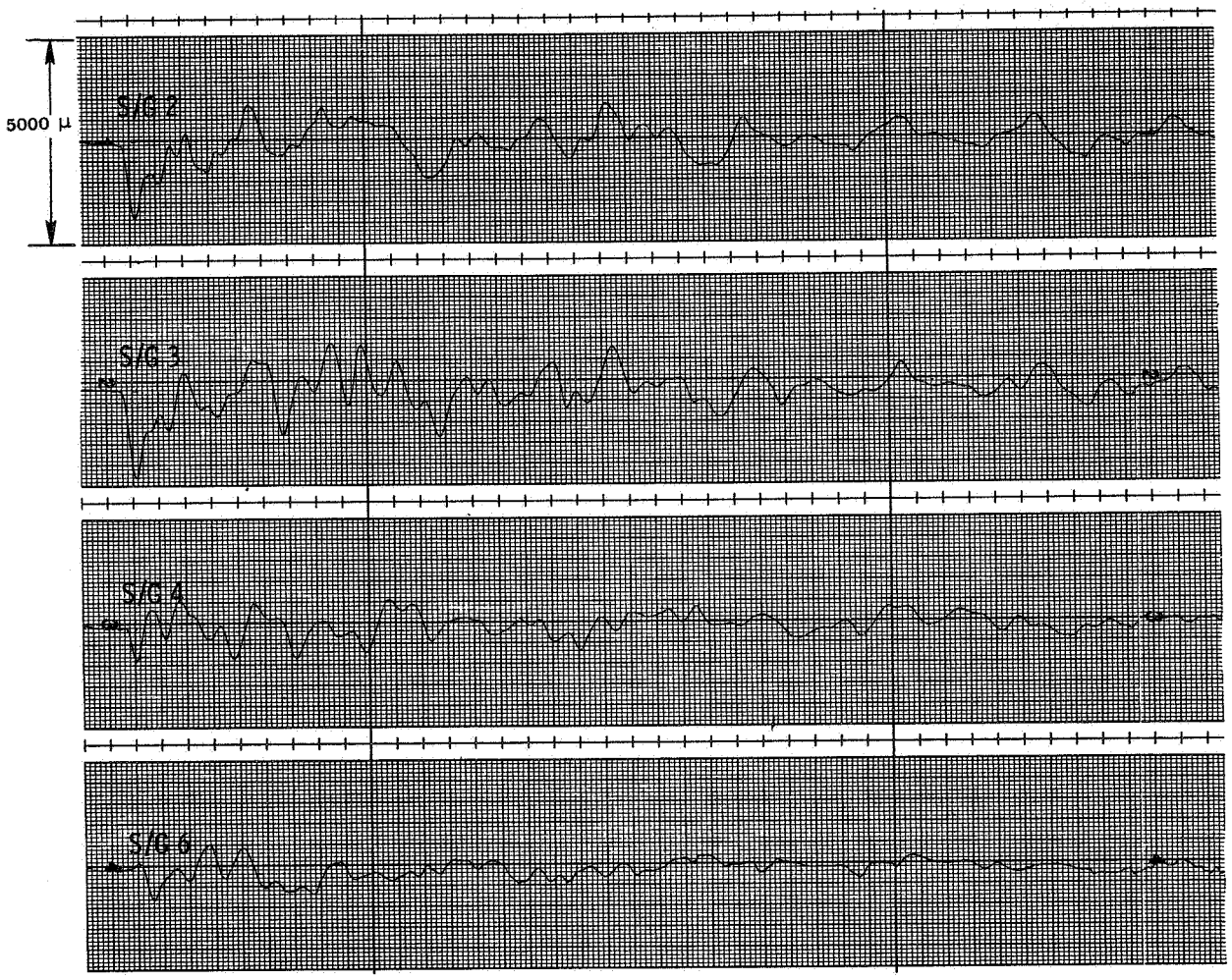

Run No. 2 (Concluded)

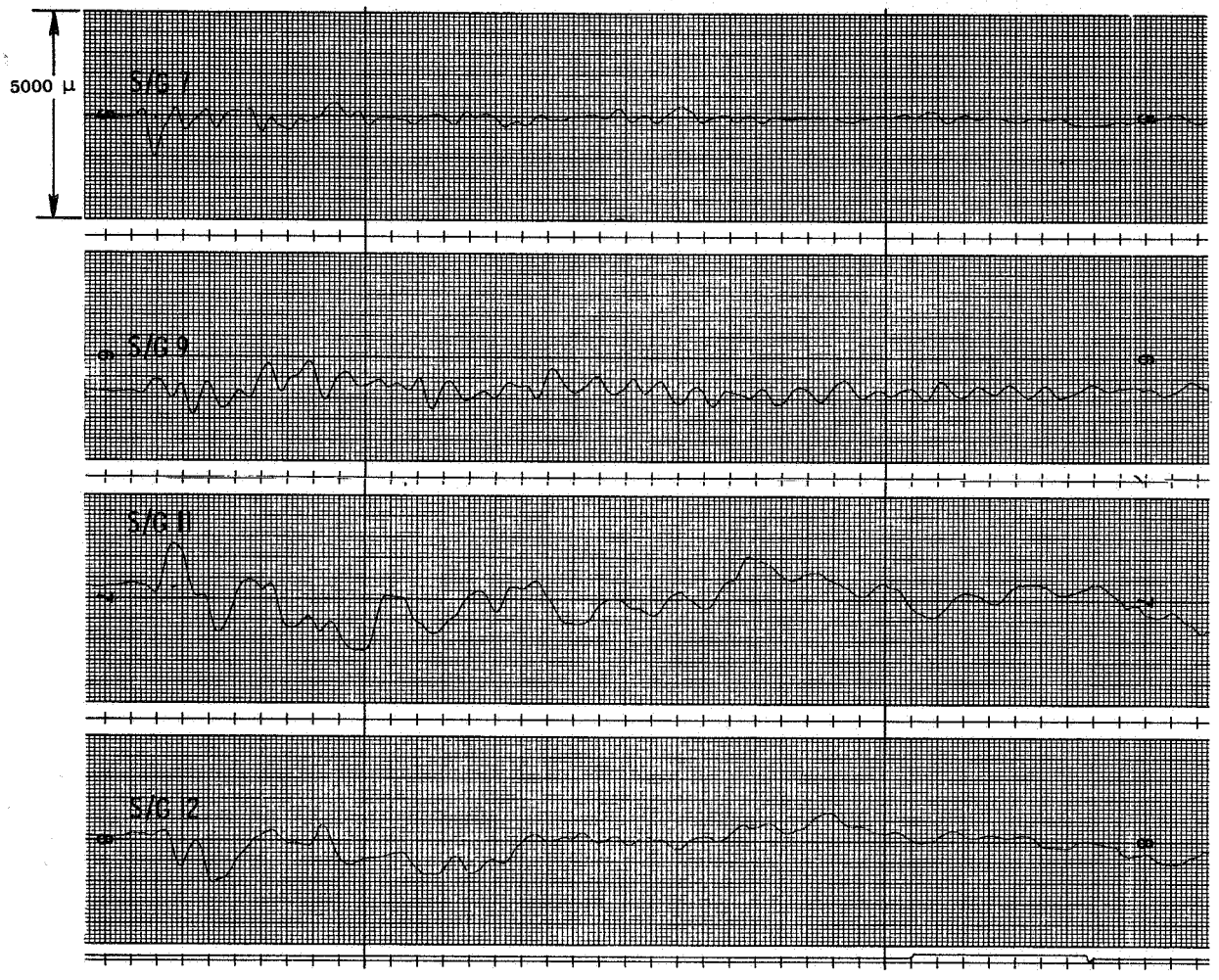

Run No. 3

24 gm Slice
75% Span
3195 rpm
23° Incidence Angle

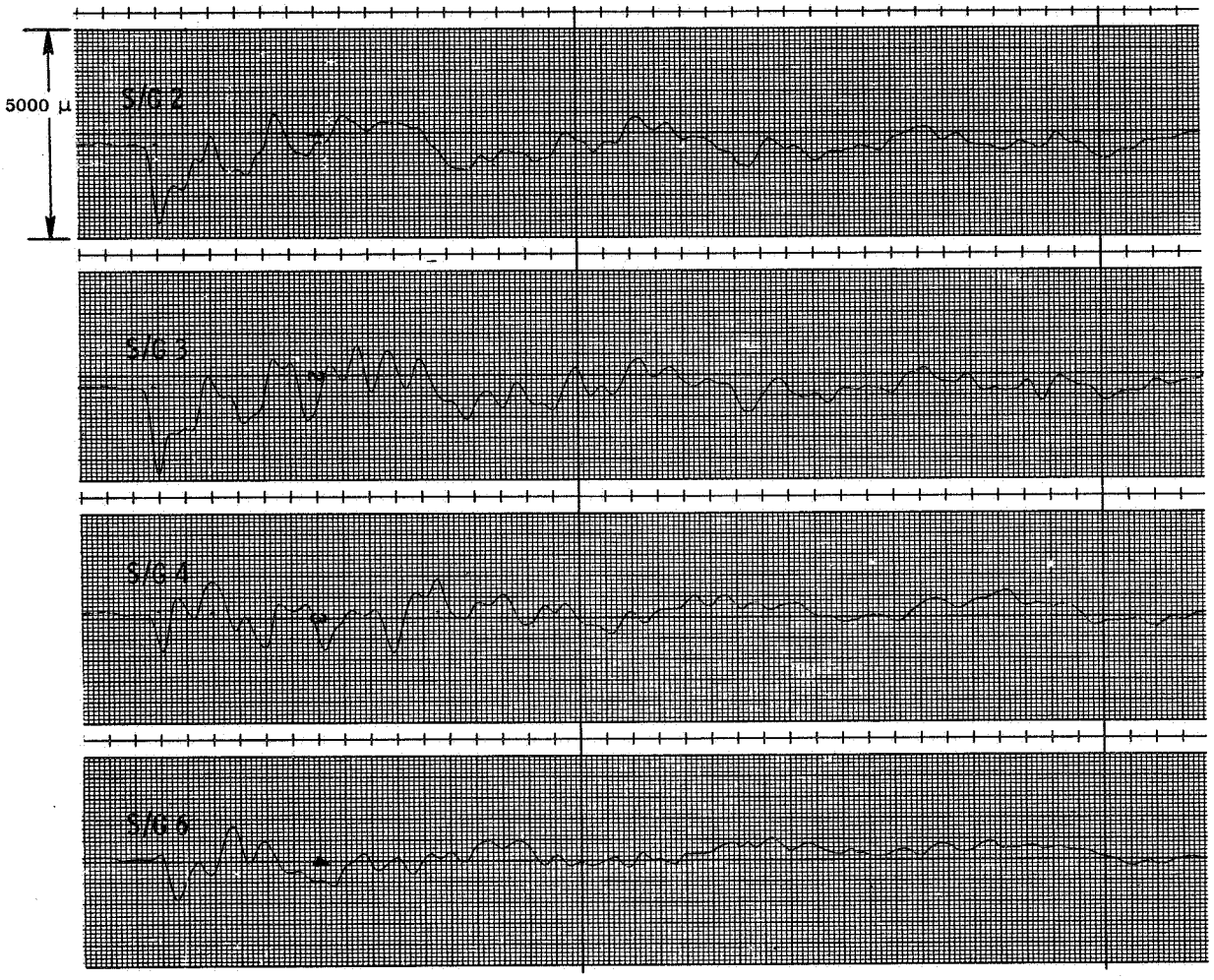

Run No. 3 (Concluded)

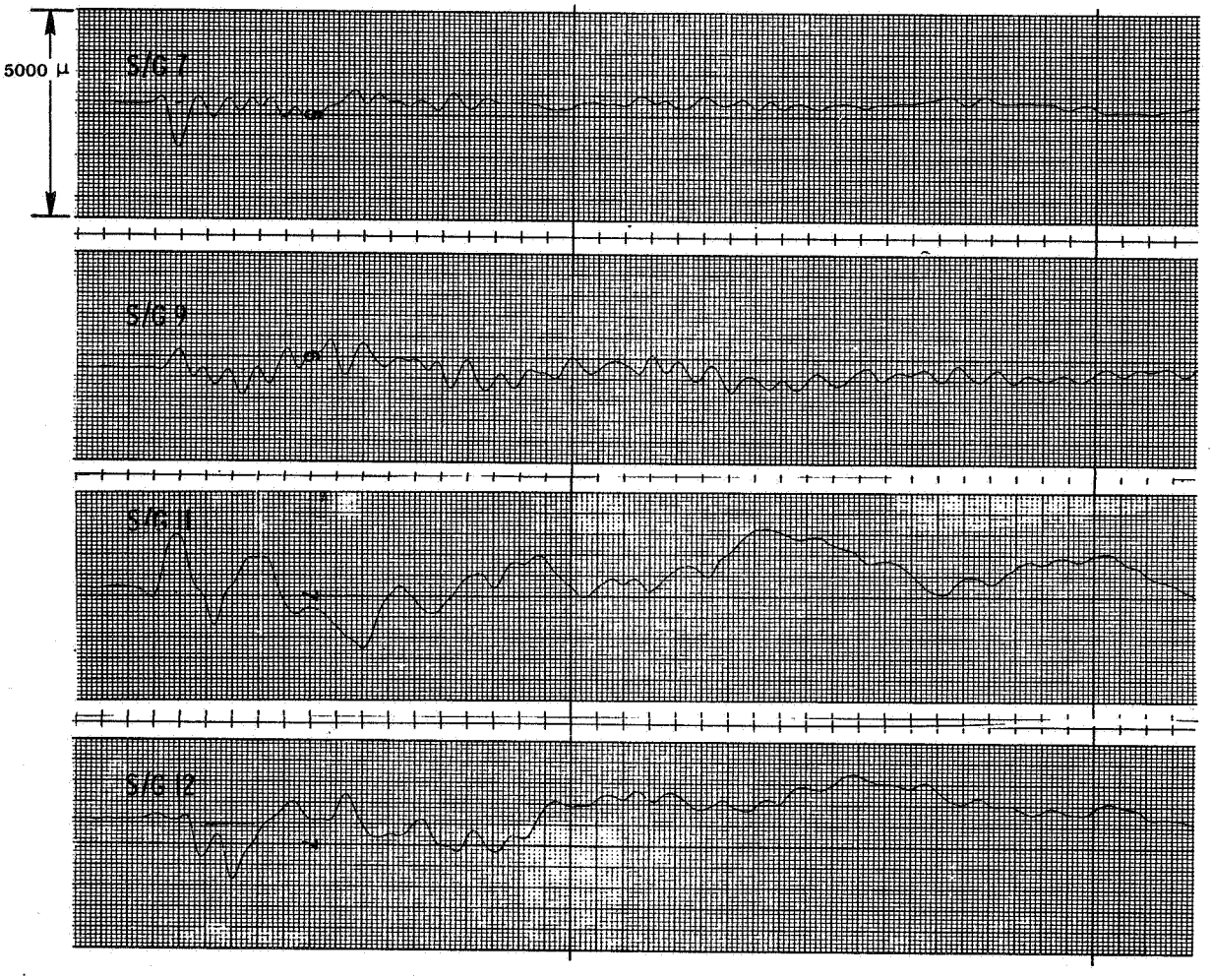

Run No. 4

19 gm Slice
75% Span
2260 rpm
23° Incidence Angle

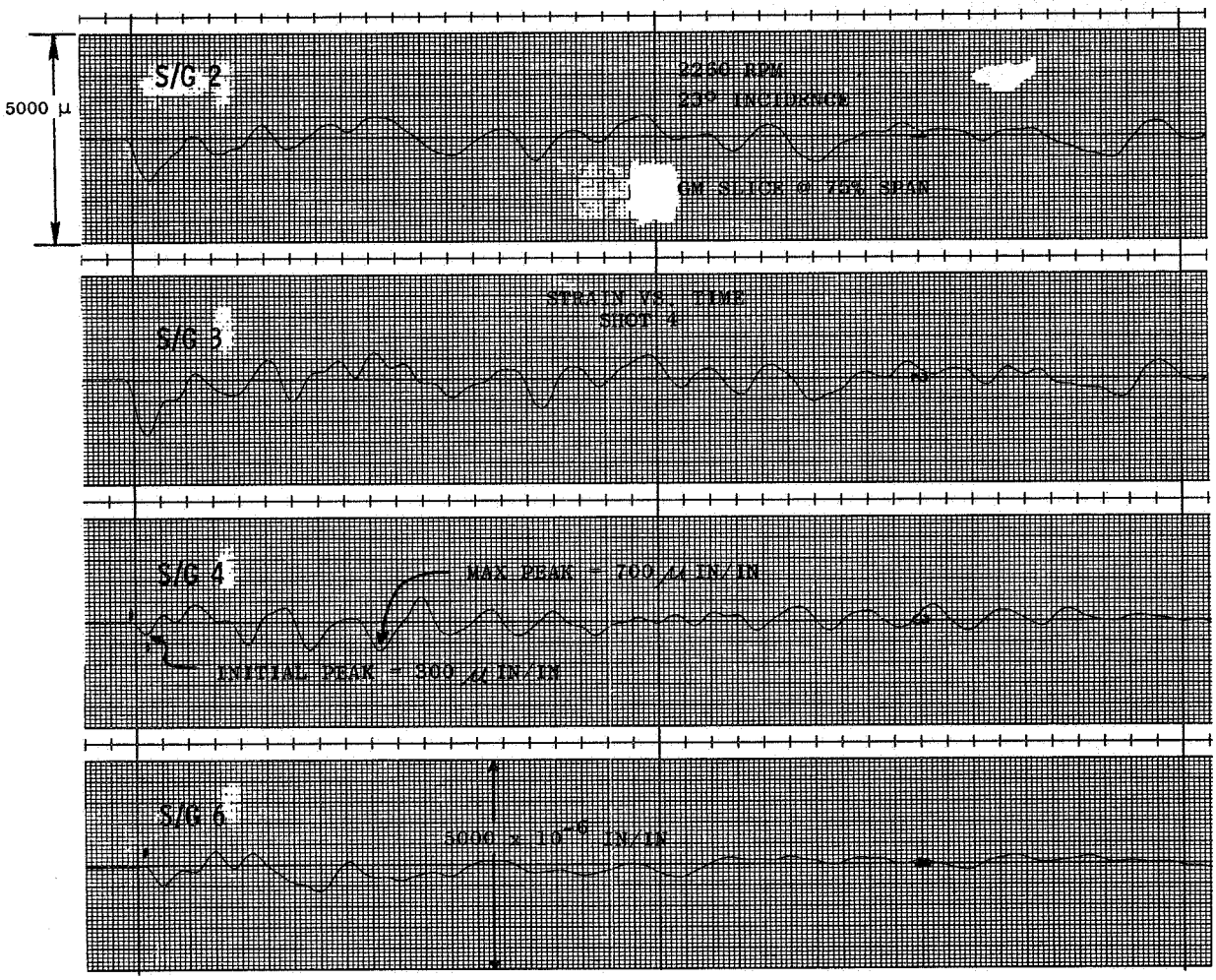

Run No. 4 (Concluded)

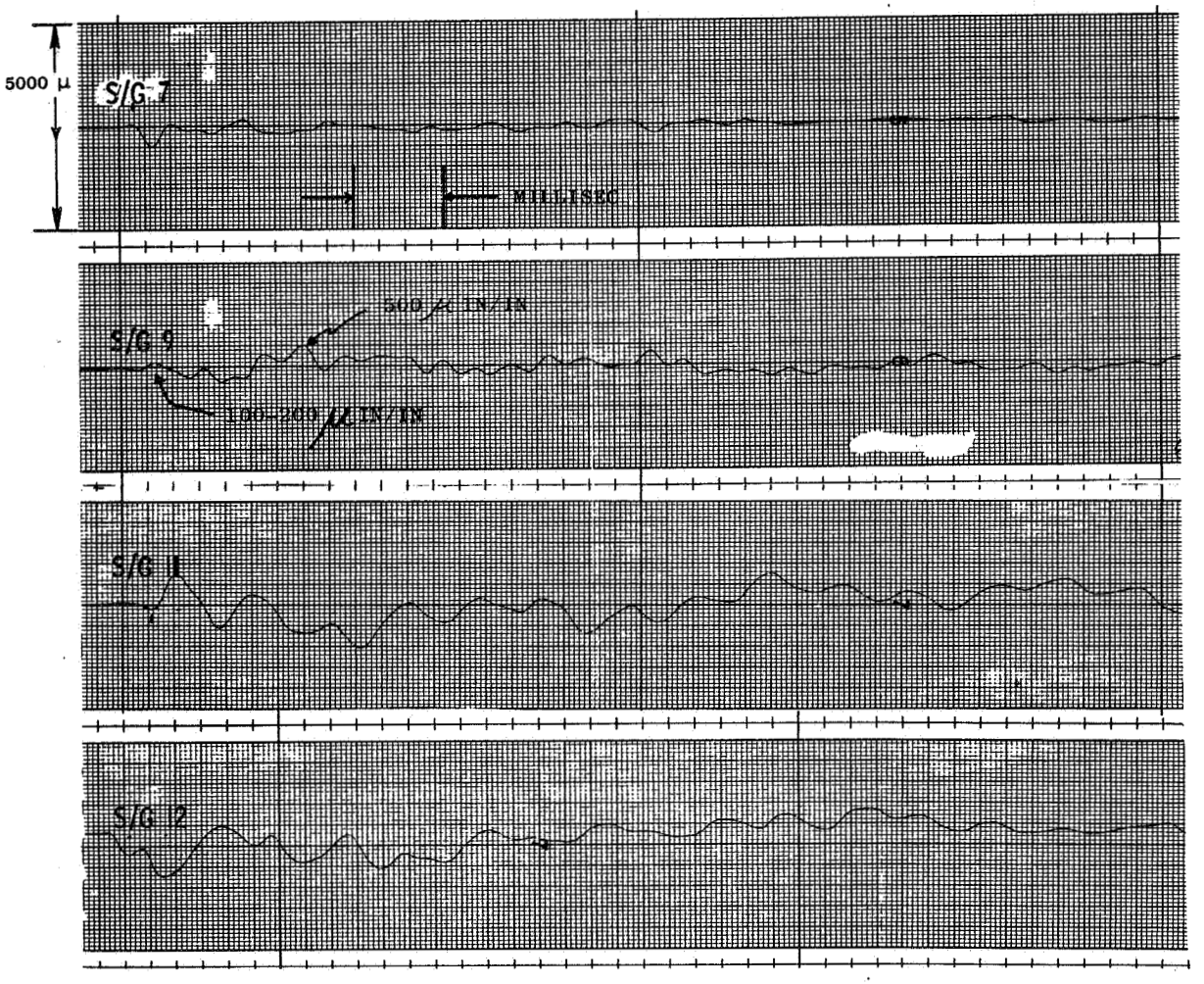

Run No. 5

18 gm Slice
37% Span
3202 rpm
40° Incidence Angle

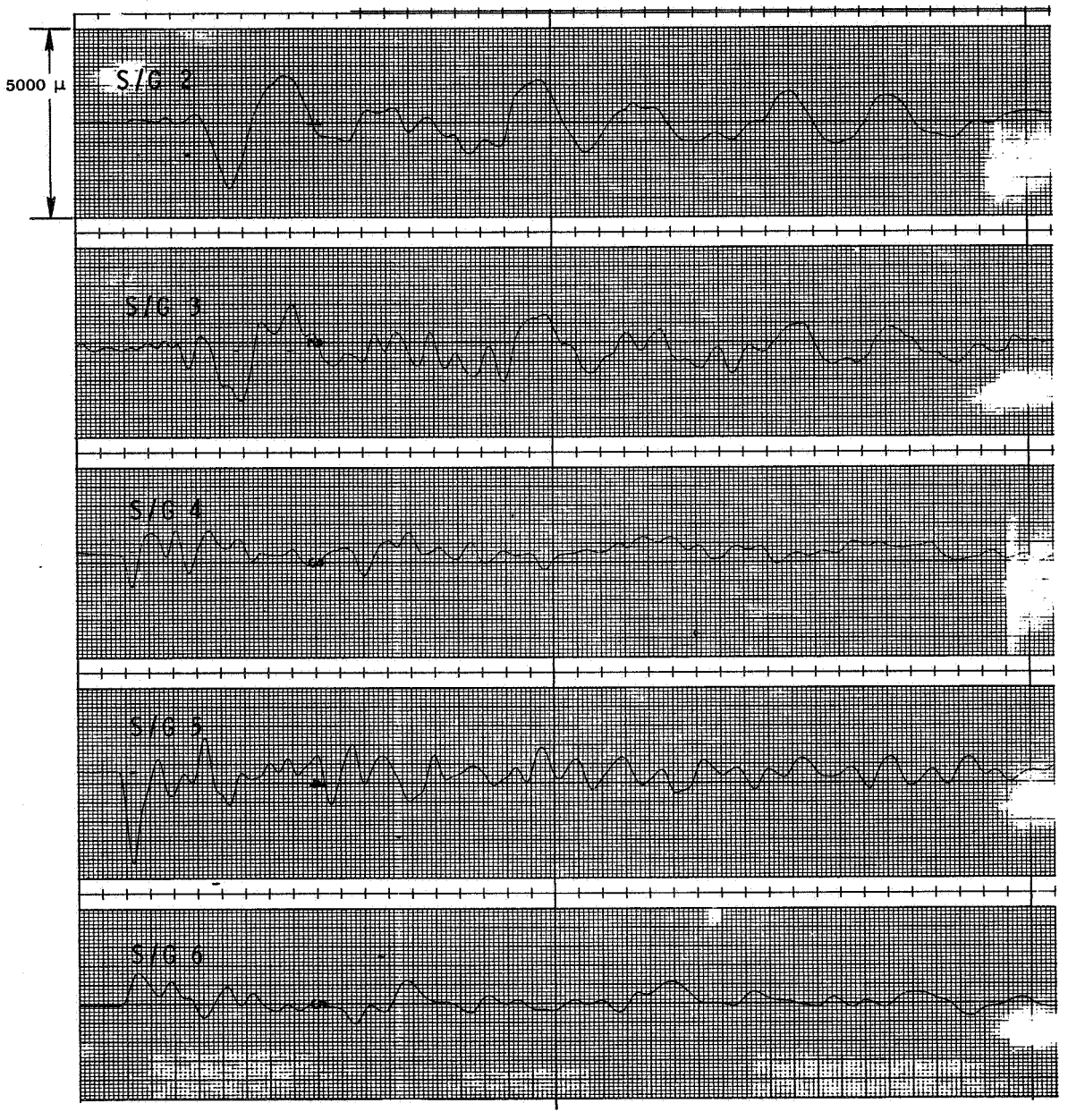

Run No. 5 (Concluded)

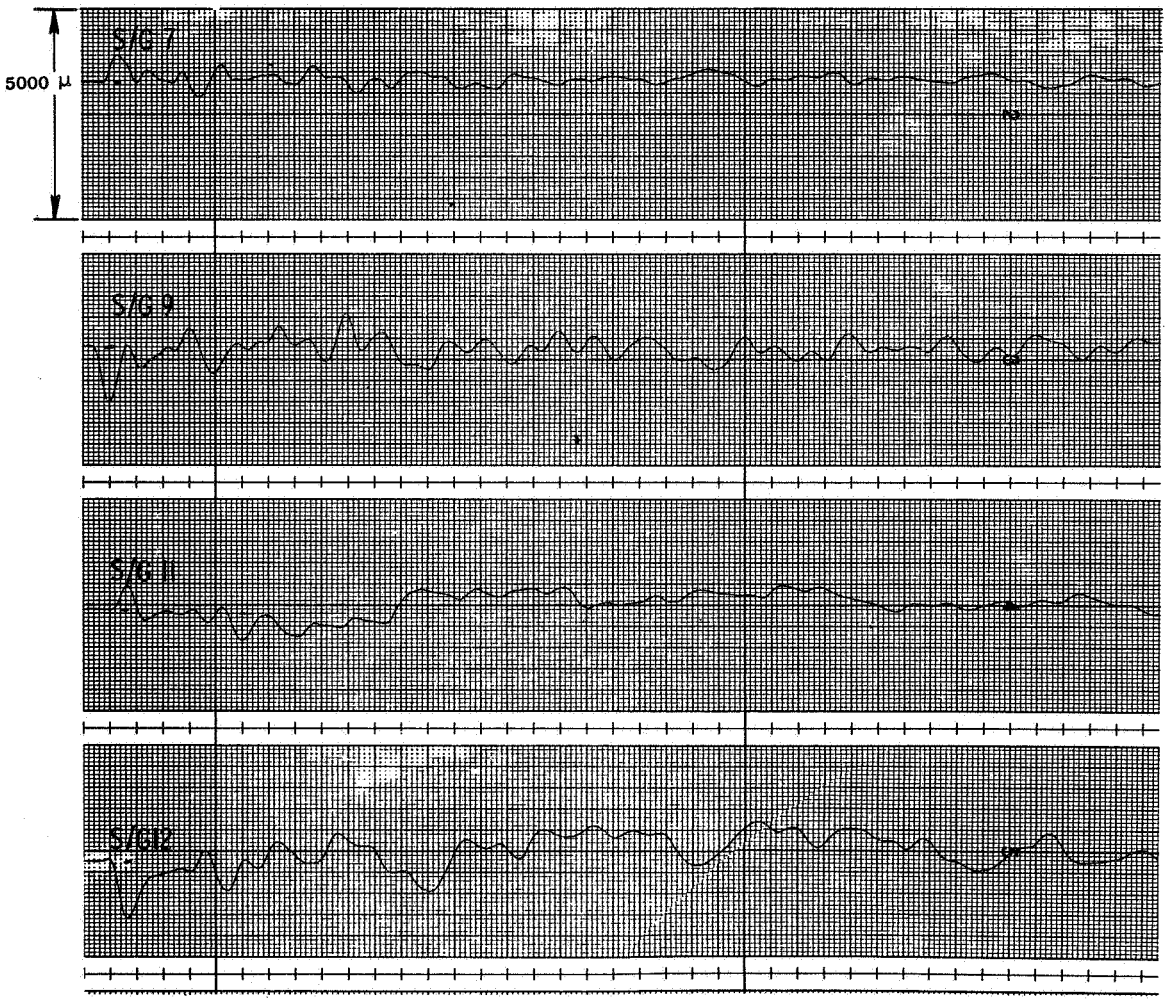

Run No. 6

11 gm Slice
37% Span
3797 rpm
40° Incidence Angle

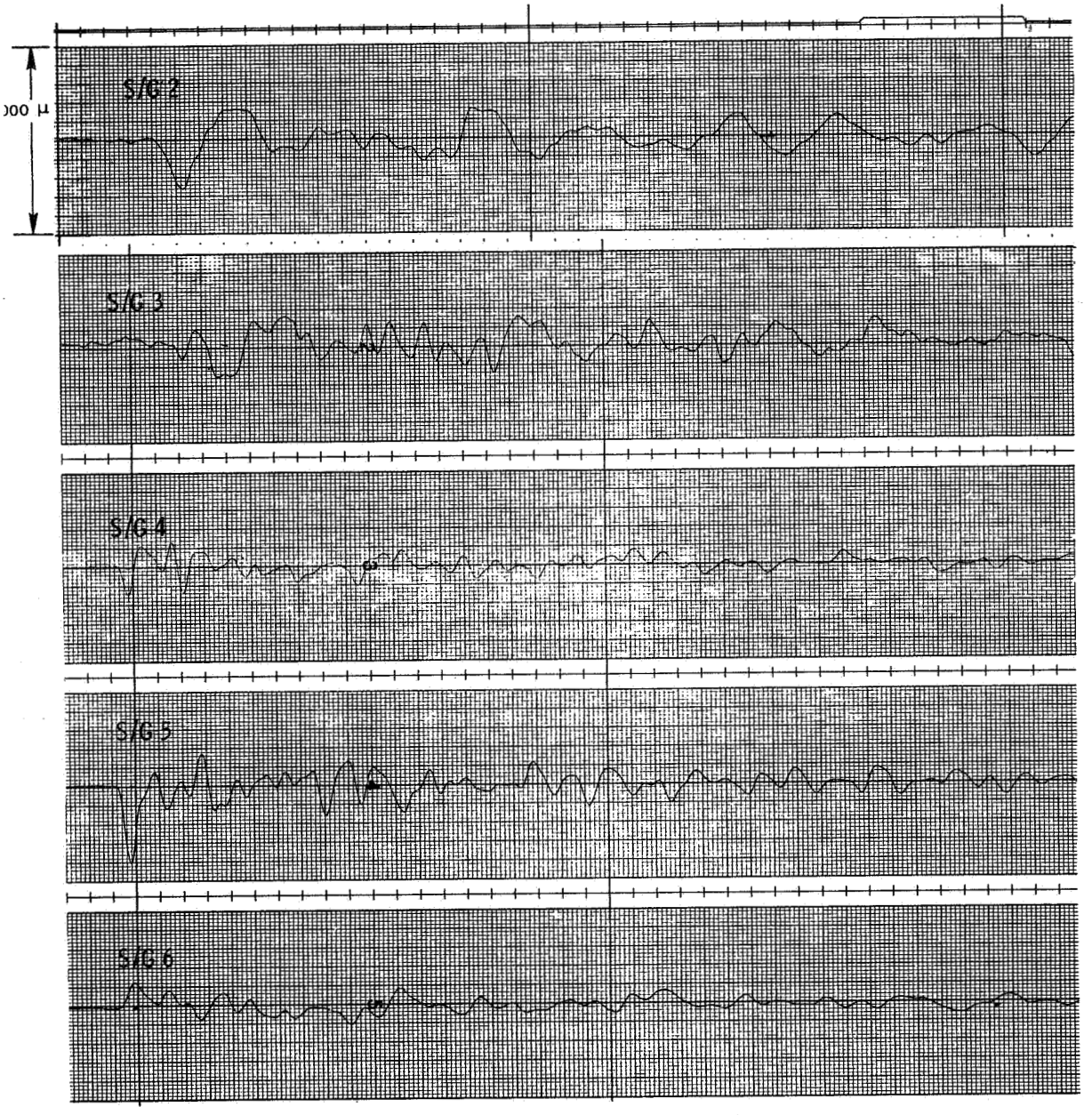

Run No. 6 (Concluded)

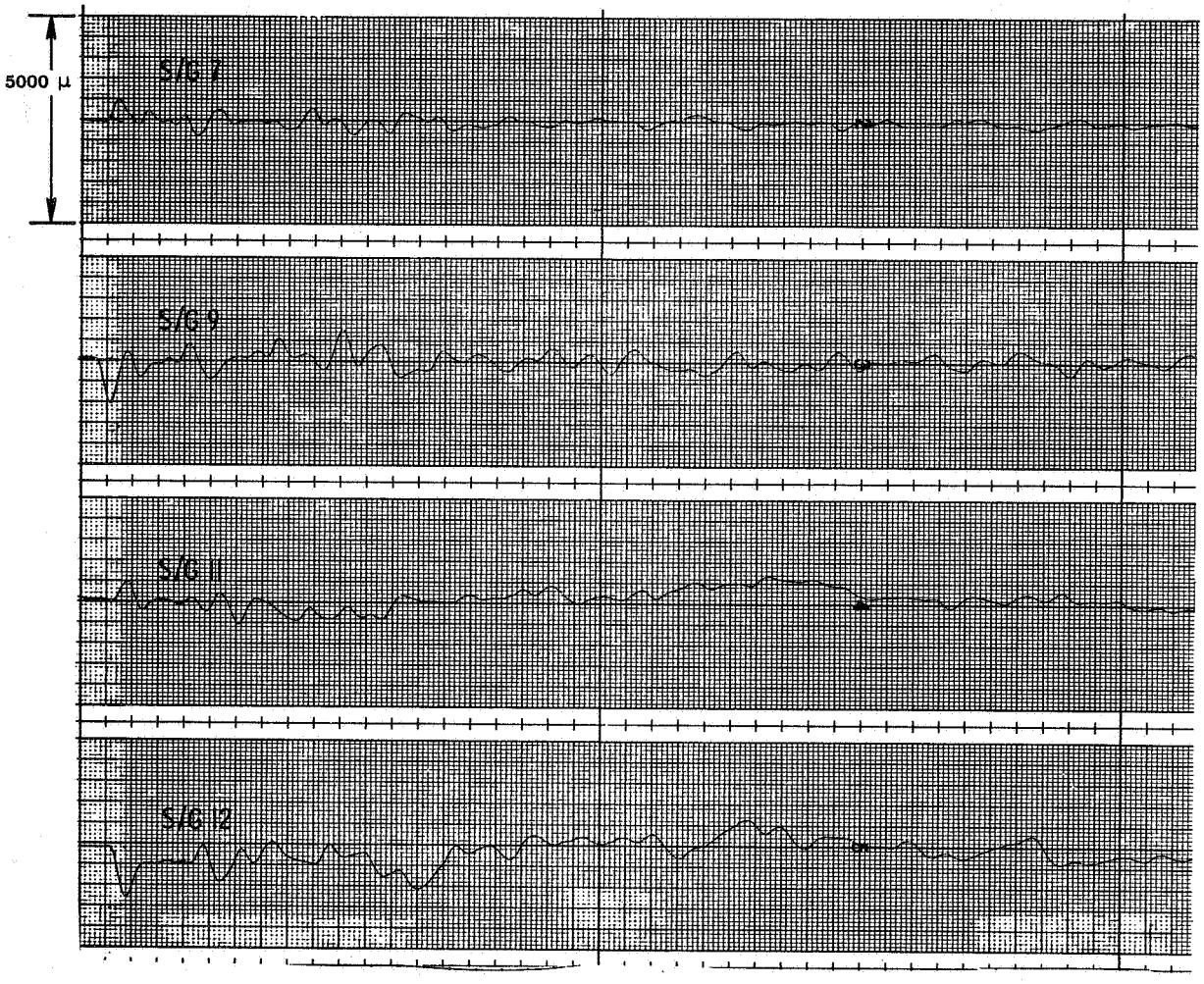

Run No. 7

21 gm Slice
37% Span
3196 rpm
40° Incidence Angle

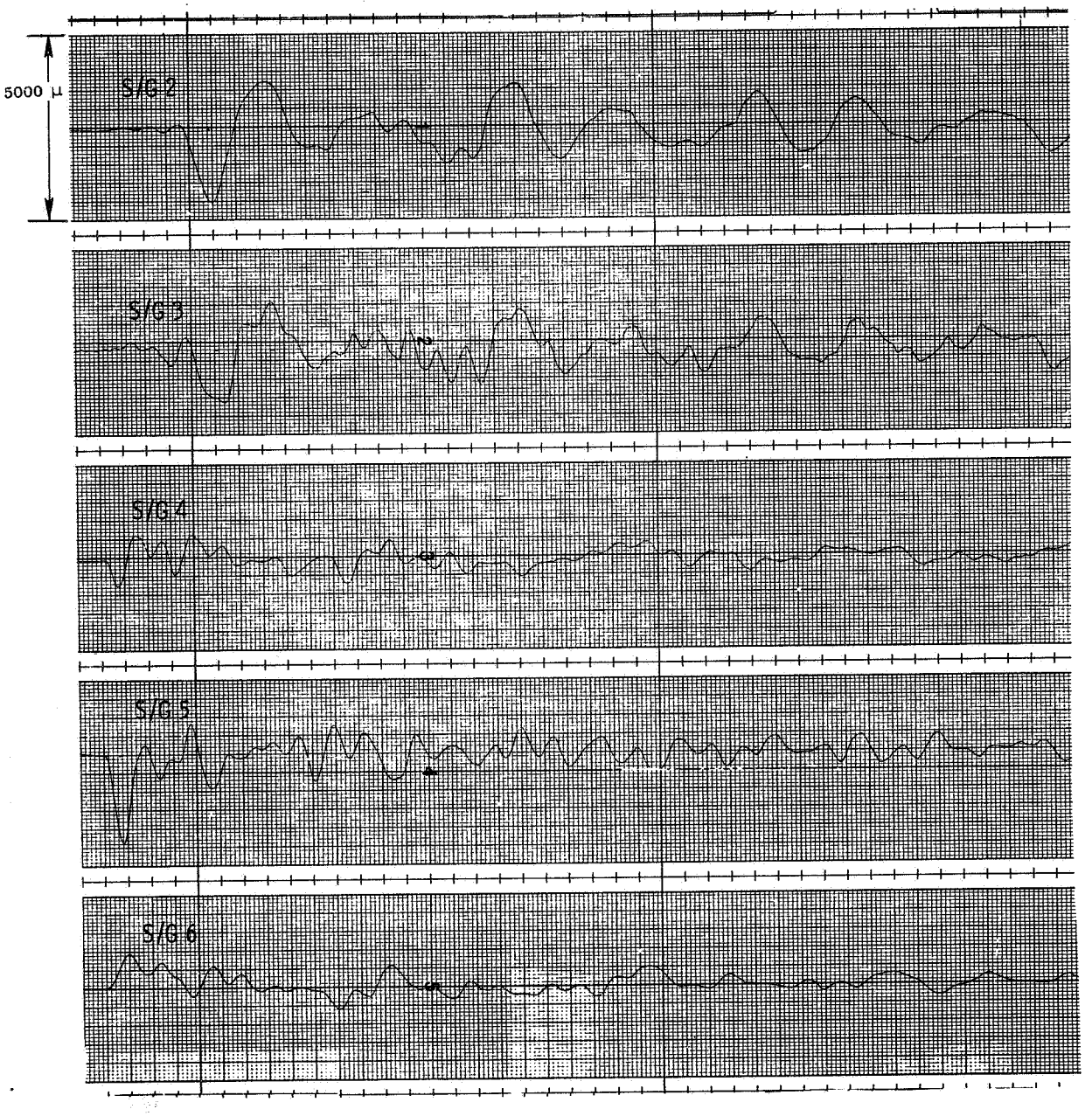

Run No. 7 (Concluded)

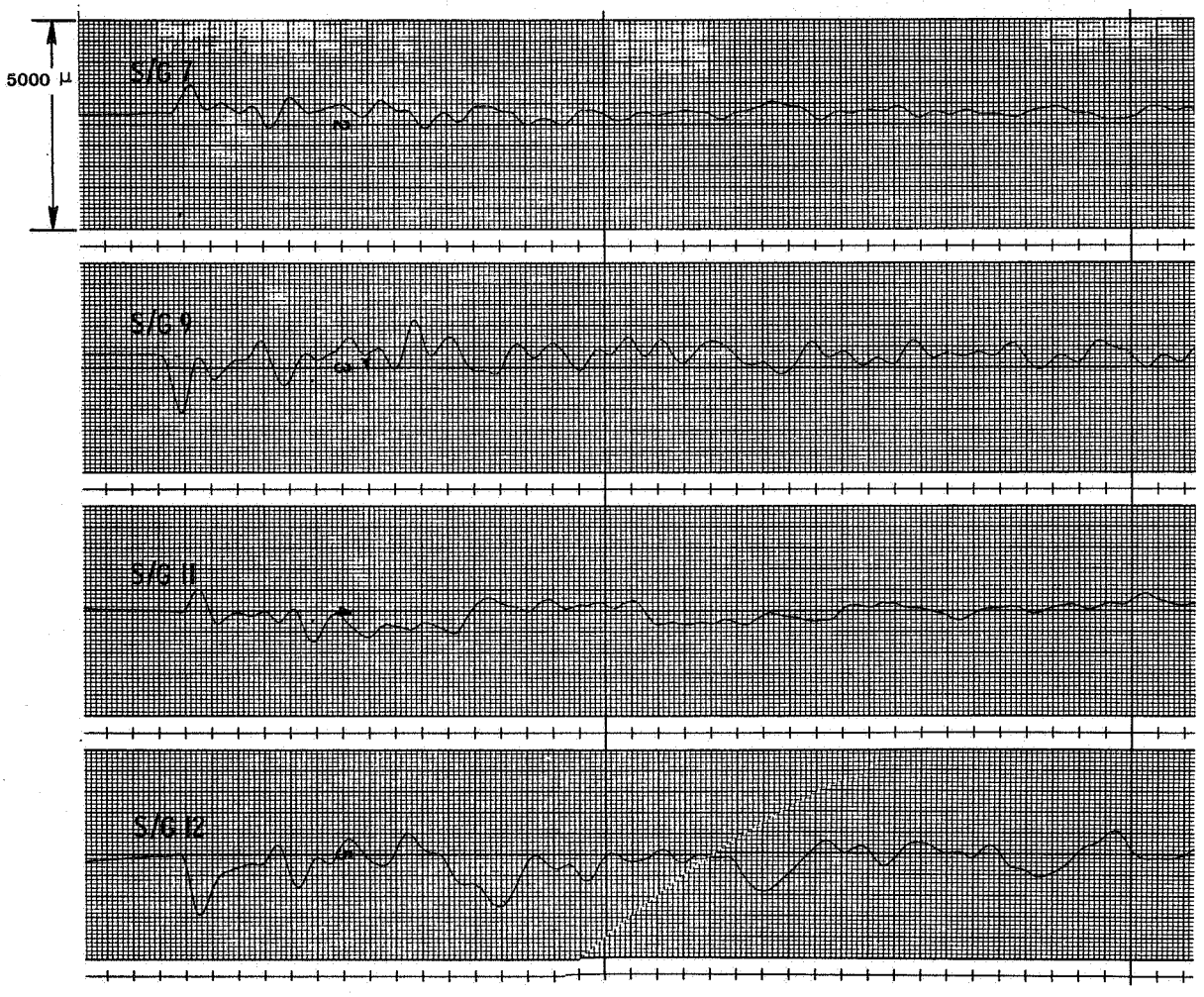

Run No. 8

14 gm Slice
75% Span
3200 rpm
33° Incidence Angle

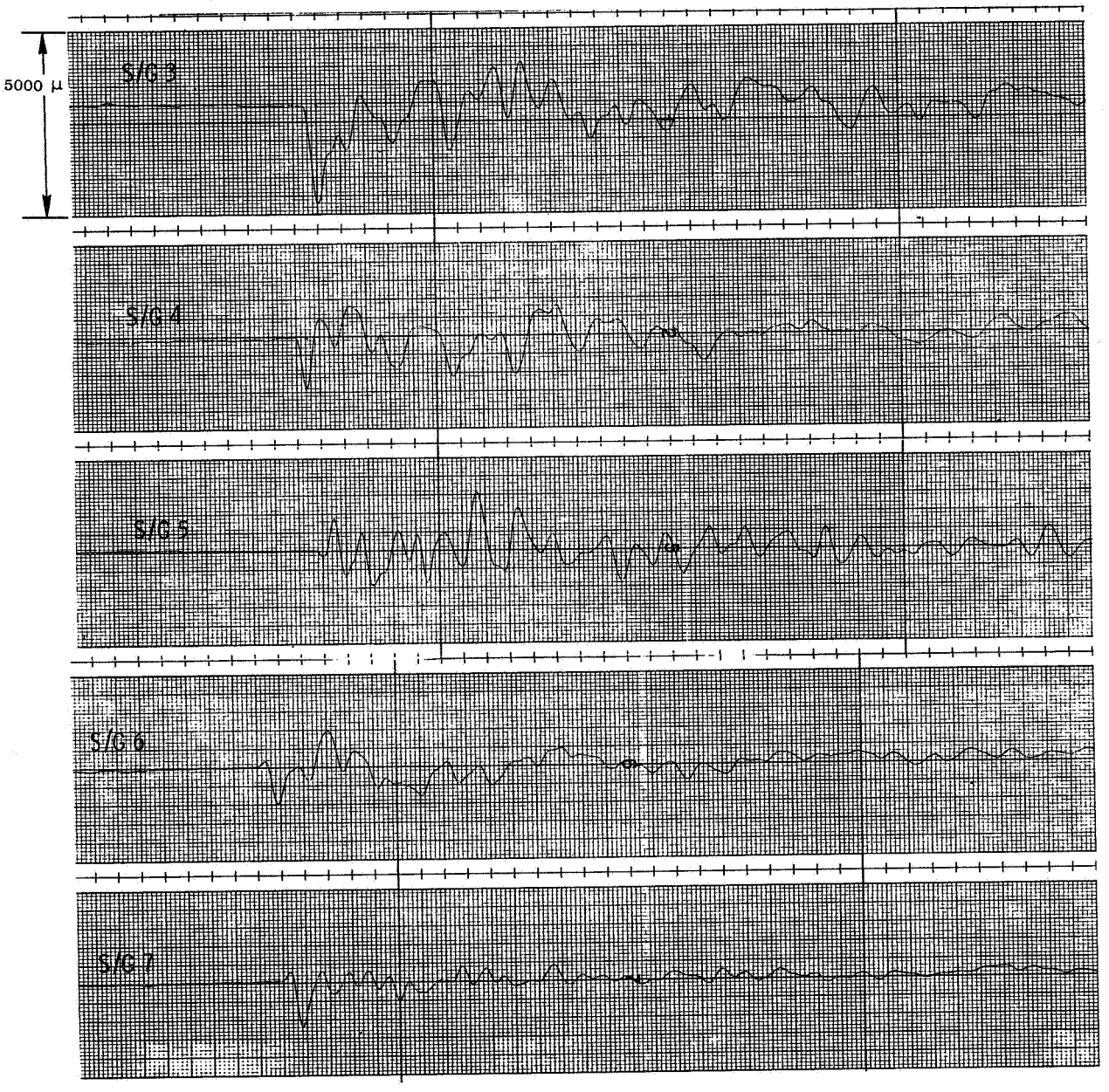

Run No. 8 (Concluded)

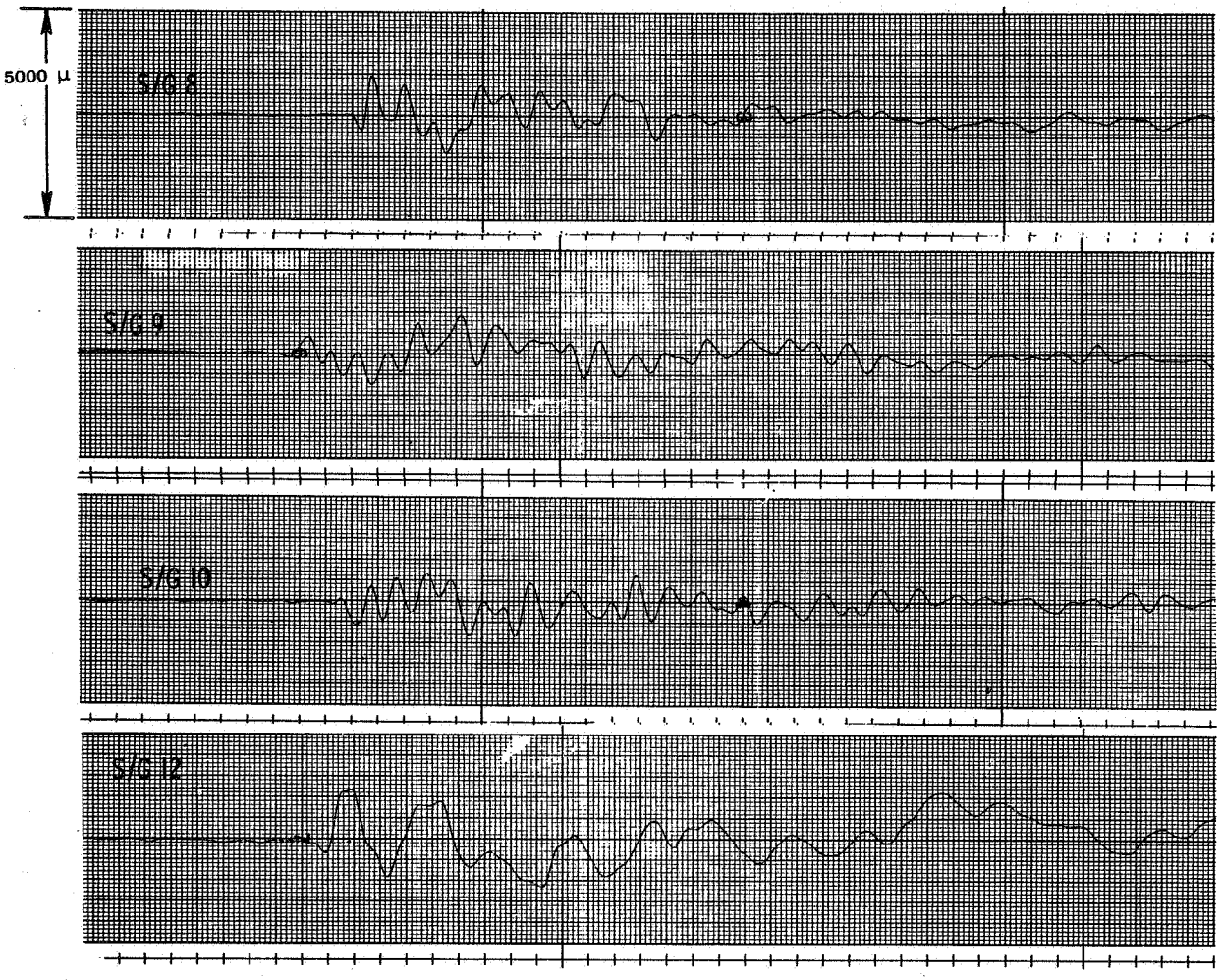

Run No. 9

12 gm Slice
75% Span
3804 rpm
33° Incidence Angle

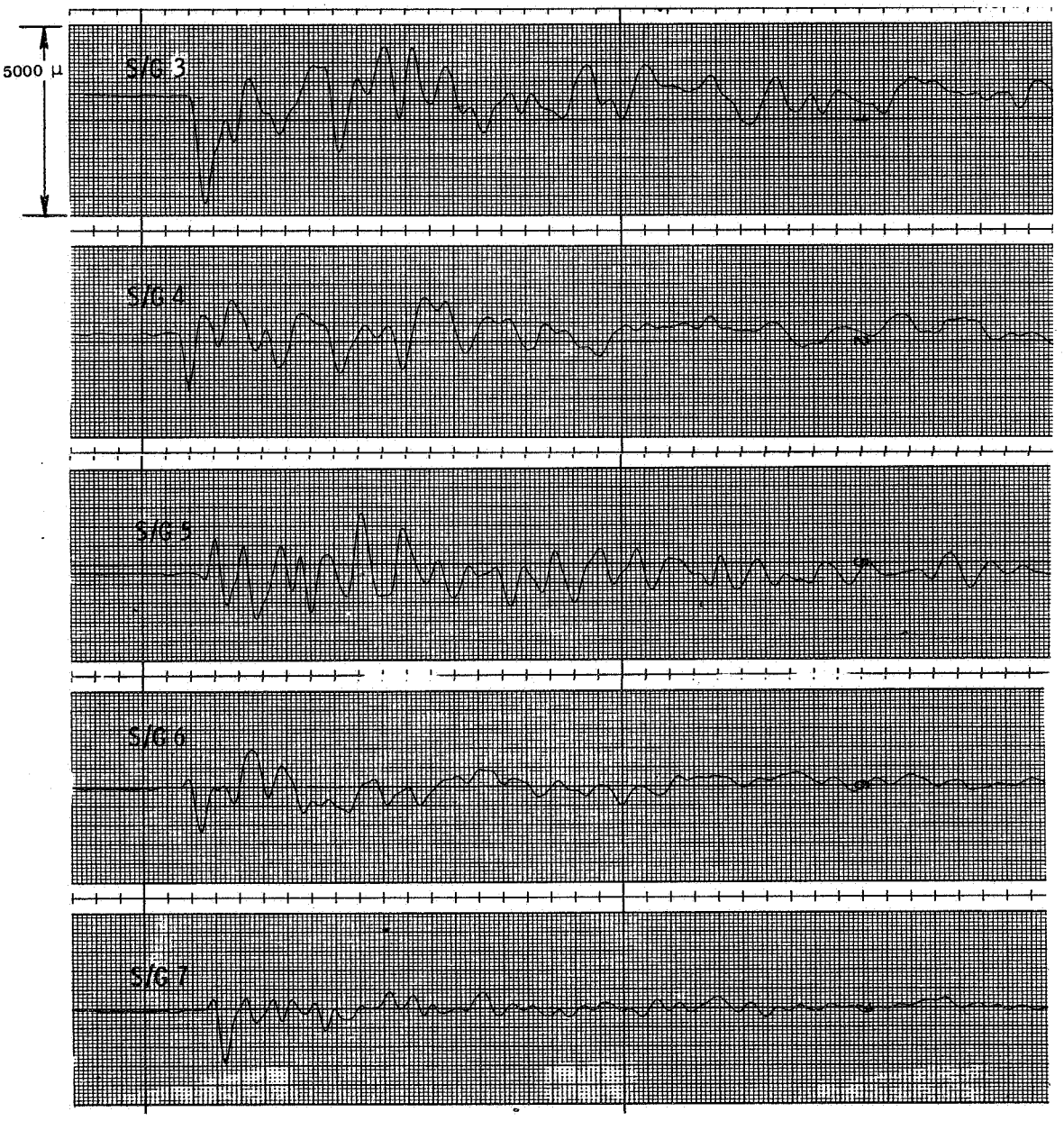

Run No. 9 (Concluded)

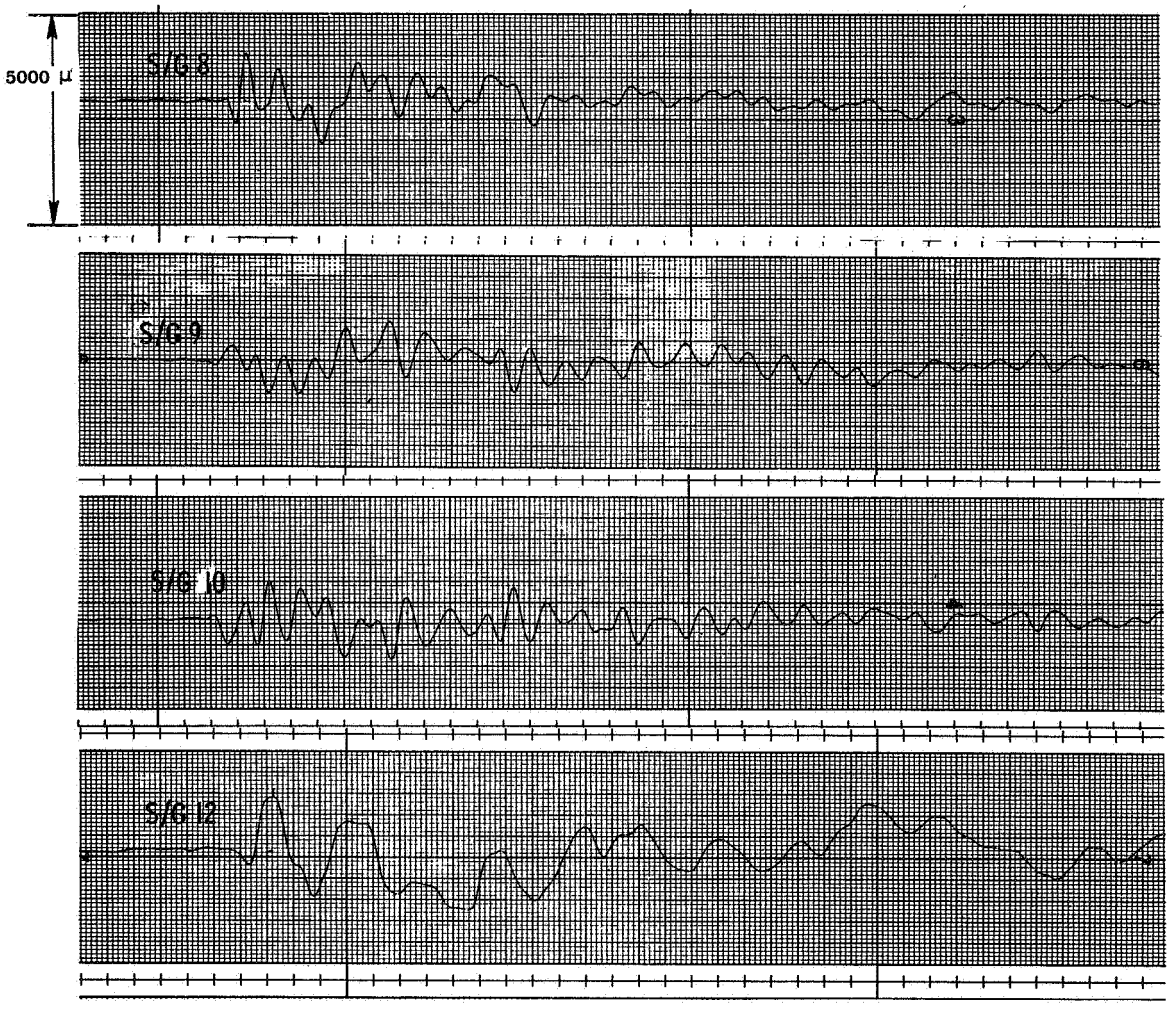

The following six figures present the analytical results obtained as strain versus time for Runs 1, 5 and 8, as discussed in Section 3.4. These curves are to the same scale as the test data curves found elsewhere in the Appendix.

- Run No. 1
- 16 g Slice
- 75% Span
- 3200 rpm
- 23° Incidence Angle

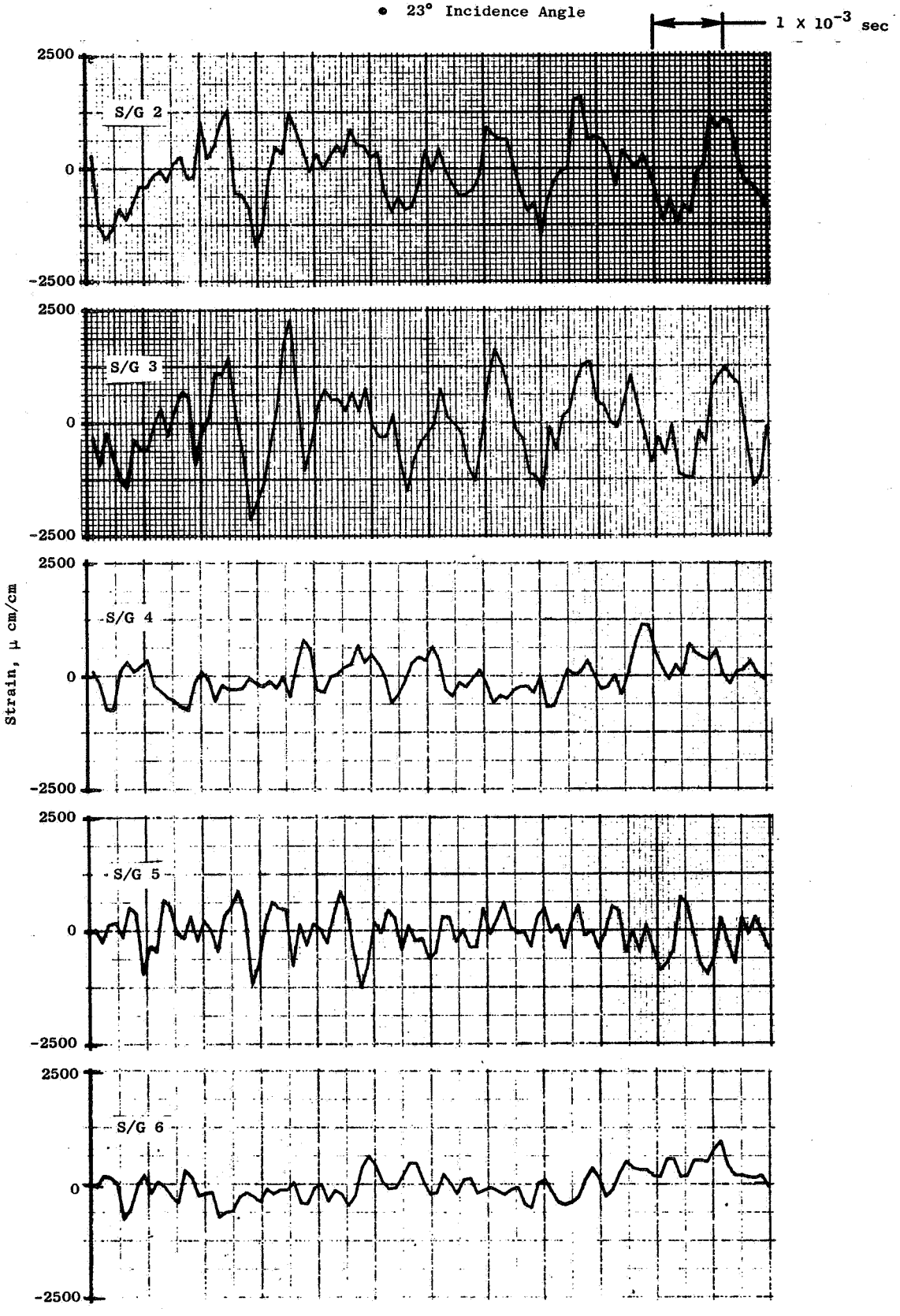

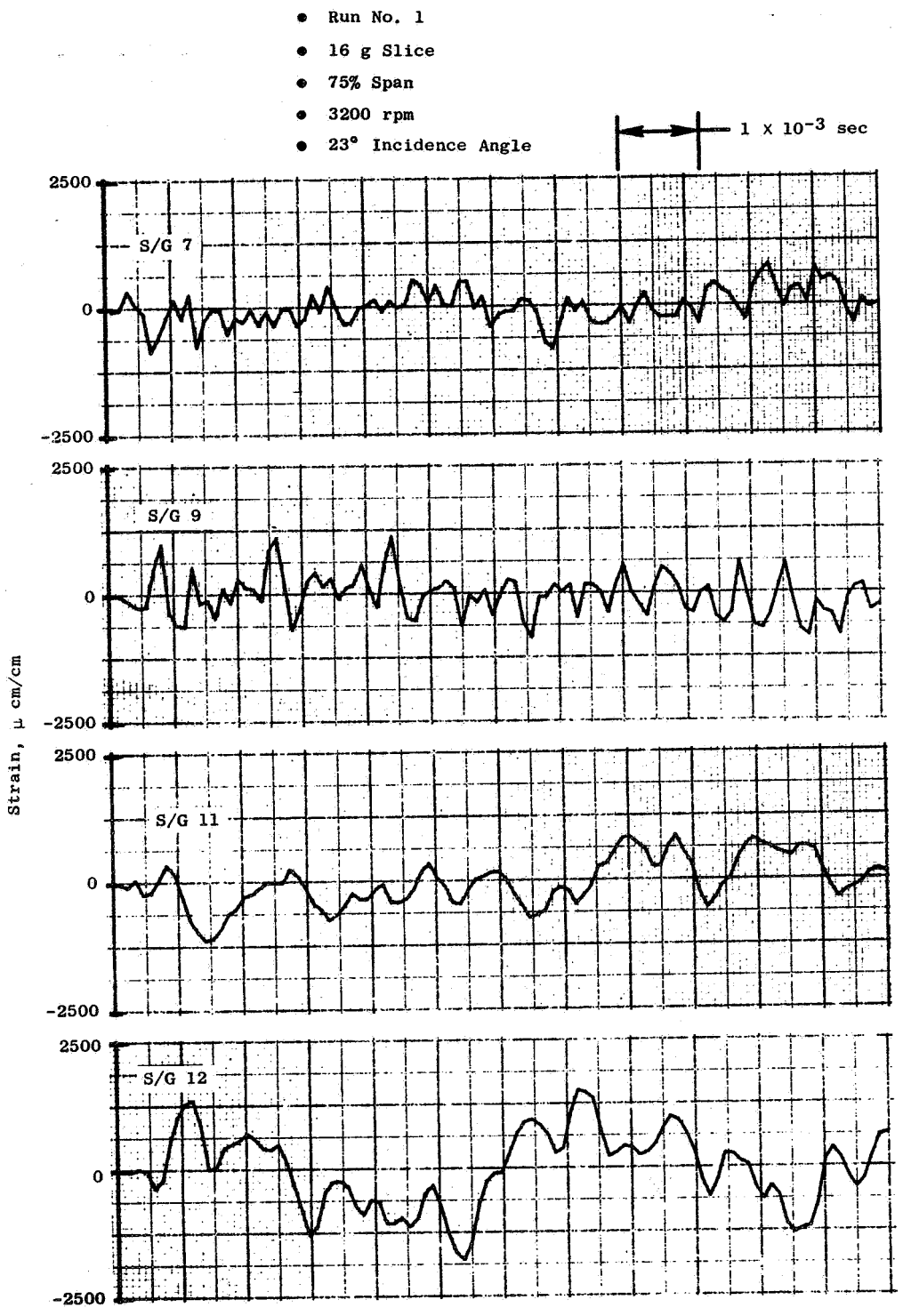
Run No. 1
16 g Slice
75% Span
3200 rpm
23° Incidence Angle
1 x 10-3 sec
S/G 7
S/G 9
S/G 11
S/G 12
2500
0
-2500
Strain, μ cm/cm

- Run No. 5
- 18 g Slice
- 37% Span
- 3202 rpm
- 40° Incidence Angle

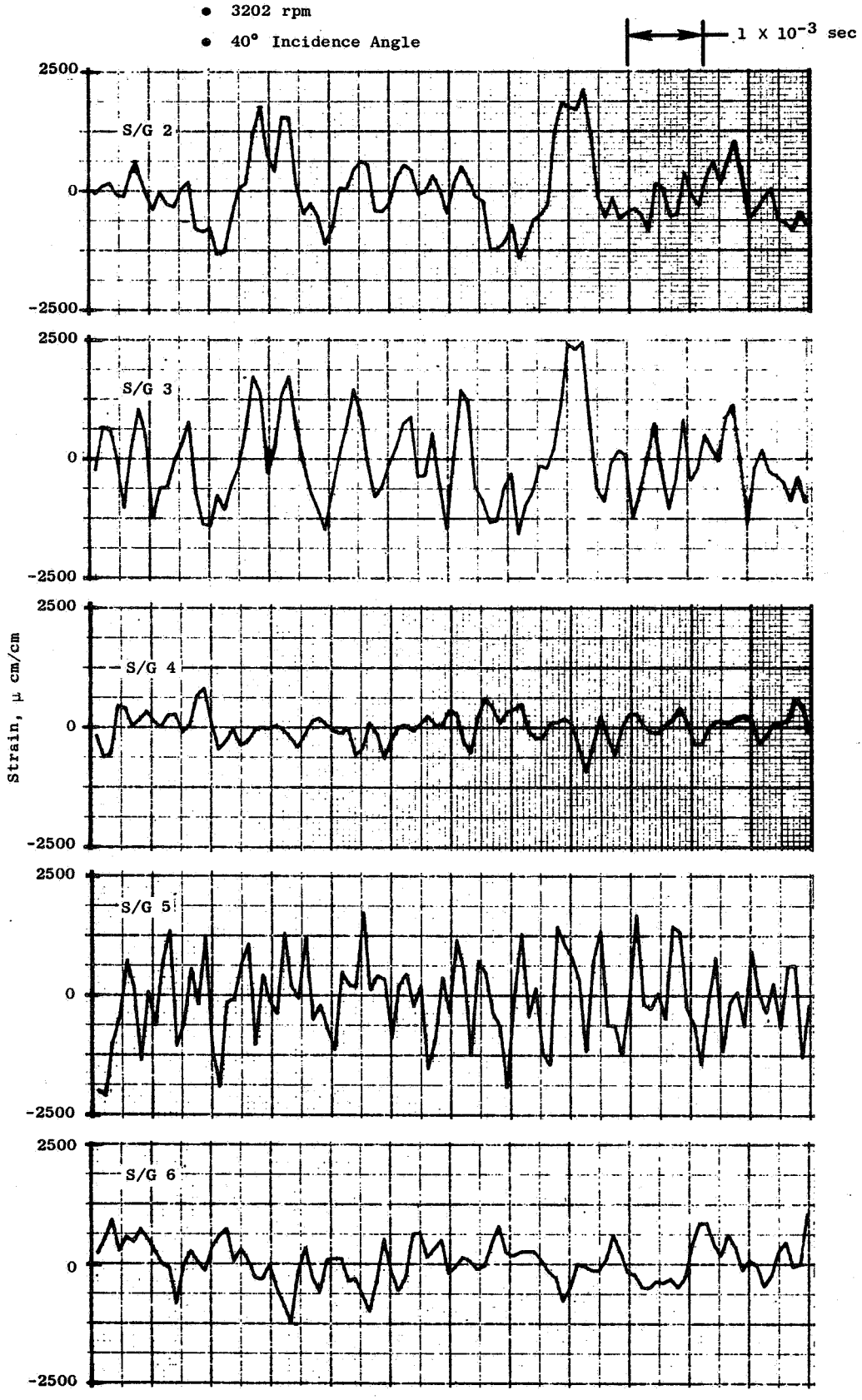

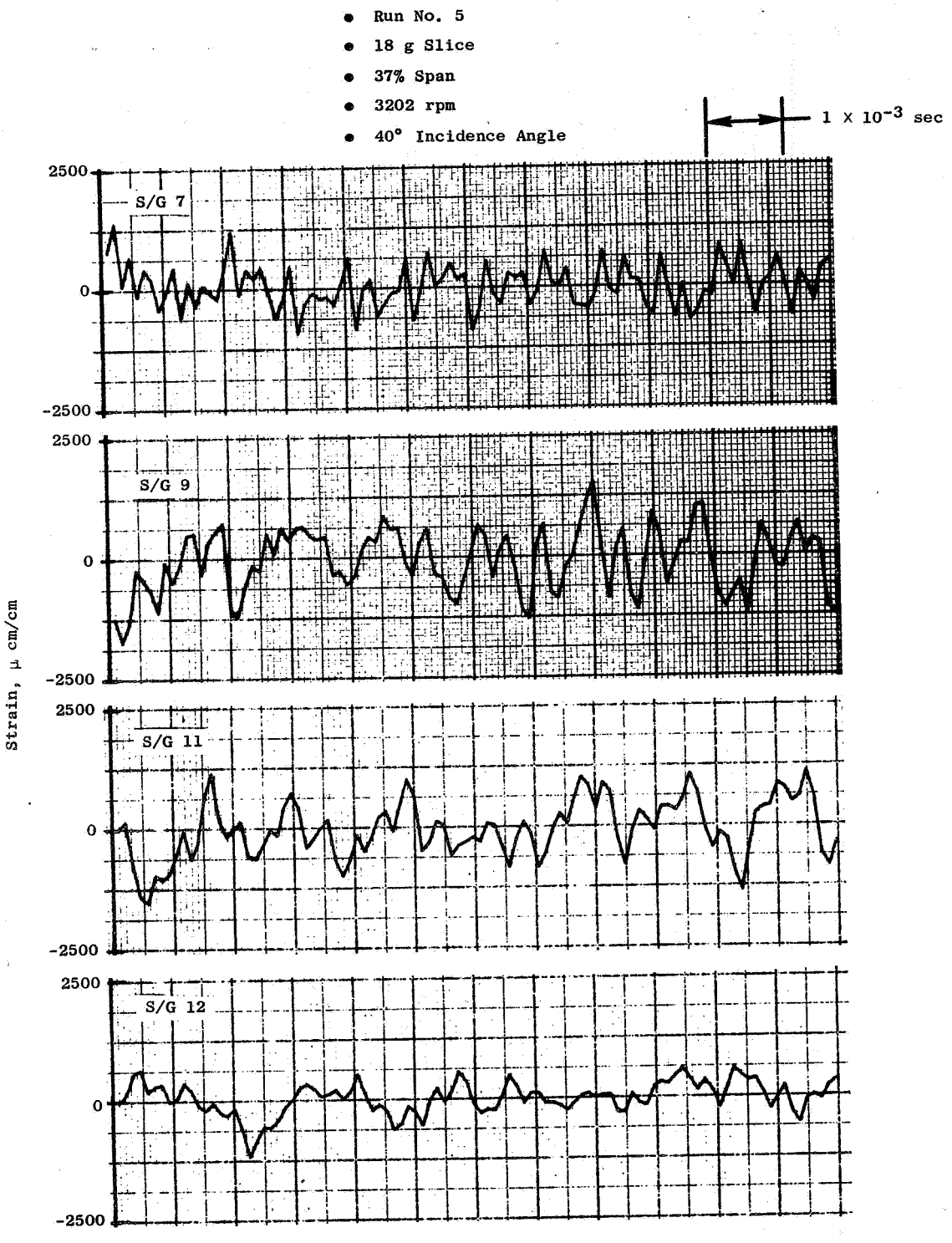
Run No. 5
18 g Slice
37% Span
3202 rpm
40° Incidence Angle
1 X 10-3 sec
Strain, μ cm/cm
S/G 7
S/G 9
S/G 11
S/G 12
2500
0
-2500

- Run No. 8
- 14 g Slice
- 75% Span
- 3200 rpm
- 33° Incidence Angle

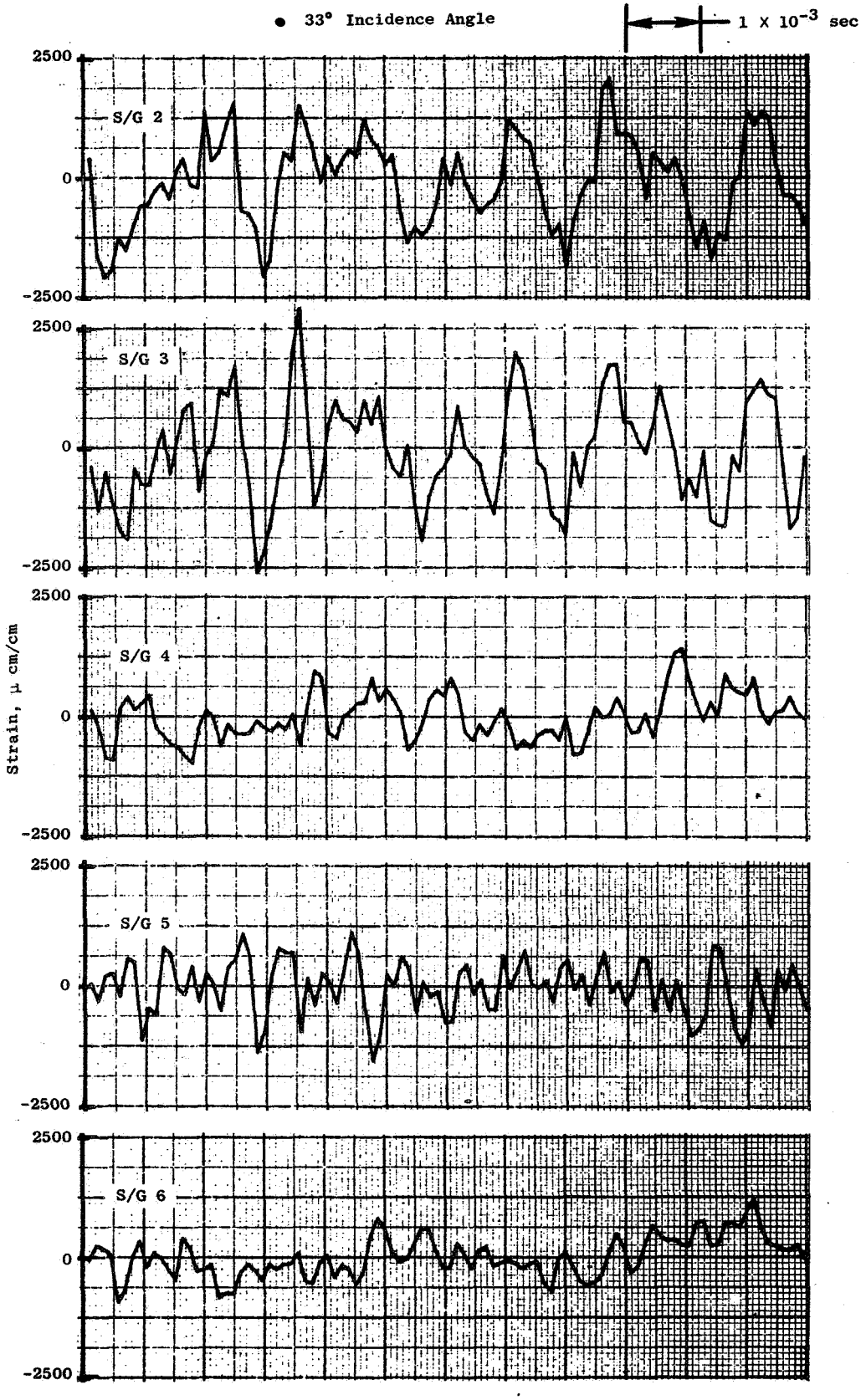

- Run No. 8
- 14 g Slice
- 75% Span
- 3200 rpm
- 33° Incidence Angle

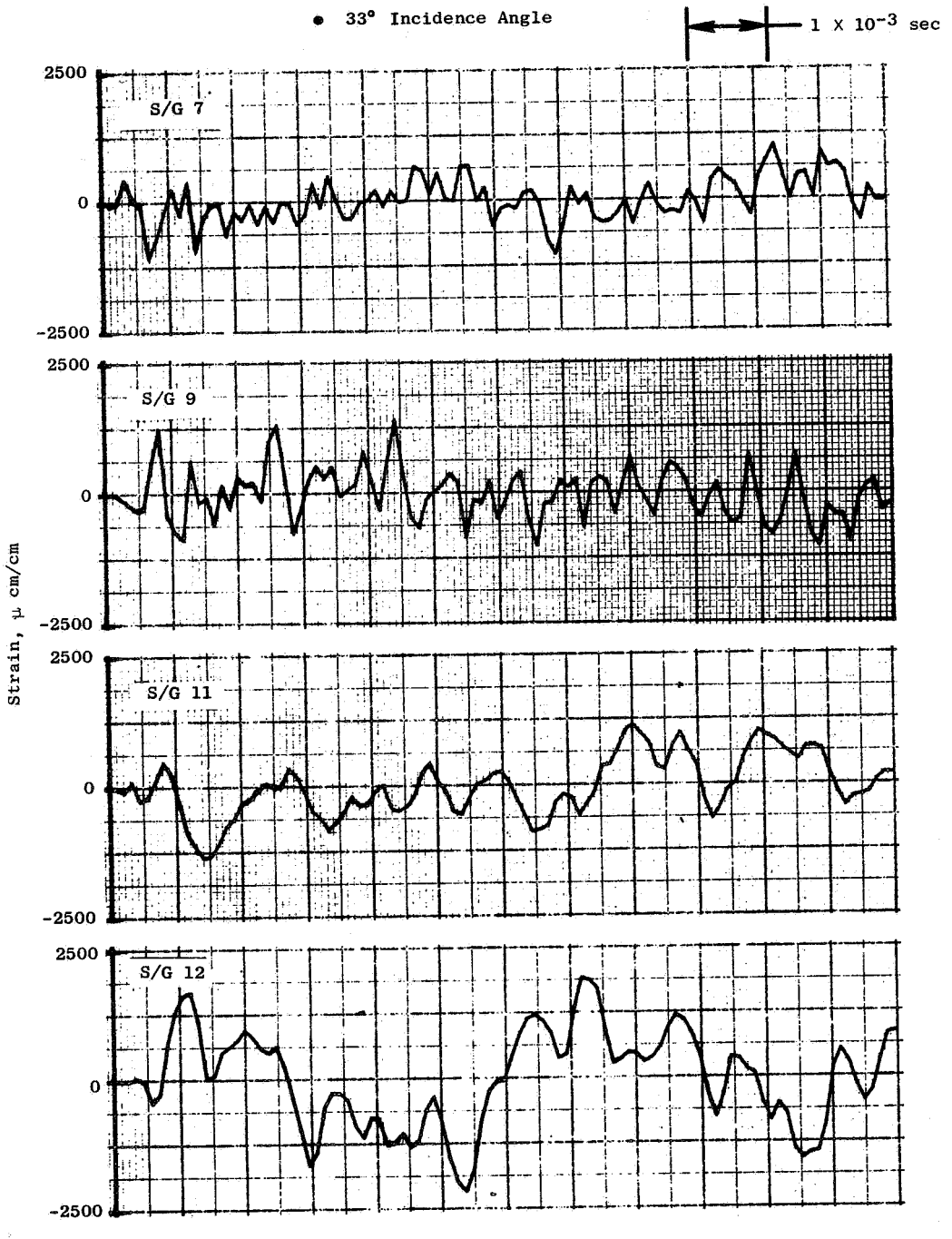

DISTRIBUTION LIST

FIBER COMPOSITE FAN BLADE IMPACT IMPROVEMENT PROGRAM

NAS3-17836 NASA CR 135078

Addressee	No. of Copies
NASA-Lewis Research Center 21000 Brookpark Road Cleveland, OH 44135 Attn: Contract Section B, MS 500-313	1
Technology Utilization Office, MS 3-19	1
AFSC Liaison Office, MS 501-3	1
AAMRDL Office, MS 500-317	1
Library, MS 60-3	2
Report Control Office, MS 5-5	1
C. C. Ciepluch, MS 501-7	1
R. J. Denington, MS 501-7	1
R. H. Kemp, MS 49-3	1
R. H. Johns, MS 49-3	1
N. T. Saunders, MS 105-1	1
C. C. Chamis, MS49-3	1
R. L. Lark, MS49-3	1
J. R. Faddoul, MS 49-3	10
NASA-Ames Research Center Moffett Field, CA 94035 Attn: Library	1
NASA-Flight Research Center P.O. Box 273 Edwards, CA 93523 Attn: Library	1
NASA-George C. Marshall Space Flight Center Huntsville, AL 35812 Attn: Library	1
NASA-Goddard Space Flight Center Greenbelt, MD 20771 Attn: Library	1
Jet Propulsion Laboratory 4800 Oak Grove Drive Pasadena, CA 91103 Attn: Library	1

Addressee	No. of Copies
NASA-Langley Research Center Hampton, VA 23365 Attn: Library	1
NASA-Lyndon B. Johnson Space Center Houston, TX 77001 Attn: Library	1
NASA-Office of Aeronautics and Space Technology Washington, DC 20546 Attn: RWS/N. Mayer RWM/J. J. Gangler	1 1
NASA-Scientific and Technical Information Facility P.O. Box 8757 Baltimore/Washington International Airport Baltimore, MD 21240 Attn: Accessioning Branch	2
Advanced Research Projects Agency Washington, DC 20525 Attn: Library	1
Air Force Aeronautical Propulsion Laboratory Wright-Patterson Air Force Base, OH 45433 Attn: TBP/T. Norbut CA/Heiser (Dr.) TBP/L. J. Obery	1 1 1
Air Force Flight Dynamics Laboratory Wright-Patterson Air Force Base, OH 45433 Attn: C. C. Wallace (FBC) P. A. Parmley	1 1
U.S. Army Materials and Mechanics Research Center Watertown Arsenal Watertown, MA 02192 Attn: Library	1
Commander Naval Air Systems Command Washington, DC 20360	1
Commander Naval Ordinance Systems Command Washington, DC 20360	1

Addressee	No. of Copies
Defense Metals Information Center Battelle Memorial Institute Columbus Laboratories 505 King Avenue Columbus, OH 43201	1
Department of the Army U.S. Army Material Command Washington, DC 20315 Attn: AMCRD-RC	1
Department of the Army U.S. Army Aviation Materials Laboratory Fort Eustis, VA 23604 Attn: Library	1
Department of the Army U.S. Army Aviation Systems Command P.O. Box 209 St. Louis, MO 63166 Attn: Library	1
Department of the Army Watervliet Arsenal Watervliet, NY 12189 Attn: Library	1
Department of the Army Plastics Technical Evaluation Center Picatinny Arsenal Dover, NJ 07801 Attn: H. E. Pebly, Jr.	1
Department of the Navy Office of Naval Research Washington, DC 20360 Attn: Library	1
Department of the Navy U.S. Naval Ship R&D Laboratory Annapolis, MD 21402 Attn: Library	1
Director Naval Research Laboratory Washington, DC 20390	1

Addressee	No. of Copies
Naval Ship Systems Command Code 03423 Washington, DC 20360 Attn: C. H. Pohler	1
National Science Foundation Engineering Division 1800 G Street, N.W. Washington, DC 20540 Attn: Library	1
National Technical Information Service Springfield, VA 22151	20
U.S. Naval Ordnance Laboratory White Oak Silver Spring, MD 20910 Attn: F. R. Barnet	1
Avco Space Systems Division Lowell Industrial Park Lowell, MA 01851 Attn: T. L. Moore M. Salkind (Dr.)	1 1
Babcock and Wilcox Company Advanced Composites Department P.O. Box 419 Alliance, OH 44601 Attn: R. C. Young	1
Battelle Memorial Institute 505 King Avenue Columbus, OH 43201 Attn: L. E. Hulbert (Dr.)	1
Bell Aerospace Division of Textron Buffalo, NY 14240 Attn: Library	1
Boeing Aerospace Company P.O. Box 3999 Seattle, WA 98124 Attn: J. T. Hoggatt, MS 47-01	1
Detroit Diesel-Allison Division General Motors Corporation Indianapolis, IN 46219 Attn: M. Herman (Dr.)	1

Addressee	No. of Copies
Deposits & Composites, Incorporated 1821 Michael Faraday Drive Reston, VA 22090 Attn: R. E. Engdahl, President	1
Douglas Aircraft Company 3855 Lakewood Boulevard Long Beach, CA 90846 Attn: R. Kawai	1
Drexel University Philadelphia, PA 19104 Attn: P. C. Chou (Professor)	1
E. I. duPont deNemours and Company, Inc. Experimental Station Wilmington, DE 19898	
Library	1
Attn: C. H. Zweben (Dr.), Bldg. 262, Rm. 433	1
Fiber Science, Incorporated 245 East 157th Street Gardena, CA 90248 Attn: L. J. Ashton	1
The Garrett Corporation AiResearch Manufacturing Company 402 South 36th Street Phoenix, AZ 85034 Attn: Dr. R. F. Kirby, Dept. 93-39M	1
General Dynamics Convair Aerospace Division Ft. Worth Operation P.O. Box 748 Ft. Worth, TX 76101 Attn: C. W. Rogers	1
General Dynamics Convair Aerospace Division P.O. Box 80847 San Diego, CA 92138 Attn: J. E. Ashton (Dr.)	1
General Electric Company Corporate Research and Development Center 1 River Road Schenectady, NY 12305 Attn: S. Levy	1

Addressee	No. of Copies
General Electric Company Lynn River Works 1000 Western Avenue Mail Drop 34505 Lynn, MA 01910 Attn: F. Erich	1
General Technologies Corporation 1821 Michael Faraday Drive Reston, VA 22070 Attn: R. G. Shaver (Dr.) Vice-President, Engineering	1
George Washington University St. Louis, MO 63130 Attn: E. M. Wu (Professor)	1
Grumman Aerospace Corporation S. Oyster Bay Road Bethpage, Long Island, NY 11714 Attn: R. N. Hadcock B. J. Aleck	1 1
Hartzell Propeller, Inc. Ben Harlamert 350 Washington Avenue Piqua, OH 45356	1
Hercules, Inc. Allegheny Ballistics Laboratory P.O. Box 210 Cumberland, MD 21052 Attn: W. T. Freeman	1
Hercules, Incorporated Wilmington, DE 19899 Attn: G. C. Kuebler	1
Hughes Aircraft Company Aerospace Group Culver City, CA 90230 Attn: R. W. Jones, (Dr.) Mail Stop D 132	1
IITRI 10 West 35th Street Chicago, IL 60616 Attn: I. M. Daniel (Dr.)	1

Addressee	No. of Copies
Illinois Institute of Technology 10 West 32nd Street Chicago, IL 60616 Attn: L. J. Broutman (Professor)	1
Lawrence Livermore Laboratory University of California P.O. Box 808, L-421 Livermore, CA 94550 Attn: T. T. Chiao	1
Lockheed - California Company Burbank, CA 91503 Attn: R. H. Stone, Dept. 74-52 Bldg. 243, Plant 2	1
Lockheed-Georgia Company Marietta, GA 30060 Attn: W. G. Juveric	1
Martin-Marietta Corporation P.O. Box 179 Denver, CO 80201 Attn: A. Holston Library	1 1
Massachusetts Institute of Technology Department of Civil Engineering Cambridge, MA 02139 Attn: F. J. McGarry (Professor)	1
Materials Science Corporation 1777 Walton Road Blue Bell, PA 19422 Attn: B. W. Rosen (Dr.)	1
McDonnell-Douglas Astronautics Company 5301 Bolsa Avenue Huntington Beach, CA 92647 Attn: R. W. Seibold, A3-253 L. B. Greszczuk	1 1
National Bureau of Standards Engineering Mechanics Section Washington, DC 20234 Attn: R. Mitchell (Dr.)	1

Addressee	No. of Copies
North American Aviation Division Rockwell, Incorporated International Airport Los Angeles, CA 90009 Attn: L. M. Lockman (Dr.)	1
Northwestern University Evanston, IL 60201 Attn: J. D. Achenbach (Professor)	1
United Technologies Corporation Hamilton Standard Division Windsor Locks, CT 06096 Attn: L. Stoltze E. Rothman W. Percival	1 1 1
Pratt & Whitney Aircraft Division United Technologies Corporation 400 Main Street East Hartford, CT 06108 Attn: F. Ver Schneider T. Zupnik F. Mahler T. Dennis	1 1 1 1
Purdue University West Lafayette, IN 47906 Attn: C. T. Sun (Professor)	1
Sikorsky Aircraft Division United Technologies Corporation Stratford, CT 06602 Attn: Library	1
Southwest Research Institute 8500 Culebra Road San Antonio, TX 78284 Attn: T. Anyos	1
Structural Composites Industries, Inc. 6344 North Irwindale Avenue Azusa, CA 91702 Attn: E. E. Morris Vice President	1

Addressee	No. of Copies
TRW, Incorporated 23555 Euclid Avenue Cleveland, OH 44115	
Attn: W. E. Winters	1
I. Toth (Dr.)	1
E. Barrett, T/M 3417	1
Union Carbide Corporation Carbon Products Division P.O. Box 6116 Cleveland, OH 44101	
Attn: J. C. Bowman, Director Research and Advanced Technology	1
United Aircraft Research Laboratories United Technologies Corporation East Hartford, CT 06108	
Attn: M. DeCrescente (Dr.)	1
University of California, Los Angeles School of Engineering and Applied Science Los Angeles, CA 90024	
Attn: B. S. Dong (Professor)	1
University of Dayton Research Institute Dayton, OH 45409	
Attn: F. K. Bogner	1
University of Florida Gainesville, FL 32611	
Attn: R. L. Sierakowski (Professor)	1
University of Illinois Department of Theoretical and Applied Mechanics Urbana, IL 61801	
Attn: H. T. Corten (Professor)	1
Vertol Division The Boeing Company Philadelphia, PA 19142	
Attn: R. A. Pinkney	1
Whittaker Corporation Research and Development Center 3540 Aero Court San Diego, CA 92123	
Attn: Library	1